

PRODUCTION OF INORGANIC CHARGE SELECTIVE LAYERS FOR
MESOSCOPIC PEROVSKITE SOLAR CELLS

A THESIS SUBMITTED TO
THE GRADUATE SCHOOL OF NATURAL AND APPLIED SCIENCES
OF
MIDDLE EAST TECHNICAL UNIVERSITY

BY

KEREM AĐATAY İLİ

IN PARTIAL FULFILLMENT OF THE REQUIREMENTS
FOR
THE DEGREE OF DOCTOR OF PHILOSOPHY
IN
THE DEPARTMENT OF MICRO AND NANOTECHNOLOGY

MAY 2018

Approval of the thesis:

**PRODUCTION OF INORGANIC CHARGE SELECTIVE LAYERS FOR
MESOSCOPIC PEROVSKITE SOLAR CELLS**

submitted by **KEREM ÇAĞATAY İÇLİ** in partial fulfillment of the requirements
for the degree of **Doctor of Philosophy in Micro and Nanotechnology**
Department, Middle East Technical University by,

Prof. Dr. Halil Kalıpçılar
Dean, Graduate School of **Natural and Applied Sciences**

Prof. Dr. Burcu Akata Kurç
Head of Department, **Micro and Nanotechnology**

Prof. Dr. Ahmet Macit Özenbaş
Supervisor, **Metallurgical and Materials Eng. Dept., METU**

Prof. Dr. Burcu Akata Kurç
Co-Supervisor, **Micro and Nanotechnology Dept., METU**

Examining Committee Members:

Prof. Dr. Mehmet Parlak
Physics Dept., METU

Prof. Dr. Ahmet Macit Özenbaş
Metallurgical and Materials Eng. Dept., METU

Prof. Dr. Aynur Eray
Physics Eng. Dept., Hacettepe Uni.

Assoc. Prof. Dr. Hüsni Emrah Ünalın
Metallurgical and Materials Eng. Dept., METU

Assoc. Prof. Dr. Nurdan Demirci Sankır
Materials Science and Nanotechnology Eng., TOBB
Economy and Technology University

Date:

...

I hereby declare that all information in this document has been obtained and presented in accordance with academic rules and ethical conduct. I also declare that, as required by these rules and conduct, I have fully cited and referenced all material and results that are not original to this work.

Name, Last name : Kerem aęatay İli

Signature :

ABSTRACT

PRODUCTION OF INORGANIC CHARGE SELECTIVE LAYERS FOR MESOSCOPIC PEROVSKITE SOLAR CELLS

İçli, Kerem Çağatay

PhD, Micro and Nanotechnology Program

Supervisor: Prof. Dr. A. Macit Özenbaş

Co-Supervisor: Prof. Dr. Burcu Akata Kurç

May 2018, 210 pages

In this work, nanoparticles of lithium doped nickel oxide (NiO) were synthesized by common wet chemistry methods like precipitation, ultrasonic spray pyrolysis and flame spray pyrolysis methods. Synthesized nanoparticles were employed in fully metal oxide mesoscopic perovskite based solar cells. Lithium doping of NiO was achieved by ultrasonic spray pyrolysis method and flame spray pyrolysis methods. Flame spray pyrolysis method was used to synthesize yttrium doped titanium dioxide (TiO₂) and magnesium oxide (MgO) nanoparticles. NiO nanoparticles which were produced by precipitation technique yielded 20-30 nm particles sizes with homogeneous distribution size and dispersed in isopropanol by ball milling without addition of any surfactants. Stable dispersions were deposited on a mesoscopic perovskite solar cell as the hole transport medium as a replacement of polymeric hole conductors and 10.89% efficiency was obtained for the optimized structure. Electrochemical impedance spectroscopy measurements revealed that recombination resistance of cells were greatly enhanced upon addition of the NiO electron blocking layer and electron blocking property of the NiO was also confirmed by ultraviolet photoelectron spectroscopy. Lithium doped NiO nanoparticles, yttrium doped TiO₂ nanoparticles and MgO nanoparticles were produced by a unique methanol combustion flame synthesis method and employed as the mesoporous layers

in carbon based perovskite solar cells. It was shown that enhancement of the electrical conductivity of the lithium doped NiO and yttrium TiO₂ layers lead to a reduction of the overall resistivity of the carbon based perovskite solar cell and efficiency of 9.63% was achieved.

Keywords: Lithium doped nickel oxide, flame synthesis method, perovskite solar cell

ÖZ

MEZOSKOPİK PEROVSKİT GÜNEŞ HÜCRELERİ İÇİN İNORGANİK SEÇİCİ TAŞIYICI KATMANLARIN ÜRETİLMESİ

İçli, Kerem Çağatay

Doktora, Mikro ve Nanoteknoloji Programı

Tez Yöneticisi: Prof. Dr. A. Macit Özenbaş

Ortak Tez Yöneticisi: Prof. Dr. Burcu Akata Kurç

Mayıs 2018, 210 sayfa

Bu çalışmada lityum katkılı nikel oksit (NiO) nanoparçacıkları, çöktürme, ultrasonik sprej ve alev sprej gibi kimyasal metotlar ile sentezlenmiştir. Sentezlenen nanoparçacıklar tamamen metal oksit yapıları mezoskopik perovskit esaslı hücrelerin yapımında kullanılmıştır. NiO parçacıklarının lityum katkılanması ultrasonik sprej ve alev sprej metotlarıyla yapılmış olup, bu metotlarla aynı zamanda yttriyum katkılı titanyum dioksit (TiO₂) ve magnezium dioksit (MgO) nanoparçacık sentezi de gerçekleştirilmiştir. Çöktürme metodu ile sentezlenen NiO nanoparçacıkları 20-30 nm boyutunda ve homojen boyut dağılımı göstermektedir ve isopropanol içerisinde yüzey ajanı olmadan toplu öğütme ile disperse edilmiştir. Stabilize edilmiş dispersiyonlar, mezoskopik perovskite hücrelerindeki polimerik boşluk taşıyıcı tabakalar yerine kaplanmıştır ve %10,89 verim değeri elde edilmiştir. Elektrokimyasal empedans spektroskopisi yöntemi ile NiO elektron bloklayıcı tabakanın yeniden birleşme kayıplarını büyük ölçüde azalttığı görülmüş ve NiO tabakanın bu özelliği ultraviyole fotoelektron spektroskopisi ölçümleri ile de onaylanmıştır. Lityum katkılı NiO, yttriyum katkılı TiO₂ ve MgO nanoparçacıkları özgün bir metanol yanma yöntemi ile sentezlenmiş ve karbon esaslı perovskit hücrelerdeki mezoskopik tabakaların üretimi için kullanılmıştır. Lityum katkılı NiO ve yttriyum katkılı TiO₂ parçacıklarının katkılanma sonucu elektriksel iletkenliğinin

arttırılması ile hücre içi direncin azaltıldığı gösterilmiştir ve karbon esaslı perovskit güneş hücresinde %9.63 verim değeri elde edilmiştir.

Anahtar Sözcükler: Lityum katkılı nikel oksit, alevle sentezleme metodu, perovskit güneş hücresi

To My Family

ACKNOWLEDGEMENTS

I am very grateful to my supervisor Prof. Dr. A. Macit Özenbaş for his guidance and support during this work, and his great attention and patience on me from beginning until the end of my graduation.

I am very grateful to my laboratory colleagues Murat Güneş, Bahadır Can Kocaoğlu, Halil İbrahim Yavuz, Burak Coşar, Berk Akbay, Utku Er, Merve Ertuğrul, Burak Yurdakul, Başar Süer and Çağrı Özdilek for their support and friendship at every stage of this work and my graduation.

I am very grateful to METU Metallurgical and Materials Engineering Department for all the support provided during this study. I want to thank to Prof. Dr. Hüsnü Emrah Ünal and staff of Nanomaterials and Devices Laboratory for hospitality during the work in their facility.

I want to acknowledge İbrahim Çam and İlker Yıldız from METU Central Laboratory for their attention during the characterization studies in this work.

This work was also supported by GÜNAM (Center for Solar Energy Research and Applications) at METU. I want to thank to Prof. Dr. Mehmet Parlak for support during the characterizations in the facilities.

I want to thank to my family, for their great patience and intense support, not only during this work but at every stage of my life.

TABLE OF CONTENTS

ABSTRACT	v
ÖZ	vii
ACKNOWLEDGEMENTS	x
TABLE OF CONTENTS	xi
LIST OF TABLES	xv
LIST OF FIGURES	xvi
ABBREVIATIONS.....	xxiii
CHAPTERS	
1. INTRODUCTION	1
REFERENCES.....	5
2. SOLAR ENERGY MATERIALS AND MESOSCOPIC PEROVSKITE	
SOLAR CELLS	7
2.1. Photovoltaic Energy Production	7
2.1.1. Solar Spectrum and Irradiance	8
2.1.2. Semiconductors and Structure of Solar Cells	10
2.1.3 Formation of pn Junctions	12
2.1.4 Absorption of Light by The Solar Cell	13
2.1.5 Carrier Transport in Solar Cells	14
2.1.6 Recombination in Solar Cells	16
2.2 Solar Cell Materials and Solar Cell Types	18
2.2.1 Crystalline Silicon Solar Cells	18
2.2.2 Thin Film Silicon Solar Cells	20
2.2.3 Gallium Arsenide Solar Cells	21
2.2.4 Cadmium Telluride Solar Cells.....	22
2.2.5 Copper (Indium, Gallium) Diselenide Solar Cells	22
2.2.6 Dye Sensitized Solar Cells	23
2.3 Perovskite Solar Cells	25
2.3.1 Perovskite Crystal Structure	27

2.3.2 Organic-Inorganic Hybrid Mesoporous Perovskite Solar Cells	30
2.3.3 Device Architectures of Perovskite Solar Cells	35
2.3.3.1 Mesoscopic Architecture Perovskite Solar Cells	36
2.3.3.2 Planar Architecture Perovskite Solar Cells	40
2.3.4 Deposition Methods of Perovskite Layers	43
2.3.4.1 One-step Deposition	44
2.3.4.2 Two-step Deposition	45
2.3.5 Hole Transport Materials For Perovskite Solar Cells	47
2.3.5.1 Organic Hole Transport Materials	47
2.3.5.2 Nickel Oxide (NiO) Based Inorganic Hole Transport Materials	49
2.3.5.2.1 Nickel Oxide In Mesoporous Cells	50
2.3.5.2.2 Nickel Oxide In Planar Cells	54
REFERENCES	57
3. EXPERIMENTAL METHODS	67
3.1 Nanopowder Synthesis	68
3.1.1 Precipitation Technique	68
3.1.2 Hydrothermal Synthesis	70
3.1.3 Ultrasonic Spray Pyrolysis (USP) Synthesis of Nanoparticles	71
3.1.4 Flame Spray Pyrolysis (FSP) Synthesis of Nanoparticles	73
3.2 Thin Film Deposition	75
3.2.1 Ultrasonic Spray Pyrolysis Deposition of Thin Films	75
3.2.2 Spin Coating for Thin Film Deposition	77
3.2.3 Screen Printing Method	79
3.3 Construction of Hybrid Mesoporous Perovskite Based Solar Cells	81
3.3.1 Etching and Substrate Cleaning	81
3.3.2 Preparation of Blocking Layer	82
3.3.3 Preparation of Mesoporous Layers	83
3.3.3.1 Preparation of Screen Printing Pastes	83
3.3.3.2 Deposition of Mesoporous Layers by Spin Coating	84
3.3.3.3 TiCl ₄ Treatment of Mesoporous Layers	85

3.3.4 Deposition of Perovskite Layers	85
3.3.4.1 One-Step Perovskite Deposition	85
3.3.4.2 Two-step Perovskite Deposition	86
3.3.4.3 Adduct Method For Perovskite Deposition	87
3.3.5 Deposition of Back Contacts	89
3.4 Characterizations of The Perovskite Solar Cells	90
3.4.1 Electrochemical Impedance Spectroscopy (EIS)	90
3.4.1.1 Fundamentals of Electrochemical Impedance Spectroscopy	90
3.4.1.2. Impedance Analysis of Mesoporous Perovskite Solar Cells	93
REFERENCES	97
4. PRODUCTION OF Li DOPED NiO NANOPARTICLES AND THIN FILMS FOR MESOPOROUS PEROVSKITE SOLAR CELLS	101
4.1 NiO Nanoparticle Synthesis	102
4.1.1 Production of NiO and Li:NiO nanoparticles with solvothermal method	102
4.1.1.1 Experimental	102
4.1.1.2 Characterization of NiO and Li:NiO Nanoparticles Produced by Solvothermal Method	102
4.1.2 Production of NiO and Li:NiO Nanoparticles with USP	109
4.1.2.1 Experimental	109
4.1.2.2 Characterization of NiO and Li:NiO Nanoparticles Produced by USP Method	110
4.2 NiO and Li:NiO Thin Film Deposition	113
4.2.1 Production of NiO and Li:NiO Thin Films with USP Method	113
4.2.1.1 Experimental	113
4.2.1.2 Characterization of NiO and Li:NiO Thin Films Deposited by USP	113
4.2.2 Production of NiO and Li:NiO Thin Films with Spin Coating Method	116

4.2.2.1 Experimental	116
4.2.2.2 Characterization of NiO and Li:NiO Thin Films Deposited by Spin Coating Method	117
4.3 Construction and Characterization of Mesoporous Perovskite Cells	122
4.3.1 Experimental	122
4.3.2 Characterizations of the perovskite solar cells	123
4.4 Conclusions	133
REFERENCES	135
5. NICKEL OXIDE NANOPARTICLES FOR N-I-P STRUCTURED PEROVSKITE SOLAR CELLS	
5.1 Introduction	137
5.2 Experimental Studies	139
5.2.1 NiO nanoparticle dispersion preparation	139
5.2.2 Cell construction	139
5.2.3 Characterizations	140
5.3 Results and discussion	141
5.4 Conclusions	161
REFERENCES	163
6. PRODUCTION OF MESEPOROUS LAYERS IN CARBON BASED PEROVSKITE SOLAR CELLS BY FLAME SPRAY METHOD	
6.1 Introduction	169
6.2 Experimental	171
6.2.1 Production and deposition of metal oxide nanoparticles by flame spray coating	171
6.2.2 Construction of carbon based perovskite solar cells	172
6.2.3 Characterizations	173
6.3 Results	173
6.4 Conclusion	195
REFERENCES	197
7. CONCLUSIONS AND SUGGESTIONS.....	201
CURRICULUM VITAE.....	207

LIST OF TABLES

TABLES

Table 2.1 Elements used in semiconductors	10
Table 2.2 Type of mesoporous layers and deposition method of carbon based cell..	52
Table 3.1 Common circuit elements used in EIS analysis.....	91
Table 4.1 BET surface area measurements of the powders produced by direct precipitation method (DP) and assisted precipitation (AP) method.....	104
Table 4.2 Cell parameters of perovskite solar cells depending on the blocking layer thickness, prepared by one-step method.....	123
Table 4.3 Cell parameters of perovskite solar cells depending on the mesoporous layer thickness, prepared by one-step method.....	124
Table 4.4 Cell parameters of perovskite solar cells depending on perovskite layer deposition method.....	124
Table 4.5 Cell parameters of perovskite solar cells employing nickel oxide, CuSCN and hole conductor free configuration.....	133
Table 5.1 BET surface area and corresponding particle size values of NiO nanopowders heat treated at different temperatures.....	145
Table 5.2 Cell parameters of the devices prepared by different spin speeds of NiO dispersion.....	154
Table 6.1 BET specific surface area of the synthesized powders before and after heat treatment at 500°C.....	176
Table 6.2 Actual doping concentration of powders compared to the precursor solutions of Y:TiO ₂ and Li:NiO nanoparticles.....	178
Table 6.3 Cell parameters of the carbon based solar cells constructed using flame spray deposited nanoparticles.....	187
Table 6.4 Charge transfer resistance (R _{ct}) and recombination resistance (R _{rec}) values of the NiO and Li:NiO based cells calculated from the impedance data.....	194

LIST OF FIGURES

FIGURES

Figure 2.1 Distribution of light intensities for each wavelength in solar spectrum in space and on sea level.....	9
Figure 2.2 Positions of donor and acceptor states in semiconductors upon doping.....	11
Figure 2.3 Band diagram of a pn junction and band bending.....	12
Figure 2.4 Summary of recombination processes in semiconductors.....	17
Figure 2.5 Structure of a silicon solar cell.....	19
Figure 2.6 Schematic structure of a DSSC.....	24
Figure 2.7 National Renewable Energy Laboratory best research cell efficiencies chart.....	26
Figure 2.8 Structure of perovskite type crystals with the general ABX_3 form.....	28
Figure 2.9 Phase transition of perovskite lattice from tetragonal to high temperature stable phase of cubic structure.....	29
Figure 2.10 Device architectures of mesoporous solar cells with different absorber and hole conductors.....	31
Figure 2.11 Schematic representation and SEM image of a typical solid state perovskite sensitized solar cell.....	34
Figure 2.12 Device architectures of perovskite solar cells.....	36
Figure 2.13 Cross-sectional SEM image of a mesoporous perovskite solar cell employing insulating Al_2O_3 scaffolding layer.....	38
Figure 2.14 Energy levels of components of perovskite solar cells in n-i-p and p-i-n inverted configurations.....	42
Figure 2.15 Anti-solvent approach for one-step perovskite deposition.....	45
Figure 2.16 Various hole conducting materials employed in perovskite solar cells so far.....	47
Figure 2.17 Energy band diagrams of the inorganic p-type materials which satisfy the electronic band condition in perovskite solar cells.....	49

Figure 2.18 Schematic representation a mesoporous carbon based device.....	50
Figure 2.19 Schematic illustration of a p-type mesoscopic p-i-n solar device employing NiO mesoporous layers.....	53
Figure 2.20 Schematic structure of an inverted p-i-n type planar perovskite solar cell employing NiO layers.....	55
Figure 3.1 Scheme of particle formation and agglomerate formation in colloidal solutions during precipitation.....	69
Figure 3.2 Schematic representation of an USP particle generation system.....	72
Figure 3.3 USP system used in nanoparticle synthesis during the work.....	73
Figure 3.4 Particle formation processes under vapor feeding or liquid feeding conditions in flame spray pyrolysis method.....	74
Figure 3.5 Schematic representation of ultrasonic spray deposition system equipped in this work.....	76
Figure 3.6 USP thin film deposition device used for thin film coatings during the work.....	77
Figure 3.7 Stages of film formation during spin coating process.....	78
Figure 3.8 Apparatus for screen printing of thick films used during the work in this study and screen printing deposition process stages.....	80
Figure 3.9 SEM image of a 50 nm TiO ₂ blocking layer on FTO substrate deposited by spin coating in this work.....	82
Figure 3.10 SEM image of a 200 nm mesoporous TiO ₂ layer deposited on FTO substrate by spin coating in this work.....	84
Figure 3.11 SEM of perovskite layer deposited on mesoporous TiO ₂ layer by one- step deposition method, showing the perovskite crystals embedded inside mesoporous matrix, in this work.....	86
Figure 3.12 SEM image of the cuboid shaped perovskite crystals deposited on TiO ₂ mesoporous matrix by two-step deposition, in this work.....	87
Figure 3.13 SEM image of the perovskite layers deposited on TiO ₂ matrix by adduct method showing the continuous and regular perovskite layer on the mesoporous matrix compared to one-step and two-step methods, in this work.....	88

Figure 3.14	A typical mesoporous perovskite solar cell constructed in this work after Au evaporation and deposition of silver contacts.....	89
Figure 3.15	Nyquist plot of a typical Randles cell with the equivalent circuit.....	93
Figure 3.16	Transmission line model for interpretation of EIS spectrum of a mesoporous sensitized based solar cell.....	94
Figure 3.17	Nyquist plot of a NiO based mesoporous perovskite solar cell constructed in this work and the equivalent circuit used to model the cell.....	95
Figure 4.1	SEM images of NiO powders produced by direct precipitation (a, b, c) and agent assisted precipitation methods (d).....	104
Figure 4.2	XRD patterns of direct precipitated powders before (a) and after (b) heat treatment.....	106
Figure 4.3	Variation of resistivity values of NiO nanopowders with Li doping amount (a), Li content of powders measured with ICP-OES (b) and XRD spectra of Li:NiO powder with Li/Ni ratio of 0.4 (c).....	109
Figure 4.4	SEM images of Li:NiO particles produced by ultrasonic method from methanolic precursors having molarities of 0.3M (a), 0.15M (b), 0.075M (c), 0.035M (d).....	110
Figure 4.5	Resistivity values of Li:NiO powders for different doping amounts (a), XRD spectra of the $\text{Li}_{0.1}\text{Ni}_{0.9}\text{O}$ powders (b).....	112
Figure 4.6	SEM images of NiO thin films deposited by direct spraying on hot substrate (a,b) and the two stage coated substrate (c,d).....	114
Figure 4.7	Change of resistivity values of Li:NiO thin films with varying Li content in the starting solution (a), XRD spectra of Li:NiO sample with Li/Ni ratio of 0.6 (b).....	115
Figure 4.8	SEM images of Li:NiO films produced by spin coating of a DMF based solution and fired at 400°C (a,b) and fired at 625°C (c,d).....	117
Figure 4.9	Resistivity values of Li:NiO thin films for different Li doping amounts fired at 450°C (a) and 625°C (b).....	119

Figure 4.10 I-V characteristic of the FTO/Li:NiO heterojunction(a), cross sectional SEM view of the junction (b) and XRD spectra of the heterojunction (c).....	121
Figure 4.11 SEM images of the surfaces and cross sections of the devices produced by one-step method (a,b), two-step method (c,d) and adduct method (e,f).....	125
Figure 4.12 XRD of perovskite layers on glass substrates deposited by adduct method (a) and two step method (b) and photoluminescence spectra of the adduct perovskite layer (c).....	128
Figure 4.13 SEM image (a) and J-V curve (b) of the inverted type solar cell.....	129
Figure 4.14 SEM images of solar cells without hole conductor (a), with CuSCN (b) and with nickel oxide layer (c,d).....	130
Figure 4.15 J-V curves (a) and PL spectra (b) of nickel oxide, CuSCN and hole conductor free cells.....	132
Figure 5.1 XRD spectra of NiO powders heat treated at different temperatures....	142
Figure 5.2 XPS spectra of powders heat treated at 300°C for 5 min showing Ni 2p core levels.....	143
Figure 5.3 XPS spectra of powders heat treated at 300°C for 5 min showing O 1s core levels.....	14
Figure 5.4 Particle size distribution of particles ball milled at 24 h (I), 48 h (II), 12 h (III) and non milled (IV), measured by laser diffraction. The inset image shows dispersions of the powders in isopropanol after storage of 3 days.....	146
Figure 5.5 3D-AFM image of the powders deposited on glass substrates from stable dispersions.....	146
Figure 5.6 High resolution SEM image of the powders after milling for 24 h.....	147
Figure 5.7 TEM image of the agglomerates, revealing the fine crystallite size about 5-7 nm.....	147
Figure 5.8 UPS spectra of the NiO powders employed in the perovskite cells at the cut-off and onset energies.....	148

Figure 5.9 UV-Visible light transmission of the powders deposited from isopropanol dispersion on glass substrates and Tauc plot given in the inset image...	149
Figure 5.10 Band diagram of nickel oxide particulate films showing the fermi level (E_f), conduction band minimum (CBM) and valence band maximum (VBM) derived from UPS measurements with respect to that of perovskite.....	150
Figure 5.11 Photoluminescence quenching measurements of the perovskite films deposited on bare glass substrates and on the NiO layer.....	151
Figure 5.12 Schematic illustration of mesoscopic n-i-p configuration of perovskite solar cell constructed in this work.....	151
Figure 5.13 Cross sectional SEM image of the cells prepared in this work.....	152
Figure 5.14 J-V curves of the hole conductor free and NiO based cells with different spin speeds under simulated AM 1.5 conditions.....	153
Figure 5.15 Efficiency distribution of NiO based perovskite solar cells deposited by 3000 rpm speed, using the NiO dispersion, calculated from 20 individual cells.....	155
Figure 5.16 Dependence of J-V characteristics of the NiO based cell on scan direction.....	156
Figure 5.17 Dependence of J-V characteristics of hole conductor free cell on scan direction.....	156
Figure 5.18 Stability of photocurrent density of the hole conductor free and NiO based cells under constant illumination of 100 mW/cm^2 for 1 min....	157
Figure 5.19 Nyquist plots of the perovskite solar cells with NiO layer at 0V and 0.5V. Inset image shows the equivalent circuit model used to fit impedance data.....	158
Figure 5.20 Nyquist plots of hole conductor free devices at 0V and 0.5V.....	159
Figure 5.21 Charge transport resistances of two cells with increasing applied voltage.....	160
Figure 5.22 Recombination resistances of the cells with increasing applied voltage.....	161

Figure 6.1 XRD spectrum of nanoparticles produced by flame spray method, TiO ₂ (a), NiO (b) and MgO (c).....	174
Figure 6.2 SEM images of nanoparticles produced by flame spray on FTO substrates, TiO ₂ (a), MgO (b), NiO (c) and TiO ₂ , MgO, NiO stacking layers (d).....	175
Figure 6.3 Two point resistivity values of Y:TiO ₂ and Li:NiO nanoparticles depending on the dopant amount in the precursor solution.....	177
Figure 6.4 XPS spectra of Ti 2p core levels for undoped TiO ₂ nanoparticles.....	179
Figure 6.5 XPS spectra of Ti 2p core levels for 2% yttrium doped TiO ₂ nanoparticles.....	179
Figure 6.6 XPS spectra of O1s core levels for undoped TiO ₂ nanoparticles.....	180
Figure 6.7 XPS spectra of O 1s core levels for 2% yttrium doped TiO ₂ nanoparticles.....	180
Figure 6.8 XPS spectra of Y 3d core levels for 2% yttrium doped TiO ₂ nanoparticles.....	181
Figure 6.9 XPS spectra of Ni 2p core levels for undoped NiO nanoparticles.....	182
Figure 6.10 XPS spectra of Ni 2p core levels for 10% lithium doped NiO nanoparticles.....	182
Figure 6.11 XPS spectra of O1s core levels for undoped NiO nanoparticles.....	183
Figure 6.12 XPS spectra of O1s core levels for 10% lithium doped NiO nanoparticles.....	183
Figure 6.13 J-V curves of the carbon based cells with and without 5-AVAI addition to the perovskite precursor solution.....	185
Figure 6.14 SEM image of a stacking layer of TiO ₂ /MgO/NiO (a) and the corresponding line EDX analysis (b).....	186
Figure 6.15 J-V curves of the carbon based perovskite solar cells constructed using undoped particles.....	186
Figure 6.16 J-V curves of the carbon based perovskite solar cells constructed using doped particles.....	187

Figure 6.17 Onset (a) and cut-off (b) energies of TiO ₂ nanoparticles and onset (c) and cut-off (d) energies of NiO nanoparticles extracted from UPS measurements.....	189
Figure 6.18 Schematic representation of band structures of the particles produced in this work extracted from UPS measurements, together with that of perovskite and MgO layer.....	190
Figure 6.19 Nyquist plots of the best performing cell in a TiO ₂ /MgO/Li:NiO configuration recorded under dark and illumination for 0V and 0.8 V applied bias.....	192
Figure 6.20 Nyquist plots of doped and undoped NiO cells (a), variation of charge transfer resistance at the carbon electrode (b) and recombination resistance at TiO ₂ /perovskite interface (c) and Nyquist plot of yttrium doped TiO ₂ based cell (d).....	193

ABBREVIATIONS

DSSC	: Dye Sensitized Solar Cell
PSC	: Perovskite Solar Cell
FTO	: Fluorine doped Tin Dioxide
ITO	: Indium Tin Oxide
SEM	: Scanning Electron Microscope
XPS	: X-Ray Photoelectron Spectroscopy
EIS	: Electrochemical Impedance Spectroscopy
XRD	: X-Ray Diffraction
UPS	: Ultraviolet Photoelectron Spectroscopy
BET	: Brunauer–Emmett–Teller
PCBM	: [6,6]-phenyl-C61-butyric acid methyl ester
PEDOT:PSS	: Poly(3,4-ethylenedioxythiophene) polystyrene sulfonate
spiro-OMETAD	: 2,2',7,7' - tetrakis - (N,N - di - p - methoxyphenyl - amine) – spiro bifluorene
BL	: Blocking layer
HTM	: Hole Transport Medium
Voc	: Open Circuit Voltage
Jsc	: Short Circuit Density
FF	: Fill Factor

CHAPTER 1

INTRODUCTION

Perovskite organic-inorganic hybrid halide photovoltaic materials with perovskite crystal structure have been a hot topic since 5 years and tremendous progress have been achieved in perovskite solar technology, efficiencies boosted to 22% already. Perovskite mesoscopic solar cells have evolved from the third generation solar devices like organic solar cells and mostly dye sensitized solar cells. In addition to enhanced efficiencies offered by these materials, perovskite solar cells also promise improved robustness and outdoor stability by means of solid state devices and inorganic materials used in the construction of these cells, where liquid electrolyte used in dye sensitized solar cells or highly unstable polymeric materials in organic solar cells is a major drawback of the large scale producibility of the third generation photovoltaics.

Although highest efficiencies for perovskite solar cells reported to date are based on polymeric hole conductors like spiro-ometad or PCBM, due to insufficient air stability and high cost of these materials or cyanide containing toxic inorganic materials like CuSCN, the mass production of perovskite based solar cells is still limited. Attempts have been focused on replacing the hole conductors with robust oxide counter parts or directly eliminating the hole conductor layer. After realization of electron conducting ability of the perovskite layer, hole conducting perovskite layers are under investigation. First demonstration of a hole conductor free perovskite solar cell was achieved by Etgar et al. [1], where TiO_2 nanosheets were used as the electron transport layer supporting a perovskite layer as the absorber and hole conducting layer and gold as the back contact, in a similar configuration to early reported depleted heterojunction devices employing inorganic

quantum dots. An efficiency of 5.5% was reported showing the impressive hole conducting ability of the perovskite nanocrystals. Following works revealed that in this structure, a depletion arises between the mesoporous TiO₂ layer and the perovskite layer and by estimating the doping density of TiO₂ and perovskite layer using Mott-Shottky analysis, a built in potential of 0.67 V was calculated which is close to the Voc of the cell [2]. An ideal current voltage model developed for further investigation of the junction properties of cell also confirmed the heterojunction nature [3]. Optimization of the mesoporous layer thickness and application of sequential deposition technique yielded efficiencies up to 10.85% and also a correlation between depletion layer width and cell efficiency has been found in the same work [4], suggesting that extending the depletion region width to whole cell may lead to further improvements.

In another approach to avoid hole conducting layers, Ku et al. used porous carbon back contact as the current collecting electrode. Perovskite nanocrystals were deposited inside the TiO₂ mesoporous layer and into a mesoporous ZrO₂ layer which acts as an insulating barrier between TiO₂ and carbon layer in order to avoid direct contact between two layers. Carbon is an appropriate back contact material with a work function of -5 eV where gold has a work function of -5.1 eV. This configuration not only possess an hole conducting free cell configuration, but also eliminates high vacuum requiring gold evaporation process and whole cell components are prepared by simple solution based and printing techniques yielding an efficiency value up to 6.7% [5]. This efficiency value then further improved to impressive 12.8% by introduction of 5-aminovaleic acid (5-AVAI) into perovskite layer [6]. Role of 5-AVAI here is explained as a template assisted preferential growth of perovskite crystals in the c axis resulting in better pore filling inside mesoporous layers which reduces recombination rates and improved contact between TiO₂ and perovskite crystals.

Nickel oxide is a well known p type material and a suitable candidate for robust and low cost hole conducting layers. However, deposition of nickel oxide layers

requires high temperature heat treatments so inverted type cell architectures are used. In this cell design, hole transport materials are deposited on the transparent and conducting electrode like ITO or FTO and cells are illuminated from the cathode part. First attempts to employ nickel oxide (NiO) mesoporous layers on an inverted structure yielded an efficiency of 1.5% [7] and this value was quickly enhanced to 9.51% by solution processed NiO_x compact layer and a mesoporous layer similar to conventional TiO₂ based devices [8]. Perovskite crystals are infiltrated into the mesoporous layer and PCBM is used as the electron selective layer on top of the nickel oxide matrix. Transient absorption studies verified that cell working mechanism of the cell is based on an effective p-type sensitization of mesoporous NiO layers which could not be possible for dye sensitized solar cells. The unique electron transport property of perovskite crystals is responsible from high efficiency values obtained from p-type layers. NiO compact layers were also used in an inverted planar cell structure in order to replace low stability PEDOT:PSS hole accepting layers. Jeng et al. demonstrated that in a planar heterojunction configuration, NiO_x blocking layers outperforms PEDOT:PSS layers by means of efficiency and open circuit voltage related to proper band energy level alignment between NiO_x and perovskite layer [9]. In a similar work, planar NiO_x layers were employed as blocking layers in planar configuration and in comparison to CuSCN deposited by electrodeposition method, giving two fold higher efficiencies [10]. Deposition of dense and uniform NiO layers were also conducted by vacuum techniques like magnetron sputtering and effect of thin film morphology was investigated. Magnetron sputtered NiO blocking layers in a planar cell configuration are reported to create more homogeneous and dense layers compared to spin coated solution processed layers and by benefiting from solution engineered fully covered perovskite layers, an efficiency of 9.83% and impressive open circuit voltage of 1.1 V was achieved thanks to minimized recombination between adjacent layers [11]. In addition to morphology, electrical properties of the magnetron sputtered compact NiO layer was also investigated in an inverted cell structure in combination with a mesoporous NiO layer and oxygen doping was demonstrated to be an effective way of enhancing the electrical conductivity of the

layer and an efficiency of 11.6% was achieved [12]. Modification of the electrical properties of NiO layers by dopant atoms for enhanced conductivity was further investigated by copper addition to NiO lattice and a planar heterojunction solar cell achieved 15.4% efficiency compared to undoped NiO layer and PEDOT:PSS layer which have 8.73% and 10.87% efficiencies respectively. It was also observed that perovskite layer on top of copper doped NiO layers shows micrometer scale grain sizes compared to undoped NiO layer which may be attributed to difference in grain sizes of the NiO layers and surface chemistry change upon copper doping leading to the high efficiency value observed in the devices [13]. Mesoporous NiO layers were also used in conventional anode side illuminated cell configuration as a hole transport layer on top of a mesoporous TiO₂ layer. In this work, a porous carbon based back contact is employed similar to the hole conducting free design which make it possible to infiltrate the perovskite nanocrystals into the porous layers printed and fired together in one batch and 11.4% efficiency value is reported [14].

The objective of this work is to develop mesoscopic perovskite solar cells with no polymeric components, in a robust fully metal oxide structure for prolonged stability of the perovskite solar technology. For this purpose, lithium doped conductive nickel oxide nanoparticles were synthesized with common wet chemistry methods and employed as the p-type hole conducting mediums. In addition, electrical conductivity of the titanium dioxide layers employed as the electron transport layers in perovskite solar cells were enhanced by doping with yttrium and mesoscopic solar devices were constructed. Synthesized particles and solar cells were characterized by means of structural, optical and electrical aspects. Effect of synthesis conditions on device performances were studied and electronic processes inside the cells and between the interfaces were revealed by spectroscopic analysis and correlated to particles parameters like particle size, doping amount and structure of the cells.

REFERENCES

1. L. Etgar, P. Gao, Z. Xue, Q. Peng, A. K. Chandiran, B. Liu, Md. K. Nazeeruddin, M. Grätzel, Mesoscopic $\text{CH}_3\text{NH}_3\text{PbI}_3/\text{TiO}_2$ Heterojunction Solar Cells *J. Am. Chem. Soc.*, 134 (2012) 17396–17399.
2. W. A. Laban, L. Etgar, Depleted hole conductor-free lead halide iodide heterojunction solar cells, *Energy Environ. Sci.*, 6 (2013) 3249.
3. J. Shi, J. Dong, S. Lv, Y. Xu, L. Zhu, J. Xiao, X. Xu, H. Wu, D. Li, Y. Luo, Q. Meng, Hole-conductor-free perovskite organic lead iodide heterojunction thin-film solar cells: High efficiency and junction property, *Appl. Phys. Lett.* 104 (2014) 063901.
4. S. Aharon, S. Gamliel, B. E. Cohen, L. Etgar, Depletion region effect of highly efficient hole conductor free $\text{CH}_3\text{NH}_3\text{PbI}_3$ perovskite solar cells, *Phys. Chem. Chem. Phys.*, 16 (2014) 10512.
5. Z. Ku, Y. Rong, M. Xu, T. Liu, H. Han, Scientific Reports, Full Printable Processed Mesoscopic $\text{CH}_3\text{NH}_3\text{PbI}_3/\text{TiO}_2$ Heterojunction Solar Cells with Carbon Counter Electrode, 3 (2013) 3132.
6. A. Mei, X. Li, L. Liu, Z. Ku, T. Liu, Y. Rong, M. Xu, M. Hu, J. Chen, Y. Yang, M. Grätzel, H. Han, A hole-conductor-free, fully printable mesoscopic perovskite solar cell with high stability, *Science*, 345 (6194)(2014) 295.
7. H. Tian, B. Xu, H. Chen, E. M. J. Johansson, G. Boschloo, Solid-State Perovskite-Sensitized p-Type Mesoporous Nickel Oxide Solar Cells, *Chem. Sus. Chem.*, 7 (2014) 2150 – 2155.
8. K. Wang, J. Jeng, P. Shen, Y. Chang, E. W. Diau, C. Tsai, T. Chao, H. Hsu, P. Lin, P. Chen, T. Guo, T. Wen, p-type Mesoscopic Nickel Oxide/Organometallic Perovskite Heterojunction Solar Cells, *Scientific Reports*, 4 (2014) 4756.

9. J. Jeng, K. Chen, T. Chiang, P. Lin, T. Tsai, Y. Chang, T. Guo, P. Chen, T. Wen, Y. Hsu, Nickel oxide electrode interlayer in $\text{CH}_3\text{NH}_3\text{PbI}_3$ perovskite/PCBM planar-heterojunction hybrid solar cells, *Adv. Mater.*, 26 (2014) 4107–4113.
10. A. S. Subbiah, A. Halder, S. Ghosh, N. Mahuli, G. Hodes, S. K. Sarkar, Inorganic Hole Conducting Layers for Perovskite-Based Solar Cells, *J. Phys. Chem. Lett.*, 5 (2014) 1748–1753.
11. J. Cui, F. Meng, H. Zhang, K. Cao, H. Yuan, Y. Cheng, F. Huang, M. Wang, $\text{CH}_3\text{NH}_3\text{PbI}_3$ -Based Planar Solar Cells with Magnetron-Sputtered Nickel Oxide, *ACS Appl. Mater. Interfaces*, 6 (24) (2014) 22862–22870.
12. K. Wang, P. Shen, M. Li, S. Chen, M. Lin, P. Chen, T. Guo, Low-Temperature Sputtered Nickel Oxide Compact Thin Film as Effective Electron Blocking Layer for Mesoscopic $\text{NiO}/\text{CH}_3\text{NH}_3\text{PbI}_3$ Perovskite Heterojunction Solar Cells, *ACS Appl. Mater. Interfaces*, 6 (2014) 11851–11858.
13. J. H. Kim, P. Liang, S. T. Williams, N. Cho, C. Chueh, M. S. Glaz, D. S. Ginger, A.K.Y. Jen, High-performance and environmentally stable planar heterojunction perovskite solar cells based on a solution-processed copper-doped nickel oxide hole-transporting layer, *Adv. Mater.*, 27 (2015) 695–701.
14. Z. Liu, M. Zhang, X. Xu, L. Bu, W. Zhang, W. Li, Z. Zhao, M. Wang, Y. Cheng, H. He, p-Type mesoscopic NiO as an active interfacial layer for carbon counter electrode based perovskite solar cells, *Dalton Trans.*, 44 (2015) 3967.

CHAPTER 2

SOLAR ENERGY MATERIALS AND MESOSCOPIC PEROVSKITE SOLAR CELLS

2.1 Photovoltaic Energy Production

Since discovered by Bacquerel, photovoltaic effect is known for a century. With the motivation of space applications and satellites, first solar modules were developed and still being researched. Photovoltaic energy conversion harvesting the sunlight is one of the most popular research topics both in academy and industry as it offers many advantages compared to other energy resources like fossil fuels, nuclear energy or renewable energy systems which can be summarized as:

- Photovoltaic energy production units have no moving parts and require no maintenance.
- Sunlight is a limitless and renewable energy resource.
- Photovoltaic panels are made from non-hazardous, long lifetime materials and service times are long.
- Photovoltaic systems possess no potential health hazards to public..
- Photovoltaic panels are produced from earth abundant materials and have no risk of raw material shortage.
- Photovoltaic panels are mobile and can be installed and transported in every area.
- Photovoltaic energy conversion is a major research topic in academy and industry and fast development in technology is expected..
- Due to extensive research and development, solar energy electricity production costs showed tremendous decline in the past years [1].

Photovoltaic energy conversion materials are semiconducting materials like silicon or germanium, properties of which can be manipulated by doping with certain elements. Devices are mainly based upon junctions of these materials. Semiconducting materials are responsible from capturing and absorbing the solar radiation incident on the devices and generated electrons and holes are separated and transported through the device in order to generate current or electricity. Generated current and attainable voltage from the photovoltaic devices primarily depends on the solar radiation or the solar spectrum reaching on earth.

2.1.1 Solar Spectrum and Irradiance

Solar irradiance reaches the earth in the form electromagnetic radiation like other light sources which is a flux of photons with the associated the energy. Photons are massless particles and possess wavelike behaviour, energy of (E_λ) which is determined by the wavelength (λ ,) of the photon according to:

$$E_\lambda = \frac{hc}{\lambda}$$

Eq. [2.1]

where c is the speed of light and h represents the Planck constant.

If sun is treated like a black body, energy coming from the sun to earth can be calculated from black body radiation corresponding to the surface temperature of the sun, which is around 5762 °K. Distribution of this energy is homogenous and isotropic, however, due to atmospheric effects, solar energy on earth varies in different parts of the world. In open space just above the earth's atmosphere, intensity of solar radiation is measured as 1353 kW/m² and referred as air mass zero, AM0. Air mass is defined as the deviation of solar irradiance on earth by the atmosphere and calculated by the angle of incidence (θ) according to:

$$\text{Air Mass} = \frac{1}{\cos\theta}$$

Eq. [2.2]

Air mass 1.5 (AM1.5) is the solar irradiation on sea level with an intensity of 100 mw/cm^2 and this value has been the standard intensity for solar cell measurements except for solar cell types of extra terrestrial applications. In Figure 2.1, intensity of each wavelength for different irradiation levels coming from the sun is given.

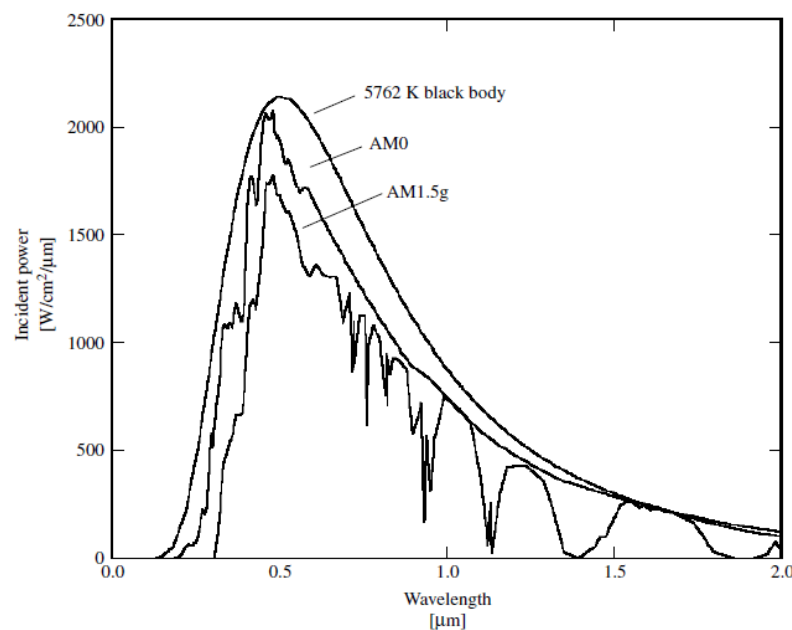


Figure 2.1 Distribution of light intensities for each wavelength in solar spectrum in space and on sea level [1].

The distribution of sun light for each wavelength given in Figure 2.1 transport the energy in sun with radiation, however it is not possible to harvest this energy with 100% efficiency. The efficiency of conversion is determined by the performance of the materials and the architectures of the solar devices.

2.1.2. Semiconductors and Structure of Solar Cells

Semiconductors are the building blocks of solar cells, which show intermediate conduction character between insulating and conducting materials. They are characterized by their intrinsic band gaps in electronic band structure and show crystallinity which gives rise to unique electronic behaviour among electronic materials. Semiconductors mostly belong to group IV in the periodic table. Binary or ternary compounds of group II, III, V and VI also yields semiconducting properties and widely used in modern photovoltaic devices. In Table 2.1, most popular elements used in semiconducting devices are given.

Table 2.1 Elements used in semiconductors.

I	II	III	IV	V	VI
		B	C	N	O
		Al	Si	P	S
Cu	Zn	Ga	Ge	As	Se
Ag	Cd	In	Sn	Sb	Te

Conventional solar cells used in industry today are mainly made up of silicon, gallium arsenide and cadmium telluride. They have all their characteristic band gap and charge carrier mobility values which determine the light absorption and charge collection abilities. Band gap is an intrinsic property of any given semiconductor and arises from the band electronic band structure of the material. In a semiconducting material, there are forbidden energy states in the band structure and separates the band into two distinct bands, the valence and the conduction band. In contrast to metals, which have a fully occupied band structure, only valence band is filled with electrons in semiconductors and conduction band is mostly empty, depending on the temperature and the energy difference between the bands, the band gap. Electrons in the valence band are not mobile carriers so cannot contribute

to conduction. Upon absorption of a photon by the crystal, an electron is excited to conduction band and becomes free to travel along the lattice. Doping process or addition of certain impurities inside the lattice also leads to formation of free charge carriers in the lattice and new electronic states occur in the forbidden band. These states are referred as donor states which supply electrons into conduction band or acceptor states which supply holes into the valence band. Depending on the dopant atom, creation of donor states is referred as n-type doping and creation of acceptor states is referred as p-type doping. In the case of a group V element like phosphorus being doped into group IV element like silicon, n-type doping is achieved because of the contribution of an extra electron of the phosphorus atom to the conduction band of silicon. Similarly, doping process of boron of group III, results in a deficiency of an electron and manifests itself as a hole in the valence band and p-type doping is achieved. Effect doping on the electronic band structure and formation of donor and acceptor states are illustrated in Figure 2.2.

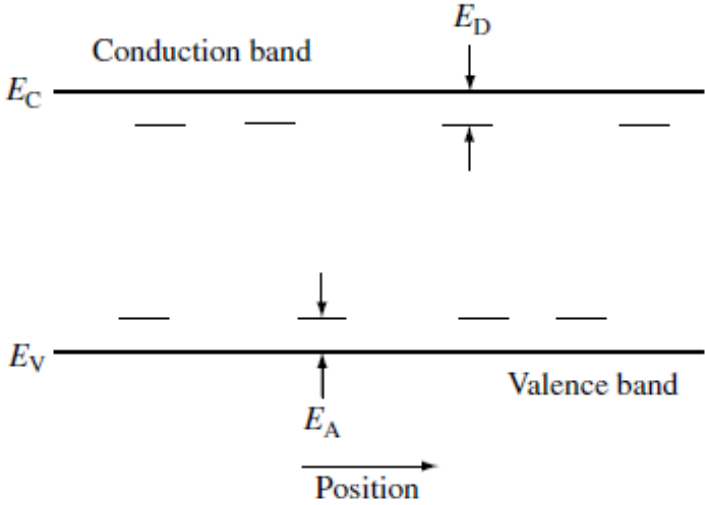


Figure 2.2 Positions of donor and acceptor states in semiconductors upon doping [1].

For doped semiconductors at room temperature, due to thermal excitation, there are free holes and electrons in the valence and conduction band and these carriers are mobile. However, random motion of these carriers cannot generate a net current

flowing in one direction. In order to create a driving force inside the semiconductors, pn junctions are constructed where a metallurgical bond is created between p-type and n-type semiconductor and a junction is formed.

2.1.3 Formation of pn Junctions

Energy band diagram of a typical pn junction formed by a p-type and n-type material is given in Figure 2.3. Bands are bent upon contact of the semiconductors giving rise to band bending.

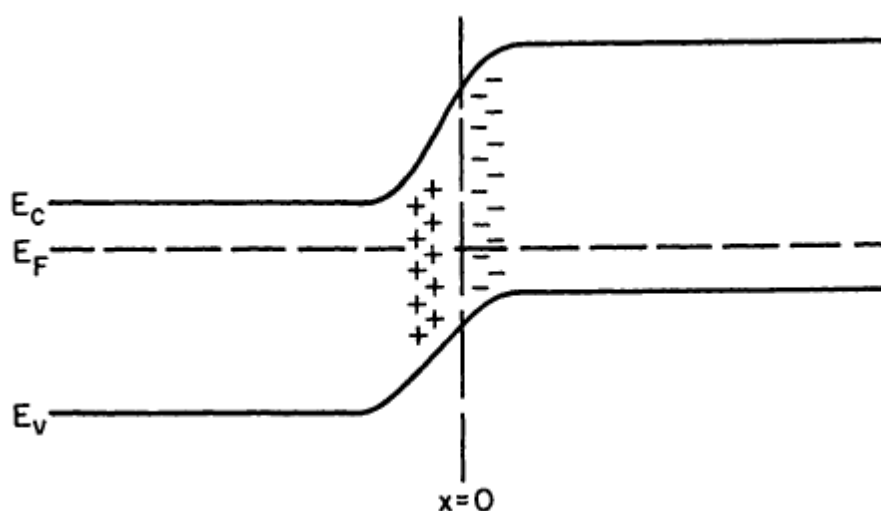


Figure 2.3 Band diagram of a pn junction and band bending [2].

The holes in the p-type material and the electrons of the n-type material recombine in the junction interface and diffusion goes on until equilibrium condition is reached. This diffusion results in the depletion of the semiconductors from free carriers and creation of a negatively charged and positively charged interface in the junction. This type of depletion and charge accumulation lead to a net built in potential or an electrical field across the junction, the strength of which is primarily depend on the doping concentrations. Equilibration of the Fermi levels of the two semiconductors

give rise to an event called as band bending due to rearrangement of the band positions with respect to each other. Electrons favor the low energy states and travel towards the n-type region where holes flow towards the p-type region. During solar cells operation, upon light absorption by the semiconductor, charge carriers are separated from each other and driven by an internal electrical field at the junction area.

2.1.4 Absorption of Light by The Solar Cell

A solar cell is a device which converts sunlight or any light coming from other resources to electricity. For this purpose, understanding the interaction of light with any given material is of importance. 3 basic processes occur during the illumination of a semiconductor:

1. Reflection
2. Transmission
3. Absorption

In semiconductors, due to the presence of the band gap, absorption events are determined by the energy of the incoming photons which are higher than the band gap value of the semiconductors. Upon absorption of the photon, an electron excites to the conduction band and this situation results in the creation of a hole in the valence band due to the unoccupied states left behind in the valence states. Photons with insufficient energy to create an electron hole pair, either pass through the semiconductor, which is the transmission event, or are reflected back from the surface of the semiconductor depending on the angle of incidence and refractive index of the material.

The excitation events involving transitions between conduction band and valence band in semiconductors, is defined as the band to band transitions. According to quantum physical rules, these transitions obey the conservation of momentum and

energy. Direct semiconductors have the conduction band and the valence band minima at the same lattice momentum value and only energy conservation principle rule applies in this case. Photons with energy higher than the band gap value is sufficient enough for band to band transitions. However in indirect semiconductors, where conduction and valence band minima do not have the same lattice momentum, although incoming photon have the sufficient energy to excite an electron from the valence band, lattice momentum must also be supplied for the transition. This momentum is supplied to the transition event from the lattice vibrations or phonons present inside the lattice. However, this process is random and statistical, so indirect transitions are less possible than the direct transitions. Due to this reason, indirect band gap semiconductors have less absorption coefficients compared to direct semiconductors. In silicon for instance, due to indirect band gap, thicknesses around 200 μm are required for absorption of the solar spectrum, where for direct band gap GaAs based cells, much lower thickness values are sufficient enough to absorb most of the sunlight.

In a semiconductor, in addition to band to band transitions, electrons in the conduction band or holes in the valence band also have the ability to absorb light, which is called free carrier absorption. In free carrier absorption, upon light absorption, carriers are excited to higher energy levels inside the same band and this type of absorption does not contribute to creation of new electron hole pairs. Free carrier absorption is observed and becomes significant only in heavily doped semiconductors and under illumination with high intensities [2].

2.1.5 Carrier Transport in Solar Cells

There is thermal equilibrium conditions in a pn junction in dark, the electrons and hole are distributed randomly. Upon illumination and light absorption begins, electron hole pairs are created and mobile free carriers are generated. In the junction part, where the device is depleted of holes and electrons, created electron hole pairs are separated from each other and forced flow in one direction under the internal

electrical field. This flow is observed as a net current and governed by the transport equations defining the photocurrent densities (J) according to:

$$J_n = q\mu_n n \varepsilon + q \cdot D_n \nabla_n$$

Eq. [2.3]

$$J_p = q\mu_p p \varepsilon - q \cdot D_p \nabla_p$$

Eq. [2.4]

In transport equation, n and p represent electron and hole concentrations, μ_n and μ_p represent electron and hole mobilities, D_n and D_p represent electron and hole diffusion coefficients, respectively, where q is the elementary charge and ε is the electrical field. The first part of the equation defines the drift current which is the motion of carriers under the electrical field. Second part of the equation describes the diffusion current due to diffusional the motion of carriers with their unique diffusion coefficient. It can be seen from Eq. 2.4 that the flow of carriers inside a pn junction is mainly governed by the drift and diffusion events which can be expressed in terms of their associated mobility and diffusion coefficient values. These values are characteristic to each semiconductor and vary dramatically among the semiconducting materials, however there are several parameters influencing the transport abilities of any given material. Temperature of the device, doping concentrations and impurity content of a semiconductor directly determines the mobility values. Mechanisms like carrier carrier scattering, ionized impurity scattering or scattering due to lattice vibrations affect the transport ability of the carriers during cell operation. In addition, these factors are also directly related to the life time of carriers and diffusion length values through a mechanism called recombination of electron hole pairs [3].

2.1.6 Recombination in Solar Cells

Recombination of electron holes pairs generated by the absorption of light by the semiconductor is an important loss mechanism for solar cells. This recombining events may occur through several ways in a solar cell but may be categorized to two main types, surface and bulk recombinations. Another way of categorizing the recombination processes rely on the optical nature of the recombination where recombining of an electron and a hole may either emit photons, referred as radiative recombination, or emit phonons, referred as non-radiative recombination. Recombinations may occur by:

- Band to band transitions
- Recombination in trap levels
- Auger recombination
- Surface states recombinations

Recombination of carriers in the valence band and conduction band is the reverse of a light absorption event and referred as band to band transition. This type of recombinations are quite often and results in emission of a photon, so they are classified as radiative. Similar to light absorption, this process also requires additional momentum from the lattice and observed more common in direct semiconductors compared to the indirect ones.

During the recombination process, excess energy emitted from the electron hole pair may be transmitted to another electron in the conduction band which results in excitement of the electron to higher energy levels. Such a process may or may not be radiative depending on the electronic band structure of the material and referred as Auger recombination or the inverse Auger process. If non-radiative Auger occurs, due the relaxation of the excited electron, phonon emission is observed.

Among the recombination types, most widely observed recombination process is the recombination through defect states or namely defect assisted recombination. The donor and acceptor states are also trap states introduced by the dopants, which can also be considered as defects inside lattice, however trap states lying around or close to middle of the band gap can not contribute to electron and hole donation, instead they act like traps for carriers in the valence and conduction band. Structure of these states are give in Figure 2.4. Trap states may be introduced to the band gap by either impurity atoms or by the point defetcs or dislocations inside the crystal lattice. This type of recombination is usually non-radiative and results in phonon emissions. Trap states recombination rates highly depend on the impurity concentration of the semiconducting material and using high purity materials is quite important for solar cell applications.

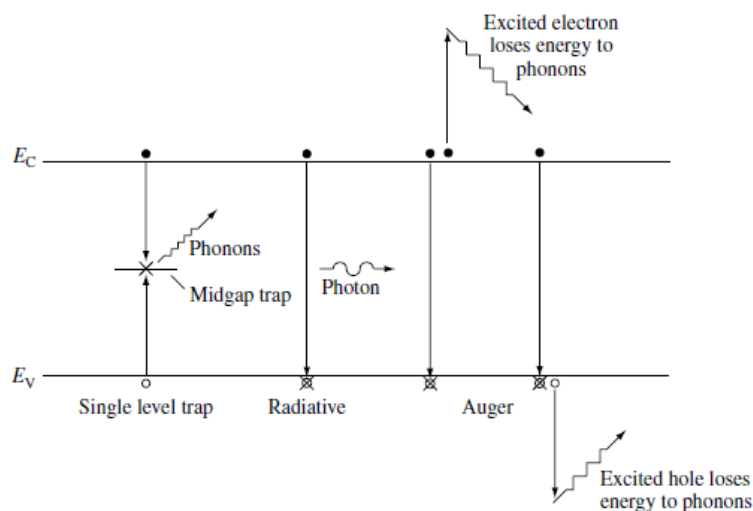


Figure 2.4 Summary of recombination processes in semiconductors. [1].

Another type of practically important recombination type is the surface states recombination. Surfaces in materials are defective regions which contain high concentration of unbound atoms, vacancies or dangling bonds. These regions are strong recombination centers with high recombination rates for carriers in the bulk of the material. Surface passivation is conducted by modifying the surfaces with

certain compounds or depositing buffer layers and concentration of the defects in the surface can be minimized. Such coatings or modifications are widely used for passivation of thin film solar cells where surface to bulk ratio is higher than the silicon based solar cells [4].

2.2 Solar Cell Materials and Solar Cell Types

2.2.1 Crystalline Silicon Solar Cells

Crystalline silicon based solar cells dominate the solar cell market since their introduction and 85% of the market is based on these materials. There are huge advances in other technologies, however silicon based solar technology is still growing due to the silicon supplied by microelectronics industry and price of silicon is going down. Three types of silicon based solar cells can be found on the market.

1. Mono Crystalline
2. Poly Crystalline
3. Amorphous

Ingots, ribbons or wafers are produced from molten silicon and categorized according to their grain sizes, which is one of the main parameter determining the performance of the materials. The major recombination loss mechanism in crystalline silicon is the defect assisted losses, so production of high purity and large grain sized materials is quite important. Czochralski process is the worldwide accepted technique for production of high purity single crystalline silicon wafers. Molten silicon together with the dopant elements is used to grow single crystalline silicon ingots on a seed crystal by pulling the crystal from the molten silicon at highly controlled drawing speeds and temperature gradients. Produced ingots are single crystal and impurity free. For production of poly crystalline silicon, molten silicon is directly casted and the formed ingots possess poly crystalline structure.

Silicon has a band gap of 1.17 eV and can absorb most of the visible spectrum, however, indirect band gap of silicon leads to poor absorption coefficient, so wafers for silicon solar cell production must be thick enough to absorb the light. Thickness around 200 μm is required for sufficient light absorption, but in this case diffusion length of charge carriers are lower than this value. For high efficiency silicon solar cells, a surface passivation process and surface texturing or anti reflective coatings are mandatory for enhancing the absorption ability of the cells (Figure 2.5).

There are many steps involved in production of silicon base solar cells and these steps applied on boron doped silicon wafers can be summarized as following:

- Etching by acidic and alkaline solutions for saw damage
- Surface texturing with NaOH
- Phosphorus doping by diffusion in belt furnaces
- Junction isolation
- Deposition of TiO_2 or SiN anti reflective coatings
- Metallization by screen printing silver contacts
- Contact firing
- Testing and characterization

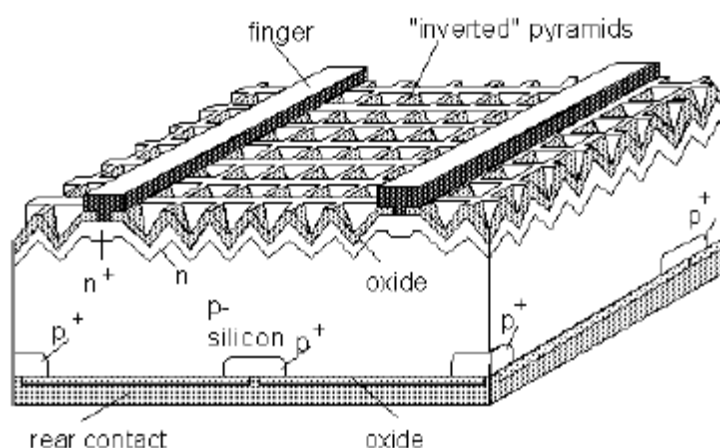


Figure 2.5 Structure of a silicon solar cell [5].

Crystalline silicon solar cells have reached their theoretical maximum limits of 27% efficiency and poly crystalline silicon gives around 20% efficiency at best reported cells. Scaling up of silicon solar cells, however, results in decline in efficiencies due to resistive effect of large area substrates and module efficiencies of 18% can be found commercially. This value depends on the materials and processes employed in production of the modules and varies among the manufacturers around the world. Another important aspect of the silicon based solar cells is the variation of module efficiency during the day depending on the application area in outdoor. Silicon base solar cells require high light intensity for performing at their top efficiency value and performance of the cells change dramatically under low light intensity and high temperature conditions. Due to this reason, the energy output of a commercial module must be tested on real outdoor conditions and must be chosen according to the installation area. Besides all, silicon solar cells promise high stability and long service lives to customers where most companies give warranty of energy production for around 20 years [5].

2.2.2 Thin Film Silicon Solar Cells

Crystalline wafer based silicon solar cells are the most popular photovoltaic materials in the market for years due to high efficiency combined with long durability but due to the high prices of these devices, the widespread application of photovoltaics is still poor compared to fossil fuel based energy production. The major contribution to the cost of wafer based technology comes from the materials used. High purity single crystal growth is an energy intensive process and limits the reduction in cost of silicon wafers. Thin film silicon solar cells have the advantage of less material consumption and reduced cost of the panels. Evaporation technique, chemical vapour deposition methods or liquid phase epitaxial growth have been researched and used for deposition of silicon thin films. Unfortunately, due to limited light absorption of silicon, efficiencies were constrained to 16% at best by applying antireflective coatings surface passivation and light trapping.

Amorphous silicon offers two orders higher absorption coefficient compared to crystalline silicon and can be a promising alternative for thin film applications. However, lack of crystallinity and long range order lead to high concentration of defects dangling bonds and as a result high recombination rates. The unbounded atoms can be passivated by hydrogen and a huge reduction in defect density can be achieved. Nevertheless, upon doping after passivation, recombination centers reactivate and an efficient pn junction formation is not possible. In order to overcome these problems, p-i-n structure was developed where intrinsic amorphous silicon is placed between a p-type layer and a n-type layer. Amorphous silicon acts like the absorption layer and built in electrical field is created by the n-type silicon and p-type silicon layers, magnitude of which is related to the doping concentrations of the layers. Deposition of amorphous silicon is conducted by CVD technique employing silane (SiH_4) gas. 10% efficiency values are reachable for amorphous silicon based cells, however stability of the devices are poor due to degradation of Si-H bonds under light soaking. An additional heat treatment is required for recovery of the cells [6].

2.2.3 Gallium Arsenide Solar Cells

Gallium arsenide (GaAs) is a group III-V semiconductor widely used in the industry which possess excellent opto-electronic characteristics. Because of the 1.42 eV band gap value, which is close to the optimum band gap for solar energy conversion, it is an excellent photovoltaic material. In addition, GaAs has a direct band gap and has high absorption coefficient which makes it very suitable for thin film solar cell applications. Most common dopants are Al and Zn for junction formation. In addition, doping or alloying results in variation in the band gap value and band gap tuning is possible which opens the way of creating tandem films deposited on each other for enhanced efficiency. Highly efficiency tandem devices are deposited by epitaxy techniques like molecular beam epitaxy or liquid phase epitaxy. GaAs is an expensive material and widespread application is limited. There are researches to replace GaAs with silicon or germanium layers but thermal

mismatch problems are being experienced so far. In addition to high cost, both gallium and arsenide are hazardous materials to human health. 26% efficiencies have been reached and GaAs panels are being used in satellite applications [4].

2.2.4 Cadmium Telluride Solar Cells

Cadmium Telluride (CdTe), similar to gallium arsenide, is advantageous for photovoltaic action by means of a proper band gap which is around 1.45 eV, the optimum band gap value for light absorption without a tandem structure. CdTe belongs to metal chalcogenides and is a II-VI compound. CdTe is intrinsically p-type material and possess high absorption coefficient. N-type junctions of CdTe are conducted by depositing a CdS layer on top of it and referred as superstrate configuration. CdTe solar cells are very popular by means of commercialization because of the ease of production. CdTe shows a strong ionic bonding and as a result, it is a very robust material and highly stable. It is especially suitable for outdoor and space applications among all photovoltaic materials. Efficiencies of 16% on laboratory cells and 10% for modules have been realized. However, maximum theoretical efficiency limit around 29% is still too far and efforts have focused on developing highly efficient CdTe based cells, although there are many concerns and restrictions because of the toxicity of Cd. CdTe based cells can be produced by many techniques including vacuum processes like sputtering or CVD methods. Wet chemistry techniques like screen printing, spray deposition or electrodeposition techniques are also used for the production and offer reduced production cost and mass manufacturing [6].

2.2.5 Copper (Indium, Gallium) Diselenide Solar Cells

Chalcopyrites are the compounds of I-III-V group of periodic table with a tetragonal crystal structure and possess semiconducting properties like copper indium diselenide (CIS) or copper gallium indium diselenide (CIGS). By changing the stoichiometry of these compounds, it is possible to manipulate the electronic opto-

electronic properties like electrical conduction and band gap values. For example band gap of CIGS and CIS can be tailored from 1.04 to 1.68, where mostly used values are around 1.20-1.25 for high efficiency cells. They possess high absorption coefficients like CdTe and a 2 μ m thick layer can absorb most of the solar spectrum. A typical cell structure is composed of a Cu deficient layer acting like the p-type layer and CdS n-type layer. CIGS layers deposited by using different deposition methods yield similar efficiency values and performance of the cells are not affected by the grain sizes. Due to this reason it attracts attention of the industry by means of producibility with low cost wet chemistry methods. Vacuum methods like sputtering, evaporation techniques or cheaper methods like electrodeposition, spray pyrolysis and printing have been successfully employed for CIGS cells. Efficiency values are around 19% for cells and 16% module efficiencies were reported. Many research groups and companies are still working on development and commercialization of these type of cells [6].

2.2.6 Dye Sensitized Solar Cells

Dye sensitized solar cells (DSSC) belongs to a group of solar energy materials called third generation photovoltaics and have been attracting great attention since their first introduction. DSSCs are referred as artificial photosynthesis where working principle is similar to plants and distinguishes from the conventional photovoltaic materials. In Figure 2.6, components of a DSSC is given:

- Transparent and conducting oxide coated glass (TCO)
- Wide band gap semiconductor
- Dye molecules attached on the surface of nanoparticles
- Redox electrolyte
- Counter electrode coated with catalyst layer

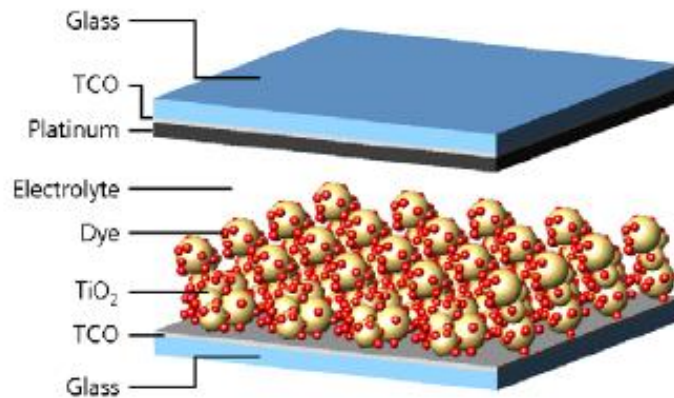


Figure 2.6 Schematic structure of a DSSC [7].

The anode part of the cell is made up of a wide band gap semiconductor like TiO_2 or ZnO nanoparticles forming the mesoporous matrix. These mesoporous structure is attached to the TCO material like fluorine doped tin dioxide (FTO) or indium tin oxide (ITO) which is the collecting electrode. A monolayer of dye molecules are chemically bonded to the surface of the nanoparticles and is responsible from the absorption of incoming photons. The difference of the HOMO and LUMO levels of the dye molecules is around 1.5 eV which is similar to most inorganic photovoltaic materials. Dye molecules, mesoporous matrix and the collecting electrode together form the photoanode of the cell. The cathode part is composed of a FTO glass coated with a thin layer of platinum or carbon which is the catalyst material responsible from the efficient redox reactions occurring on the electrolyte cathode interface. The redox electrolyte is placed between the anode and cathode part of the cell and infiltrated within the pores of the mesoporous matrix. Electrolyte contains the redox couple, I_3^-/I^- in most cases, which reduces the oxidized dye molecules after light absorption and carries oxidized species to the counter electrode for completing the cycle. They act like hole transporting p-type layers in conventional solar cells. Cells are finally sealed by hot melt glues or glass frits to prevent the electrolyte leakage[8, 9].

The working mechanism of the DSSCs differ much from the conventional pn junction solar cells by means of the driving force of the charge separation and transport. Electron hole generation occurs in the dye molecules and the electron is transferred to the mesoporous layer. The rate of this reaction is magnitudes of higher than the back reaction of the electrons with the excited dye or electrolyte species. The accumulation of the electrons in the TiO_2 conduction band results in diffusion of electrons to collecting electrode and redox couple also diffuse to the counter electrode. The ambipolar nature of charge transport distinguishes this type of cells from the pn junction solar cells where charge separation is driven by the internal electric field.

The development studies conducted on the DSSCs have been carried out since past 20 years as a low cost alternative to conventional solar cells efficiencies up to 15% have been reached containing liquid electrolyte based cells. However, due to sealing problems and low stability commercialization is still problematic. Research on the replacement of the liquid electrolyte with solid state hole conductors and application of inorganic absorber materials have led to the birth of a new material and a new era, known as the perovskite solar cells in the past 5 years.

2.3 Perovskite Solar Cells

Perovskite material has been first found and defined by Russian mineralogist L.A. Perovski. Organic-inorganic hybrid solar cells based on perovskite halide materials had a great impact on photovoltaic industry. They show superior efficiency values compared to existing organic solar cell technologies and dye sensitized solar cells. Strong optical absorption, high carrier mobility and low rate of recombination are the main reasons underlying the outstanding photovoltaic performance of these materials [10]. From point of view of fabrication and commercialization, perovskite based solar cells are also attractive because they can be produced by simple synthetic methods like wet chemistry. They are quite advantageous by means of capital investment compared to other thin film technologies. Solution processed thin

film technologies promise the low cost solution in the PV market compared to existing technologies like silicon wafer based solar cells. Techniques like spin coating, spray deposition, inkjet printing, doctor-blade coating or slot die coating can easily be integrated to produce perovskite based solar cells, which have already reached 22% efficiency values competing with CdTe, CIGS thin film solar cells and far beyond the best organic and dye sensitized solar cells, given in Figure 2.7 [11]. Far more advances and efficiencies up to 25% is expected in near future [12].

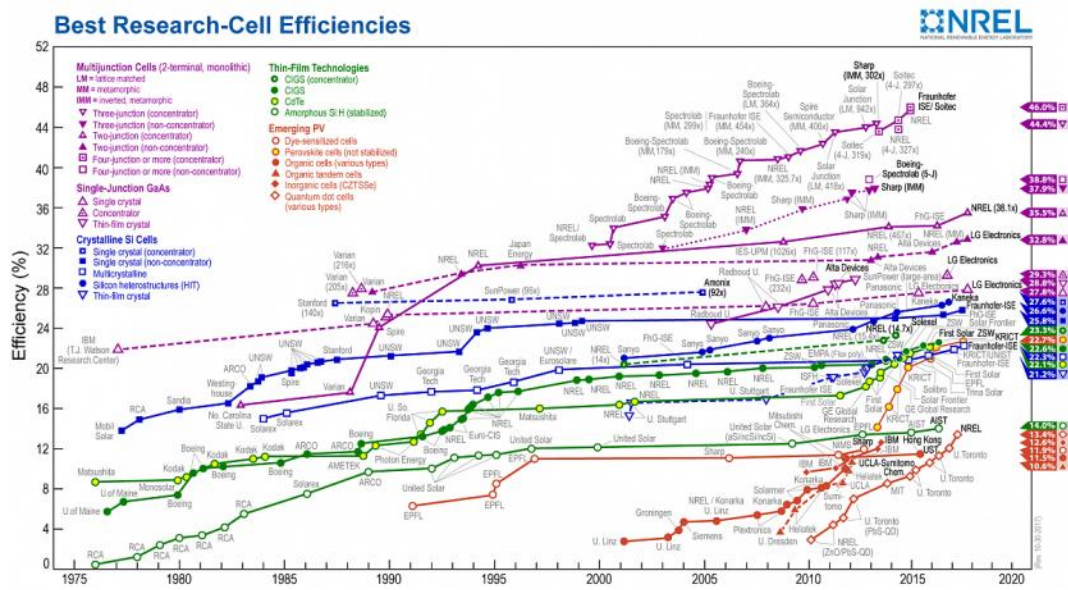


Figure 2.7 National Renewable Energy Laboratory best research cell efficiencies chart [11].

The first perovskite based solar cell was reported by Kojima et al. employing a halide perovskite material in the form of $\text{CH}_3\text{NH}_3\text{PbX}_3$ ($\text{X} = \text{Cl}$ and Br) in 2009, with a power conversion efficiency of 3.8% [13]. This value was extended to 6.54% two years later [14]. However both cells were employing liquid redox electrolyte in conjunction with the perovskite sensitizer and suffered from rapid degradation the cell. First stable perovskite solar device was constructed by Kim et al. using spiro-METAD as a solid state hole conductor and exhibited an efficiency of 9.7% [15]. After this breakthrough, a rapid progress in perovskite solar cells research has

emerged and followed by some mile-stone developments. Replacement of TiO_2 as the electron conducting medium by Al_2O_3 in a solid state device exhibiting 10.9% efficiency showed that perovskite crystals embedded in the mesoporous matrix can also conduct electrons and holes. This configuration was referred as meso-structured perovskite solar cells [16]. This demonstration opened the way of development of planar perovskite solar cell architectures without the necessity of mesoporous scaffolds and application of perovskite material as the charge conducting medium itself both functioning as the conduction medium and light harvester at the same time. Burschka et al. developed a two step sequential method for deposition of perovskite crystals into the mesoporous TiO_2 scaffold and reached an efficiency of 15%, in 2013 [17]. From that date, many deposition approaches and tuning of the composition of the perovskite layers like compositional engineering and anti solvent one step methods extended the efficiency values up to 21% [18]. Stability of the perovskite solar cells have also been improved by the compositional engineering approach by doping the perovskite crystals with Cs^+ and Rb^+ ions [19] or by replacing the TiO_2 layers with La-BaSnO_3 [20]. All these reported values are valid for small scale laboratory cells which cannot be large than 0.1 cm^2 and do not represent large area modules and sub-modules. From point of view of commercialization, scale up of the cells is also important. Another important issue related with perovskite solar cells is the stability of these devices. It is known that perovskite materials are sensitive to humidity and thermal stress conditions where structure loses its semiconducting property upon degradation [21]. Increasing the stability and device lifetime of perovskite based cells is still a major challenge and research priority for the community.

2.3.1 Perovskite Crystal Structure

CaTiO_3 is the first mineral identified as the perovskite structure. Halide perovskites which are a new class of perovskite materials, is the most widely used one and possess attractive photovoltaic features. Stoichiometric perovskite shows ABX_3 structure in general. Here, A represents the organic cation like methyl ammonium or

formamidinium, B represents the transition metal like Pb or Sn and X represents the halide like I, Br or Cl. Perovskites possess 3D structure where BX_6 octahedra with the X atoms shares the corners and B atoms in the middle of the octahedra, together with A cations are surrounded by eight octahedra (Figure 2.8). This structure is the key for the tunability of the opto-electronic properties of the perovskite like the band gap of the material and origin of the photovoltaic characteristics like high absorption coefficient, high diffusion length, ambipolar transport and low exciton binding energy [22].

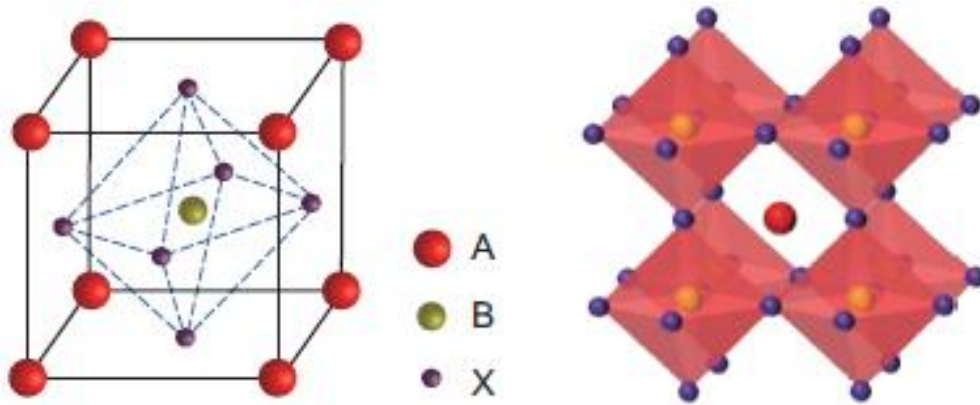


Figure 2.8 Structure of perovskite type crystals with the general ABX_3 form [23].

In general, in order to achieve crystallographic stability and the perovskite structure, in addition to A, B and X ions, an octahedral factor (μ) and tolerance factor (t) must be taken into account, where:

$$\mu = \frac{R_B}{R_X} \tag{Eq. [2.5]}$$

$$t = \frac{R_A + R_X}{\sqrt{2}(R_B + R_X)} \tag{Eq. [2.6]}$$

Here, R_A , R_B and R_X corresponds to the ionic radii of the ions A, B and X, respectively. Perovskite structure will tend to be more cubic if the t value is

between 0.89-1.0. Lower t values means structure will convert into orthorhombic or less symmetrical tetragonal phase. The ideal cubic structure can be obtained by a t value of unity. Although there are constraints, a perovskite material will show structural deviation between these phases depending on preparation conditions or by effect of heat, where cubic structure is more likely to be seen at high temperatures as seen in Figure 2.9 [24].

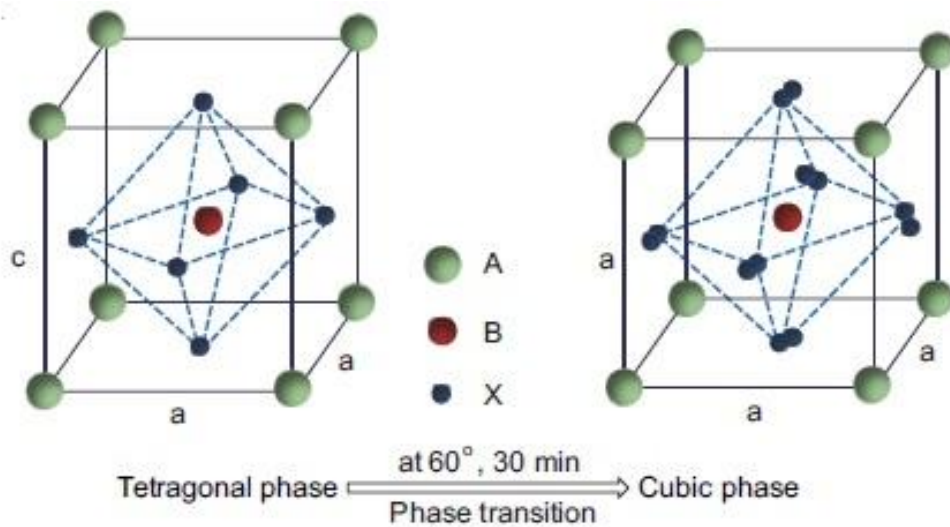


Figure 2.9 Phase transition of perovskite lattice from tetragonal to high temperature stable phase of cubic structure [24].

The deviations and variability of the perovskite structure is of considerable interest because distribution and alignment of the components strongly affect the opto-electronic properties of the perovskite materials. Cations in perovskite crystals have no significant impact on the electronic band structure of the material and contributes as a charge compensation. On the other hand for optical properties, the cation plays an important role because it determines the distribution of the octahedral network. Small sized A cations like formaminidium or methylammonium possess a 3D structure where larger A cations will lead to formation of low dimensional layers or confined structured perovskites. 3D structure is important for maintaining high extinction or absorption coefficient [25]. MAPbI_3 , which is the most widely used

perovskite halide material shows light absorption capability higher than best performance single junction solar cell material like GaAs and far more than crystal silicon. First principle calculations revealed that Pb-I bonds determine the electronic structure of MAPbI₃. Pb 6s and I Sp orbitals forms anti bonding hybrid states and determine valence band maximum. Pb 6p and I 5p orbitals are responsible from conduction band minimum making a non bonding hybrid state [26]. High absorption coefficient is related to the high density of states in the conduction band minima and direct p-p transition is believed to be reason behind it. Thanks to high absorption coefficient and reflective character of the back contact metals used in perovskite solar cells, most of the incoming photons lower than the band gap value of perovskite can be harvested.

2.3.2 Organic-Inorganic Hybrid Mesoporous Perovskite Solar Cells

Application of semiconductor inorganic materials, organic dyes or novel absorberslike perovskite materials as sensitizers in mesoporous structures or other bulk heterojunction cells have been investigated last years. Ru based organometallic complexes have dominated the photoelectrochemical cells as the best efficiencies were obtained by use of these materials. Although numerous sensitizers like organic metal free molecules have been investigated and applied in DSSC, Ru-complexes dominated the best results among others. Ultra fast electron injection dynamics of dye metal oxide couple is the main reason for electron injection efficiency of nearly unity which is considered to be the major factor of the success in DSSC. However, most Ru-based dye molecules in use today, have low absorption coefficients and molar extinction coefficients which results in thicker TiO₂ films for efficient light harvesting. As thickness of a nanocrystalline layer increases, both recombination is enhanced due to high diffusion length and open circuit voltages decreases for these type of cells. Replacing the low absorptive dye molecules with inorganic well known semiconductors seems to be a convenient way of increasing the efficiency of DSSC. The reason of incorporating inorganic semiconductors is not only the high absorption but also the quantum size effects observed in small size nanocrystals, the

quantum dots (QDs), which contributes to size dependent semiconducting properties as well as unique phenomenons like multiple exciton generation and hot electron transfer events [27]. Combination of these properties is believed to be a revolutionary milestone in DSSC as well as for all types of photovoltaic devices.

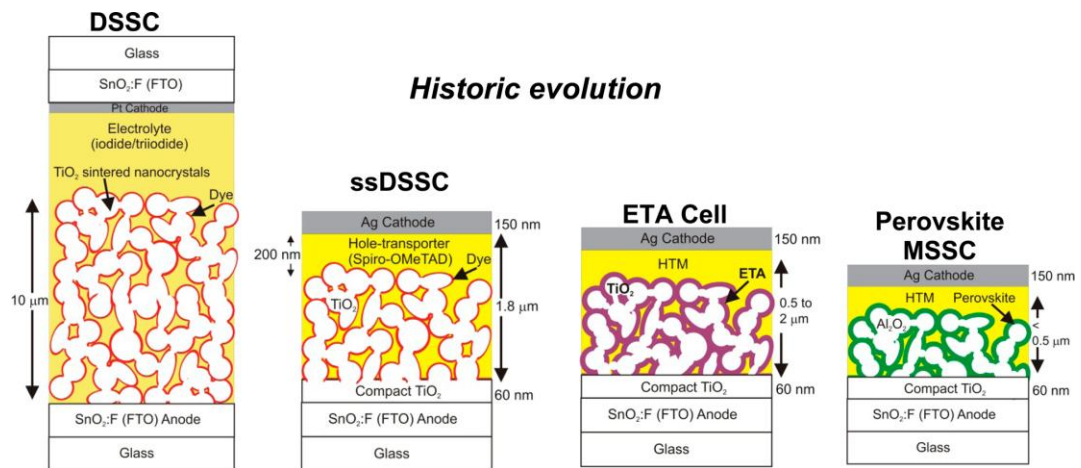


Figure 2.10 Device architectures of mesoporous solar cells with different absorber and hole conductors [29].

Most common semiconductors employed as the sensitizer in mesoporous solar cells are CdSe, CdS, CdTe, InP, InAs, PbS, PbSe and other transition metal sulfides which can absorb in the visible region of spectrum. These semiconductors have shown size dependent electronic properties in which band gaps and position of valence and conduction bands vary with decreasing crystal size. Tunable electronic structure is advantageous in designing novel architectures like tandem or donor acceptor approaches. In their individual form, recombination is the dominating event as the absorber in a typical solar cell, however coupling a semiconductor quantum dot with a wide band gap metal oxide results in an efficient charge transfer and exciton separation. Transient spectroscopy techniques have shown decreased luminous decay of electrons in quantum dots when incorporated with a TiO₂ or SnO₂ layer effectively, indicating efficient charge transfer reactions between each other. As the electronic structure of QDs can be tuned by size regulation, it is

possible to enhance, promote or suppress electronic transfers between individual QDs or nanoparticles [28]. Typical device structures of mesoporous solar cells employing different sensitizer materials and hole conductors have been given for comparison in Figure 2.10.

Perovskite sensitized solar cells belong to the group of mesoscopic solar cells or excitonic solar cells where similar to dye sensitized solar cells, an absorber layer sensitizes a wide band gap semiconductor in conjunction with a hole transporting medium (HTM). As the main difference from typical dye sensitized solar cells, absorber layer is a perovskite structured material apart from metallorganic or fully organic dyes applied in DSSCs. This type of solar cells can also be considered as the mesoscopic solar cells as similar to DSSC, absorber perovskite layer is attached to the surface of mesoporous wide band gap electron transporter and cell functions in the absence of an internal electric field.

Methylammonium lead halide ($\text{CH}_3\text{NH}_3\text{PbX}_3$, X = halogen; CH_3NH_3 : MA) and its mixed-halide crystals, corresponding to three-dimensional perovskite structures, have been used as light harvesters for perovskite sensitized solar cells. The advantages of these compounds have already been demonstrated as a noteworthy example of potentially useful physical properties such as nonlinear optical properties, electroluminescence, organic-like mobility, magnetic properties, conductivity, and so forth. Perovskite-based hybrids can be synthesized using simple and cheap techniques due to their self-assembling character. Thus, these hybrid materials have the potential to be ideal light harvesters for low-cost and highefficiency solar cells. The cell architectures for solar cells consist of a porous layer of a nanocrystalline metal oxide covered with sunlight-absorbing MAPbX_3 and a hole-transporting material. They are cost-effective due to their simple fabrication process and high efficiency.

The band gaps of MAPbI_3 and MAPbBr_3 were reported as 1.5 and 2.3 eV, respectively. These two materials have a suitable band position for heterojunction

solar cells using a mesoscopic TiO_2 photoelectrode since the conduction band energy (CBE) of both MAPbI_3 and MAPbBr_3 is higher than that for TiO_2 . Besides these materials can be prepared in alloyed form for band gap engineering and tuning of the band gap to desired values although 1.5 eV is very suitable for solar cell applications.

The solid-state perovskite sensitized solar cell structure is pseudo junction type, where an intrinsic light harvester adsorbed on an n-type TiO_2 surface is in contact with a p-type HTM. A compact thin layer, the blocking layer, forms on a transparent conductive oxide (TCO) substrate to protect recombination of the electron in TCO and the hole in HTM. A metal layer such as gold or silver is deposited on top of the HTM layer, in which the work function of the metal should be considered in order to transfer the hole from the HTM layer. Because electrons are collected at TCO, the TCO substrate with the TiO_2 film is a photoanode (minus electrode), and the metal layer on HTM is the cathode (plus electrode). The fabrication process is as follows. First, a compact TiO_2 blocking layer is deposited on a TCO substrate, where fluorinedoped tin oxide (FTO) has been usually used for TCO because the high haze surface of FTO provides a strong adhesion with the nanoparticle TiO_2 film. This is an important step because the role of the compact layer is to protect direct contact between the FTO and HTM. Once the compact layer forms, nanoparticle TiO_2 paste is deposited on the compact layer covered FTO substrate and annealed at around 450–500 °C to have a mesoporous film. In this process, the porosity and thickness should be carefully controlled because porosity and thickness governs the pore filling and conductivity of HTM. Sensitizers are then adsorbed on the annealed TiO_2 film, which is followed by spin-coating the HTM solution. During spin-coating, HTM is infiltrated into the pores of the TiO_2 film. Finally, the metal electrode is formed on the HTM layer using a thermal evaporator (Figure 2.11).

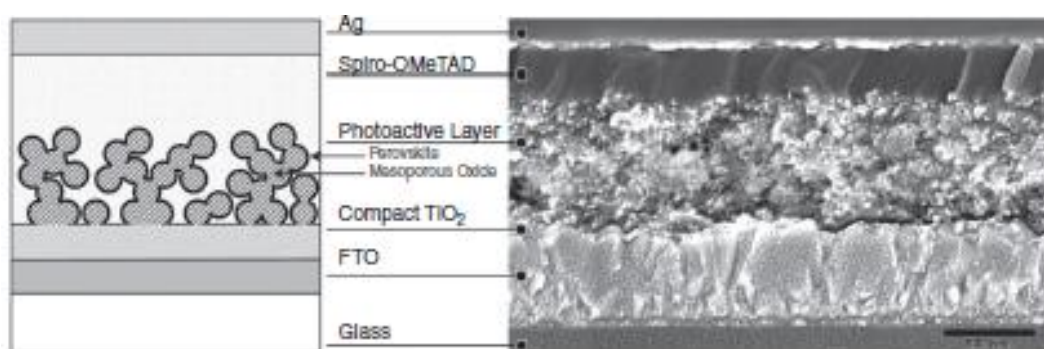


Figure 2.11 Schematic representation and SEM image of a typical solid state perovskite sensitized solar cell [30].

One of the major advantages of organometal halide perovskite absorbers is the extinction coefficient or absorption coefficient. Because the $(\text{CH}_3\text{NH}_3)\text{PbI}_3$ nanocrystals exhibit a one order of magnitude higher absorption coefficient than the conventional N719 dye, they offer advantages for use in solid state sensitized solar cells where much thinner TiO_2 layers are employed than in liquid junction devices. Most solid state hole conductors tried in dye sensitized solar cells faced penetration and wetting problems into the 10 micron thick mesoporous layers and suffered from short carrier diffusion lengths in such thick devices. High absorptivity of perovskites opens the way of using thin layers and successful hole conductor penetration. An all solid state perovskite sensitized solar cell with an efficiency value over 9% could be realized using $(\text{CH}_3\text{NH}_3)\text{PbI}_3$ as sensitizer and spiro-MeOTAD as the hole conductor medium on a submicron thick TiO_2 layer [15]. After first realization of a full solid state and high efficiency perovskite sensitized solar cell, work have been conducted on different type of hole conductor materials and cell structures. Seok et al. reported an an efficiency up to 14% using lead iodide and bromide mixture perovskite absorber based cell where hole transport medium is polytriarylamine[22]. Burscka et al. employed a sequential deposition route to deposit lead perovskite layer inside the pores of the TiO_2 layer which enhances the particle size distribution and coverage. They also used spiro OMETAD as the hole conductor but in conjunction with additives like 4-tert-butylpyridine, lithium bis

(trifluoromethylsulphonyl) imide and tris(2-(1H-pyrazol-1-yl)-4-tert-butylpyridine) cobalt (III) bis (trifluoromethylsulphonyl)imide in order to enhance the conductivity of spiro OMETAD medium, yielding an efficiency of 15% [17]. Qin et al. reported a lead iodide based perovskite absorber based cell employing CuSCN as the hole conductor medium and reached 12.4 % efficiency [32]. A lead-free solid-state organic–inorganic halide perovskite solar cell was realized substituting lead with tin and spiro OMETAD hole conductor giving an efficiency of 5.73% [33]. Snaith et al, employed methylammonium lead iodide chloride ($\text{CH}_3\text{NH}_3\text{PbI}_{3-x}\text{Cl}_x$) as the perovskite layer and used aluminium oxide as the mesoporous media different from TiO_2 and realized an efficiency of 10.9% [16]. They report that Al_2O_3 based cells yield remarkably higher photovoltage and efficiency value from TiO_2 based cells due to reduced recombination by using aluminium oxide. This finding is interesting because in this type of cell, electron transport occurs not from mesoporous layer but from the perovskite layer itself. Upon this particular finding, ideas and approaches like deposition of single junction perovskite layers, similar to conventional silicon solar cells or thin film solar cells, became popular and different device architectures like planar cells without any mesoporous scaffolding layers or hybrid structures have risen in perovskite research community. A rapid progress in device structures lead to n-i-p or p-i-n configured solar cells.

2.3.3 Device Architectures of Perovskite Solar Cells

The architecture of the perovskite solar cells have decisive effect on the performance of the devices and dictate choice of materials, deposition methods and compability between individual layers. So far, two dominant architectures have been developed and employed in perovskite solar cells, the mesoscopic and the planar architectures. Figure 2.12 shows the basic structures of these architectures based on the sequence of the layers and the employed materials for construction where the n-type and p-type materials show variation depending on the architecture.

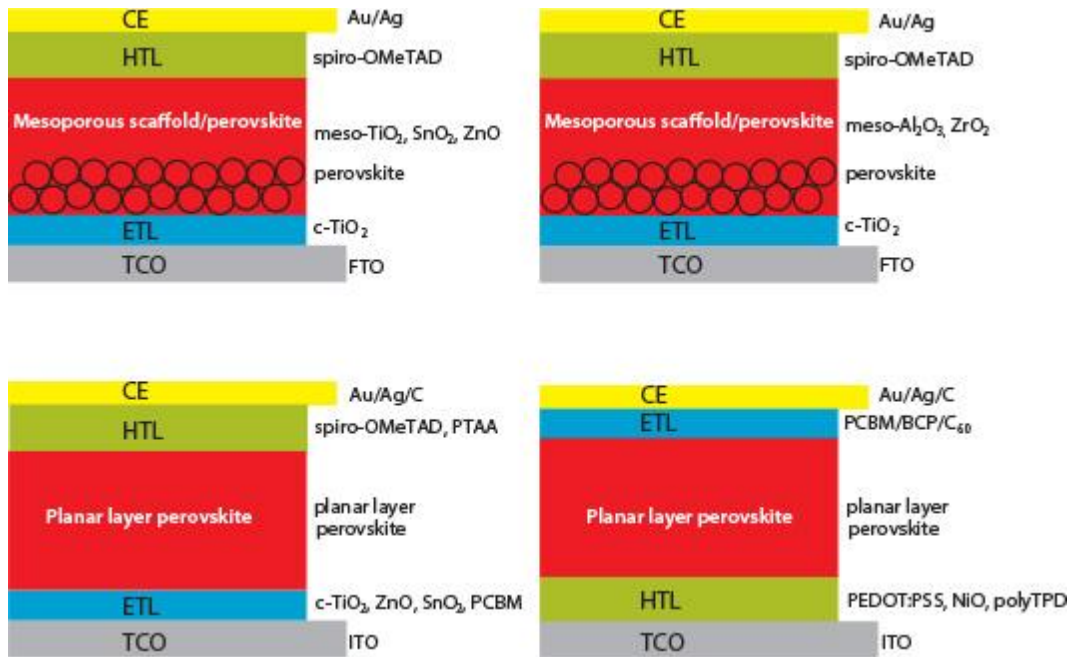


Figure 2.12 Device architectures of perovskite solar cells [34].

2.3.3.1 Mesoscopic Architecture Perovskite Solar Cells

The mesoscopic or mesostructured cells have been studied extensively because of the fact that historic evolution of perovskite solar cells rise on the mesoscopic cells, sensitized solar cells where first perovskite cell was employing perovskite crystals as a sensitizer in a dye sensitized solar cell configuration. In these studies, the mesoporous layer was an active n-type material and was contributing the cell operation by conducting electrons injected from the perovskite layer. The most widely used compound in these works was TiO_2 . Although due to development of planar architecture, the necessity of existence of TiO_2 layer is suspicious, the thickness of the TiO_2 layer is a key parameter for achieving high efficiencies. It has been showed that in contrast to DSSCs where a several microns thick TiO_2 layer is essential for efficient light absorption due to low absorption coefficient of Ru based dyes, sub-micron thick TiO_2 layers are sufficient enough for absorbing most of the solar spectrum and optimum mesoporous layer thickness is on this range [35]. This situation is also related to the fact that pore filling of the mesoporous structure plays

a dominant role in this configuration. For high concentration perovskite precursor solutions, a 300 nm thick film at least yields the best results due to the formation of continuous and interconnected perovskite crystals, instead of a randomly distributed weakly connected nanoparticles. This coverage efficiency of the TiO_2 by the perovskite crystals also plays an important role in preventing the direct contact between the hole transport material and TiO_2 layer [36]. TiO_2 can not only be deposited as a nanoparticulate structure, but other shapes like rods, nanotubes, wires or flakes are possible candidates for mesoscopic layers in perovskite solar cells. Such 2-D ordered structures offer better electron pathways and enhanced electron collection efficiency compared to 1-D nanoparticles.

The mesoporous layers employed in perovskite solar cells are not limited to n-type materials. So far, mesoscopic p-type layers were successfully demonstrated as hole collection layers similar to TiO_2 based cells. Of course, in this case a p-type blocking layer is also essential. Nickel oxide based mesoscopic perovskite solar cells possessing a ITO/NiO/mp-NiO/PCBM/BCP/Al structure was developed and efficiencies up to 11.6% was achieved by using sputtered NiO layers instead of a spin coated layer [37]. This type of a perovskite solar cell is considered as a typical mesoscopic p-i-n configuration. These studies showed the versatility of the perovskite solar cells and by removing the low stability p-type polymeric hole conductors, stability issues were also improved.

The mesoscopic layers in perovskite solar cells can also be modified with additives which are incorporated with in perovskite layer and contribute to the cell functioning by either enhancing the charge transfer processes or light absorption efficiencies. Cooperation of quantum dots of lead sulfide in a mesoscopic perovskite solar cell resulted in a panchromatic light absorption extended to near infrared region and enhanced internal quantum efficiency. These particles also are reported to contribute to electronic charge transfer between TiO_2 and the perovskite layer [38]. Similar to quantum dots, graphene and fullerenes or their composites can

be used to modify TiO₂-perovskite interface and improve charge transfer events occurring between the mesoscopic layer and the perovskite layer [39].

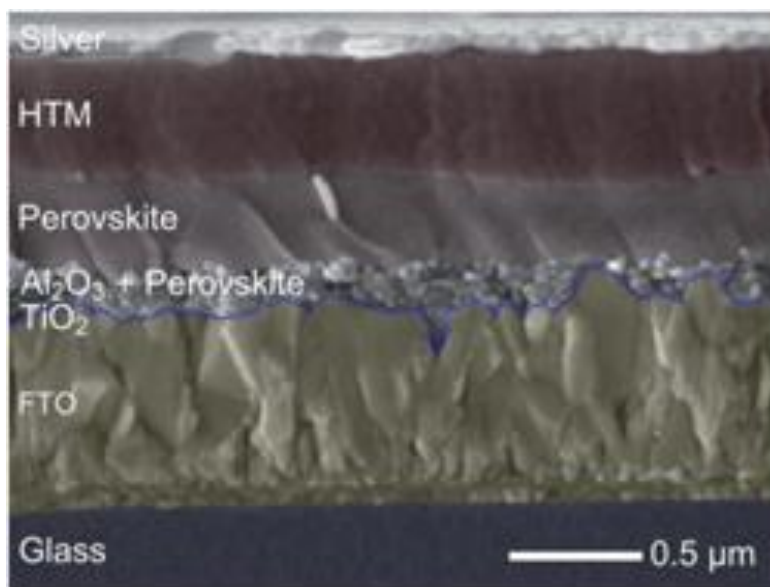


Figure 2.13 Cross-sectional SEM image of a mesoporous perovskite solar cell employing insulating Al₂O₃ scaffolding layer[40].

Mesoscopic layers used in perovskite solar cells contribute to cell functioning by transporting electrons or holes, however insulating materials like Al₂O₃ or ZrO₂ can also be employed as the mesoscopic elements (Figure 2.13) and act like scaffolding layers, which means that they do not involve in charge transport but supply the necessary room for deposition of perovskite crystals. One of the major advantages of the application of scaffolding layers is the reduction in processing temperatures. In contrast to cells employing TiO₂ or ZnO layers, no additional heat treatment for removal of organic binders in the pastes used for deposition and sintering of the nanoparticles, scaffolding layers require no heat treatments. It has been shown that scaffolding layers can be processed at temperatures around 150°C and can be used in flexible substrates [40]. The demonstration of the applicability of insulating layers in perovskite solar cells also contributed to the development of planar perovskite architectures after realization of the fact that in the case of

scaffolding layer based solar cells, the perovskite layer acts similar to a thin film solar cell.

Various hole transporting materials of polymeric or inorganic substances have been successfully employed as the hole selective layers in mesoscopic solar cells. However, hole conducting free mesoscopic perovskite solar cells also show promising results and attentions have been focused on these configurations. Organo lead halide materials possess intriguing semiconducting properties like ambipolar nature and long carrier life time and as a result, perovskite layer itself can conduct holes efficiently without the need of an hole transporting medium. The materials cost of perovskite solar cells can be greatly reduced with elimination of a hole conducting material. In addition, most p-type materials are polymeric substances like the most popular spiro-OMETAD which are quite sensitive to moisture and atmospheric effects, leading to decreased service times. It has been demonstrated that by using a mesoporous TiO₂ network, perovskite layer embedded inside pores and gold as the counter electrode, with a device architecture of FTO/bl-TiO₂/mp-TiO₂/CH₃NH₃PbI₃/Au, efficiencies up to 11% is achievable [41]. In this structure, due to the n-type TiO₂ layer and p-type perovskite layer, a depletion region is formed extending along the TiO₂ and the perovskite. The built in electrical field successfully leads to charge separation and transport through the cell and back reaction of the holes and electrons can be suppressed efficiently. Width of the depletion layer strongly correlates to the efficiency of the cell and effect of the depletion layer was clearly revealed.

Carbon based electrodes have been developed in terms of the need for hole conductor free devices and as a replacement of the noble metal counter electrodes which are all rare earth expensive metals. They are also deposited by high cost evaporation techniques. Carbon however, is an earth abundant, stable and cost effective material which has a work function of 5.0 eV, close to that of Au with 5.1 eV. Screen printed carbon electrodes have been employed as the counter electrode in a layered mesoporous structure of TiO₂ and ZrO₂. With the aid of additives like

ammonium valeric acid iodide (5-AVAI) and a structure of FTO/bl-TiO₂/mp-TiO₂/mp-ZrO₂/CH₃NH₃PbI₃/Carbon, efficiencies up to 12.8% was reported [42]. The role of the 5-AVAI is reported to reorganize the crystallization behaviour of the perovskite crystals embedded inside mesoporous network and due to a preferential orientation of the crystals, charge collection efficiencies are improved. Unsealed cells still retain their efficiencies and excellent stability is also attributed to the carbon electrode, preventing the moisture from penetrating deep inside the cells.

Various researches so far have already showed that perovskite crystals act like a p-type layer and a hole conduction medium is not a prerequisite. However, hole conductor free cells still cannot compete with the cells with polymeric hole conductors by means of efficiencies. Charge extraction efficiency and suppression of recombination are actual reasons for the superior performance of the cells with hole conductors and they yield higher open circuit potentials and fill factors. Strategies like improving the built in potentials, deposition of more homogeneous layers and suppression of recombination by employing insulating layers are on research stage and promise enhanced efficiencies for future.

2.3.3.2 Planar Architecture Perovskite Solar Cells

The low temperature processibility of perovskite solar cells was demonstrated, however most groups still employ mesoporous solar devices which require high temperature sintering stage, especially for high efficiency devices. The mesoporous layer can be excluded from the perovskite solar cells due to the ability of the perovskite layer to transport electrons and holes efficiently during cell operation, which leads to deposition of planar perovskite solar cells. One of the major advantages of the planar architecture is the low temperature deposition conditions and applications on polymer substrates for flexible photovoltaics. In addition, lack of the high temperature treatment is also economically more viable and opens the way of more versatile deposition techniques.

Planar architecture perovskite solar cells can be constructed two ways referred as the n-i-p configuration or the conventional way and the p-i-n configuration or inverted solar cells. n-i-p configuration is the most commonly employed structure where the n-type layer is deposited on the TCO glass and light passes through this layer. Cell is completed by the deposition of the perovskite layer, p-type layer and the back contact. In planar n-i-p, the actual difference is that mesoporous n-type layer is not deposited as the electron selective scaffold. The electron selective n-type layer can be deposited in different ways. First examples were simply TiO₂ nanoparticles with reduced porosity and low temperature heat treatments [43]. Chemical bath deposition of rutile TiO₂ from aqueous TiCl₄ solutions were also employed for low temperature applications and provided efficiencies up to 13.7%, which is also found to be superior compared to anatase TiO₂ [44]. ZnO has higher mobility than TiO₂ and ZnO nanoparticles were successfully employed as the electron transport layers in flexible substrates. ZnO can easily be synthesized by hydrolysis of its precursors at low temperature conditions and require no thermal treatment. 15.7% efficiency values were observed from spin coated ZnO layers on conductive flexible substrates [45]. As the hole transporting medium, similar to the mesoporous structures, spiro-OMETAD is the choice of the p-type material yielding the highest efficiencies. Other polymeric hole conductors were also studied in planar n-i-p configuration solar cells and gave lesser performances like P3HT or other polythiophene derivatives. On the other side, interlayer additives used for the modification of the anode part give promising results. These interlayers are useful by means of reducing the work function of the collector electrode and enhancing the charge transfer between electron transport layer and the perovskite layer like PEIE and PCBM [46].

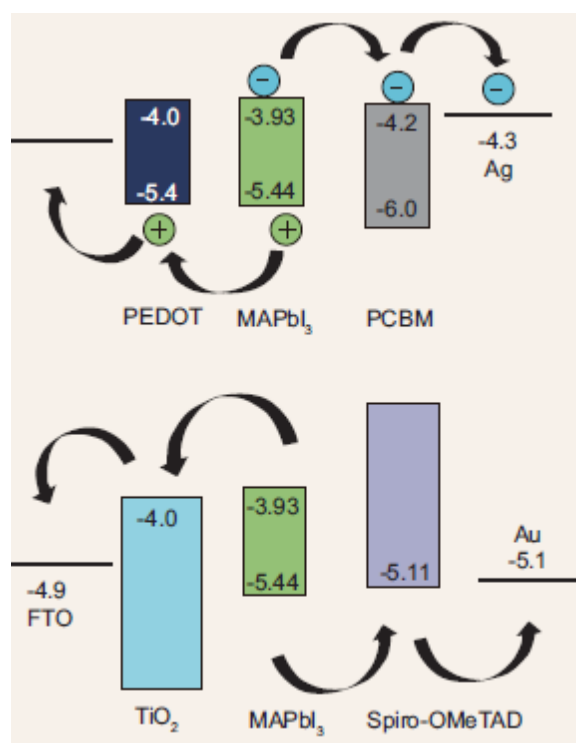


Figure 2.14 Energy levels of components of perovskite solar cells in n-i-p and p-i-n inverted configurations [47].

p-i-n architecture perovskite solar cells can basically be distinguished from the conventional n-i-p structure by the direction of the incoming light where a p-type layer is deposited on the TCO glass and perovskite and n-type layer is deposited sequentially. But this configuration actually differs from n-i-p architecture by means of the hole conducting layers where well known spiro-OMETAD is not the material of choice in this case. In the early attempts of constructing p-i-n perovskite solar cells, PEDOT: PSS was employed successfully where the n-type layer is most commonly PCBM, both of which can be deposited by spin coating [48]. Due to the stability issues regarding the highly hygroscopic PEDOT: PSS layers, nickel oxide was used as an inorganic highly stable alternative. NiO has a favorable band alignment with a valence band minimum of -5.4 eV which perfectly matches with that of perovskite layer and several groups have studied deposition of the NiO layers. The TCO layer is FTO or ITO for both configurations where back contact

metal is chosen as the high work function Au for n-i-p configuration cells for efficient charge transfer from the p-type layer. In the case of the inverted cells, a low work function metal like Ag or Al are most widely used to extract electron from the n-type layer. Figure 2.14 shows the direction of charge flow inside the cells depending on the architecture.

Device configuration of the perovskite solar cells have great impact on the efficiency and stability of the cells as well as cost and mass production is also influenced directly because of the fact that structure of the cell dictates the materials of choice. There is great effort to replace polymeric materials like the PEDOT:PSS and PCBM with inorganic counter parts in planar configurations and enhancing the efficiency of these architectures is of great importance due to the elimination of the high temperature sintering process of mesoporous layers. In addition, deposition methods like evaporation or spin coating on flexible substrates at low temperatures attract great attention from the industry.

2.3.4 Deposition Methods of Perovskite Layers

Performance of the perovskite based solar cells highly depend on the morphology and surface coverage of the perovskite layer on different substrates and perfection of the controlling of the perovskite layer resulted in the highly efficient solar cells developed until this date which have progresses rapidly. Different approaches for deposition of perovskite layers in literature, mainly rely on the crystallization of the perovskite layers from its precursors. It has been shown that by employing different crystallization strategies, it is possible to deposit large crystalline domains or large perovskite grains which is the major factor for achieving highest efficiency from a perovskite solar cell.

2.3.4.1 One-step Deposition

First solar cells with perovskite layers were constructed by a one-step deposition method, where a precursor solution containing PbCl_2 and excess MAI were dissolved in DMF coated on the mesoporous layer by a spin coating procedure. However, both PbI_2 and PbCl_2 yielded poor surface coverages with needle-like or island-like structures on the mesoporous layers. Although 10% efficiency limit was reached with this methods in the early studies, such uncovered areas are detrimental to cell functioning where p-type layer come to direct contact with the n-type layers, resulting in strong recombination centers for the carriers [49]. First attempts for the modification of the perovskite layer were focused on the solvent media and solvents like DMSO or N-methylpyrrolidone were studied for perovskite deposition which lead to more homogeneous layers and planar architecture cells could be successfully prepared with high efficiency through this solvent engineering approaches [50].

Actual boost to solar cell efficiencies by modification of the one-step deposition method was achieved by the introduction of the anti-solvent approach. Dropping an anti-solvent on the wet film during spin coating, results in fast crystallization of the precursors in the solution. Many solvents which have poor solubility of the widely used precursors of $\text{CH}_3\text{NH}_3\text{PbI}_3$ like isopropanol, toluene, chloroform or chlorobenzene have been tried so far and micron scale perovskite grains could be deposited due to induced crystallization of the precursors during the spin coating stage where solvent evaporation and nucleation is the major factor determining the morphology of the resulting films. Efficiencies up to 14% for planar architecture devices and a record efficiency of 16% was reported for that date in a mesoscopic cell by a mixed solvent of DMSO and butyrolactone where toluene was used as the anti-solvent agent [51]. As proven by the earlier studies, addition of some complexing agents into the precursor solvents also has considerable effect on the film morphology of the perovskite layer. DMSO has higher solubility of PbI_2 than DMF by complexing with the strong coordination with PbI_2 . This results in reduced reaction kinetics and o more controllable crystallization can be realized through

creation of an intermediate phase before crystallization and in turn films possess larger domains (Figure 2.15). DMSO addition forms a stable complex with PbI_2 and retards the crystallization procedure which after goes into a molecule exchange reaction with the other organic molecules in the precursor film. This type of Lewis adducts have been studied also in depth for larger grain sizes and enhanced efficiency of the perovskite cells [52-54].

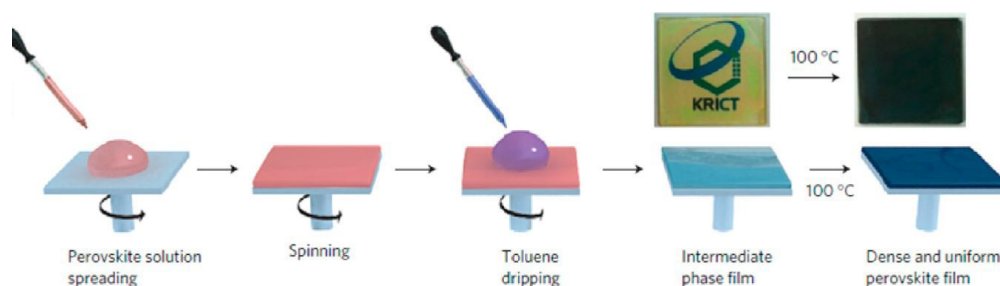


Figure 2.15 Anti-solvent approach for one-step perovskite deposition [54].

In addition to solvents used in precursor solutions, precursor materials also have high impact on the resultant films. Lead (II) salts employed in the film preparation like the halides or other anions, contributes to the defect concentration of the final films where iodine rich films have higher trap densities compared to the iodine poor growth conditions [55]. The lead salt also affects the morphology of the films due to differences of crystallization kinetics of each anion during deposition. Activation energy for crystallization is different for each salt and annealing time and temperatures can be tuned accordingly. Lead (II) acetate was proven to yield the smoothest films among all precursor solution due to increased crystallization rate and ultrasmooth pin hole free layers can be deposited to yield high efficiency planar perovskite solar cells [56].

2.3.4.2 Two-step Deposition

Apart from the one-step deposition methods, two-step deposition method was developed in the early works of perovskite research. The main difference of the two-step method is to deposit each layer for the formation of the $\text{CH}_3\text{NH}_3\text{PbI}_3$ phase sequentially so this method is also referred as the sequential deposition. For this purpose, PbI_2 was dissolved in DMF solution and deposited on the substrate by spin coating. Conversion of the PbI_2 thin film is conducted by immersing the film into a solution of MAI, concentration of which directly affects the morphology of the resultant films. Cuboidal or smaller perovskite particles were obtained through this method instead of a continuous large grain sized films produced by the one-step anti-solvent methods and efficiencies over 12% were reported in TiO_2 mesoscopic cells [57].

In-situ formation of the perovskite crystals by the two-step method are mainly governed by the diffusion, dissolution and recrystallization of the reactants in the predeposited PbI_2 film. In addition the morphology of the PbI_2 films which also affects the final form of the perovskite crystals, diffusion of MAI starting from the top the PbI_2 grains, converts the structure into perovskite in the upper layers and diffusion governs the rate of this reaction. Meanwhile perovskite crystals formed at the top go into a dissolution and recrystallization stage and a process similar to Oswald ripening grows the crystals in the perpendicular direction and stress results in the cracked and smaller grains on the top [58]. Instead of free standing individual particles grown by the low concentration MAI solutions, increased concentration of the MAI solution and depositing a separate MAI layer on the PbI_2 make it possible to grow a continuous and dense film made up of large grains for high efficiency and planar device configurations. By modification of the concentration and thickness of the each layer, films with desired thickness and continuous structure can be achieved and high efficiency cells can be prepared with controlled grain sizes [59]. Efficiencies up to 16% have been reported in an inverted planar configuration constructed by the two-step method with enhanced open circuit voltages [60].

2.3.5 Hole Transport Materials For Perovskite Solar Cells

2.3.5.1 Organic Hole Transport Materials

The emergence of perovskite solar cells was due to the outstanding properties of the perovskite material and as well as the polymeric solid state hole conductors with excellent matching with the perovskite layer. It has been pointed out in the previous sections that spiro-OMETAD is the choice of the hole conducting material and highest efficiencies reported to date still employ it. Success of spiro-OMETAD is related to the fact that it is well known and deeply studied in solid state dye sensitized solar cells and organic light emitting diodes before perovskite solar cell applications. However, the cost of this material is problematic for large scale applications and stability issues regarding the air sensitivity could still not be solved. From a point of view of commercialization and acceptance of perovskite solar cells by the industry, development of low cost alternatives is crucial.

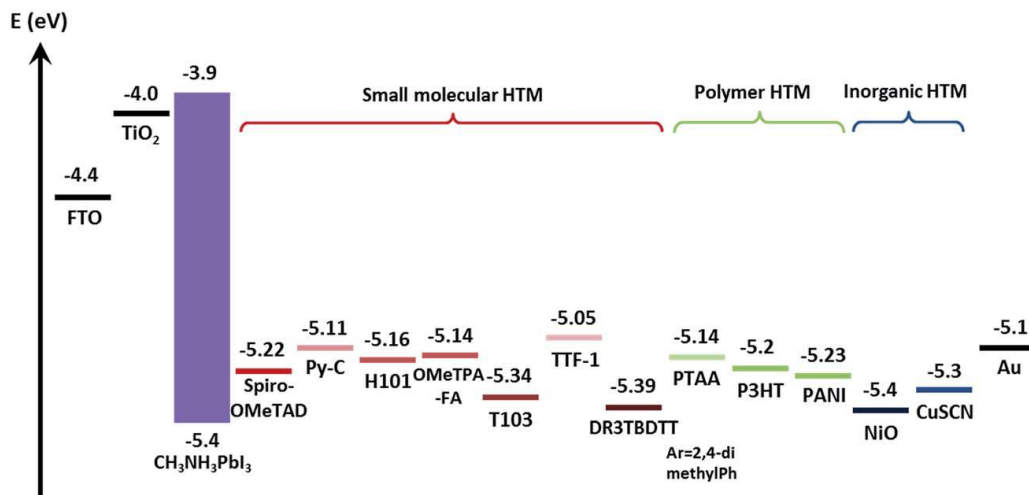


Figure 2.16 Various hole conducting materials employed in perovskite solar cells so far [61].

Hole transport materials to be applied in perovskite solar cells must meet some requirements similar to the solid state dye sensitized solar devices. Firstly they must

have a proper band alignment with that of perovskite, which means that HOMO level of the hole transport medium must be energetically compatible with the valence band of the perovskite lying around -5.4 eV. In Figure 2.16, HOMO levels of many polymeric and some inorganic materials are summarized. The desirable band alignment is a negligible energy difference of the HOMO level and valence band of the perovskite, no more than 0.05 eV. Higher differences leads to an energy barrier for hole transfer and limits the current output, where low lying levels results in reduced open circuit voltages attainable from the cell. In addition to energetic consideration, the hole conducting medium must have a good mobility and solubility in well known solvents for film formation. In contrast to solid state dye sensitized solar cells, pore filling ability is not a prerequisite for the hole conductors as long as the pores are filled with perovskite crystals and homogeneous pin-hole free film formation is more crucial for the device function.

Polymeric hole transport materials have better mobility and film forming ability than the small molecule materials and have been studied in perovskite solar cells. Poly triarylamine (PTAA) and poly 3-hexylthiophene-2,5-diyl (P3HT) were the first polymers employed in mesoporous architectures. Efficiencies up to 17.9% was reported for PTAA [62], where P3HT yielded lower efficiencies in pristine form. P3HT functionalized carbon nanotube hole conducting layers gave the highest efficiency of 15.3% so far [63]. The electrical conductivity of the polymeric materials can be greatly enhanced by certain additives like pyridine or cobalt complexes and most high efficiency cells employ polymeric conductors modified with the additives, which is also valid for the spiro-OMETAD material. Another advantage of polymeric hole conductors is the tunability of the electronic properties by modification with certain additives and deeper HOMO levels can match perfectly with halide perovskites like $\text{CH}_3\text{NH}_3\text{PbBr}_3$ which gives enhanced open circuit potentials and can be employed in tandem devices. Small molecule hole transport materials are also promising materials by means of versatility in their design and mostly pyridine and triarylamine derivatives are employed and efficiencies up to 13.8% could be achieved [64].

2.3.5.2 Nickel Oxide (NiO) Based Inorganic Hole Transport Materials

Although highest efficiencies reported to date are based on the polymeric materials like spiro-OMETAD and PTAA, the extreme cost of these materials and stability issues still stand as an obstacle for large area applications. Inorganic p-type materials offer the low cost, abundance, high hole mobility and extreme stability compared to the polymeric counter parts. There are few p-type materials which satisfy the electronic band matching and hole conduction with the organo lead halide perovskite materials (Figure 2.17). These materials are mainly copper compounds like copper (I) iodide (CuI), copper (I) thiocyanate (CuSCN), cuprous oxides (CuO, Cu₂O) and the well known nickel (II) oxide (NiO). Vanadium (II) oxide (V₂O₅) and some other novel p-type materials have also been studied and demonstrated as suitable p-type materials for perovskite solar cells applications.

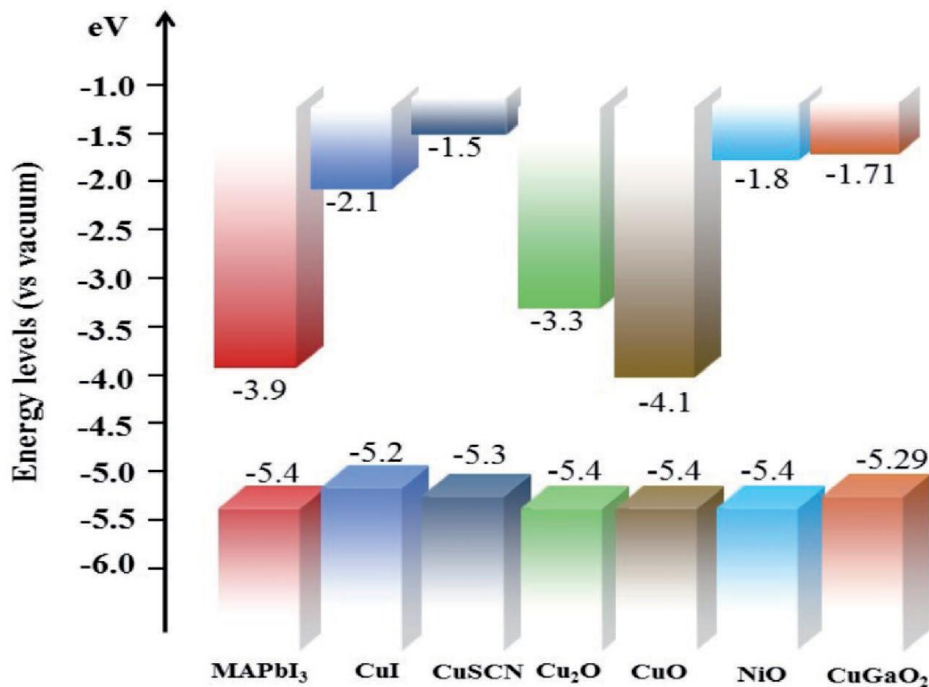


Figure 2.17 Energy band diagrams of the inorganic p-type materials which satisfy the electronic band condition in perovskite solar cells [65].

NiO is a superior candidate for perovskite solar cell applications possessing excellent thermal and chemical durability, low cost and abundance and have been proven to act like a hole transport medium thanks to its suitable work function and valence band position with respect to perovskite absorber. The high conduction band position is quite advantageous for blocking electrons from the perovskite layer. The first attempts to employ NiO as the charge selective layer in perovskite solar cells resulted with poor efficiencies around 1%, however after improving the morphological properties of the NiO layer and the perovskite layer, tremendous progress have been achieved.

2.3.5.2.1 Nickel Oxide In Mesoporous Cells

The first examples of the NiO based devices were mesoporous carbon based devices where a mesoporous TiO_2 and an insulating ZrO_2 layer were sequentially deposited below a mesoporous carbon counter electrode (Figure 2.18). In this configuration, perovskite crystals are infiltrated inside the mesopores and act like the hole transporting medium itself. The role of ZrO_2 layer is to insulate the n-type TiO_2 layer from the carbon collecting electrode.

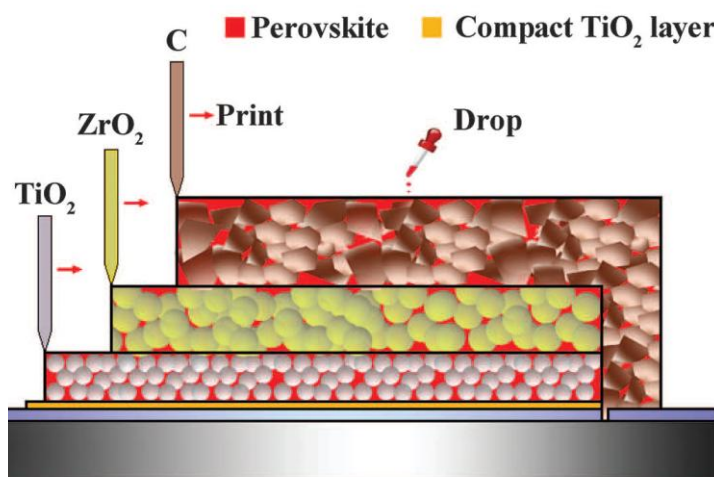


Figure 2.18 Schematic representation a mesoporous carbon based device [66].

Replacement of the ZrO_2 layer with NiO layer resulted in decreased recombination and enhanced charge collection inside the cell efficiencies up to 11.2% were reported with a FTO/ TiO_2 /NiO/Carbon configuration where perovskite layer is distributed inside the whole structure [67]. This configuration, however, resulted in a recombination center between the n-type TiO_2 layer and the NiO layer. Addition of a thin ZrO_2 layer between the two charge selective layers helps the prevention of interfacial recombination at the NiO/ TiO_2 interface and upon addition of a perovskite layer with the sequential deposition method, efficiencies up to 14.2% could be realized with a fully inorganic structure [68]. Another significant feature of these devices is the excellent producibility of the architecture by cheap production techniques like screen printing and doctor blading. Replacement of the expensive gold layers, which are also deposited by costly vacuum evaporation techniques, with abundant and ultra cheap carbon materials make the carbon based devices the most promising route to mass production and commercialization. In addition to ease of production and low cost, due to lack any organic component in carbon based cells, prolonged cell life time has also been demonstrated compared to the cells produced with polymers or small molecules. The thick carbon layer prevents the humidity from air penetrating inside cell, also due to the hydrophobic nature of carbon is also another factor for protection of the perovskite crystals inside the pores.

In carbon based perovskite solar cells, in addition to type of mesoporous layers and their sequence in the cell, distribution and orientation of the perovskite crystals is another important factor for high efficiency. Introduction of a wetting agent into the precursor solution like 5 ammoniumvaleric acid iodide (5-AVAI) resulted in the orientation of the perovskite crystals and enhanced efficiency compared to the cell not containing the agent [66]. Later on, by controlling the crystallization of perovskite crystals via employing different types of the precursor solvent [71] and thermal treatment under controlled humidity, distribution and pore filling capability of the perovskite crystals were further enhanced and efficiencies over 15% could be

achieved [72]. In Table 2.2, device architecture and production methods of the carbon based perovskite solar devices up to date have been summarized.

Table 2.2 Type of mesoporous layers and deposition methods of carbon based cells.

Ref.	Structure	Deposition method	Eff. (%)
Mei et al. 2014 [66]	TiO ₂ / ZrO ₂	5-AVAI assisted	12.8
Liu et al. 2015 [67]	TiO ₂ /NiO	One step	11.4
Xu et al. 2015 [69]	TiO ₂ / ZrO ₂ /NiO	2-step sequential	14.9
Liu et al. 2015 [68]	TiO ₂ / ZrO ₂ /NiO	5-AVAI assisted	14.2
Cao et al. 2015 [70]	TiO ₂ / Al ₂ O ₃ /NiO	2 step sequential	15.03
Tsai et al. 2017 [71]	TiO ₂ / Al ₂ O ₃	One step slow crystallization in NMP	15.0
Hashmi et al. 2017 [72]	TiO ₂ / ZrO ₂	One step humidity assisted thermal treatment	14.3

Application of NiO in mesoporous structures is not limited to carbon based devices. NiO nanoparticles were employed to create a mesoporous network on a NiO compact layer deposited on the TCO glass and perovskite layer was infiltrated by sequential deposition method, where the n-type contact was a PCBM layer incorporated with bathocuproine. The resulting device yielded an efficiency of 9.51% and a open circuit voltage of 1.04 V [73]. The high potential attained from this configuration arises from the excellent band alignment of materials employed. Valence band maxima of NiO perfectly matches with perovskite valence band and the HOMO level LUMO level of PCBM layer also matches well with perovskite conduction band, leading to minimized thermodynamic loss of open circuit

potentials. The existence of the mesoporous NiO layer contributes to the cell by means of supplying room for perovskite crystals and eliminating the irregularities in the perovskite layer which in turn may cause serious potential loss during cell operation. In addition, existence of the mesoporous layer also increases the light absorption in the longer wavelength range due to the thicker perovskite layer. The effect of compact layer morphology on the device performance was studied by depositing the NiO layer with a RF magnetron sputtering method. Solution processed NiO compact layers may include pin holes and cracks and not fully homogeneous over the entire TCO surface. Introduction of the sputtered NiO layer in conjunction with a mesoporous NiO layer, a sequentially deposited perovskite layer and a PCBM layer resulted in 11.6% efficiency [74]. It was shown that high quality NiO layers results in enhanced charge collection compared to the solution processed films (Figure 2.19).

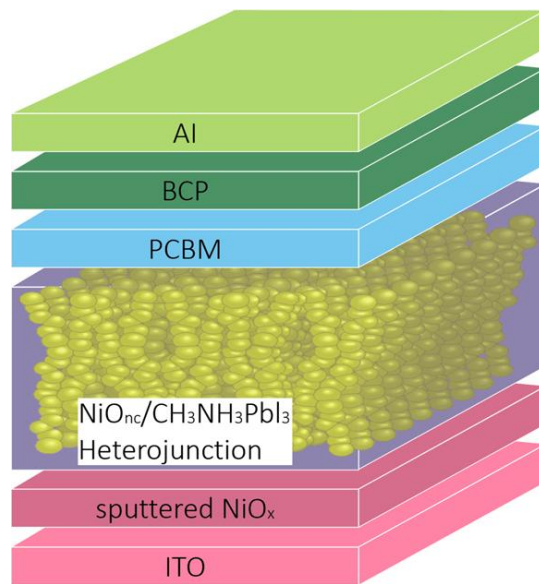


Figure 2.19 Schematic illustration of a p-type mesoscopic p-i-n solar device employing NiO mesoporous layers [74].

The mesoporous layer was later eliminated by a compact layer made up of NiO nanoparticles which was employed as the both mesoporous layer and the compact

layer with a similar configuration as ITO/NiO/CH₃NH₃PbI₃/PCBM/Au. After optimization of the thickness of the NiO layer, which was deposited around 40 nm thickness value, an efficiency of 9.11% was achieved [75]. This work also proved that scaffolding thick mesoporous layer is not a prerequisite for extracting high efficiencies from NiO based cells. Transient photo induced absorption spectroscopy revealed that the holes present in the NiO layer during charge transport have long lifetime and charge separation occurs at the NiO/perovskite interface. The optimization of the mesoporous layer thickness is crucial for efficient charge collection and reducing the recombination losses during transport. For this purpose, in a work studying the ultrathin NiO layers as a compact electron blocking layer in perovskite solar cells, Al₂O₃ was employed as the mesoporous scaffold layer, in a FTO/blocking NiO/mesoporous Al₂O₃/CH₃NH₃PbI₃/PCBM/BCP/Ag configuration. Al₂O₃ was employed as the non-charge injecting scaffolding mesoporous layer instead of a NiO mesoporous layer. This configuration maximizes the light absorption due to the transparent Al₂O₃ layer. In addition, recombination losses are also prevented by the nanoparticles passivating the pin holes in the compact layer and shunt paths between the PCBM layer and the NiO layer also blocked effectively, leading to an efficiency of 13.5% and high fill factor of 0.72 [76].

2.3.5.2.2 Nickel Oxide In Planar Cells

Application of NiO in mesoporous cells have shown the ability of NiO to extract and transport holes in the perovskite layer and it also acts as an electron blocking layer simultaneously. At the same time with the development of planar configuration perovskite solar cells, NiO was employed as the hole selective contact instead of the most popular material PEDOT:PSS in inverted type or the p-i-n structured cells. In the first attempts to construct NiO based cells, NiO layer was deposited on the TCO glass by spin coating a nickel precursor solution. It was shown that surface coverage of the perovskite layer deposited on a NiO layer was poor and wetting ability of the NiO layer was improved by a UV-Ozone treatment and efficiency around 7.8% was realized [77]. The ozone treatment also reduces the

valence band position of the NiO layer to 5.4 eV for a better band alignment with perovskite layer. A NiO based device where the compact layer of NiO was deposited by spin coating a solution of nickel acetate dissolved in methoxyethanol in a ITO/NiO/ CH₃NH₃PbI₃/PCBM/Al configuration yielded 7.6% efficiency after ozone treatment [78]. By improving the morphology of the NiO layer via using magnetron sputtering method and morphology of the perovskite layer via solvent engineering approach, efficiency of 9.84% could be achieved, proving the importance and necessity of the control of morphological properties of the interlayers seen in Figure 2.20 in planar configurations [79].

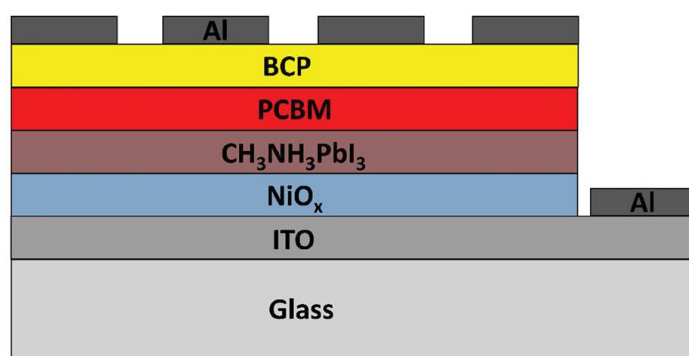


Figure 2.20 Schematic structure of an inverted p-i-n type planar perovskite solar cell employing NiO layers [77].

As a main trend, NiO based perovskite solar cells possess lower fill factors compared to the PEDOT:PSS based cells. A composite structure where NiO compact layers were treated with PEDOT:PSS, showed an efficiency value of 15.1% thanks to the improved roughness of the surface which enhances the charge transfer processes with the perovskite layers [80]. Modification of the NiO layer was conducted via doping the NiO with Cu forming a planar structured Cu doped NiO based cell and due to increased electrical conduction and improved perovskite layer quality upon Cu doping, an efficiency of 17.7% was demonstrated as a record efficiency value [81]. Significance of the work is also the low temperature combustion sol-gel process at 150°C. In a flexible solar cell design, solution

processed NiO nanoparticles were deposited on a PET substrate at room temperature in PET/ITO/NiO/CH₃NH₃PbI₃/C₆₀//Ag configuration and efficiency of 14.5% was achieved, demonstrating the performance of NiO based cells on flexible solar device applications [82].

All above works demonstrates robust NiO layer as a hole transporting medium, however they employ PCBM or fullerenes as the n-type charge collector which inhibits improved device stability in outdoor conditions. An all solution processed and fully metal oxide structure was developed by using NiO as the hole conductor and ZnO nanoparticles as the electron selective contact as a replacement of the PCBM layer. 16.1% efficiency was reported for a ITO/NiO/CH₃NH₃PbI₃/ZnO/Al configuration device and cells produced this way were proven to sustain their efficiency up to 60 days without encapsulation, which shows the superior air stability of the polymeric material free devices [83]. This concept was further improved by doping the charge selective layers and enhancing the charge collecting efficiency of the metal oxide layers. Electrical conductivity of the NiO layer was enhanced via doing with Mg and TiO₂ was deposited as the n-type layer reaching an efficiency of 18.3% efficiency and 0.83 fill factor value [84]. It was proven that the high fill factor and efficiency is related to fast charge transfer between the charge selective layers and the perovskite layer which prevents charge accumulation and reduced charge transfer resistances.

Heavy doping of the charge selective metal oxide layers in perovskite solar cells have already been proven to be effective for improving stability and power output of the cells. This concept is still under investigation and is believed to lead to highly stable and efficient perovskite solar devices for future.

REFERENCES

1. A. Luque and S. Hegedus, Handbook of Photovoltaic Science and Engineering, John Wiley & Sons, England, 2003.
2. R. C. Neville, Solar Energy Conversion The Solar Cell 2nd Edition, Elsevier Science B.V.A., Amsterdam, 1995.
3. A. Goetzberger and J. K. Bernhard, Crystalline Silicon Solar Cells, John Wiley & Sons Ltd., Chichester, 1998.
4. T. Markvart and L. Castafier, Solar Cells: Materials, Manufacture and Operation, Elsevier, Amsterdam, 2005.
5. B. Sorensen, Renewable Energy: Its physics, engineering, use, environmental impacts, economy and planning aspects 3rd Edition, Elsevier Science, Amsterdam, 2004.
6. F. Kreith and Y. Goswami, Handbook of Energy Efficiency and Renewable Energy, Taylor and Francis Group, USA, 2007.
7. R. Sastrawan, Photovoltaic modules of dye solar cells, PhD dissertation, Freiburg im Breisgau, 2006.
8. V. Ramamurthy and K. S. Schanze, Semiconductor Photochemistry and Photophysics, Marcel Dekker Inc., New York, 2003.
9. A. Luque and S. Hegedus, Handbook of Photovoltaic Science and Engineering, John Wiley and Sons, Chichester, 2003.
10. B. Saparov, D.B. Mitzi, Organic-inorganic perovskites: structural versatility for functional materials design, Chem. Rev., 116 (2016) 4558–96.
11. National Renewable Energy Laboratory Photovoltaic Research: Efficiency Chart. <https://www.nrel.gov/pv/assets/images/efficiency-chart.png> (20 March 2018, date last accessed).
12. M. Cai, Y. Wu, L. Han et al., Cost-performance analysis of perovskite solar modules, Adv. Sci., 4 (2017) 1600269.

13. A.Kojima, K. Teshima, T. Miyasaka et al., Organometal halide perovskites as visible-light sensitizers for photovoltaic cells. *J. Am. Chem. Soc.*131(2009) 6050–1.
14. J.H. Im, C.R. Lee, N.G. Park et al., 6.5% efficient perovskite quantum-dot-sensitized solar cell, *Nanoscale*, 3(2011) 4088–93.
15. H.S. Kim, M. Gratzel, N.G. Park et al., Lead iodide perovskite sensitized all-solid-state submicron thin film mesoscopic solar cell with efficiency exceeding 9%, *Sci. Rep.*, 2(2012) 591.
16. M.M. Lee, J. Teuscher, H.J. Snaith et al., Efficient hybrid solar cells based on meso-superstructured organometal halide perovskites, *Science*, 338(2012) 643–7.
17. J. Burschka, N. Pellet, M. Grätzel et al., Sequential deposition as a route to high-performance perovskite-sensitized solar cells, *Nature*, 499 (2013) 316–20.
18. M. Saliba, T. Matsui, M. Grätzel et al., Cesium-containing triple cation perovskite solar cells: improved stability, reproducibility and high efficiency, *Energy Environ. Sci.*, 9(2016) 1989–97.
19. M. Saliba, T. Matsui, M. Grätzel et al., Incorporation of rubidium cations into perovskite solar cells improves photovoltaic performance, *Science*, 354 (2016) 206–9.
20. S.S. Shin, J.H. Noh, S.I. Seok et al., Colloidally prepared La-doped BaSnO₃ electrodes for efficient, photostable perovskite solar cells. *Science*, 356(2017) 167–71.
21. N.G. Park, M. Gratzel, K. Emery et al., Towards stable and commercially available perovskite solar cells, *Nat. Energy*, 1(2016) 16152.
22. T. Baikie, Y. Fang, J.M. Kadro et al., Synthesis and crystal chemistry of the hybrid perovskite CH₃NH₃PbI₃ for solid-state sensitized solar cell applications, *J. Mater. Chem. A*, 1(2013) 5628–41.
23. M.A. Green, A. Ho-Baillie, J.H. Snaith, The emergence of perovskite solar cells, *Nat. Photon.* 8(2014) 506–14.

24. C.C.Stoumpos, C.D. Malliakas, M.G. Kanatzidis, Semiconducting tin and lead iodide perovskites with organic cations: phase transitions, high mobilities, and near-infrared photoluminescent properties, *Inorg. Chem.*, 52 (2013) 9019–38.
25. Q. Chen, H. Zhou, Y. Yang et al. Under the spotlight: The organic-inorganic hybrid halide perovskite for optoelectronic applications, *Nano Today*, 10(2015) 355–96.
26. P. Gao, M. Gratzel, M.K. Nazeruddin, Organohalide lead perovskites for photovoltaic applications, *Energy Environ. Sci.*, 7(2014) 2448–63.
27. G. Hodes and A. Zaban, *Nanostructured Materials*, 2009 Elsevier Ltd.
28. J.K. Lee, M. Yang, Progress in light harvesting and charge injection of dye-sensitized solar cells, *Mater. Sci. Eng. B*, 176 (2011) 1142.
29. H. J. Snaith, Perovskites: The Emergence of a New Era for Low-Cost, High-Efficiency Solar Cells, *J. Phys. Chem. Lett.*, 4(2013) 3623–3630.
30. M. M. Lee, J. Teuscher, T. Miyasaka, T. N. Murakami, H. J. Snaith, Efficient Hybrid Solar Cells Based on Meso-Superstructured Organometal Halide Perovskites, *Science*, 338(2012) 643-647.
31. J. H. Noh, S. H. Im, J. H. Heo, T. N. Mandal, S. I. Seok, Chemical Management for Colorful, Efficient, and Stable Inorganic–Organic Hybrid Nanostructured Solar Cells, *Nano Lett.*, 13 (2013) 1764–1769.
32. P. Qin, S. Tanaka, M. Gratzel et al., Inorganic hole conductor-based lead halide perovskite solar cells with 12.4% conversion efficiency, *Nature Comm.*, 5 (2014) 3834.
33. F. Hao, C. C. Stoumpos, D. H. Cao, R. P. H. Chang, M. G. Kanatzidis, *Nat. Photonics*, Lead-free solid-state organic–inorganic halide perovskite solar cells, 8 (2014) 489-494.
34. K. Kalyanasundaram, S. M. Zakeeruddin, M. Grätzel, Recent Advances in Hybrid Halide Perovskites-based Solar Cells, *Mater. Matt.*, 11(2016) 3.
35. H.-S. Kim, C.-R. Lee, M. Gratzel, N.G. Park et al., Lead Iodide Perovskite Sensitized All-Solid-State Submicron Thin Film Mesoscopic Solar Cell with Efficiency Exceeding 9%, *Sci. Rep.*, 591 (2012).

36. T. Leijtens, B. Lauber, G. E. Eperon, S. D. Stranks, H. J. Snaith, The Importance of Perovskite Pore Filling in Organometal Mixed Halide Sensitized TiO₂-Based Solar Cells, *J. Phys. Chem. Lett.*, 5 (2014) 1096–1102.
37. K.C. Wang, P.S. Shen, M.-H. Li, S. Chen, M.W. Lin, P. Chen, T.F. Guo, Low-Temperature Sputtered Nickel Oxide Compact Thin Film as Effective Electron Blocking Layer for Mesoscopic NiO/CH₃NH₃PbI₃ Perovskite Heterojunction Solar Cells, *ACS Appl. Mater. Interfaces*, 6 (2014) 11851–11858.
38. L. Etgar, P. Gao, P. Qin, M. Graetzel, M. K. Nazeeruddin, A hybrid lead iodide perovskite and lead sulfide QD heterojunction solar cell to obtain a panchromatic response, *J. Mater. Chem. A*, 2 (2014) 11586–11590.
39. J. T.W. Wang, J. M. Ball, E. M. Barea, A. Abate, J. A. Alexander-Webber, J. Huang, M. Saliba, I. Mora-Sero, J. Bisquert, H. J. Snaith, R. J. Nicholas, Low-Temperature Processed Electron Collection Layers of Graphene/TiO₂ Nanocomposites in Thin Film Perovskite Solar Cells, *Nano Lett.*, 14 (2013) 724–730.
40. D. Bi, S.J. Moon, L. Haggman, G. Boschloo, L. Yang, E. M. J. Johansson, M. K. Nazeeruddin, M. Gratzel, A. Hagfeldt, Using a two-step deposition technique to prepare perovskite (CH₃NH₃PbI₃) for thin film solar cells based on ZrO₂ and TiO₂ mesostructures, *RSC Adv.*, 3(2013) 18762–18766.
41. S. Aharon, B. E. Cohen, L. Etgar, Hybrid Lead Halide Iodide and Lead Halide Bromide in Efficient Hole Conductor Free Perovskite Solar Cell, *J. Phys. Chem. C*, 118 (2014) 17160–17165.
42. A. Mei, X. Li, L. Liu, Z. Ku, T. Liu, Y. Rong, M. Xu, M. Hu, J. Chen, Y. Yang, M. Gratzel, H. Han, A hole-conductor-free, fully printable mesoscopic perovskite solar cell with high stability, *Science*, 345(2014) 295–298.
43. B. Conings, L. Baeten, T. Jacobs, R. Dera, J. D'Haen, J. Manca, H.G. Boyen, An easy-to-fabricate low-temperature TiO₂ electron collection layer

- for high efficiency planar heterojunction perovskite solar cells *APL Mater.*, 2(2014) 081505.
44. A. Yella, L.P. Heiniger, P. Gao, M. K. Nazeeruddin, M. Gratzel, Nanocrystalline Rutile Electron Extraction Layer Enables Low-Temperature Solution Processed Perovskite Photovoltaics with 13.7% Efficiency, *Nano Lett.*, 14 (2014) 2591–2596.
 45. D. Liu, T. L. Kelly, Perovskite solar cells with a planar heterojunction structure prepared using room-temperature solution processing techniques, *Nat. Photonics*, 8 (2014) 133–138.
 46. J. Kim, G. Kim, T. K. Kim, S. Kwon, H. Back, J. Lee, S. H. Lee, H. Kang, K. Lee, Efficient planar-heterojunction perovskite solar cells achieved via interfacial modification of a sol–gel ZnO electron collection layer, *J. Mater. Chem. A*, 2(2014) 17291–17296.
 47. D. Li, J. Shi, Y. Xu, Y. Luo, H. Wu, Q. Meng, Inorganic–organic halide perovskites for new photovoltaic technology, *Natl. Sci. Rev.*, 0 (2017) 1-18.
 48. K.G. Lim, H.B. Kim, J. Jeong, H. Kim, J. Y. Kim, T.W. Lee, Boosting the Power Conversion Efficiency of Perovskite Solar Cells Using Self-Organized Polymeric Hole Extraction Layers with High Work Function, *Adv. Mater.*, 26(2014) 6461–6466.
 49. M. M. Lee, J. Teuscher, T. Miyasaka, T. N. Murakami, H. J. Snaith, Efficient Hybrid Solar Cells Based on Meso-Superstructured Organometal Halide Perovskites, *Science*, 338(2012) 643.
 50. G. E. Eperon, V. M. Burlakov, P. Docampo, A. Goriely, H. J. Snaith, Morphological Control for High Performance, Solution-Processed Planar Heterojunction Perovskite Solar Cells, *Adv. Funct. Mater.*, 24(2014) 151.
 51. N. J. Jeon, J. H. Noh, Y. C. Kim, W. S. Yang, S. Ryu, S. I. Seok, Solvent engineering for high-performance inorganic-organic hybrid perovskite solar cells, *Nat. Mater.*, 13(2014) 897.

52. S. J. Yoon, K. G. Stamplecoskie, P. V. Kamat, How Lead Halide Complex Chemistry Dictates the Composition of Mixed Halide Perovskites, *J. Phys. Chem. Lett.*, 7(2016) 1368.
53. Y. Jo, K. S. Oh, M. Kim, K.H. Kim, H. Lee, C.W. Lee, D. S. Kim, High Performance of Planar Perovskite Solar Cells Produced from $\text{PbI}_2(\text{DMSO})$ and $\text{PbI}_2(\text{NMP})$ Complexes by Intramolecular Exchange, *Adv. Mater. Interfaces*, 3(2016) 1500768.
54. N. J. Jeon, J. H. Noh, Y. C. Kim, W. S. Yang, S. Ryu, S. I. Seok, Solvent engineering for high-performance inorganic–organic hybrid perovskite solar cells, *Nat. Mater.*, 13 (2014) 897-903.
55. A. Buin, P. Pietsch, J. Xu, O. Voznyy, A. H. Ip, R. Comin, E. H. Sargent, Materials Processing Routes to Trap-Free Halide Perovskites, *Nano Lett.*, 14(2014) 6281.
56. F. K. Aldibaja, L. Badia, E. Mas-Marzá, R. S. Sánchez, E. M. Barea, I. Mora-Sero, Effect of different lead precursors on perovskite solar cell performance and stability, *J. Mater. Chem. A*, 3(2015) 9194.
57. J. Burschka, N. Pellet, S.-J. Moon, R. Humphry-Baker, P. Gao, M. K. Nazeeruddin, M. Grätzel, Sequential deposition as a route to high-performance perovskite-sensitized solar cells, *Nature*, 499(2013) 316.
58. J. Schlipf, P. Docampo, C. J. Schaffer, V. Körstgens, L. Bießmann, F. Hanusch, N. Giesbrecht, S. Bernstorff, T. Bein, P. M. Buschbaum, A Closer Look into Two-Step Perovskite Conversion with X-ray Scattering, *J. Phys. Chem. Lett.*, 6(2015) 1265.
59. Z. Xiao, C. Bi, Y. Shao, Q. Dong, Q. Wang, Y. Yuan, C. Wang, Y. Gao, J. Huang, Efficient, high yield perovskite photovoltaic devices grown by interdiffusion of solution-processed precursor stacking layers, *Energy Environ. Sci.*, 7(2014) 2619.
60. C. Chiang, Z. Tseng, C. Wu, Planar heterojunction perovskite/PC71BM solar cells with enhanced open-circuit voltage via a (2/1)-step spin-coating process, *J. Mater. Chem. A*, 2 (2014) 15897-15903.

61. T. Salim, S. Sun, Y. Abe, A. Krishna, A. C. Grimsdale, Y. M. Lam, Perovskite-based solar cells: impact of morphology and device architecture on device performance, *J. Mater. Chem. A*, 3 (2015) 8943-8969.
62. M. A. Green, K. Emery, Y. Hishikawa, W. Warta, E. D. Dunlop, Solar cell efficiency tables (version 44), *Prog. Photovoltaics*, 22(2014) 701–710.
63. S. N. Habisreutinger, T. Leijtens, G. E. Eperon, S. D. Stranks, R. J. Nicholas, H. J. Snaith, Carbon Nanotube/Polymer Composites as a Highly Stable Hole Collection Layer in Perovskite Solar Cells, *Nano Lett.*, 14(2014) 5561–5568.
64. H. Li, K. Fu, A. Hagfeldt, M. Gratzel, S. G. Mhaisalkar, A. C. Grimsdale, A simple 3,4-ethylenedioxythiophene based hole-transporting material for perovskite solar cells, *Angew. Chem., Int. Ed.*, 53 (2014) 4085–4088.
65. Z. Yu, L. Sun, Inorganic Hole-Transporting Materials for Perovskite Solar Cells, *Small Methods*, 2(2018) 1700280.
66. A. Mei, M. Grätzel, H. Han et al., A hole-conductor-free, fully printable mesoscopic perovskite solar cell with high stability, *Science*, 345 (2014) 295.
67. Z. Liu, M. Zhang, X. Xu, L. Bu, W. Zhang et al. P-type mesoscopic NiO as an active interfacial layer for carbon counter electrode based perovskite solar cells, *Dalton Trans.*, 44 (2015) 3967–3973.
68. Z. Liu, M. Zhang, X. Xu, F. Cai, et al., NiO nanosheets as efficient top hole transporters for carbon counter electrode based perovskite solar cells, *J. Mater. Chem.*, 3 (2015) 24121–24127.
69. X. Xu, Z. Liu, Z. Zuo, M. Wang, Hole Selective NiO Contact for Efficient Perovskite Solar Cells with Carbon Electrode, *Nano Lett.*, 15 (2015) 2402–2408.
70. K. Cao, Z. Zuo, M. Grätzel, M. Wang, Efficient screen printed perovskite solar cells based on mesoscopic TiO₂/Al₂O₃/NiO/ carbon architecture, *Nano Energy*, 17 (2015) 171–179.

71. C. Tsai, C. Wang, Eric W. Diau. et al., Control of preferred orientation with slow crystallization for carbon-based mesoscopic perovskite solar cells attaining efficiency 15%, *J. Mater. Chem. A*, 5 (2017) 739.
72. S. Hashmi, S. M. Zakeeruddin, Michael Gratzel et al., High performance carbon-based printed perovskite solar cells with humidity assisted thermal treatment, *J. Mater. Chem. A*, 5 (2017) 12060.
73. K. C. Wang, J. Y. Jeng, P. S. Shen, Y.C. Chang, E.W.G. Diau, et al., p-Type mesoscopic nickel oxide/organometallic perovskite heterojunction solar cells, *Sci. Rep.*,4 (2014).
74. K. C. Wang, P.S. Shen, M. H. Li, S. Chen et al., Low-temperature sputtered nickel oxide compact thin film as effective electron blocking layer for mesoscopic NiO/CH₃NH₃PbI₃ perovskite heterojunction solar cells, *ACS Appl. Mater. Interfaces*, 6(2014) 11851–11858.
75. Z. Zhu, Y. Bai, T. Zhang, Z. Liu, X. Long, et al., High-performance hole-extraction layer of sol-gel-processed NiO nanocrystals for inverted planar perovskite solar cells, *Angew. Chem. Int. Ed.*, 53(2014) 12571–12575.
76. W. Chen, Y. Wu, J. Liu, C. Qin, X. Yang, A. Islam, Y. .B. Cheng, L. Han, Hybrid interfacial layer leads to solid performance improvement of inverted perovskite solar cells, *Energy Environ. Sci.*,8 (2015) 629–640.
77. J. Y. Jeng, K. C. Chen, T. Y. Chiang, P. Y. Lin, T. D. Tsai et al., Nickel oxide electrode interlayer in CH₃NH₃PbI₃ perovskite/pcbm planar-heterojunction hybrid solar cells, *Adv. Mater.*,26 (2014) 4107–4113.
78. L. Hu, J. Peng, W. Wang, Z. Xia, J. Yuan, J. Lu, X. Huang, W. Ma, H. Song, W. Chen et al. Sequential deposition of CH₃NH₃PbI₃ on planar nio film for efficient planar perovskite solar cells, *ACS Photonics*, 1(2014) 547–553.
79. Cui, J.; Meng, F.; Zhang, H.; Cao, K.; Yuan, H.; Cheng, Y.; Huang, F.; Wang, M. CH₃NH₃PbI₃-based planar solar cells with magnetron-sputtered nickel oxide. *ACS Appl. Mater. Interfaces* 2014, 6, 22862–22870
80. I. J. Park, M. A. Park, D. H. Kim, G. D. Park, B. J. Kim, H. J. Son, M. J. Ko, D. K. Lee, T. Park, H. Shin et al. New hybrid hole extraction layer of

- perovskite solar cells with a planar p-i-n geometry, *J. Phys. Chem.*, 119(2015) 27285–27290.
81. J. W. Jung, C. C. Chueh, A. K. Y. Jen, A low-temperature, solution-processable, Cu-doped nickel oxide hole-transporting layer via the combustion method for high-performance thin-film perovskite solar cells, *Adv. Mater.*, 27(2015) 7874–7880.
82. H. Zhang, J. Cheng, F. Lin, H. He, J. Mao, K. S. Wong, A. K. Y. Jen, W. C. H. Choy, Pinhole-free and surface-nanostructured NiO_x film by room-temperature solution process for high-performance flexible perovskite solar cells with good stability and reproducibility, *ACS Nano*, 10(2016) 1503–1511.
83. J. You, L. Meng, T. B. Song, T. F. Guo, Y. Yang, W. H. Chang, et al., Improved air stability of perovskite solar cells via solution-processed metal oxide transport layers, *Nat. Nanotechnol.*, 11 (2016) 75–81.
84. W. Chen, Y. Wu, Y. Yue, J. Liu, W. Zhang, et al., Efficient and stable large-area perovskite solar cells with inorganic charge extraction layers, *Science*, 350(2015) 944–948.

CHAPTER 3

EXPERIMENTAL METHODS

In this work, in order to construct hybrid mesoporous perovskite solar cells, metal oxide nanostructures in particle form were synthesized with sol-gel wet chemistry methods and characterized by means of morphological, structural, electrical and optical measurements. Synthesized powders like nickel oxide (NiO), titanium dioxide (TiO₂), magnesium oxide (MgO) and doped forms of these compounds were used as the hole conducting or electron conducting mediums in perovskite absorber based hybrid mesostructured solar cells. For the synthesis of nanostructured metal oxides, methods like precipitation and ultrasonic spray pyrolysis have been employed in order to obtain nanopowders, nanospheres or nanoflakes of NiO and lithium doped NiO. Ultrasonic methanol combustion was used to synthesize TiO₂, yttrium doped TiO₂, MgO, NiO and lithium doped NiO nanoparticles. In addition to nanoparticle synthesis, thin films of NiO and Li:NiO were deposited on FTO coated glass substrates by spin coating technique from precursor solutions. These films and powders were employed in construction of perovskite solar cells. Perovskite solar cells were constructed by wet chemistry methods using spin coating technique from precursors solutions and effect of preparation conditions were examined.

For characterization of the powders, electron microscopy techniques like scanning electron microscopy (SEM), transmission electron microscopy (TEM), X-ray diffraction (XRD), ultraviolet and visible transmission and absorption, Inductively Coupled Plasma Mass Spectrometry (ICP-MS), X-ray photoelectron spectroscopy (XPS), ultraviolet photoelectron spectroscopy (UPS), Brunauer–Emmett–Teller (BET) gas adsorption, Hall effect measurements, four point and two point resistivity

measurements were used. Constructed perovskite solar devices were characterized by J-V measurements under simulated solar light and electrochemical impedance spectroscopy techniques, in order to identify cell performances and underlying electronic transfer processes during cell operation.

Details of the experimental conditions are given in the following chapters prior to characterizations of each individual device structure. A general summary of the methods employed in this work is given in the following sections.

3.1 Nanopowder Synthesis

For the synthesis of p-type or n-type metal oxide nanopowders, sol-gel based wet chemistry methods were employed. The most important expectation from the synthesized powders is the nanostructured character of the particles. In addition, for the doped particles, doping efficiency and stoichiometry are the other prerequisites. Major nanopowder synthesis method used in this work is the precipitation technique. Precipitation from metal salts by adjusting the pH of the precursor solutions or by a fuel assistance or direct precipitation by solvothermal methods have been employed. In addition to precipitation, ultrasonic spray method was also used for production of metal oxide nanospheres. A modified flame spray method was employed for synthesis of ultrafine nanopowders of NiO, TiO₂ and MgO.

3.1.1 Precipitation Technique

Precipitation of metal oxides from solutions is well known and widely used technique for the production of fine nanostructured powders. By adjusting the sol-gel chemistry of the precursor solutions, it is possible to obtain highly uniform nanoparticles using simple and cheap metal salts. Most common solvents used in this technique are water and alcohols depending on the solubility of the precursors or dispersibility of the final products. Most metal salts like nitrates, chlorides or acetates are dissolved in an appropriate solvent. By adjusting the pH of the solution

upon addition of acids or bases, it is possible to precipitate hydroxides of the desired materials. The precipitation process obeys the rules of nucleation and growth inside the solution. Precipitated particles undergo a series of particle growth processes like Oswald ripening and agglomeration. Attraction between individual particles is mainly responsible from particle growth and agglomeration. Controlling the precipitation conditions like temperature, pH or molarity of the solution, nanoparticles with homogeneous size and size distribution can be obtained. In some cases, in order to increase the dispersibility of the precipitates or for inhibiting abnormal particle growth, additives like surfactant molecules can be used. Such surfactant agents acts like physical barriers for further particle growth [1]. In addition, presence of surfactant molecules also increases the dispersibility of the precipitants by modifying the particle surfaces and charging the surface of the particles. This static electricity is responsible from the particle to particle repulsion and a stabilized dispersion can be achieved (Figure 3.1). The surfactants used in this process can have anionic, cationic or non-ionic character depending on the pH of precipitation solution or surface chemistry of the precipitated particles [2].

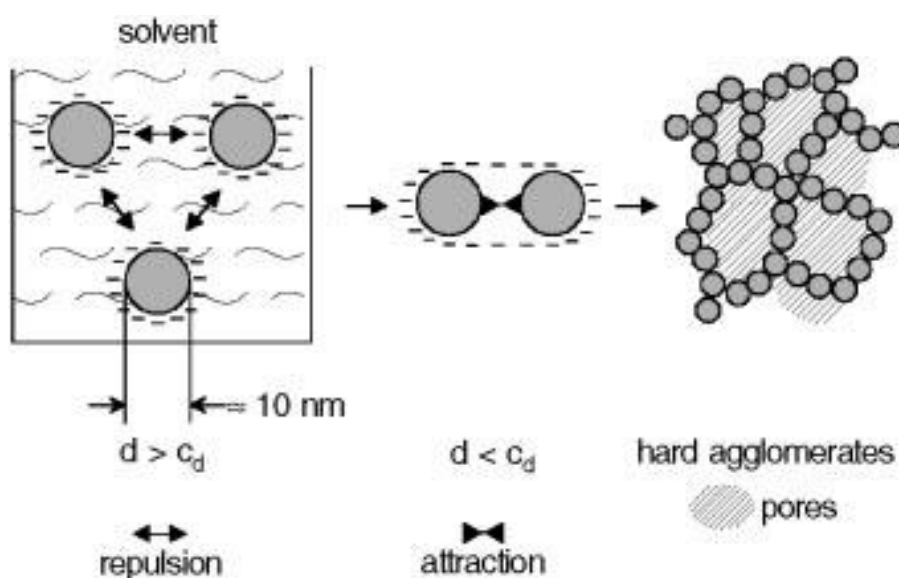


Figure 3.1 Scheme of particle formation and agglomerate formation in colloidal solutions during precipitation [1].

After precipitation, a washing and collecting procedure is essential for removal of byproducts, precipitation agents and unreacted chemicals from the precipitated particles. Precipitates, filtered or collected by centrifugation, can be in either oxide or hydroxide form, depending on the precursors used or precipitation agents. In most cases, an additional heat treatment may be necessary for crystallization and oxidation to metal oxides of the desired phase. However, duration and heat treatment temperatures must be carefully chosen in order to prevent further particle growth or agglomeration of the final nanopowders. Many widely used metal oxides can be synthesized by this process like TiO₂ [3], ZnO [4], NiO [5], Al₂O₃ [6] etc.

3.1.2 Hydrothermal Synthesis

Hydrothermal synthesis or synthesis under supercritical water is a well known nanoparticle synthesis method employed for production various metal oxides. It can be defined as crystal growth under high temperature and pressure conditions. The main advantage of synthesis under elevated temperature and pressure conditions is reaction time and efficiency, where reaction rate can be enhanced dramatically with the increasing temperature and vapor pressure. Precursor materials or dispersions of the powders subject to hydrothermal growth are fed into closed reactors in presence of solvents like water or alcohol, which in this referred as solvothermal method. Crystallinity of the synthesis products are far advanced than conventional heating conditions in which a post heat treatment is unavoidable for obtaining desired final products. In addition, supercritical water has higher solubility of the inorganic compounds and dispersibility and solubility of the precursor and final product is greatly enhanced. Fine particle sizes with high surface area are achievable in this technique. High surface area of the products are quite advantageous for photocatalysis or photoelectrochemical applications. Hydrothermal method have been used extensively for production of nanomaterials, especially for production of highly catalytic TiO₂ nanoparticles and titanates [7,8].

3.1.3 Ultrasonic Spray Pyrolysis (USP) Synthesis of Nanoparticles

Ultrasonic spray pyrolysis (USP) method is a versatile and high batch, high volume production technique used for the synthesis nanomaterials. It is a continuous and ambient atmosphere process which is economically very advantageous. Fine ceramics of metal oxides can be produced with controlled stoichiometry and desired phase. USP method includes 4 basic steps for formation of particles:

- Precursor droplet generation by an ultrasonic generator
- Droplet size reduction due to thermal evaporation of the solvent
- Chemical reaction and conversion of the precursor compound into oxide
- Formation of the solid particles in either sphere or hollow sphere forms

Droplet formation can be achieved by two methods, by fluid fluid interaction where a gas stream is used to atomize the precursor solution, or by using ultrasound generated by an ultrasonic nebulizer. Gas atomization has the advantage of high throughput but lacks homogeneous droplet formation. Coarse particles with wide size distribution is seen in gas atomized systems. On the other hand, ultrasonic nebulization has the advantage of homogeneous size distribution of droplets and final powders. Schematic of a typical ultrasonic spray pyrolysis particle generation setup is given in Figure 3.2.

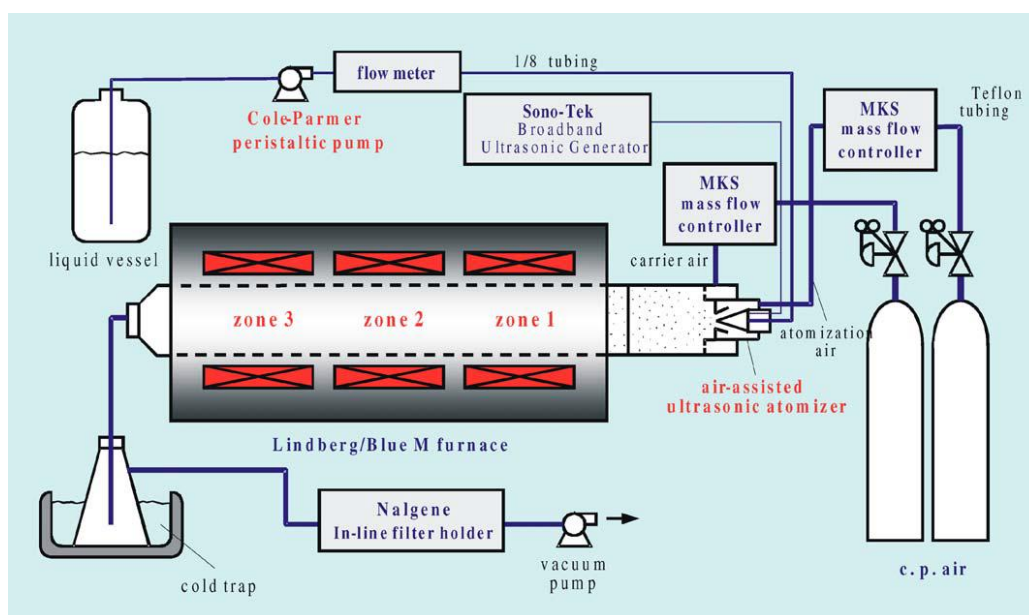


Figure 3.2 Schematic representation of an USP particle generation system [9].

The main system includes an ultrasonic generator of which has nebulization frequencies ranging between 150 kHz to 2 MHz. The frequency of the generator directly influences the droplet sizes. In a gas atomized systems, droplet sizes range between 30-100 μm , where in common household nebulizers droplet sizes down to 6-9 μm can be achieved. However, these values also depend on the solvent type and concentration of the precursor solution. Polar solvents react with ultrasonic waves more efficiently and lower droplet sizes are obtained in contrast to apolar solvents which may not even generate any droplet or mist. Generated droplets are fed into reaction furnaces, into tubular reaction chambers in most cases, and subject to thermal treatment. Inside the reaction zone, firstly solvent evaporation process occur and droplets shrink down to 1 μm . This solid contains precursor materials and as the temperature increases gradually inside the reactor, oxide formation and phase transition is completed. Particles are collected at the end of the reactor by a filter or by passing the stream from a collection bubbler (Figure 3.3). Many compounds have been synthesized using this method like binary or ternary oxides [9].



Figure 3.3 USP system used in nanoparticle synthesis in this work.

3.1.4 Flame Spray Pyrolysis (FSP) Synthesis of Nanoparticles

FSP method is a well established and widely used method of nanoparticle or powder production for synthesis of catalytic materials, pigments or carbon black. In flame synthesis, particle production is carried out inside a flame which is realized by combustion of two gases. Flame is used to initiate the chemical reactions and form the solid products. A cloud of desired materials emerges together with the combustion products. Volatile precursors are oxidized within the flame creating the monomers. These monomers come together to form small nucleotides and grow inside the combustion exhaust, obeying the rules of nucleation and growth similar to USP method. The main advantage of this approach is the crystalline structure of the produced particles, which require no post heat treatment or a calcination step because the necessary heat is supplied by the flame itself. The main fuels used in the production flames in this method are hydrogen, methane, acetylene or ethylene and air or oxygen as the oxidizer. In most cases, an inert gas like argon or nitrogen is introduced into the system in order to decrease the flame temperatures. The amount of inert gas is determined by the fuel itself. Each fuel has a different combustion enthalpy and must be chosen depending on the materials to be produced. By adjusting the flame temperature, it is possible produce different phases of the materials [10].

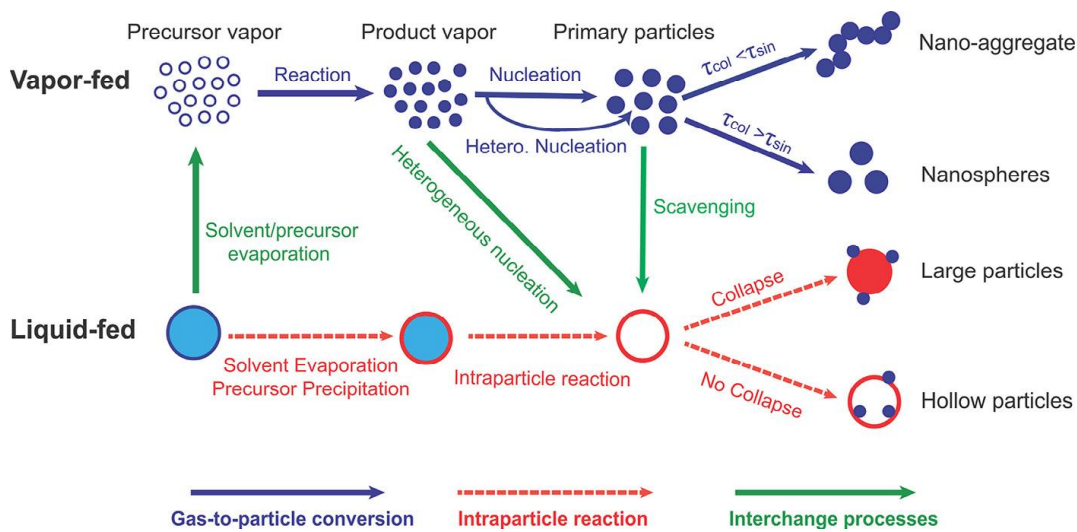


Figure 3.4 Particle formation processes under vapor feeding or liquid feeding conditions in flame spray pyrolysis method [11].

Stages of particle formation in flame synthesis method is given in Figure 3.4. Flame synthesis can be categorized into two different methods depending on the feeding form of the precursors into the flame, vapor-fed aerosol flame synthesis and liquid-fed aerosol flame synthesis. In vapor-fed synthesis, precursors are sent into the flame in gaseous form evaporated from volatile precursors like alkoxides. Advantage of this system is the fine structure of the resulting particles due to less particle to particle interaction and particle growth mechanism inside the flame. In the case of liquid-fed design, solutions containing precursor materials are atomized through pressurized gas and sent into the flame. Droplet evaporation and nucleation results in larger spheres or in case of rapid evaporation, hollow spheres can form. Besides, droplet size and size distribution plays a major role in the quality of final products [11]. Many binary and ternary compounds can be synthesized easily and in large quantities using flame aerosol technique [12]. Ultrafine silica and titania particles are most widely produced particles using this technique [13, 14].

3.2 Thin Film Deposition

Thin films of NiO and TiO₂ have been deposited in this study to be employed as the charge selective layers or charge blocking layers in perovskite solar devices. For this purpose, thin films of NiO were deposited on FTO coated glass substrates by ultrasonic spray pyrolysis method and spin coating method. Perovskite layers were also deposited by the spin coating technique. In order to form mesoporous structures on for hybrid mesoporous perovskite devices, screen printing technique was employed after preparation of the screen printing pastes. SEM, XRD, UV-Vis and Hall Effect studies were performed on the deposited films in order to reveal the morphological, optical and electrical characteristics of the films.

3.2.1 Ultrasonic Spray Pyrolysis Deposition of Thin Films

USP method for thin film production is a modified spray pyrolysis process used for deposition of thin films on substrates in addition to particle production method explained in the previous sections. In conventional spray pyrolysis method, precursor solutions are atomized by help of a pressurized gas like air or oxygen. Solutions are converted into droplets ranging from 35 μm to 100 μm diameters and sent to a hot plate or hot surface. In USP method, atomization is carried out by ultrasonic waves and precursor solutions are turned into fine mist of homogeneous droplet size around 30-40 μm. Generated mist is sent onto the hot substrates by a carrier gas and film formation occurs directly on the substrates. In this process, different from USP method for particle production, evaporation of the solvent occurs just over the substrate and before the particle formation, precursor materials are deposited on the substrate which results in growth of the underlying films. Chemical reactions and oxidation of the precursor materials like nitrates, chlorides, acetates or alkoxides are stimulated by the heat transfer from the hot substrate.

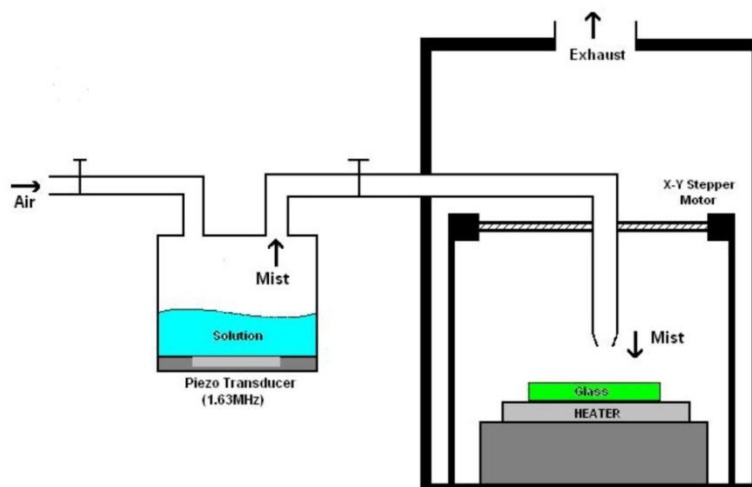


Figure 3.5 Schematic representation of USP system equipped in this work [15].

In general, a USP system is composed of a mist generator which is made up of a piezo transducer operating between 150 kHz to 2 MHz. A carrier gas collects the generated mist and transport onto the substrate. A nozzle scans the substrate with the help of a stepper motor and films are grown by succesful sequences until films with desired thicknesses are achieved. Many metal oxides and ternary compounds can be coated on tempearture resistant substrates, especially transparent and conducting oxides like fluorine doped tin dioxide can be deposited succesfully using this method [15]. A schematic representation of a USP thin film deposition apparatus and a photo of the system equipped in our laboratory are given in Figure 3.5 and Figure 3.6, respectively.



Figure 3.6 A photo of USP thin film deposition device used for thin film coatings in this work.

3.2.2 Spin Coating for Thin Film Deposition

Spin coating is probably most widely used and understood technique for deposition of thin films of organic, inorganic and hybrid structures on various substrates. In every field of research and production in many areas utilize spin coating technique for device construction or conformal coatings on both laboratory type research applications or on industrial level production. Spin coating process can be summarized as an asymmetric spreading of a Newtonian fluid over a planar substrate under centrifugal forces in order to form a thin film on the substrate. The centrifugal force spreads the fluid over the substrate, while at the same time, surface tension and viscous force keep the fluid on the substrate to form a thin film. Film thicknesses ranging from 10 nm to 200 μm can be deposited with this method.

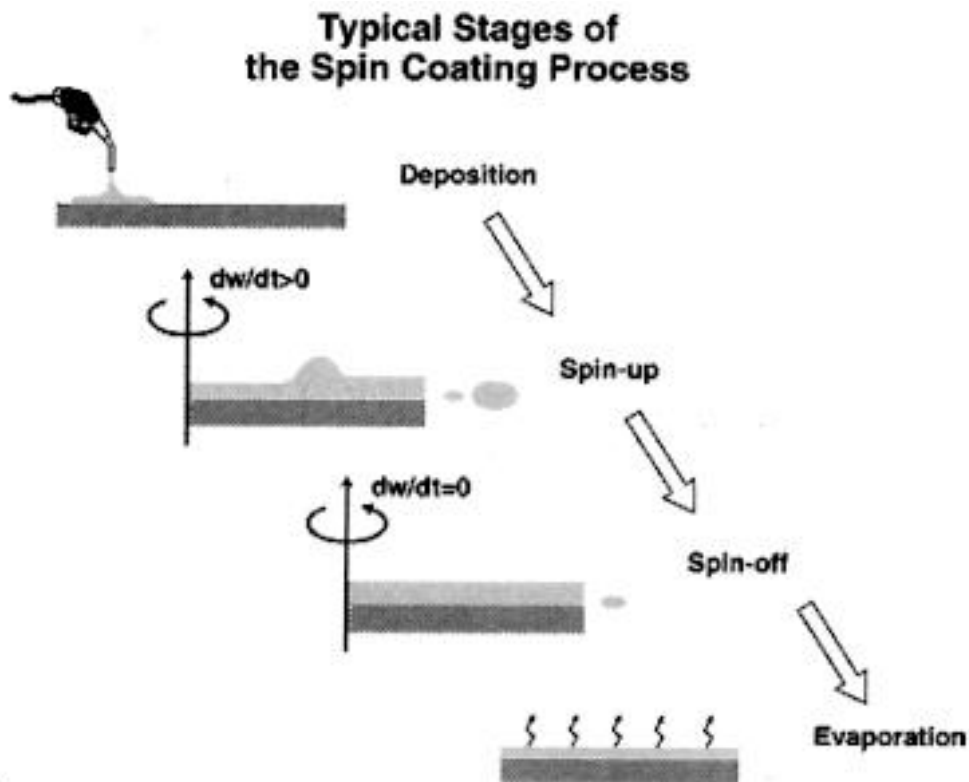


Figure 3.7 Stages of film formation during spin coating process [16].

Spin coating process can be divided into four main stages; fluid dispensing, spinning, formation of stable fluid and evaporation of the solvent (Figure 3.7). The last two stages actually occur during all stages and determine the quality of the final film mostly. There are other parameters affecting the film quality like spin speed, acceleration rate, solution viscosity, dispense volume and spin duration. At the dispensing stage, precursor materials are spread onto the substrate by automated syringes or manually with by the experimenters. Usually excess fluid is dispensed each time for full coverage of the substrate. Wetting of the substrate by the precursor solution is important for homogeneous film formation. Surface modification the substrate for non-wetting fluids may be necessary by applying surface agents by treating the surface plasma cleaners or UV-Ozone treatment. In spin-up stage, solution spreads across the substrate due to centrifugal forces. Some spiral or vortexes may form during this stage and lead to non-uniformities on the

surface which is governed by the viscositic behaviour of the solvents used. After balancing of the centrifugal and shear forces, stable liquid film formation occurs on the substrate thickness of which is determined by the spin speed. Edge effects usually occur at this stage because excess solution repelled to the corners and due to surface tension, tends to accumulate at the edges. Using solvents with low surface tension is critical for eliminating the edge irregularities. At the final stage, solvent is evaporated from the film and an additional shrinkage also occurs and final film thickness is determined. A post heat treatment may also be necessary for conversion of precursors to oxides or for crystallization of the deposited precursors [17].

3.2.3 Screen Printing Method

Screen printing or serigraphy is a widely used technique in textile and ceramic industry for coatings of pigment or dyes and coloration of various substrates. Basically, a viscous paste containing the desired material is passed through openings of a mesh defined by number of threads in a given area and thread size. Larger the thread size or lower the mesh number, deposited material is larger in volume. For this technique, preparation of a viscous paste is essential, viscosity of which must be high enough to prevent the paste from spreading across the surface but also fluid enough to relax the paste in order to form a film. Various patterns of desired shape can be formed on the mesh by using emulsions and paste is first dispensed onto the mesh. With the help of a squeegee, paste is forced to pass through the openings in the mesh and left to relax for a while (Figure 3.8).

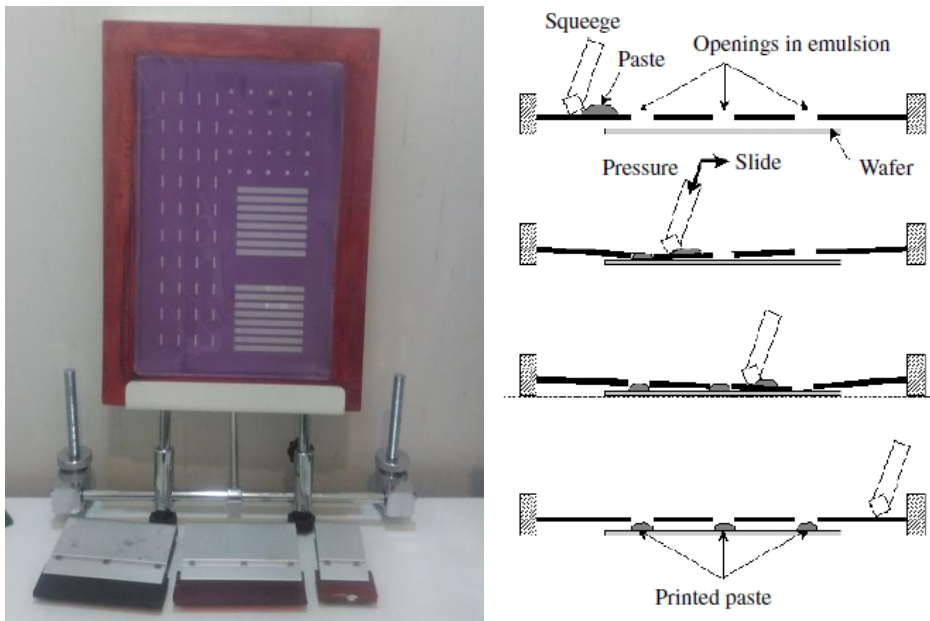


Figure 3.8 A photo of the apparatus for screen printing of thick films used during the work in this study and screen printing deposition process stages [18].

For thick film deposition of technical ceramic particles, screen printing paste preparation is the critical step of process. Many dispersing mediums with high viscous materials like polyethylene glycol, glycerol or terpineol is employed in paste preparation. Upon addition of some binders or thickening agents like ethyl cellulose or PMMA or PVA, water based dispersions can also be prepared. Fine particles of ceramics, the solvent and thickening agent pass through a homogenization procedure which is held by ultrasonic treatment, ball milling or roll milling. Thickness of the deposited layers depend on the ceramic concentration of the paste and mesh number and size. Thicker films can be deposited by sequential deposition of layers on top of each other after a drying step. Substrates are then transferred to high temperature heat treatment in order to remove the organic constituents of the pastes. During high temperature treatment, particles of the ceramics also undergo a sintering and densening step. Resultant thick films possess a stable, durable and porous structure depending on the binder concentration of the ceramic particles or

particle sizes. Many metal oxides and industrial ceramics can be deposited up to 100 μm thickness on large areas and large volumes [18].

3.3 Construction of Hybrid Mesoporous Perovskite Based Solar Cells

Doped and intrinsic n-type and p-type materials have been synthesized and employed in perovskite based mesostructured solar cells in this work. For this purpose perovskite solar cells were constructed and characterized. Performance of solar devices highly depend on preparation conditions and routes followed for construction of the cells. In this work, n-i-p configurated solar cells were constructed and studied. A typical n-i-p perovskite based solar cell consists of:

- Transparent and conducting oxide coated charge collection layer
- N-type electron transport or hole blocking layer
- Mesoporous layer
- Perovskite layer
- P-type hole tranport or electron blocking layer
- Metallic back contact

For deposition of perovskite layers, different routes were studied and highest efficiency route was selected for preparation of the cells. Deposition of subsequent layers and construction of the cells was summarized in the following sections.

3.3.1 Etching and Substrate Cleaning

In order to insulate the metallic back contacts from FTO layer and prevent possible short circuits during measurements, FTO layers were etched using zinc powder and hydrochloric acid. FTO coated glass substrates were cut down to size of 15 mm x 2 mm. Zinc powder was spread on the half of the cells and other part was protected by a tape. Upon pouring the diluted hydrochloric acid on the zinc powder, due to

formation of hydrogen gas, tin dioxide is reduced and washed away by the acid. Cells were then rinsed with lots of water.

Formation of dense and pinhole free layers is possible with a clean substrate surface. Etched FTO coated glass substrates were sequentially cleaned by detergent solution, ultrapure water, acetone, ultrapure water and isopropanol for 10 min and stored in isopropanol. Before each blocking layer deposition, cells were dried with nitrogen flow and then placed into a UV-Ozone cleaning chamber. Substrates were subjected to ozone cleaning for 15 min and blocking layer deposition was carried out immediately after ozone treatment.

3.3.2 Preparation of Blocking Layer

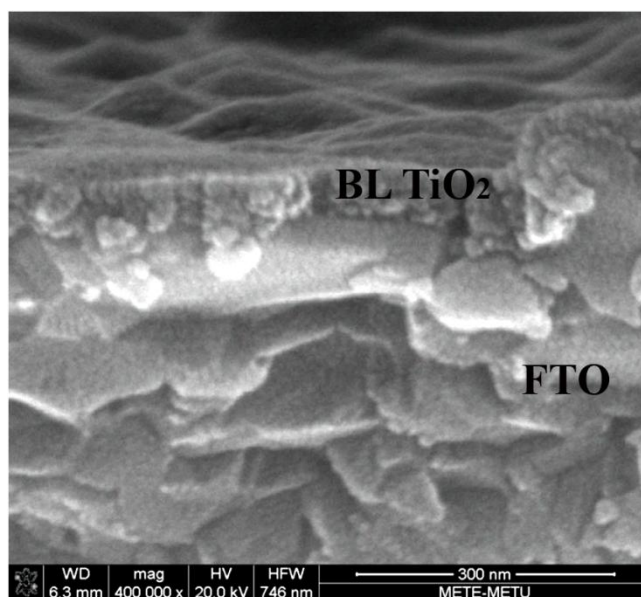


Figure 3.9 SEM image of a 50 nm TiO₂ blocking layer on FTO substrate deposited by spin coating in this work.

Blocking layer TiO₂ thin films were deposited on the clean FTO coated glass substrates by spin coating method. For this purpose, titanium diisopropoxide bis(acetylacetonate) was dissolved in n-butanol with a molarity of 0.15M. Before

each deposition, this solution was filtered through a 0.45 μm syringe filter. A volume of 50 μl of this solution was dispensed onto the substrate and spun at 2000 rpm for 20 s and then films were dried at 125°C for 5 min. This recipe yields a TiO_2 film of approximately 50 nm as seen in Figure 3.9. For thicker films, this procedure was repeated after drying. Finally, films were heat treated at 500°C and a thin TiO_2 film was formed on the FTO glass substrates, acting as the hole blocking layer.

3.3.3 Preparation of Mesoporous Layers

3.3.3.1 Preparation of Screen Printing Pastes

Screen printing pastes are the highly viscous precursor materials for deposition thick films, containing a binder, the deposited material in powder form and a vehicle or the solvent. Pastes used for the deposition of nanoparticles must contain a binder to hold the nanoparticles during sintering stage and achieve a mesoporous self standing network. For preparation of screen printing pastes employed in this work, terpineol was chosen as the solvent and ethyl cellulose as the binder. Synthesized nanopowders of TiO_2 , MgO and NiO were firstly ground in a mortar and ethanol was added drop by drop to prevent aggregate formation. Prepared dispersions were subjected to ultrasonic treatment with a titanium horn for 30 min. After stirring the dispersion for 10 min, a solution of ethyl cellulose in ethanol was added to this solution together with the terpineol. This mixture was again subjected to ultrasonic treatment and stirring procedures for ensuring the complete dispersion of the nanoparticles. Ethanol was evaporated with a rotary evaporator under vacuum at 40°C. The composition of the pastes were 2:1:7 by weight for nanopowder, ethyl cellulose and terpineol, respectively. The highly viscous pastes were sealed with parafilm and stored until the end of the work.

3.3.3.2 Deposition of Mesoporous Layers by Spin Coating

Prepared pastes were deposited on the blocking layer coated FTO substrates by spin coating method. For this purpose, pastes were diluted with ethanol for satisfying fluidity and spreading of the paste on the substrate. Ethanol and paste were mixed in weight ratio of 3:1 and stirred for several hours. Similar to blocking layer deposition on FTO substrates, blocking layer coated substrates were also subjected to UV-Ozone treatment for 15 min before dispensing the paste solution. This is also important for achieving homogeneous distribution the paste on the substrate during spin coating. Spin coatings were conducted at 2000 rpm for 5 s and dried at 125°C for 5 min. With this recipe, a TiO₂ mesoporous layer of 250 nm can be achieved after firing at 500°C (Figure 3.10). For thicker layers, the above procedure can be repeated and films up to 1 µm can be obtained.

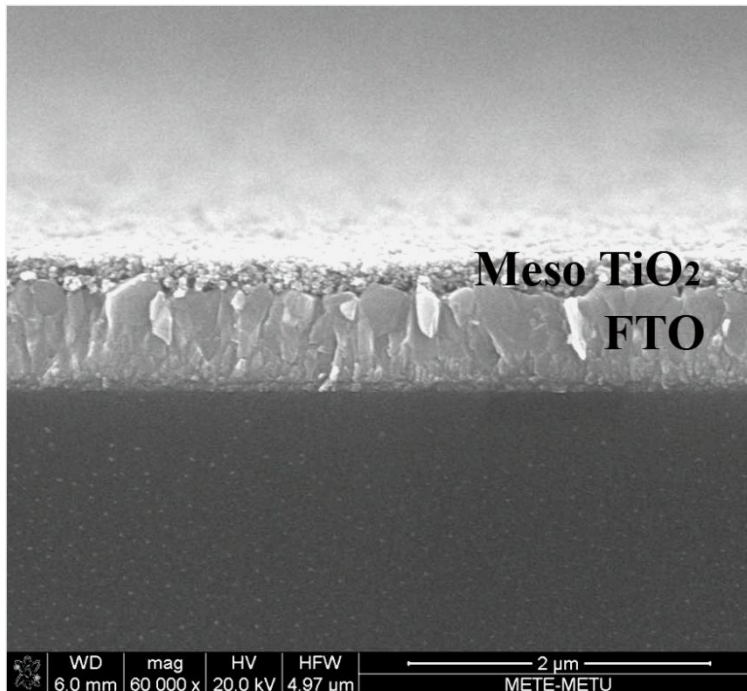


Figure 3.10 SEM image of a 200 nm mesoporous TiO₂ layer deposited on FTO substrate by spin coating in this work.

3.3.3.3 TiCl₄ Treatment of Mesoporous Layers

Mesoporous TiO₂ coated substrates were treated with titanium tetrachloride (TiCl₄) before perovskite deposition. Objective of the TiCl₄ treatment is to coat the mesoporous structure with a thin layer ultrafine TiO₂ particles and increase the connectivity between each individual nanoparticle for enhanced electronic conduction. For this purpose, a 0.2 mmol TiCl₄ aqueous solution was prepared and glass substrates were immersed into this solution at 90°C for 10 min. During treatment, TiCl₄ hydrolyzes and oxidizes to TiO₂ nanoparticles, which settle down on the particles and interconnections between particles, especially. After treatment, substrates were cleaned thoroughly with DI water and an additional heat treatment was conducted at 500°C for 15 min.

3.3.4 Deposition of Perovskite Layers

There are different routes for deposition of perovskite layers in literature. In this work, 3 different routes were followed and examined in order to obtain highest efficiency from the cells. One step deposition, two step deposition and adduct methods were studied for deposition of methylammonium lead iodide layers (CH₃NH₃PbI₃) and cells were characterized.

3.3.4.1 One-Step Perovskite Deposition

In this method, perovskite precursor solution is prepared and spin coated directly on the TiO₂ coated substrates. For this purpose, lead chloride (PbCl₂) and methylammonium iodide (MAI) were dissolved in N,N-Dimethylformamide (DMF) with a molar ratio of 3:1. PbCl₂ has limited solubility in DMF so firstly MAI was dissolved in DMF and then PbCl₂ was added. The resultant solution contains 40% precursor materials by weight. This solution was stirred at 70°C overnight. Spin coating was conducted at 2000 rpm for 45 s and films were heat treated at 90°C for 2 h. Solution preparation and film depositions were carried out under laboratory

conditions. The resulting films are not pristine perovskite, which are slightly Cl⁻ doped and denoted as CH₃NH₃PbI_{3-x}Cl_x [19]. Perovskite crystals embedded inside the mesoporous network can be seen in Figure 3.11.

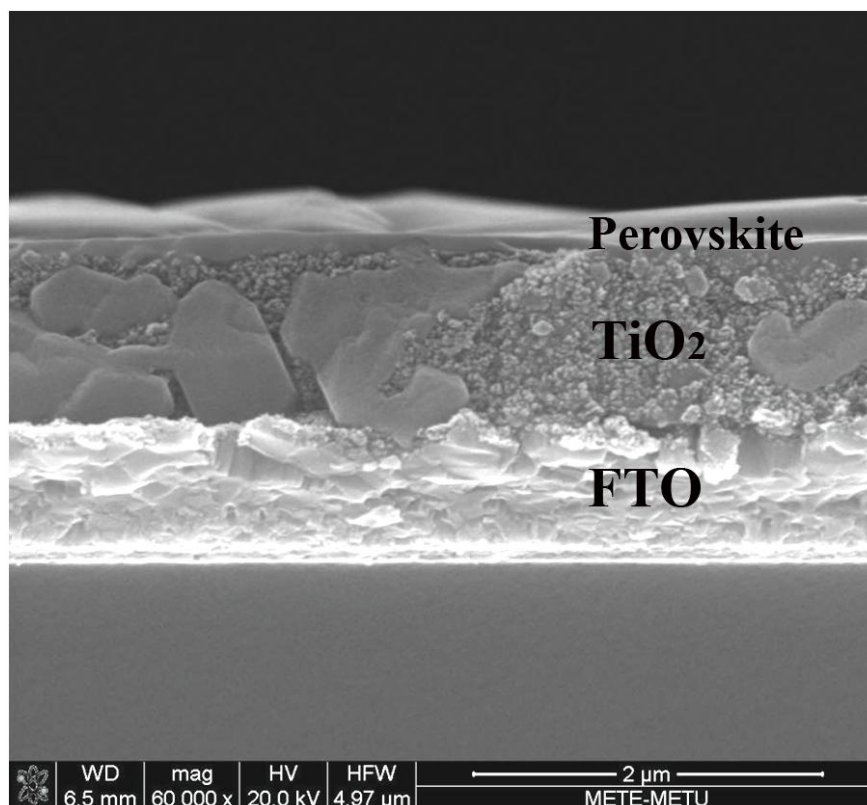


Figure 3.11 SEM of perovskite layer deposited on mesoporous TiO₂ layer by one-step deposition method, showing the perovskite crystals embedded inside mesoporous matrix.

3.3.4.2 Two-step Perovskite Deposition

In two-step perovskite deposition method, apart from the one step method where precursor materials are dissolved in one solvent and deposited once at a time, two layers are separately deposited on the substrate and perovskite formation is completed on the substrate. For this purpose, PbI₂ was first dissolved in DMF by stirring at 70°C overnight. The molarity was set to 1M. In a separate container, a

solution containing 10 mg/ml MAI in isopropanol was prepared. PbI_2 was coated onto the substrate by spin coating the solution at 4000 rpm for 30 s. This layer was dried at 100°C for 5 min and cooled down to room temperature. On top of this layer, 200 μl of the prepared MAI solution is poured and waited for 20 s. Films changed color from yellow to black during the waiting time and substrate was spinned at 4000 rpm for 30 s and dried at 100°C for min. This method is reported to yield large cuboid shaped crystals inside the mesoporous matrix and on top of the mesoporous layer [20] and can be seen in Figure 3.12.

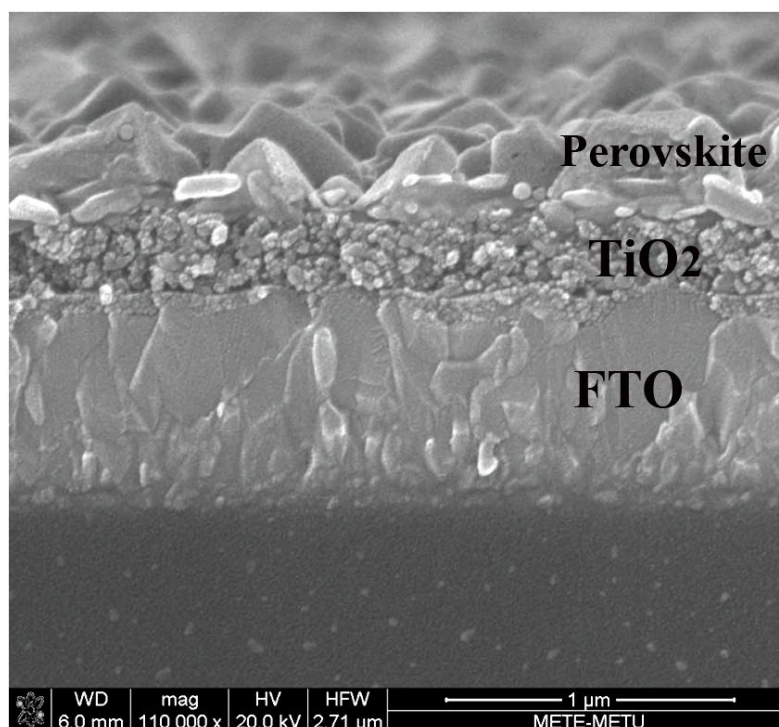


Figure 3.12 SEM image of the cuboid shaped perovskite crystals deposited on TiO_2 mesoporous matrix by two-step deposition.

3.3.4.3 Adduct Method For Perovskite Deposition

Adduct method is based on creation of a Lewis adduct of PbI_2 and dimethyl sulfoxide (DMSO). Such an adduct structure leads to formation of an intermediate

layer during spin coating which then converted into pure perovskite film with a homogeneous and dense film in a reproducible way. For this purpose, firstly, a 40% weight DMF solution containing equimolar PbI_2 , MAI and DMSO was prepared similar to one-step method, except solution was prepared without additional heating and stirred for 1 h. This solution was dispensed onto the substrates and spinned at 4000 rpm for 30 s. At the 5th second of spin coating, 400 ml diethyl ether was poured on the spinning substrate at once, similar to solvent engineering approaches of perovskite deposition. The objective of diethyl ether treatment is to wash away the DMF solvent and retarding the irregularities in film deposition during solvent evaporation. The resultant films are transparent and contain the PbI_2 .DMSO adduct. Films were heat treated at 100°C for 5 min in order to evaporate the DMSO and complete the crystallization of the $\text{CH}_3\text{NH}_3\text{PbI}_3$ layer. Films transform to shiny black films with good coverage and no visible irregularity upon heat treatment. This method is known to yield continuous and large grain sized perovskite layers compared to other perovskite deposition methods [21] as seen in Figure 3.13.

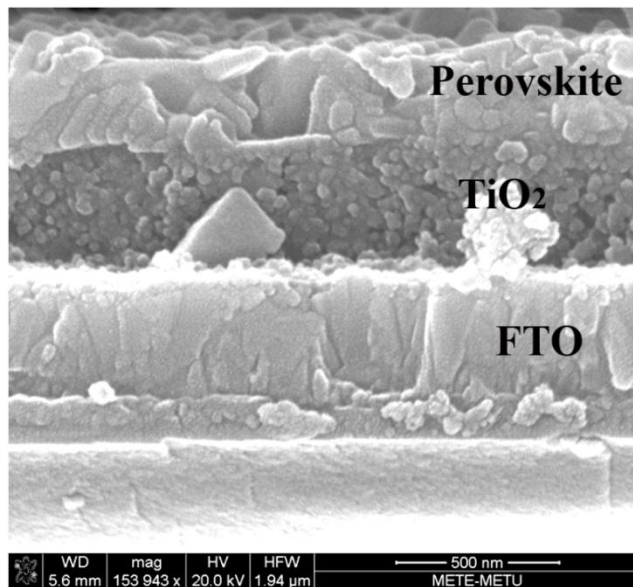


Figure 3.13 SEM image of the perovskite layers deposited on TiO_2 matrix by adduct method showing the continuous and regular perovskite layer on the mesoporous matrix compared to one-step and two-step methods, in this work.

3.3.5 Deposition of Back Contacts

The prepared perovskite solar cells were finished by depositing the back metal contact. Preferred metal contact in this work is gold because of the low work function around 5.2 eV and have high capability to collect most of the holes from both hole conducting mediums or the perovskite layer itself. Also, gold have high binding quality on many substrates and layers. Gold evaporation was conducted by e-beam evaporation at a base pressure of 3×10^{-6} mbar from gold targets. Thickness of the layers were around 100 nm which is sufficient enough to collect and transport charges through the cells. For proper contact between the measurement probes and the electrodes on the cell, silver paste was deposited on the FTO coated glass and gold grids. Each cell contains 8 individual contacts which are considered as single cells at one substrate with an active area of 0.07 cm^2 defined by the edge of the golden grid and the edge of the etched FTO substrate (Figure 3.14).

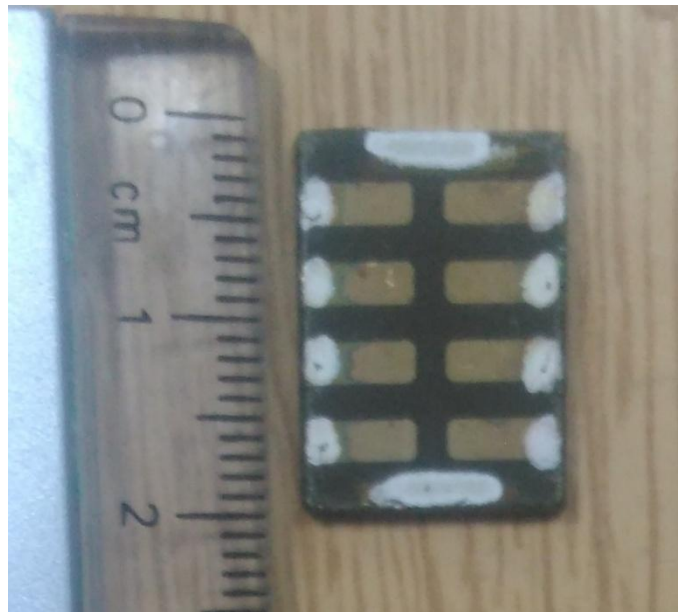


Figure 3.14 A typical mesoporous perovskite solar cell constructed in this work after Au evaporation and deposition of silver contacts.

3.4 Characterizations of The Perovskite Solar Cells

In addition to morphological, optical and electrical characterizations of the produced nanoparticles and perovskite based solar devices using SEM, TEM, XRD, BET, UV-Vis and four point resistivity measurement techniques, produced solar cells were examined by current-voltage measurements under simulated solar light. Efficiency values of the cells and internal resistances were determined. Electrochemical impedance spectroscopy (EIS) technique was employed in order to reveal charge transfer processes and associated resistances of each layer deposited using the nanoparticles synthesized during the studies and performance and contribution of each layer were determined.

3.4.1 Electrochemical Impedance Spectroscopy (EIS)

3.4.1.1 Fundamentals of Electrochemical Impedance Spectroscopy

Electrochemical impedance spectroscopy (EIS) in general is a steady state measurement technique for evaluation of the response of an electrochemical system to a small amplitude AC signal as a function of the frequency. It is widely used in investigation of electrochemical systems and photoelectrochemical devices where ionic and electronic transfer processes occur between individual layers and interfaces. EIS is conducted by application of an harmonic AC $V(\omega, t)$ perturbation with defined frequency range ($f=\omega/2\pi$) to an electrochemical system and measuring the current inside the system where ω is the angular frequency. The range of the applied potential varies from millihertz to kilohertz and the corresponding current $I(\omega, t)$ is measured. Then impedance of the system $Z(\omega, t)$ is calculated by:

$$Z(\omega, t) = \frac{V(\omega, t)}{I(\omega, t)}$$

Eq. [3.1]

In electrochemical systems, the amplitude and the phase of the measured $I(\omega, t)$ may be different from the $V(\omega, t)$ for a particular ω value, depending on the electrochemical processes involved. If angular frequency is zero, then the system can be considered as under DC conditions and the calculated resistances obey the ohm rule and the impedance is equal to the resistance of the component. In this case there is zero phase difference (θ). For systems with a non-zero phase difference, it is more convenient to define the system with complex numbers and a complex component of the impedance arises:

$$Z(j\omega) = |Z|(\cos\theta + j\sin\theta) \quad \text{Eq. [3.2]}$$

where j is defined as $\sqrt{-1}$. In this equation, the real part of the impedance is denoted as Z' and imaginary part is denoted as Z'' . For any given electrochemical system, for components that lead to a phase difference like a capacitor (C) or inductor (L), there will be a phase difference between the $I(\omega, t)$ and $V(\omega, t)$. In Table 3.1, common elements of electrochemical systems are shown.

Table 3.1 Common circuit elements used in EIS analysis.

Element	Impedance
Resistor	R
Capacitor	$1/j\omega C$
Inductor	$j\omega L$
W (Warburg)	$1/Y_o\sqrt{j\omega}$
CPE (Constant Phase Element)	$1/Y_o(j\omega)^\alpha$

A CPE is a non-ideal capacitance element, taking into account the irregularities or inhomogeneous character of the layers, where Y_o is the actual capacitance of the

layer and α is an ideality factor being 1 for an ideal capacitor. Warburg element defines the diffusional component of an electrochemical systems is employed for electrochemical systems in liquid media or containing electrolyte, and widely used in analysis of dye sensitized solar cell [22]. Here, it is seen that a typical resistor do not have an imaginary part and do not contain any capacitive element.

Results of the impedance measurement are often presented by Nyquist or Cole-Cole plots, where the real and imaginary part of the impedances are plotted. However, interpretation of the results require a modelling of the components of the measured systems by using the above mentioned elements, which are referred as equivalent circuit models. Most electrochemical systems are composed of resistive elements and unavoidably capacitive elements acting on the system simultaneously. By combining these elements in series and parallel, equivalent circuit model of a system is developed and value of each element can be extracted from the EIS spectra. In Figure 3.15, a typical Randles is represented by resistive, capacitive and diffusional elements and the measured Nyquist plot is presented, where mixed kinetic and diffusional processes occur simultaneously. It is seen that, kinetic processes dominates at high frequencies and a semicircle, referred as an arc, appears at this region, At lower frequencies, diffusional control of the impedance spectra becomes dominant. Using the plot, it is possible to extract the series resistance, capacitance of the kinetic and diffusional processes and the associated resistances.

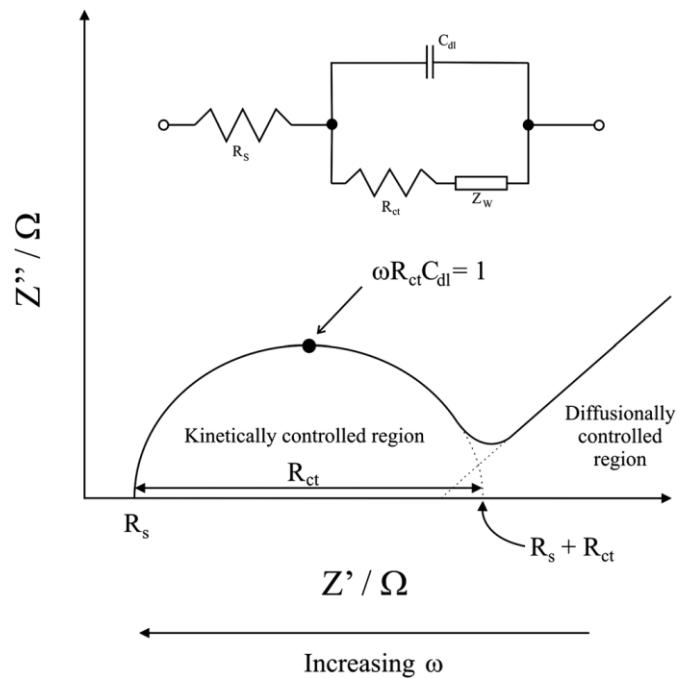


Figure 3.15 Nyquist plot of a typical Randles cell with the equivalent circuit [23].

3.4.1.2. Impedance Analysis of Mesoporous Perovskite Solar Cells

Electrochemical impedance spectroscopy have been widely used in characterization of photovoltaic cells and is a powerful tool for revealing charge transfer processes and recombination events. Mesoporous electrochemical devices like dye sensitized solar cells (DSSC) have been studied in depth by impedance spectroscopy and many equivalent circuits and elements have been adopted for the interpretation of the IS response of the cells successfully. In an electrochemical cells like a DSSC, there are many electronic and chemical processes going on simultaneously during operation. R-C circuits and transmission line models have been adopted to resemble a mesoporous layer, an electrolyte and the reactions in the counter electrode. R-C circuits modified with a Warburg diffusion element have been developed to explain the reactions in counter electrode and the TiO_2 layer and a diode model was proposed to model the reactions in the TiO_2 electrolyte interface assuming the interface as a diode. However both diode model and the R-C circuit

approaches are far from explaining the all ongoing processes inside a mesoporous layer and capacitive behaviours are excluded. The best model for a sensitized mesoporous matrix have been achieved by the transmission line model given in Figure 3.16 and was used by many reserachers to explain the behaviour of DSSCs. This model includes all possible electronic and ionic transport pathways and the electron transport resistances, recombination resistances and the chemical capacitance of the mesoporous film. Measurements are conducted under certain conditions in order to simplify the model like under applied bias or low illumination intensity conditions to increase the rate of back reaction of electrons from TiO_2 to electrolyte or to keep the TiO_2 layer in insulating conditions.

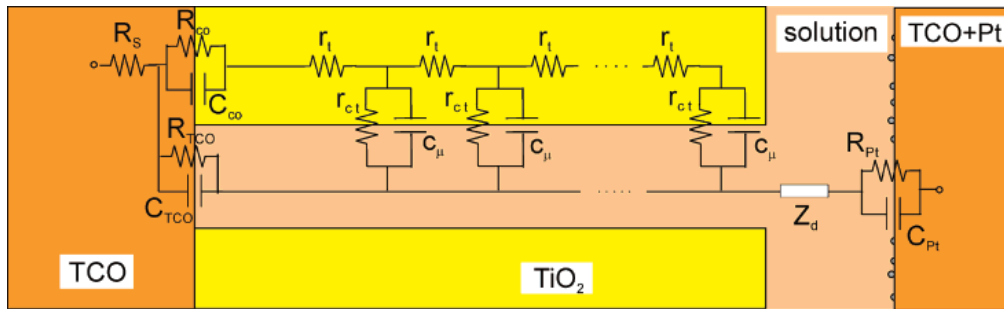


Figure 3.16 Tranmission line model for interpretation of EIS spectrum of a mesoporous sensitized based solar cell [24].

The transmission line model model have been succesfully employed in DSSCs, however, for perovskite based solar cells, this model lose its validity. Although a perovskite solar can be considered as a sensitized cell employing perovskite crystals instead of a dye molecule, impedance spectrum of perovskite and other quantum dot sensitized solar cells do not show a transmission line feature in their spectra. The actual reason of this situation is the fact that mesoporous layers employed in perovskite solar cells are limited to submicron thickness ranges in contrast to DSSCs which have mesoporous TiO_2 layers up to $15 \mu\text{m}$. In addition, perovskite solar cells employ solid state hole conductors instead of a liquid electrolyte. Most perovskite solar cells are defined by two simple R-C circuits connected in series.

Warburg component used to define the diffusional processes is no longer valid for perovskite solar cells. However, this situation also depends on the measurement conditions. At high forward biases or under intensive illumination, ion migration inside the perovskite layer may contribute to diffusional resistance and be seen as a third arc in the low frequency region in the Nyquist plot. Similarly, an additional resistance and capacitance may be observed at low biases due to poor contact between blocking layer and mesoporous TiO_2 . At most perovskite solar devices, two distinct arcs are observed at moderate illumination and forward bias conditions, as shown in Figure 3.17.

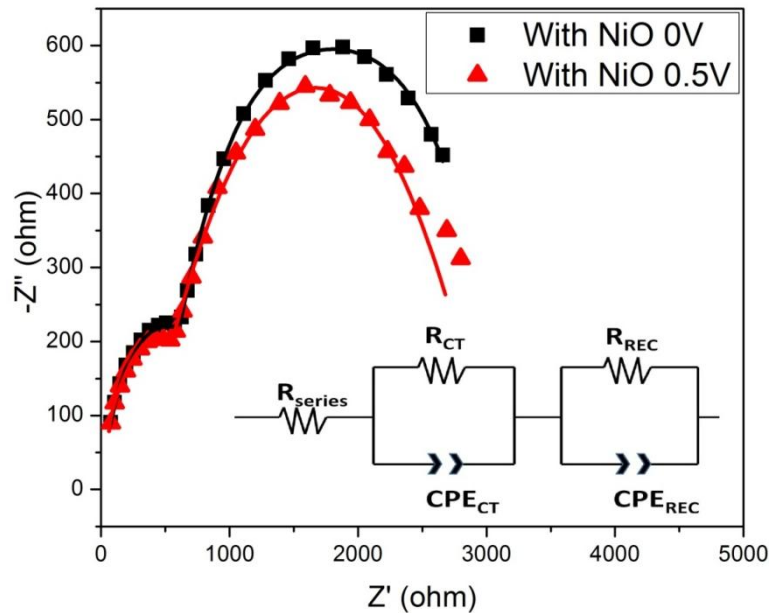


Figure 3.17 Nyquist plot of a NiO based mesoporous perovskite solar cell constructed in this work and the equivalent circuit used to model the cell.

In general, parameters of each process involved in a mesoporous perovskite solar cell can be estimated from the Nyquist plot as follows:

- In the high frequency region, charge transfer resistance of the HTM/Au interface can be estimated from the diameter of the semicircle. Capacitance

of the counter electrode can be estimated from the maximum frequency of the semicircle.

- In the middle to low frequency region, recombination resistance at the photoelectrode or perovskite/TiO₂ interface can be estimated from the diameter of the semicircle. Characteristic time constant of the recombination or recombination life time can be estimated from the maximum frequency of the semicircle.
- In the low frequency region, the diffusion resistance and the capacitance in electrolyte in the DSSCs and ion migration for the perovskite solar cells can be estimated similar to the above. This feature is rarely observed for perovskite solar cells.

REFERENCES

1. H. Schmidt, Nanoparticles by chemical synthesis, processing to materials and innovative applications, *Appl. Organometal. Chem.*, 15(2001) 331–343.
2. W.H. Zhon, B. Li, R.G. Maguire et al., (2012) *Nanoscience and nanomaterials: synthesis, manufacturing and industry impacts*. DEStech Publications Inc, USA
3. S. J. Kim, S.D. Park, Y. Jeong, S. Park, Homogenous Precipitation of TiO₂ Ultrafine Powders from Aqueous TiOCl₂ Solution. *J. Am. Ceram. Soc.*, 82 (1999) 927 - 932.
4. S. Music, D. Dragcevic, S. Popovic, M. Ivanda, Precipitation of ZnO particles and their properties, *Mater. Lett.*, 59 (2005) 2388-2393.
5. J. Moghaddam, E. Hashemi, Fabrication and characterization of NiO nanoparticles by precipitation from aqueous solution, *Korean J. Chem. Eng.*, 31 (2014) 503.
6. Z. Wu, Y. Shen, Y. Dong, J. Jiang, Study on the morphology of α -Al₂O₃ precursor prepared by precipitation method, *J. Alloys Compd.*, 467 (2009) 600-604.
7. H. Hayashi, K. Torii, Hydrothermal synthesis of titania photocatalyst under subcritical and supercritical water conditions, *J. Mater. Chem.*, 12(2002) 3671–3676.
8. R. B. Yahya, H. Hayashi, T. Nagase, T. Ebina, Y. Onodera, N. Saitoh, Hydrothermal synthesis of potassium hexatitanates under subcritical and supercritical water conditions and its application in photocatalysts, *Chem. Mater.*, 13(2001) 842–847.
9. S. C. Tsai, Y. L. Song, C. S. Tsai et al., Ultrasonic spray pyrolysis for nanoparticles synthesis, *J. Mater. Sci.*, 39 (2004) 3647.
10. K. Buyukhatipoglu, A. M. Clyne, Controlled flame synthesis of α -Fe₂O₃ and Fe₃O₄ nanoparticles: effect of flame configuration, flame temperature, and additive loading, *J. Nanopart. Res.*, 12 (2010) 1495–1508.

11. S. Li, Y. Ren, P. Biswas, S. D. Tse, Flame aerosol synthesis of nanostructured materials and functional devices: Processing, modeling, and diagnostics, *Prog. Energy Combust. Sci.*,55 (2016) 1–59
12. L. Mädler, H. K. Kammler, R. Mueller, S. E. Pratsinis, Controlled synthesis of nanostructured particles by flame spray pyrolysis, *J. Aerosol Sci.*,33 (2002) 369–89.
13. T. Tani, L. Mädler, S. E. Pratsinis, Synthesis of zinc oxide/silica composite nanoparticles by flame spray pyrolysis, *J. Mater. Res.*37 (2002) 4627–32.
14. R. Jossen, M. C. Heine, S. E. Pratsinis, S. M. Augustine, M. K. Akhtar, Thermal stability and catalytic activity of flame-made silica-vanadia-tungsten oxide-titania, *Appl. Catal. B*,69 (2007) 181–8.
15. K. C. Icli, B. C. Kocaoglu, M. Ozenbas, Comparative study on deposition of fluorine-doped tin dioxide thin films by conventional and ultrasonic spray pyrolysis methods for dye-sensitized solar modules, *J. Photon. Energy* 8 (2018) 015501.
16. N. Sahu, B. Parija, S. Panigrahi, Fundamental understanding and modeling of spin coating process: A review, *Indian J. Phys.*, 83 (2009) 493.
17. D. P. Birnie, Spin Coating Technique. In: M. A. Aegerter, M. Mennig (eds) *Sol-Gel Technologies for Glass Producers and Users*. Springer, Boston, MA(2004).
18. A. Goetzberger, J. K. Bernhard, *Crystalline Silicon Solar Cells*, John Wiley & Sons Ltd., Chichester, (1998).
19. A. Dualeh, N. Tétreault, T. Moehl, P. Gao, M. K. Nazeeruddin, M. Grätzel, Effect of Annealing Temperature on Film Morphology of Organic–Inorganic Hybrid Perovskite Solid-State Solar Cells, *Adv. Funct. Mater.*, 24(2014) 3250–3258.
20. J.H. Im, I.H. Jang, N. Pellet, M. Grätzel, N.G. Park, Growth of $\text{CH}_3\text{NH}_3\text{PbI}_3$ cuboids with controlled size for high-efficiency perovskite solar cells, *Nat. Nanotechnol.* 9 (2014) 927–932.

21. J.W. Lee, H.S. Kim, N.G. Park, Lewis Acid–Base Adduct Approach for High Efficiency Perovskite Solar Cells, *Acc. Chem. Res.*, 49 (2016) 311–319.
22. A. Sacco, Electrochemical impedance spectroscopy: Fundamentals and application in dye-sensitized solar cells, *Renew. Sustain. Energy Rev.*, 79 (2017) 814–829.
23. E. P. Randviir, C. E. Banks, Electrochemical impedance spectroscopy: an overview of bioanalytical applications, *Anal. Methods*, 5 (2013) 1098.
24. Q. Wang, S. Ito, M. Gratzel, F. Fabregat-Santiago, I. Mora-Sero, J. Bisquert, T. Bessho, H. Imai, *J. Phys. Chem. B*, 110(2006) 25210–25221.

CHAPTER 4

PRODUCTION OF Li DOPED NiO NANOPARTICLES AND THIN FILMS FOR MESOPOROUS PEROVSKITE SOLAR CELLS

There is a considerable scientific and technological interest for synthesis of nanostructured p-type semiconducting metal oxides. However, few metal oxides tend to show p-type conductivity. Nickel(II) oxide, NiO, is one of the most popular and most widely used p-type material with high stability and wide band gap around 3.6 – 4.0 eV [1]. Transparent p-type conductivity of NiO have already been demonstrated in the past years and nickel oxide (NiO) has received great attention thanks to outstanding magnetic, optical, electrical and catalytic features. Wide range of applicaiton areas in industry made NiO one of the most important transition metal oxide among others.

High electrical conduction of NiO compared to other p-type metal oxides is explained by the localized Ni³⁺ ions in the NiO lattice. Conduction in NiO films can be increased by introduction of Ni vacancies or oxygen interstitials into the host lattice, where this strategy cannot be controlled precisely. However, upon introduction of monovalent ions like Li⁺, Na⁺ and K⁺, concentration of Ni³⁺ ions can be greatly enhanced and p-type conductivity can be achieved [1].

Nanostructured NiO have been synthesized by many groups so far and methods like sol–gel method [2], surfactant-mediated synthesis method [3], thermal decomposition of precursors [4], solvothermal synthesis [5], and polymer-matrix assisted method [6] have been adopted for NiO nanoparticle synthesis. NiO thin films have been deposited on various substrates by PVD [7], pulse laser deposition [8], and the spray pyrolysis methods [9-12]. Among the vacuum based deposition

techniques, spray pyrolysis offer simple and cheap solutions for transparent and conducting oxide applications due to the atmospheric deposition conditions and low cost of precursors used in synthesis, especially for large area applications.

In this work, high surface area and mesoporous nickel oxide nanoparticles, nanosheet or nanosphere shaped structures have been synthesized by solvothermal route, ultrasonic spray pyrolysis (USP), precipitation technique and electrical conductivity of the powders were enhanced by lithium doping for mesoporous solar cell applications. Thin films of lithium doped nickel oxide were deposited on glass substrates using USP method and spin coating technique from aqueous solutions of lithium and nickel salts. Morphological and electrical characterizations of the powders and films were conducted by SEM, BET, XRD and electrical resistivity and Hall effect measurements. Produced nanoparticles and thin films of Li doped NiO were employed in mesoporous perovskite solar cells as hole conducting medium.

4.1 NiO Nanoparticle Synthesis

4.1.1 Production of NiO and Li:NiO nanoparticles with solvothermal method

4.1.1.1 Experimental

In the experimental studies, in order to synthesize intrinsic and lithium doped nickel oxide (Li:NiO) nanoparticles, solvothermal method was chosen and two different approaches have been investigated. As a novel approach, which has no previous example in literature, a direct precipitation method was developed where decomposition of nickel precursor was conducted in absence of a precipitating agent, only using solvothermal treatment. In this recipe, 0.1 M $\text{NiNO}_3 \cdot 6\text{H}_2\text{O}$ solutions were prepared using methanol as solvent and with addition of Triton-X 100 as the surface protecting agent to inhibit particle growth and agglomeration. For lithium doping, LiNO_3 was added to this solution for different Li/Ni atomic ratios,

0, 0.2, 0.4, 0.6, 0.8 and 1. Solvothermal treatment was conducted at 160°C for 12 hours in a sealed teflon lined laboratory made stainless steel autoclave. After treatment, green particles were collected by centrifugation and washed three times with ultrapure water to remove residual Triton-X 100. Obtained powders were dried in a drying oven overnight at 120°C and dried particles were ground in a mortar. For further crystallization and oxidation, grounded powders were heat treated at 500°C for 2 hours which yielded dark green to black coloured NiO powders. As an alternative to above procedure, urea was added to the solutions as a precipitating agent. Urea decomposes to CO₂ and ammonia above 80°C and increases the pH of the solution to precipitate nanoparticles. SEM, BET and XRD methods were used to characterize the morphological properties of the powders. ICP-OES method was employed to determine lithium content of the powders. Van der Pauw resistivity measurements and Hall effect measurements were used to characterize the electrical properties of the powders. For this purpose, powders were pressed into 13 mm diameter pellets and heat treated at 500°C for 2 hours again.

4.1.1.2 Characterization of NiO and Li:NiO Nanoparticles Produced by Solvothermal Method

SEM images of the powders produced by direct precipitation and urea assisted precipitation methods are given in Figure 4.1. It is seen that direct precipitation method under solvothermal conditions yields rose like structures which are composed of submicron sized nanosheets or nanoflakes where in the case of urea assisted method, spherical nanoparticles can be obtained. For mesoporous solar cell applications like dye sensitized cells or perovskite type cells, main criteria for the transport layer is that this layer can maintain a high surface area and binding site for absorber molecules to ensure sufficient light absorption. Most nanoparticles employed in DSSCs or perovskite cells have surface area values ranging between 45-70 m²/g and objective of this work is to reach surface areas values within this range. In Table 4.1, BET surface area measurement results of the powders have been given.

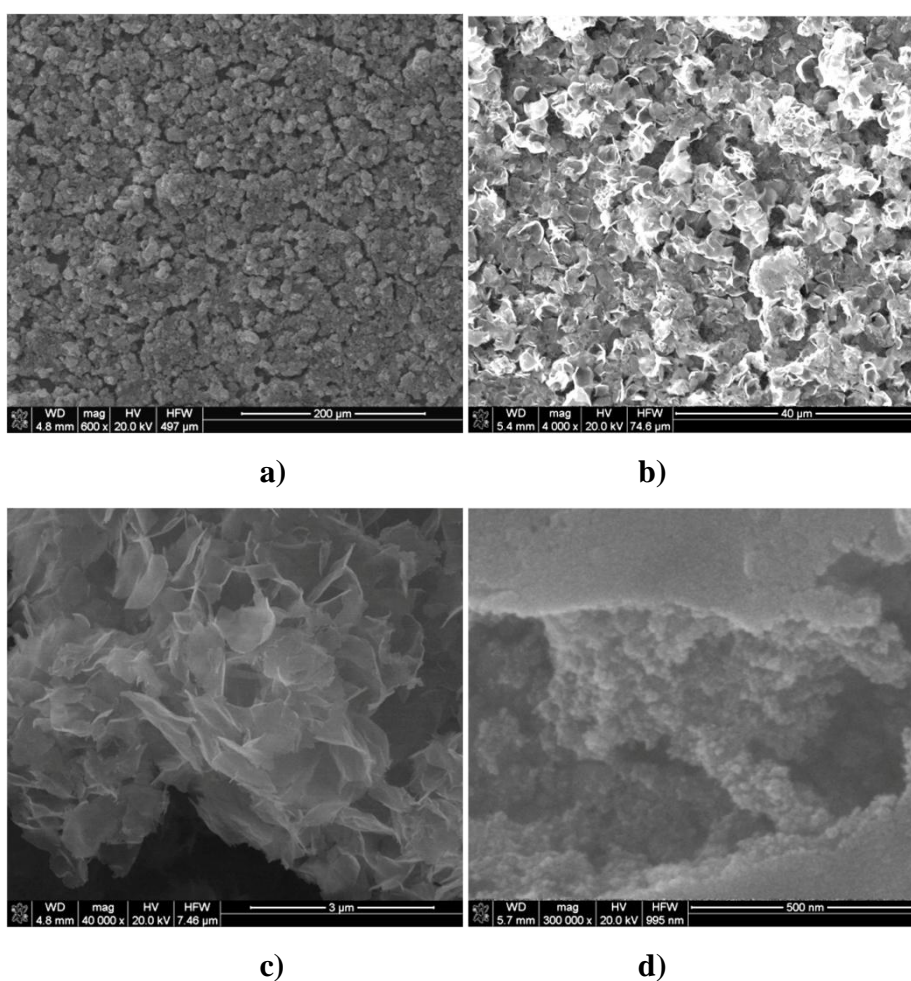


Figure 4.1 SEM images of NiO powders produced by direct precipitation (a, b, c) and agent assisted precipitation methods (d).

Table 4.1 BET surface area measurements of the powders produced by direct precipitation method (DP) and assisted precipitation (AP) method.

Sample	DP	DP (5 ml Triton-X)	DP (10 ml Triton-X)	DP (15 ml Triton-X)	AP
Surface Area (m ² /g)	15	25	33	46	3

BET surface area measurements reveal that although urea assisted precipitation method gives uniform spherical nanoparticles around 30 nm, surface area value is inferior compared to direct precipitation method which yields powders achieving 46 m²/g surface area value after addition of 15 ml Triton-X 100. At this point, it is interesting to note that surface area value of this sample increases to 49 m²/g after heat treatment of the powder at 500°C in contradiction to most nanoparticles which undergo surface area reduction upon heat treatments. We explain this situation with some sort of morphology change in nanosheets due to a phase transformation. In Figure 4.2, XRD spectra of the as synthesized powders after solvothermal treatment and after heat treatment at 500°C are given. As synthesized powders contain Ni(OH)₂ (JCPDS 73-1520) and small amount of NiO (JCPDS 78-0429) phases. After heat treatment, Ni(OH)₂ is fully converted to NiO phase successfully. Powders show the cubic bunsenite phase of NiO.

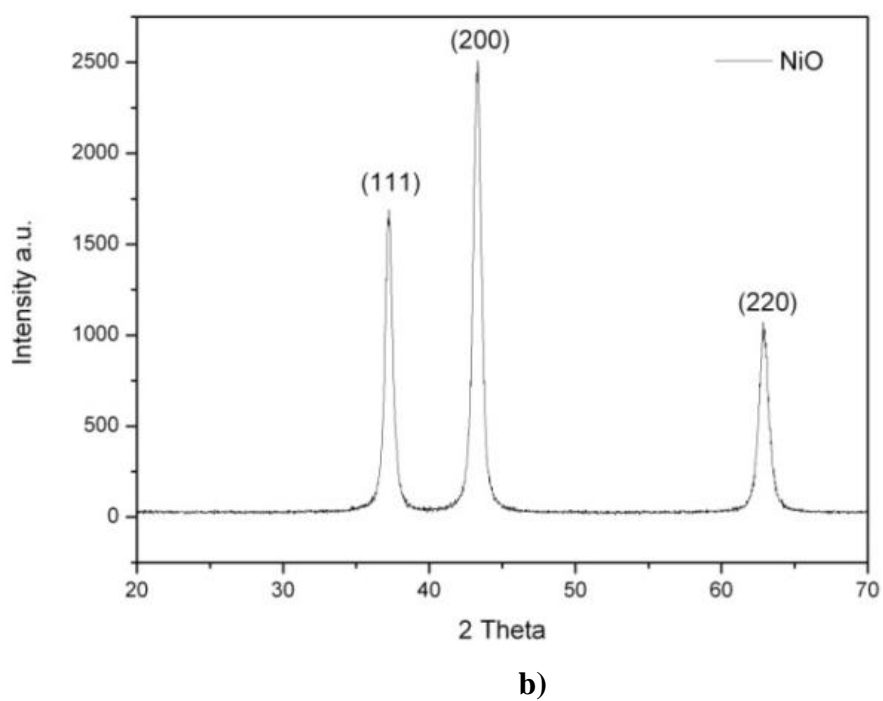
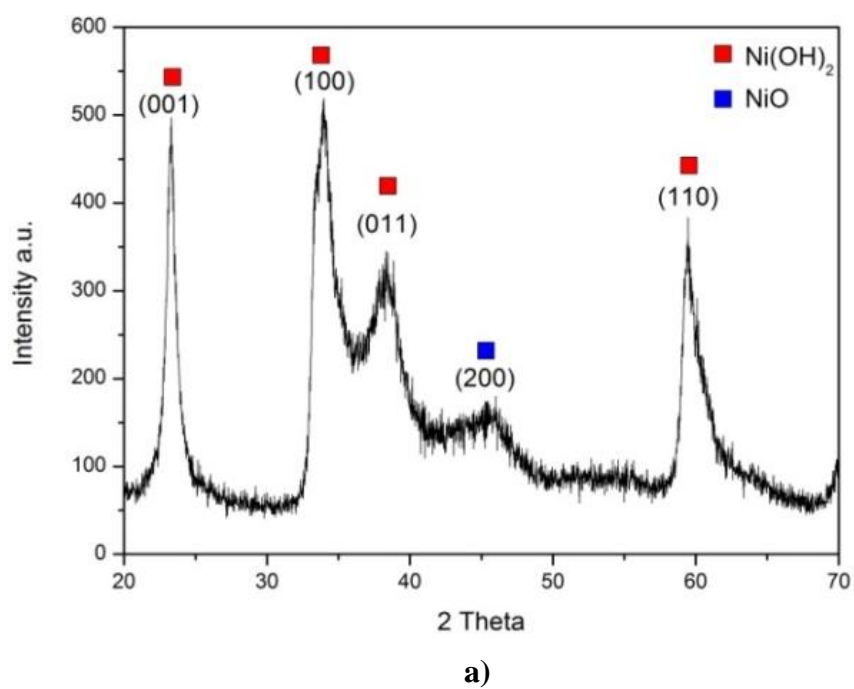
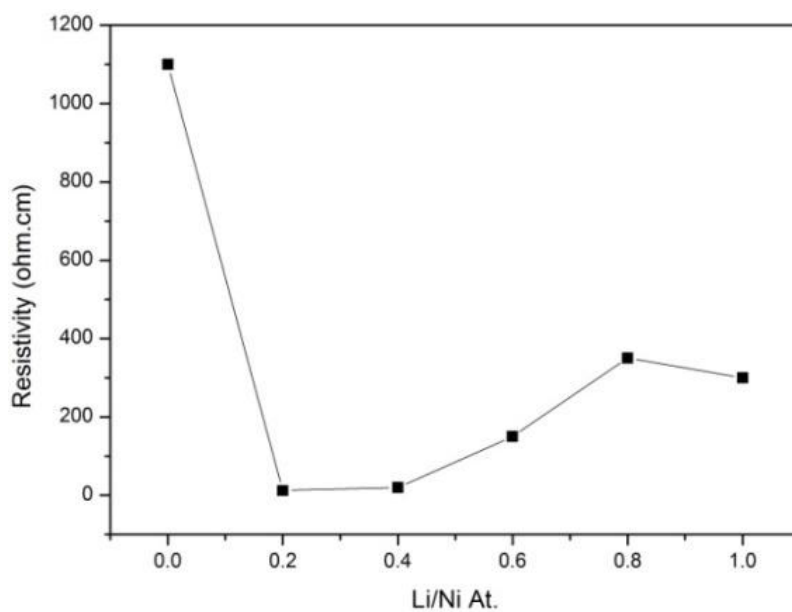


Figure 4.2 XRD patterns of direct precipitated powders before (a) and after (b) heat treatment.

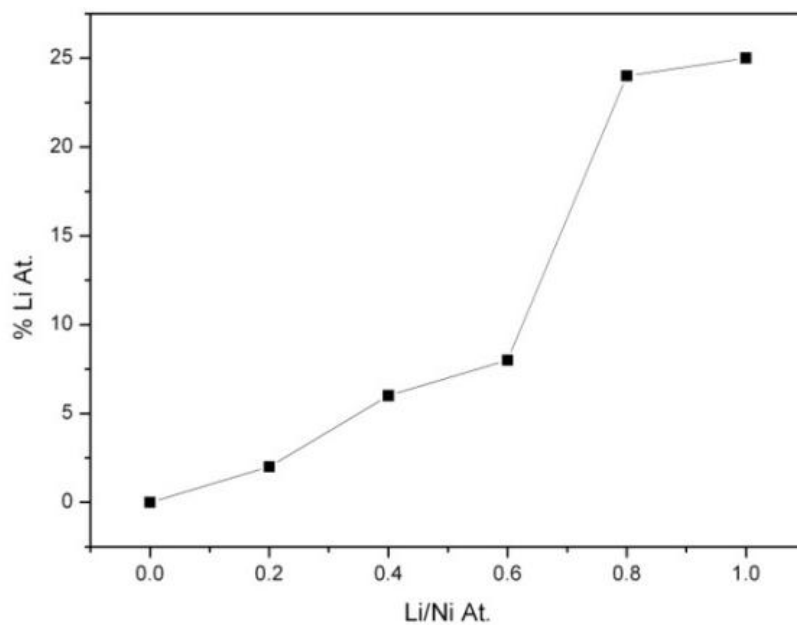
For solar cell applications, ordered structures like nanotubes, nanosheets or nanorods seem to be advantageous by means of electrical transport through 1D structure instead of a random network of interconnected nanoparticles. Nanosheets or flakes obtained in this work fulfill the required NiO phase and sufficient surface area values so these particles are proper candidates to be the hole transport material in the planned perovskite solar cell. Another objective of the work is to enhance the electrical conductivity of the powders by lithium substitution and to reduce charge transfer resistances inside the cell. In order to examine the effect of lithium doping on the electrical properties of the NiO nanoflakes, powders were pressed into pellets and resistivity values were measured and given in Figure 4.3a. Upon Li doping, resistivity value of the undoped NiO is enhanced from several ohm.cm down to a minimum of 10 ohm.cm value for a Li/Ni atomic ratio of 0.2 in the starting solution. The hole mobility and carrier concentration values of this sample measured by Hall effect studies are $5.1 \text{ cm}^2.\text{V}^{-1}.\text{s}^{-1}$ and $9.7 \times 10^{17} \text{ cm}^{-3}$. Further increase in lithium doping amount beyond this level slightly increases the resistivity which can be explained by scattering effect of the ions retarding hole motion. The optimized resistivity value achieved in this work is close to best Li:NiO thin films produced by sputtering methods and shows the successful electrical conduction power of the synthesized powders, especially compared to undoped sample. The lithium content of the powders measured by ICP-OES are shown in Figure 4.3b and it is seen that actual amount of lithium inside the powders is around a half of the starting solution which is the degree of doping achievable under the synthesis conditions in this work.

The XRD spectra of the powder produced from Li/Ni ratio of 0.4 is given in Figure 4.3c and shows no secondary lithium or nickel containing compound proving that lithium is successfully doped into NiO lattice. Actually this situation is also evident from huge enhancement in electrical conductivity of the powders. We also state that observed conductivity of the powders in pellet form which is close to best reported literature thin film values, arises from the sheet like ordered structure of the synthesized powders. These sheets provide scattering free pathways for electron

percolation during electrical transport with reduced grain boundary scattering compared to nanoparticulate random network of particles.



a)



b)

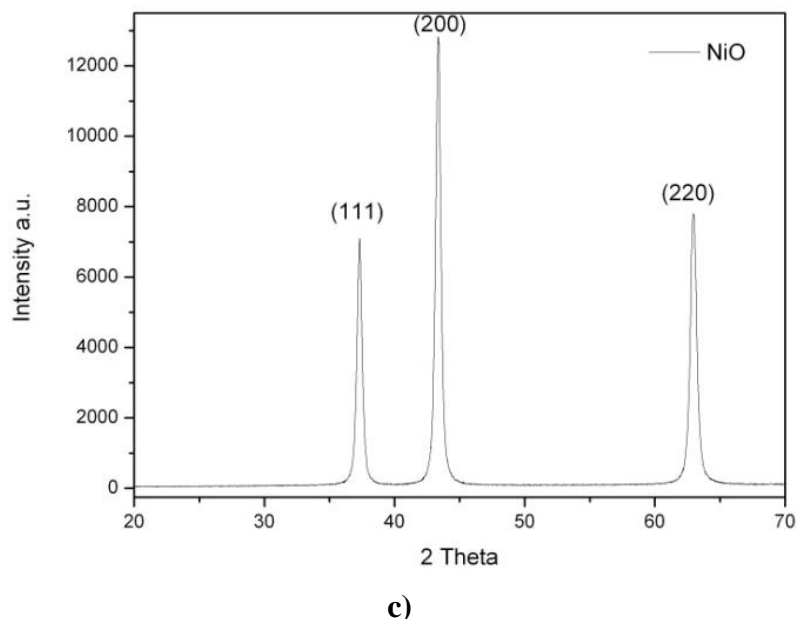


Figure 4.3 Variation of resistivity values of NiO nanopowders with Li doping amount (a), Li content of powders measured with ICP-OES (b) and XRD spectra of Li:NiO powder with Li/Ni ratio of 0.4 (c).

4.1.2 Production of NiO and Li:NiO Nanoparticles with USP Method

4.1.2.1 Experimental

Lithium doped nickel oxide particles were synthesized by ultrasonic method similar to thin film production where mist produced by the generator was fed into a reaction chamber instead of a hot substrate. Precursors of $\text{NiNO}_3 \cdot 5\text{H}_2\text{O}$ and LiNO_3 were dissolved in methanol for different molarities and different Li doping ratios. Mist generated by the ultrasonic generator was carried by air into a tubular oven at 600°C which is connected to a bubbler containing water and ethanol. Collected powders were obtained by evaporating or centrifuging the solvent and dried at 120°C overnight. Stoichiometric powders of $\text{Li}_x\text{Ni}_{1-x}\text{O}$ were produced by this method where x is 0.1, 0.25, 0.33 and 0.5.

4.1.2.2 Characterization of NiO and Li:NiO Nanoparticles Produced by USP Method

The SEM images of NiO particles produced by ultrasonic method for different molarities are given in Figure 4.4.

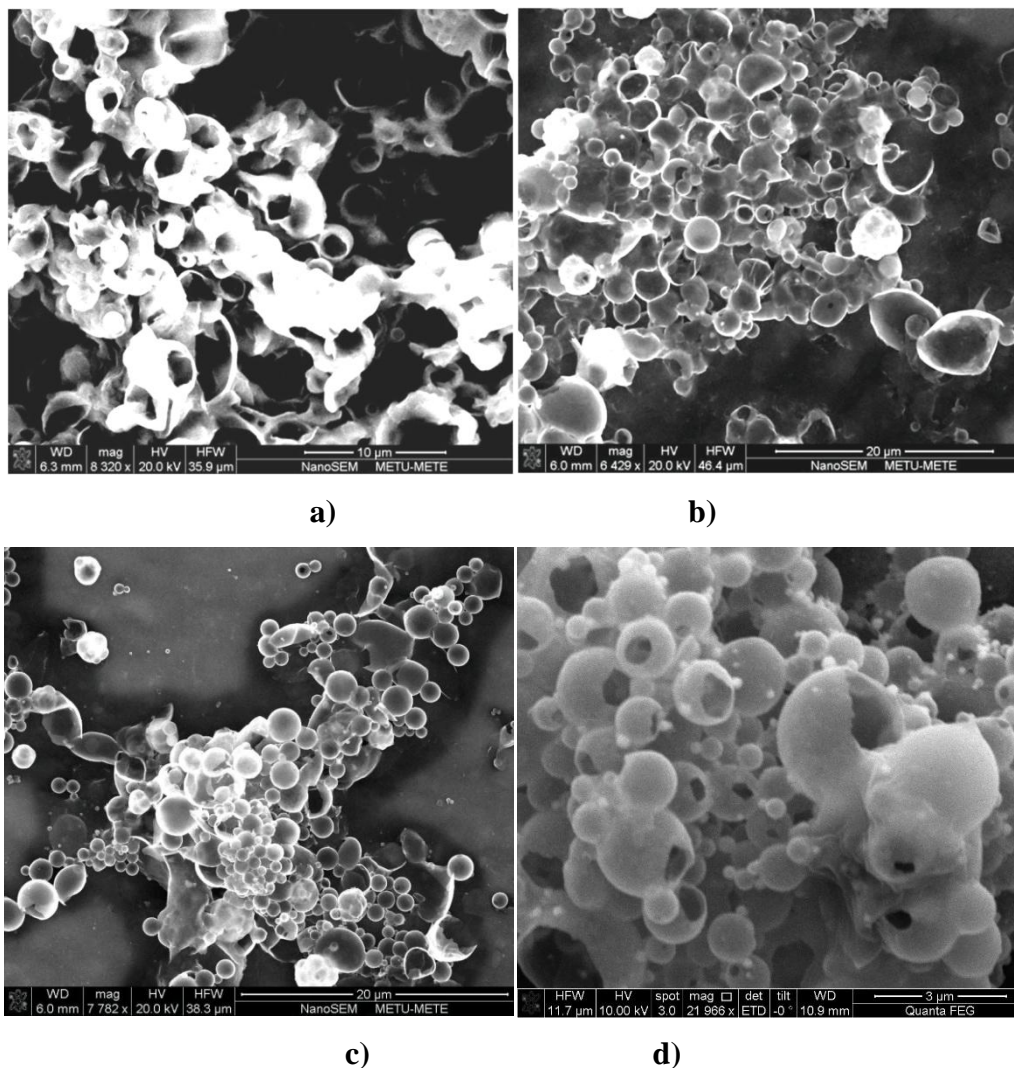
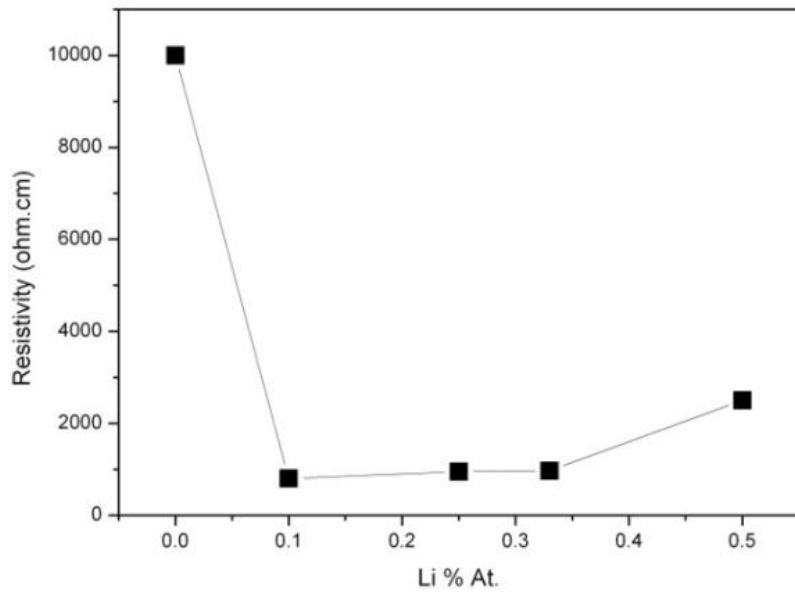
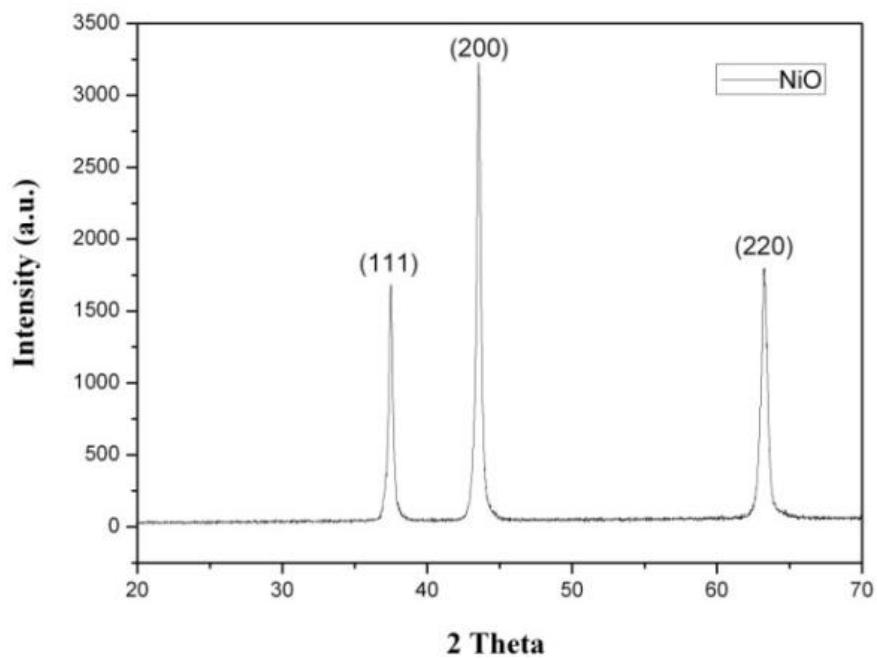


Figure 4.4 SEM images of Li:NiO particles produced by ultrasonic method from methanolic precursors having molarities of 0.3M (a), 0.15M (b), 0.075M (c), 0.035M (d).

It is seen for high molarities particles tend to form large and irregular shaped hollow spheres. By decreasing molarity of the solution, regular spheres can be obtained and size of the particles can be reduced down to 100 nm, however there are still larger particles above 1 micron. Formation of the hollow spheres in this method is due to fast solvent evaporation and rapid reaction of the precursor materials inside each individual droplet created by the ultrasonic generator. By sending the methanol containing droplet inside a high temperature chamber results in a combustion like reaction where methanol quickly burns and forms a NiO outer layer. In this methodology, it seems essential to employ inorganic solvents having higher boiling points in order to overcome the formation of outer layers and reducing the size of the particles. Produced particles for 0.075M were pressed into pellets and resistivity values were measured by four point method for different Li doping amounts and given in Figure 4.5a. Best resistivity values were obtained for $\text{Li}_{0.1}\text{Ni}_{0.9}\text{O}$ powders and for higher doping amounts resistivity increases slightly until 50% doping amount. Resistivity of 850 ohm.cm could be achieved using this method and XRD spectra of the powders (Figure 4.5b) reveals a pure nickel oxide structure with no secondary phases (JCPDS 78-0429). For the perovskite based mesoporous solar cells, it is mandatory to deposit mesoporous layers around 1 micron thickness at most and prevention of large particles like 3 micron seen in the SEM images should be prevented.



a)



b)

Figure 4.5 Resistivity values of Li:NiO powders for different doping amounts (a), XRD spectra of the $\text{Li}_{0.1}\text{Ni}_{0.9}\text{O}$ powders (b).

4.2 NiO and Li:NiO Thin Film Deposition

4.2.1 Production of NiO and Li:NiO Thin Films with USP Method

4.2.1.1 Experimental

For deposition of Li:NiO thin films, ultrasonic spray pyrolysis (USP) method was used. 0.3 M NiNO₃.6H₂O aqueous solutions were prepared and deposited on clean solar glass substrates. Lithium doping was achieved by adding LiNO₃ to the precursor solutions for Li/Ni ratios of 0, 0.2, 0.4, 0.6, 0.8 and 1 similar to powder production. A 1.3MHz ultrasonic generator was used to convert this solution to fine mist and this mist was transported to preheated 5x5 cm sized glass substrates (450°C) using clean air. However, it was observed during experiments that this method yields highly irregular and inhomogeneous coatings visible by eye which we relate to fast and unstable decomposition of precursor at elevated temperatures and high tendency of nitrate precursor to decompose instantaneously. Due to this reason, a two stage procedure was employed. In the first stage, deposition is conducted at 150°C which gives transparent to greenish and homogeneous coatings. This coating is then heat treated at 450°C in air and transparent to slightly black coatings were obtained with no visible irregularity.

4.2.1.2 Characterization of NiO and Li:NiO Thin Films Deposited by USP

Deposition of NiO and Li:NiO thin films on glass substrates by spray pyrolysis method from aqueous solutions were conducted by a two stage process with varying Li content in the starting solutions. Direct spraying of these solutions onto hot substrates resulted in inhomogeneous and discontinuous films even visible by eye. SEM images of direct sprayed and two stage produced films are given in Figure 4.6.

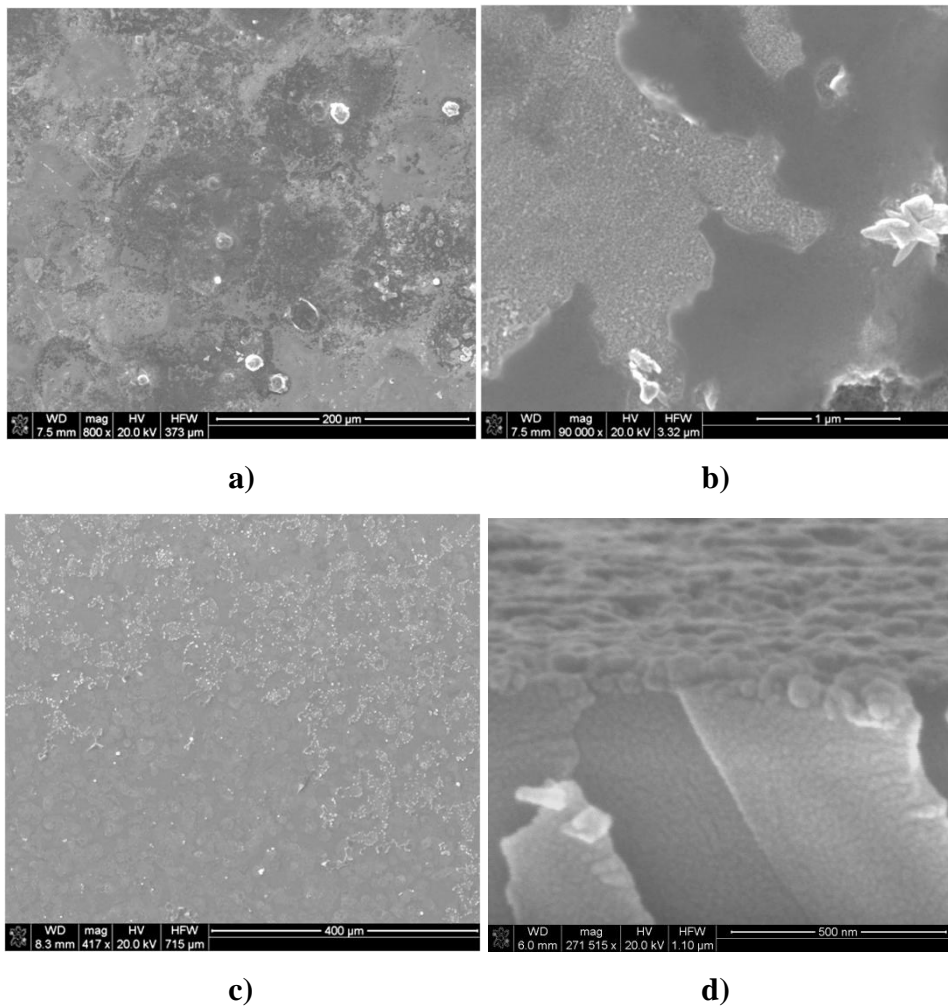
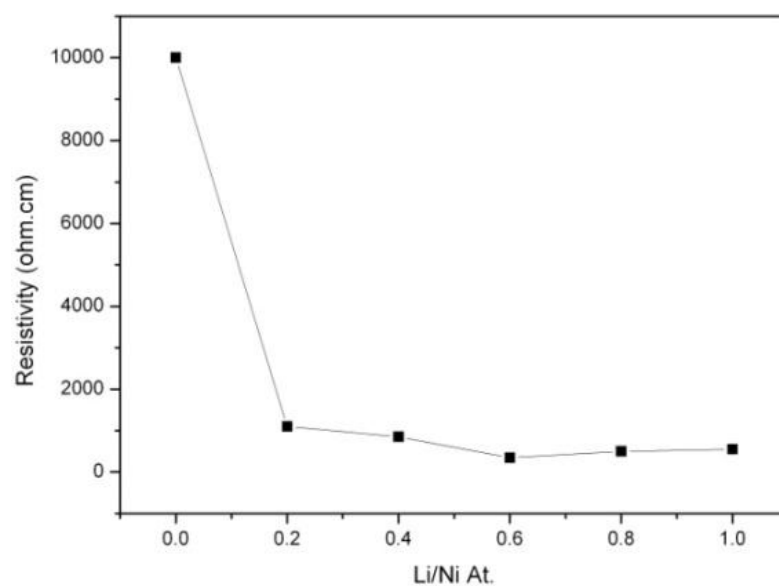
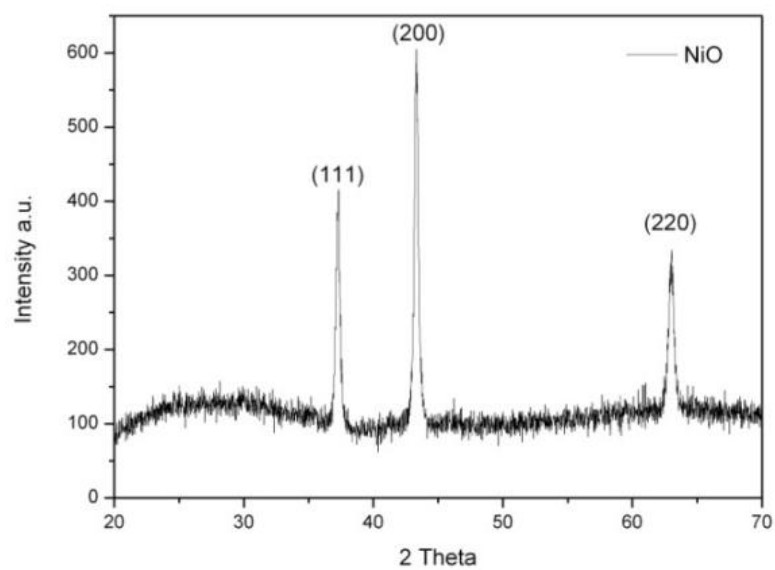


Figure 4.6 SEM images of NiO thin films deposited by direct spraying on hot substrate (a,b) and the two stage coated substrate (c,d).

As it is seen in Figure 4.6a and b, direct sprayed NiO films exhibit large voids and discontinuities on the substrate surface. Observation by eye reveals that these films tends to grow in certain columnar vessel like paths leaving large uncoated bare parts. We speculate that this tendency can be explained with a fast evaporation and precursor decomposition on hot substrate leading to uncontrolled nucleation and growth of crystals. In order to eliminate this tendency, two stage process was employed and results shown in Figure 4.6c and d.



a)



b)

Figure 4.7 Change of resistivity values of Li:NiO thin films with varying Li content in the starting solution (a), XRD spectra of Li:NiO sample with Li/Ni ratio of 0.6 (b).

Such films are smoother and large cracks or voids are absent compared to direct deposition. In Figure 4.6d, cross sectional image of the NiO film is given.

Homogeneous and continuous films down to 60 nm size can be coated with this method. However, SEM images reveals that both methods yield particulate structures but not dense films.

Four point resistivity measurements were conducted on the films for Li/Ni ratios in the starting solution ranging from 0-1 and given in Figure 4.7. For the case of sprayed films, lowest resistivity value was observed for the sample having Li/Ni ratio of 0.6 in the starting solution with a resistivity value of 355 ohm.cm. Hole mobility and carrier concentration values are $12.4 \text{ cm}^2.\text{V}^{-1}.\text{s}^{-1}$ and $1.6 \times 10^{16} \text{ cm}^{-3}$. XRD spectra of this sample given in Figure 4.7b shows that film is completely composed of cubic NiO phase with no secondary lithium or nickel containing compound. The resistivity value is consistent with the literature examples of sprayed Li:NiO films but somehow lower than the value observed in the pelletized nanopowders synthesized in the previous section. Nanoparticulate nature of sprayed NiO films is the origin of lower conductivity of these films compared to dense structures like sputtered films or the pellets in this work.

4.2.2 Production of NiO and Li:NiO Thin Films with Spin Coating Method

4.2.2.1 Experimental

Lithium doped nickel oxide particles were coated on pre-cleaned solar grade glass substrates by spin coating method. For this purpose $\text{NiNO}_3.5\text{H}_2\text{O}$ was dissolved in dimethylformamide (DMF) with addition of LiCO_3 as the lithium source. Lithium doping amount was arranged to be between $x=0.1, 0.25, 0.33$ for $\text{Li}_x\text{Ni}_{1-x}\text{O}$ thin films. Films were coated on 1x1 cm glass substrates for electrical characterization and on FTO coated glass substrates for morphological characterization as a blocking layer for temperatures of 400°C and 625°C . Morphologies of powders and thin films of Li:NiO were characterized by scanning electron microscopy and X-ray diffraction techniques. Electrical resistivities of films were determined by four point method.

4.2.2.2 Characterization of NiO and Li:NiO Thin Films Deposited by Spin Coating Method

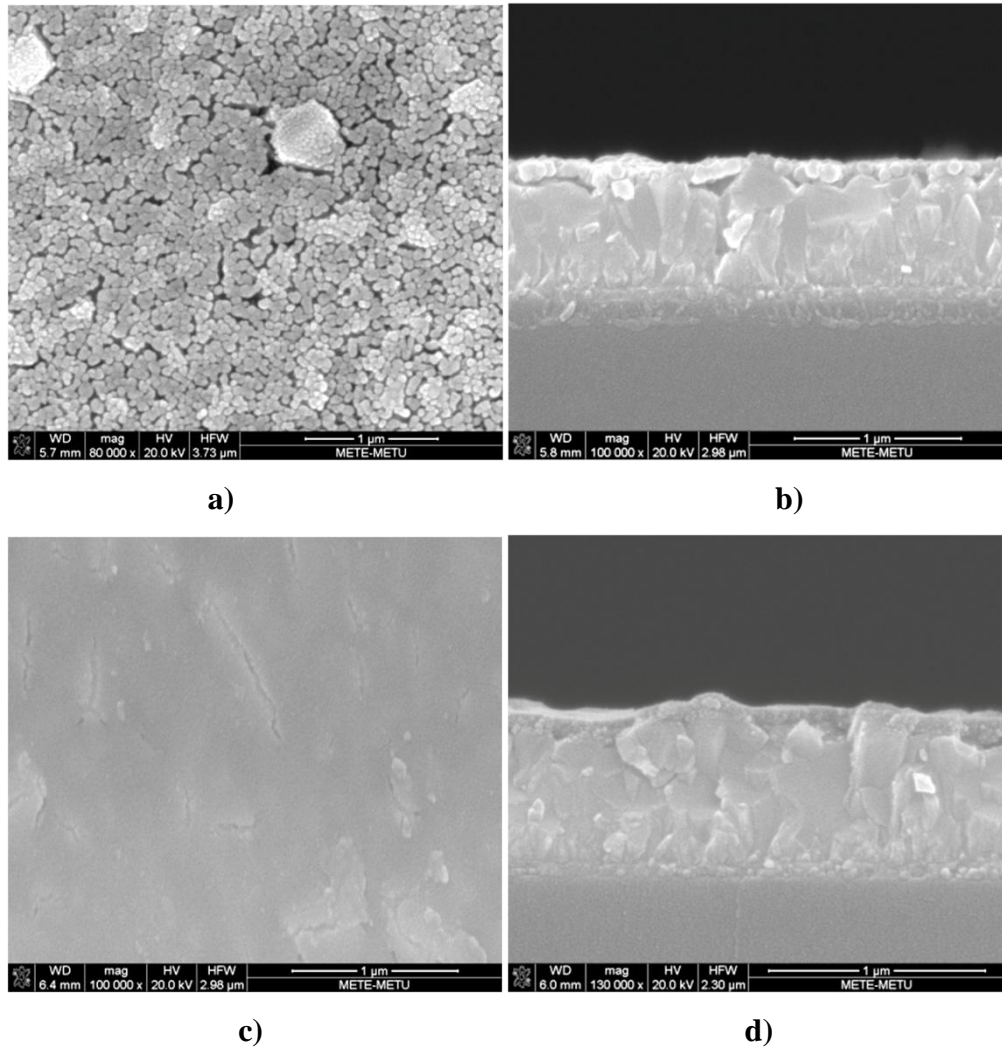
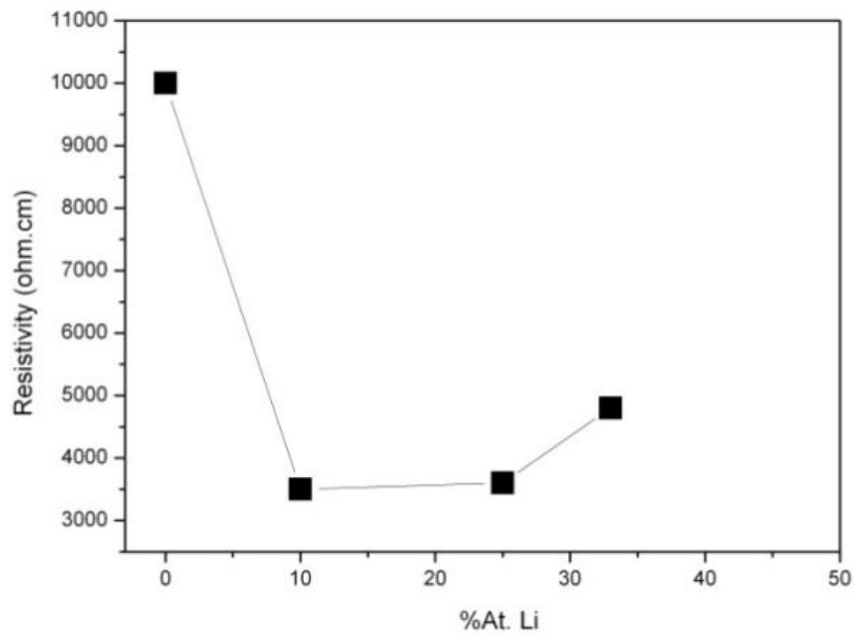


Figure 4.8 SEM images of Li:NiO films produced by spin coating of a DMF based solution and fired at 400°C (a,b) and fired at 625°C (c,d).

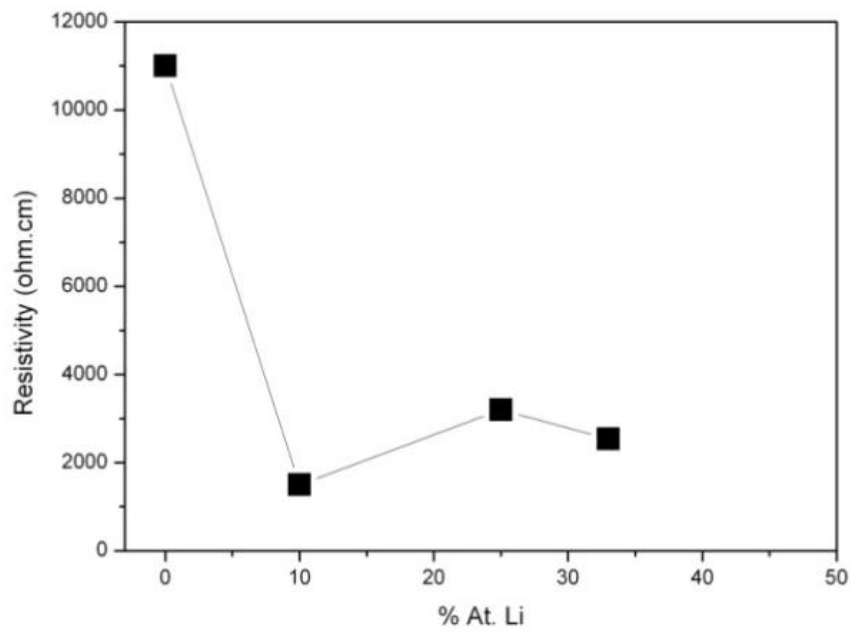
In Figure 4.8 SEM images of the thin films of Li doped NiO deposited on FTO substrates are given for firing temperatures of 400°C and 650°C. It can be seen that films fired at 650°C are composed of connected nanoparticles of 70-100 nm and there are pores and cracks inside the films. However films fired at 400°C composed

of smaller nanoparticles without pores and a more dense film is obtained. From cross sectional images, continuity of the films fired at 400°C is better than the films fired at 650°C which possess particle like structure and discontinuity. A discontinuous and porous layer is undesirable for blocking layer applications in perovskite solar cells considering that contact of the perovskite layer should be avoided with the FTO substrate for preventing shunt losses and recombination.

Films fired at 400°C seems to be more suitable for blocking layer application. However, resistivity values of these films are higher than the films fired at 650°C. In Figure 4.9, resistivity values of the thin films deposited on glass substrates for different Li doping amounts is given for 400°C. A minimum resistivity is observed for Li doping amount of 10% which is consistent with the films fired at 650°C, but minimum resistivity of 3800 is higher than for films fired at 650°C which shows minimum resistivity of down to 1500 ohm.cm.



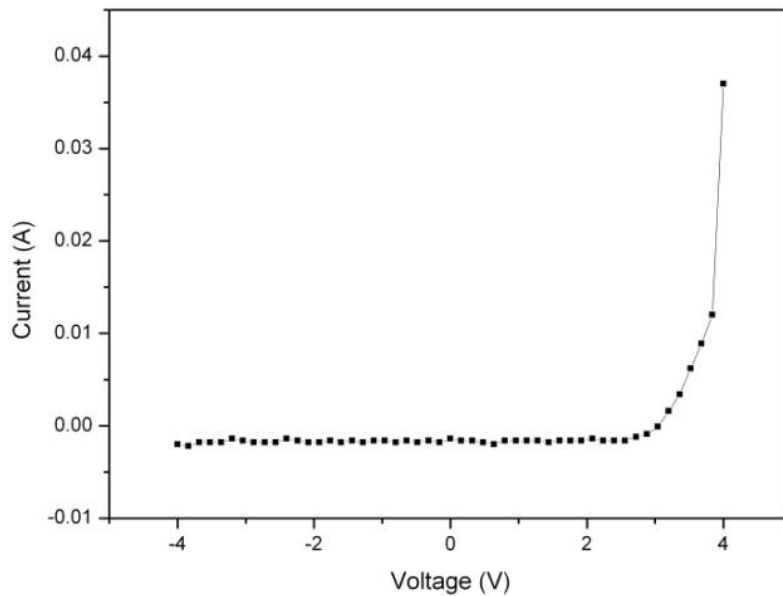
a)



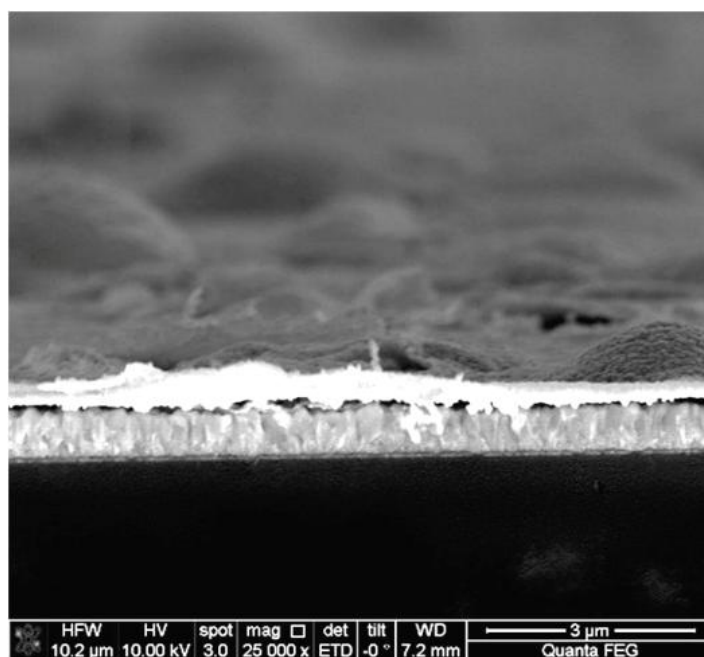
b)

Figure 4.9 Resistivity values of Li:NiO thin films for different Li doping amounts fired at 450°C (a) and 625°C (b).

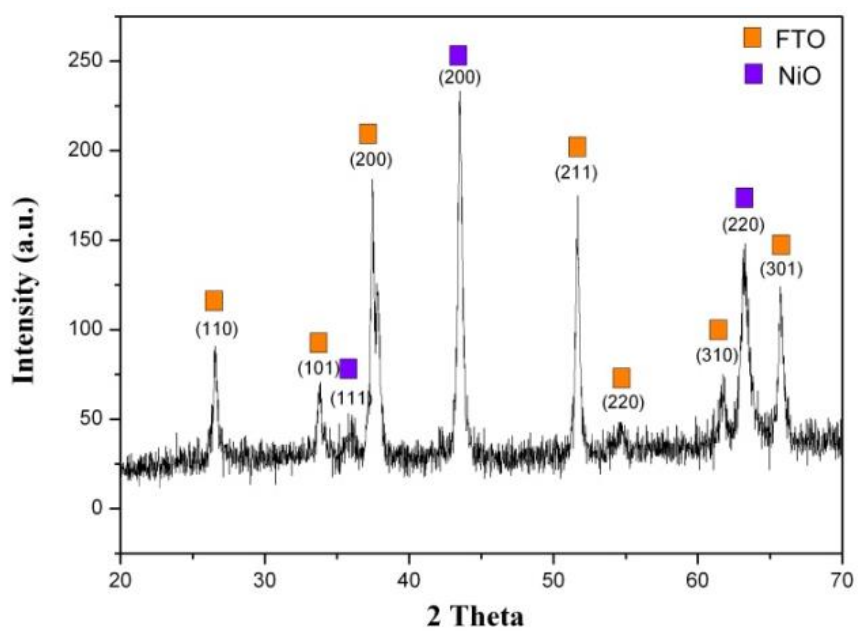
These films are intended to be employed as the cathode part of the perovskite based solar cells in an inverted type cell structure which acts like a hole transport layer or electron blocking layer. However, as long as FTO is an n-type material and NiO is a p-type material, a junction formation is expected to form between two layers. In Figure 4.10a, I-V characteristic of the formed heterojunction is given for $\text{Li}_{0.1}\text{Ni}_{0.9}\text{O}$ films deposited on the FTO substrate. The curve clearly indicates the diode behaviour of the heterojunction which shows the succesful formation of an internal depletion layer and an electrical field for a device of 600 nm FTO layer and 200 nm Li:NiO film (Figure 4.10b). XRD spectra of the device given Figure 4.10c reveals only SnO_2 and NiO phases. Formation of such a depletion layer and an internal electrical field is expected to further enhance the carrier transport properties of the hole transport medium which is believed to lead efficient charge collection inside the cells.



a)



b)



c)

Figure 4.10 I-V characteristic of the FTO/Li:NiO heterojunction(a), cross sectional SEM view of the junction (b) and XRD spectra of the heterojunction (c).

4.3 Construction and Characterization of Mesoporous Perovskite Solar Cells

4.3.1 Experimental

FTO (coated glass substrates Solaronix 7 ohm/sq) were firstly etched with zinc powder and 0.1M HCl for separating anode and cathode part of the cells. FTO glasses were cleaned ultrasonically using DI water, acetone and isopropanol subsequently. A compact TiO₂ layer was deposited by spin coating a solution of 0.15 M titanium diisopropoxide bis acetylacetonate in 1-butanol at 2000 rpm for 20 s. Mesoporous TiO₂ layer was deposited on this layer by using a commercial TiO₂ paste (Dyesol 90T) diluted in ethanol by 1:3.5 weight percent. Spin coating was conducted at 5000 rpm for 25s and films were fired at 500°C for 30 min. For one-step perovskite deposition method, a DMF solution containing methyl ammonium iodide (MAI) purchased from Dyesol and lead chloride (PbCl₂) (3:1 mol ratio) was spin coated on the substrate at 2000 rpm for 30 s and annealed at 100°C for 45 min in air. In order to compare the performance of different perovskite layer deposition approaches, in addition to one-step method, two-step method and adduct methods have been compared. For this purpose, in the case of two-step approach, first a 1M lead iodide (PbI₂) solution in DMF was deposited on the TiO₂ layer and dried at 100°C for 15 min. Then a solution of 6mg/ml MAI in isopropanol was dropped on the substrate and waited for 40 s and spun at 4000 rpm for 20 s. For crystallization, films were heat treated at 100°C for 5 min. For adduct methodology, a %40 wt. solution of dimethyl sulfoxide, PbI₂ and MAI was prepared in DMF for a molar ratio of 1:1:1. This solution was spin coated on the substrate at 4000 rpm for 30 s, however after 5 s, diethyl ether was dropped on the spinning substrate. For crystallization, films were heat treated at 100°C for 5 min. For deposition of p-type hole conducting layers, copper thiocyanate (CuSCN) dissolved in dipropyl disulfide (10 mg/ml) and NiO nanoparticle dispersion, prepared by dispersing the synthesized NiO nanoparticles in isopropanol, were spin coated on the cells at 4000 rpm for 30 s and left to dry in fume hood. For inverted type solar cells, PEDOT:PSS was spin-coated on FTO at 5000 rpm for 50 s and then annealed at 100 C for 15 min. After

depositing the perovskite layer by adduct method, the acceptor layer was prepared by spin coating (1000 rpm, 30 s) 2 wt% PCBM in chlorobenzene onto the surface of the perovskite film. The PCBM film was solvent annealed by covering the film with a Petri dish for 24 hours. The trace amount of solvent (chlorobenzene) in the film will continuously infiltrate PCBM to form a close contact with the perovskite film underneath. For both devices, gold contacts were deposited by e beam evaporation at a thickness of 100 nm. Devices were characterized by SEM and J-V curves were recorded under simulated AM 1.5 conditions.

4.3.2 Characterizations of the perovskite solar cells

In the experimental work, in order to identify the best methodology for deposition of perovskite layers, different approaches for perovskite synthesis in literature have been tried and characterized. For this purpose, first of all, one step method has been employed on TiO₂ based configuration where a compact layer and a mesoporous layer were used without any hole conductor. Optimization of the blocking layer thickness and mesoporous layer thickness was conducted using lead chloride and methylammonium iodide based DMF solution at a molar ratio of 1:3. Results are summarized in Table 4.2 and Table 4.3.

Table 4.2 Cell parameters of perovskite solar cells depending on the blocking layer thickness, prepared by one-step method.

Blocking layer	V _{oc} (V)	J _{sc} (mA/cm ²)	Fill factor	Eff.(%)
50 nm	0.63	9.51	0.47	3.00
70 nm	0.67	11.42	0.53	4.36
110 nm	0.65	9.042	0.58	3.65

Table 4.3 Cell parameters of perovskite solar cells depending on the mesoporous layer thickness, prepared by one-step method.

Mesoporous layer	V_{oc} (V)	J_{sc} (mA/cm²)	Fill factor	Eff.(%)
200 nm	0.63	6.77	0.47	2.12
400 nm	0.66	8.82	0.49	3.08
600 nm	0.64	7.21	0.53	2.65
800 nm	0.61	7.23	0.54	2.54

For blocking layer optimization, spin cycles of the blocking layer precursor solution was repeated up to 3 times and a 400 nm mesoporous TiO₂ layer was kept constant for all devices. For mesoporous layer optimization, 1 cycle of blocking layer was kept constant and spin cycles of mesoporous layer solution was varied up to 3 times. It was observed that best efficiency values were obtained from 2 layer spin coating of blocking layer corresponding to 70 nm thick blocking layer and 2 times spin coating of mesoporous layer corresponding to 400 nm mesoporous layer. Thicker and thinner layers lead to reduction in cell potential while thick layers lead to higher fill factors which can be explained as a reduction in shunt between FTO and gold layer.

Table 4.4 Cell parameters of perovskite solar cells depending on perovskite layer deposition method.

Method	V_{oc} (V)	J_{sc} (mA/cm²)	Fill factor	Eff.(%)
One-step method	0.67	11.42	0.53	4.36
Two-step method	0.85	12.79	0.40	4.33
Adduct method	0.85	12.64	0.42	4.56

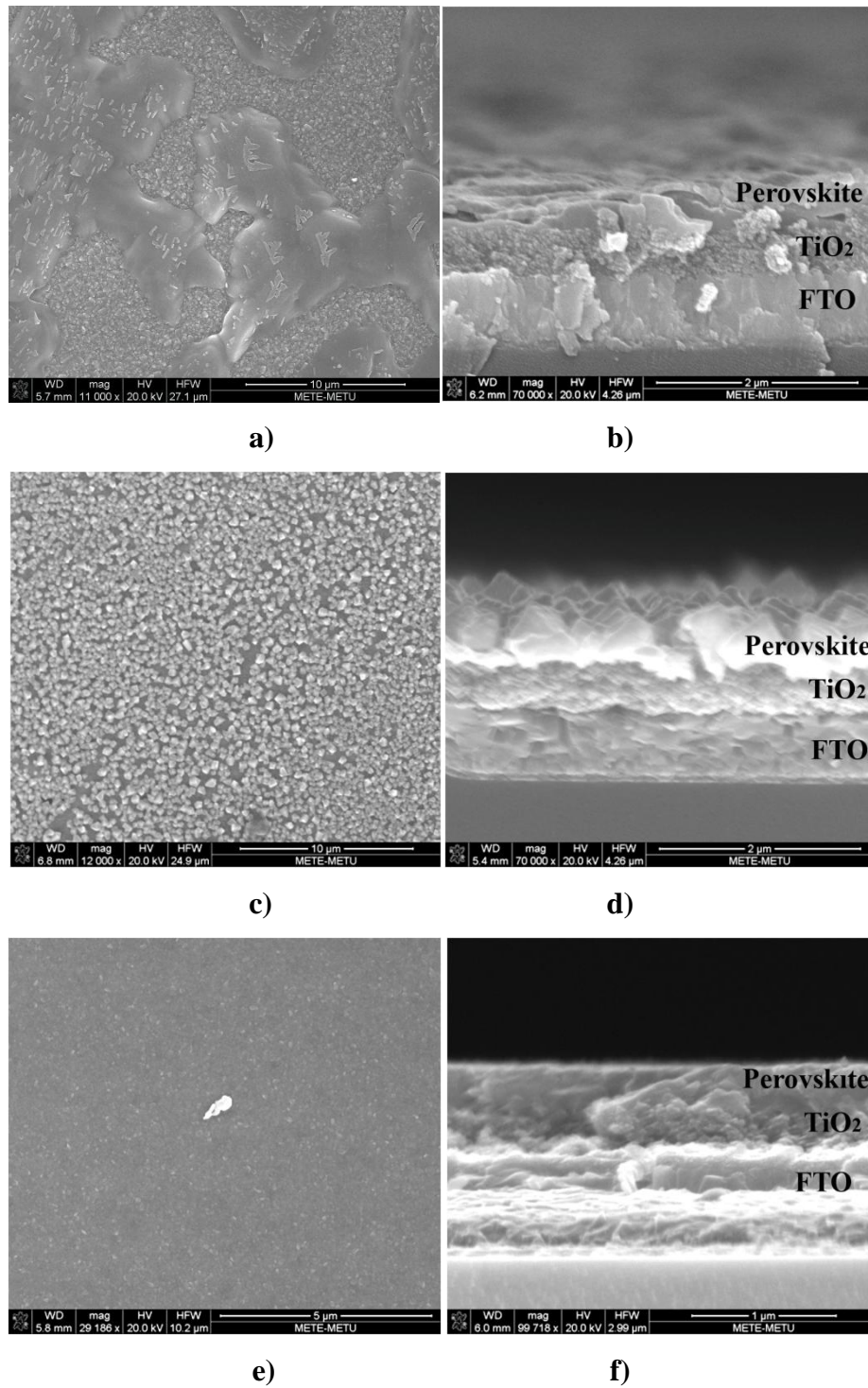
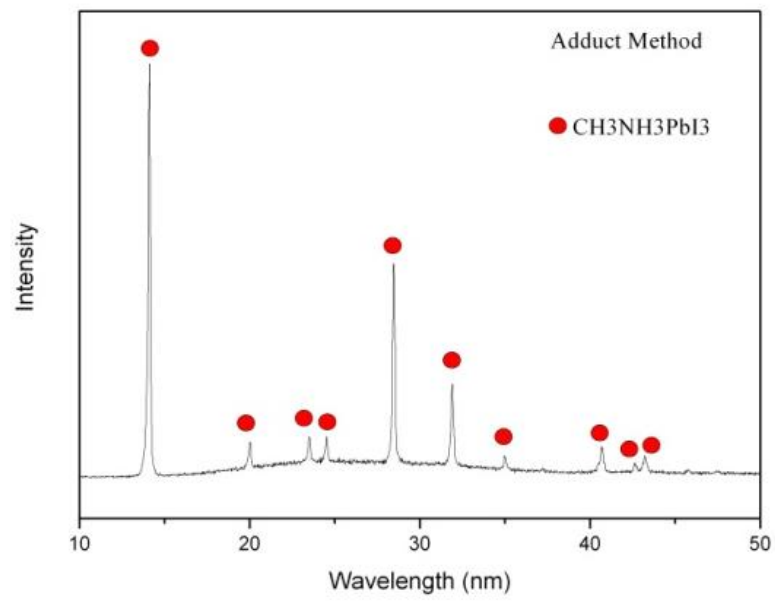


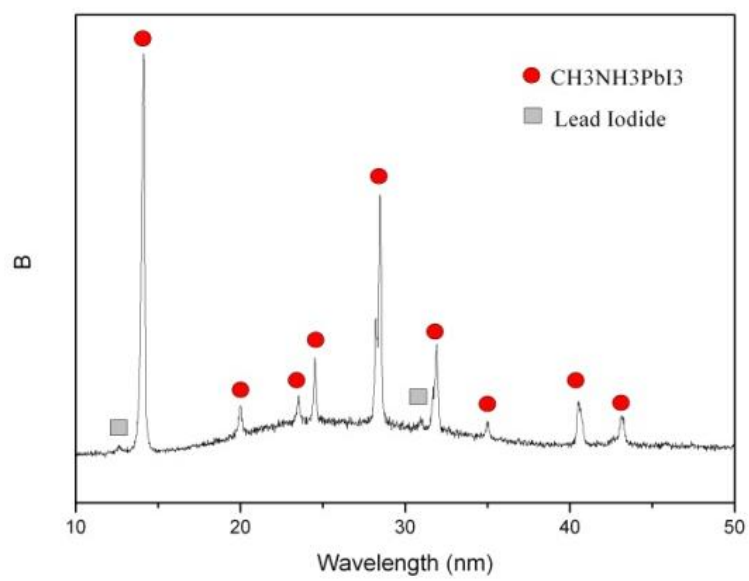
Figure 4.11 SEM images of the surfaces and cross sections of the devices produced by one-step method (a,b), two-step method (c,d) and adduct method (e,f).

In order to determine the effect of perovskite layer deposition method, in addition to lead chloride based method, using the above optimized cell structure, two-step deposition method and adduct methodology approaches have been studied. Cell parameters of the devices are given in Table 4.4. It is seen that two-step and adduct approaches yield an obvious enhancement in open circuit potential of the cells while current densities are almost same. In order to identify the origin of this situation, SEM studies have been conducted on the devices and are given in Figure 4.11. It is seen from the SEM images that one-step route leads to formation of a non continuous and island like perovskite film formation. Two step method yields formation of cuboids and adduct methodology gives the smoothest films with full coverage on the top of the films. Reduction of the open circuit potential in one-step method may be explained in terms of a shunt between electron transporting TiO_2 layer and the gold contact which is avoided in two step and adduct methods. However, this situation has little effect on the fill factor and current densities. It is known that PbCl_2 one step route can be used in open air atmosphere and other two methods are more appropriate for deposition in an inert environment in contrast to method in this work.

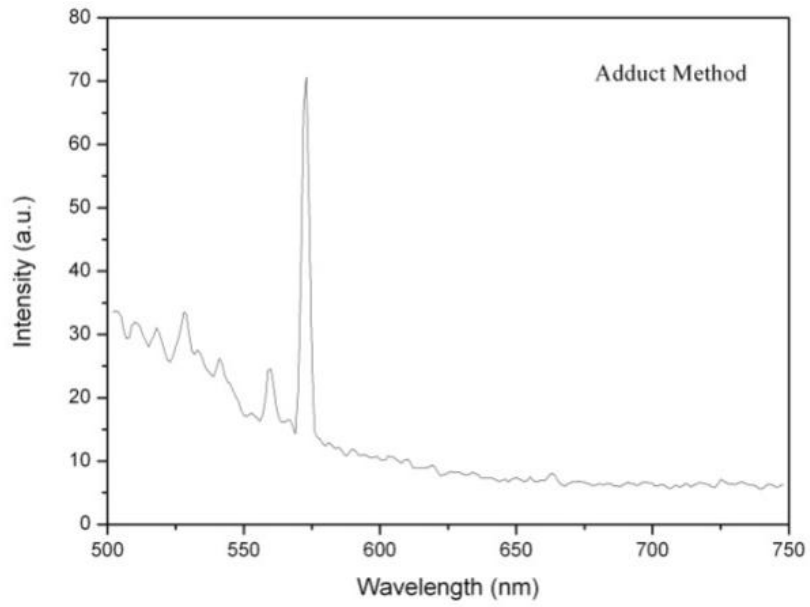
In order to determine the crystal structure of the perovskite layers and possible impurities which may form due to deposition under open atmosphere conditions, XRD analysis was performed on perovskite layers deposited on glass substrates by adduct method and two step method and given in Figure 4.12a,b. It is seen that perovskite layers deposited by adduct method show crystalline $\text{CH}_3\text{NH}_3\text{PbI}_3$ structure without any secondary phases, however layers produced by two step method show residual PbI_2 inside the structure. The photoluminescence spectra of the perovskite layer produced by adduct method (Figure 4.12c) reveals that layer shows strong emission peak at 573 nm upon excitation with a 420 nm laser. There is no additional emissions in the longer wavelengths indicating the absence of native defects inside the structure.



a)

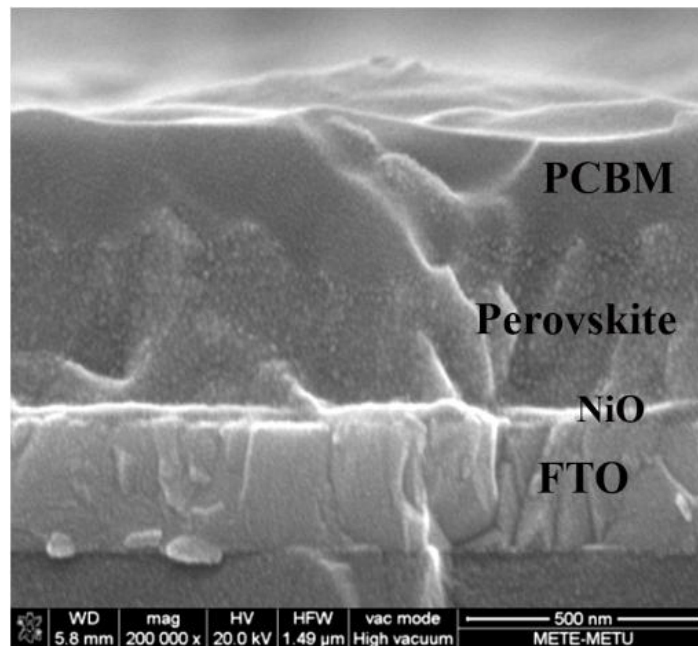


b)

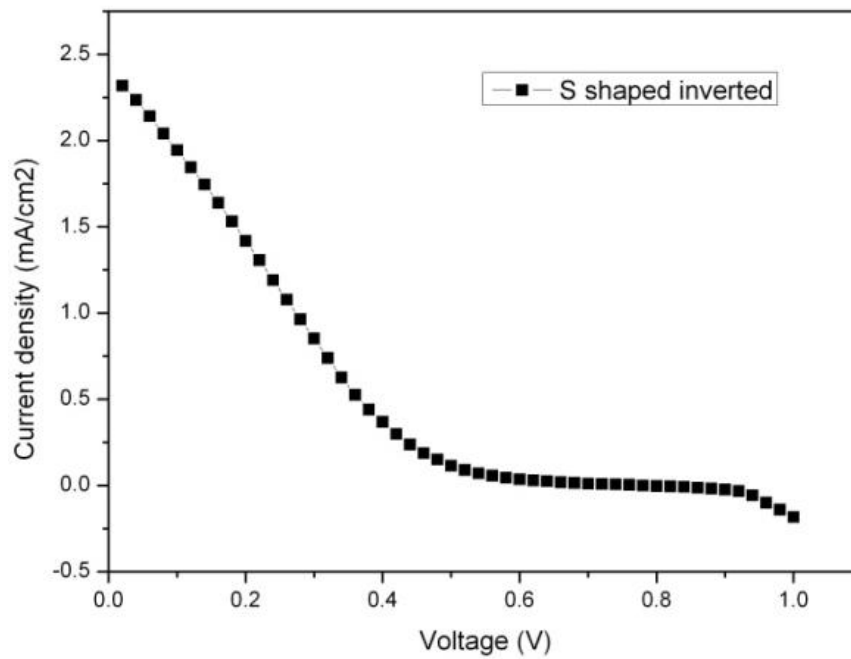


c)

Figure 4.12 XRD of perovskite layers on glass substrates deposited by adduct method (a) and two step method (b) and photoluminescence spectra of the adduct perovskite layer (c).



a)



b)

Figure 4.13 SEM image (a) and J-V curve (b) of the inverted type solar cell.

In order to employ Li:NiO thin films produced during the study in perovskite solar cells, inverted type solar cells were constructed where NiO layers were deposited on

ITO glass, on which perovskite layer was deposited by adduct method and PCBM layer was deposited on top. In Figure 4.13b, a typical J-V characteristic of an inverted type solar cell is given and it is seen that a strong S-shaped J-V characteristic is seen. This type of behaviour is mostly related to charge accumulation and injection resistance at selective contacts in this case PCBM/Au interlayer, which arises from poor adhesion or sticking problems associated with two layers.

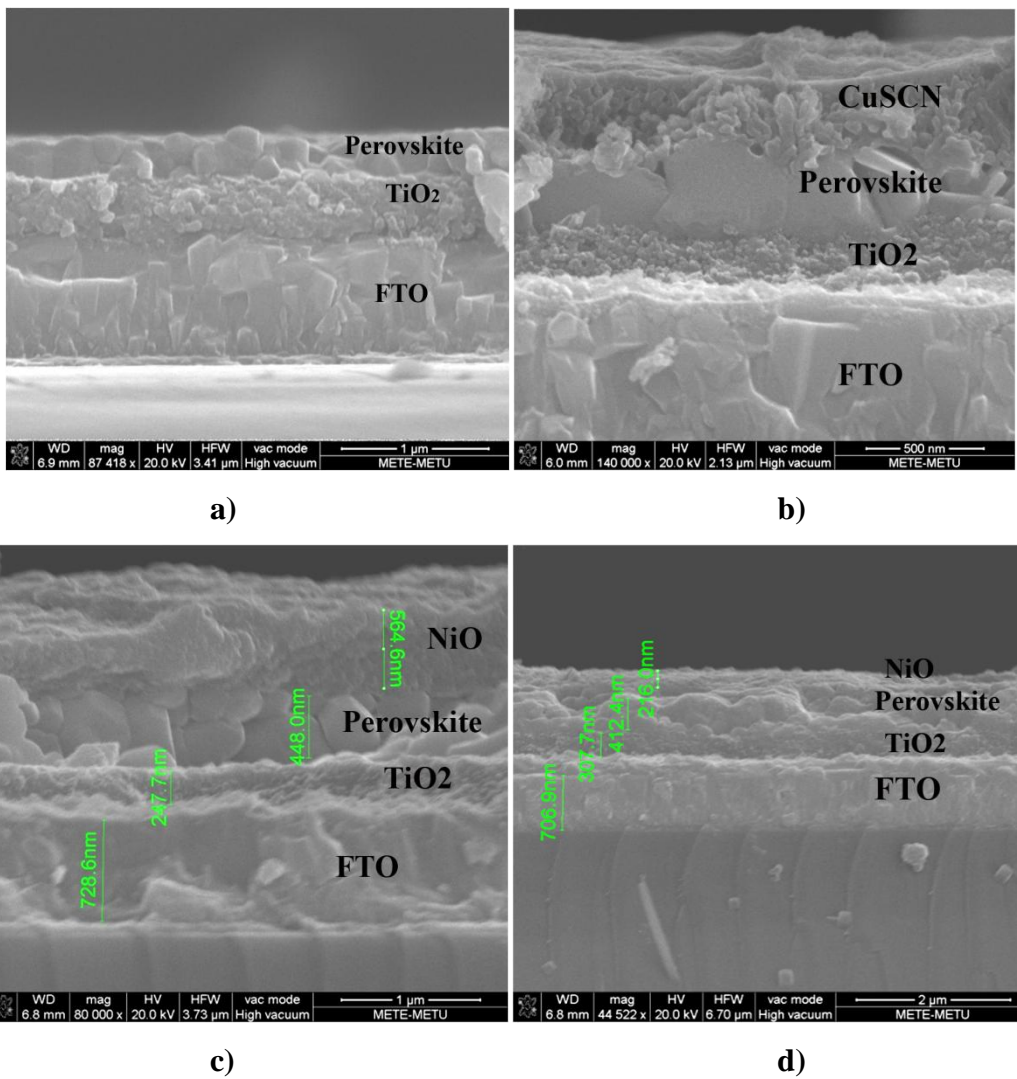
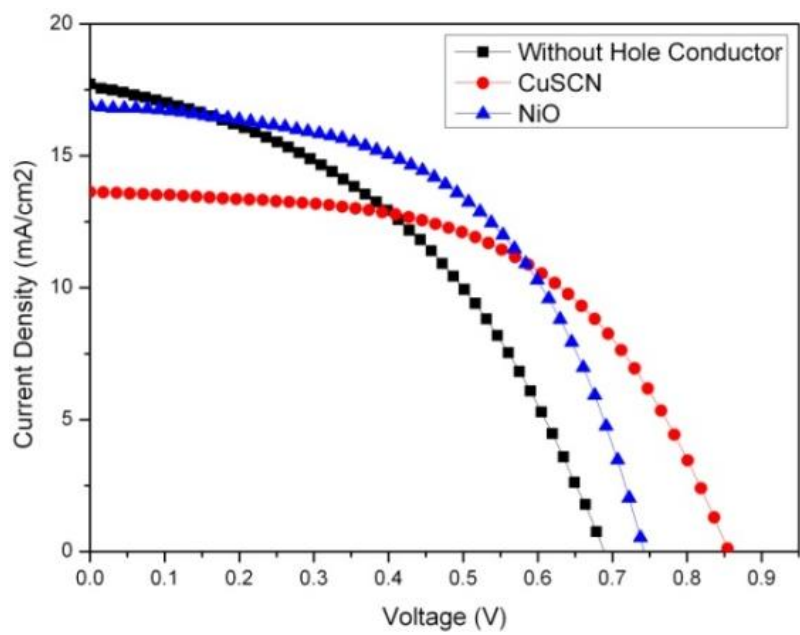


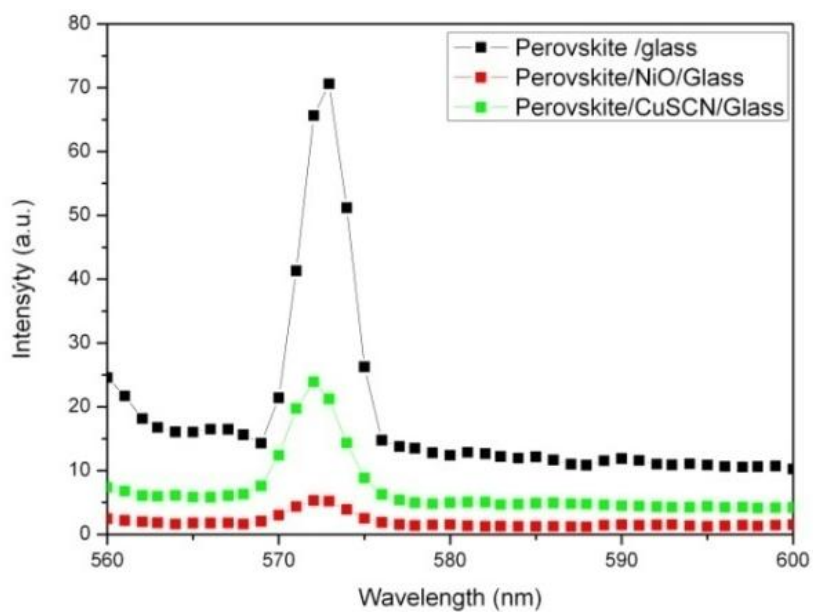
Figure 4.14 SEM images of solar cells without hole conductor (a), with CuSCN (b) and with nickel oxide layer (c,d).

For conventional non-inverted type solar cells, a thin blocking and mesoporous TiO_2 layers were deposited on FTO glass and perovskite layer was deposited by adduct method. From Figure 4.14a, such layer can be seen as perovskite layer infiltrated into TiO_2 and as a capping layer on top of it. In Figure 4.14b, a layer of CuSCN can be on the perovskite capping layer with a thickness of 200 nm approximately. For NiO layers deposited from colloidal suspension, it is seen from Figure 4.14c,d that a non-homogeneous coating ranging between 200-550 nm is present.

In Figure 4.15 a and Table 4.5, d evic parameters of cells has been given. Upon coating the hole conductor free devices with hole conductor NiO and CuSCN, both fill factor and open circuit voltages are enhanced simultaneously. However, such thick layers also hinders electronic transport and leads to reduction in short circuit current and adds unwanted series resistances. From PL quenching measurements in Figure 4.15b, it is seen that NiO can quench perovskite more efficiently than CuSCN, however, highest value has been obtained with CuSCN based device as a more homogeneous layer could be achieved compared to NiO based cell.



a)



b)

Figure 4.15 J-V curves (a) and PL spectra (b) of nickel oxide, CuSCN and hole conductor free cells.

Table 4.5 Cell parameters of perovskite solar cells employing nickel oxide, CuSCN and hole conductor free configuration.

Device	V_{oc} (V)	J_{sc} (mA/cm ²)	Fill factor	Eff.(%)
Hole conductor free	0.72	17.72	0.40	5.09
Nickel oxide	0.75	16.80	0.53	6.67
CuSCN	0.85	13.63	0.61	7.06

4.4 Conclusions

Nanoparticulate Li doped NiO particles and thin films have been successfully produced during the studies and characterized by means of structural and electrical properties. Particles and films with enhanced electrical conductivity were produced and according to XRD measurements, possess pure NiO structure, which confirms successful Li doping. Produced particles and films were employed as hole conducting mediums in inverted and conventional mesoporous structured perovskite solar cells. Although inverted type cells yielded poor efficiencies which was related to insufficient charge transfer efficiencies between individual layers, nanoparticles of NiO, which were deposited on perovskite solar cells with n-i-p configuration, possess promising performance compared to other inorganic hole conductors like CuSCN. For this reason, production techniques and deposition conditions of NiO nanoparticle dispersions in n-i-p configured cells were studied in depth for optimization and enhancing the device performance. Details of the NiO nanoparticle based perovskite solar cells are given in the next chapter.

REFERENCES

1. U.S. Joshi, Y. Matsumoto, K. Itaka, M. Sumia, H. Koinuma, Combinatorial synthesis of Li-doped NiO thin films and their transparent conducting properties, *Appl. Surf. Sci.*, 252 (2006) 2524–2528.
2. K.C. Liu, M.A. Anderson, Porous Nickel Oxide/Nickel Films for Electrochemical Capacitors, *J. Electrochem. Soc.*, 143 (1996) 124–30.
3. Y.D. Wang, C.L. Ma, X.D. Sun, H.D. Li, Preparation of nanocrystalline metal oxide powders with the surfactant-mediated method, *Inorg. Chem. Commun.*, 5 (2002) 751–5.
4. L. Xiang, X.Y. Deng, Y. Jin, Experimental study on synthesis of NiO nanoparticles, *Scripta Mater.*, 47 (2002) 219–24.
5. E.R. Beach, K.R. Shqaue, S.E. Brown, S.J. Rozesveld, P.A. Morris, Solvothermal synthesis of crystalline nickel oxide nanoparticles, *Mater. Chem. Phys.*, 115 (2009) 373–9.
6. S. Deki, H. Yanagimoto, S. Hiraoka, NH₂-Terminated Poly(ethylene oxide) Containing Nanosized NiO Particles: Synthesis, Characterization, and Structural Considerations, *Chem. Mater.*, 15 (2003) 4916–22.
7. H. Sato, T. Minami, S. Takata, T. Yamada, Transparent conducting p-type NiO thin films prepared by magnetron sputtering, *Thin Solid Films*, 236 (1993) 27–31.
8. H. Moulki, D.H. Park, B.K. Min, H. Kwon, S.J. Hwang, J.H. Choy, T. Toupance, G. Campet, A. Rougier, Improved electrochromic performances of NiO based thin films by lithium addition: From single layers to devices, *Electrochim. Acta* 74(2012) 46–52.
9. H. A. Juybaria, M. M. Mohagheghia, M. S. Saremi, Nickel–lithium oxide alloy transparent conducting films deposited by spray pyrolysis technique, *J. Alloys Compounds*, 509 (2011) 2770–2775.

10. W. Chia-Ching, Y. Cheng-Fu, Investigation of the properties of nanostructured Li-doped NiO films using the modified spray pyrolysis method, *Nanoscale Res. Lett.*, 8 (2013) 33.
11. I.A. Garduno, J.C. Alonso, M. Bizarro, R. Ortega, L. Rodriguez-Fernandez, A. Ortiz, Optical and electrical properties of lithium doped nickel oxide films deposited by spray pyrolysis onto alumina substrates, *J. Cryst. Growth*, 312 (2010) 3276–3281.
12. V. Gowthami, P. Perumal, R. Sivakumar, C. Sanjeeviraj, Structural and optical studies on nickel oxide thin film prepared by nebulizer spray technique, *Physica B*, 452 (2014) 1–6.

CHAPTER 5

NICKEL OXIDE NANOPARTICLES FOR n-i-p STRUCTURED PEROVSKITE SOLAR CELLS

5.1 Introduction

Organo-lead halide perovskite based solar cells have been breakthrough photovoltaic materials recently achieving outstanding power conversion efficiencies around 20% [1,2]. Simple production routes and cheap raw materials for construction are distinct features of these devices and attracting researchers around the world and photovoltaic industry. In simplest form, the structure is a multilayer stack of light absorbing perovskite layer sandwiched between electron and hole selective contacts. Efforts have focused on deposition of crack and void free dense perovskite layers with maximum grain sizes and several deposition methods like solvent engineering [3,4], additive assisted deposition [5,6] and two step techniques[7,8] have been developed yielding grain sizes up to millimeter scale. Detailed analysis of defect structure for achieving defect free perovskite layers by suitable additives[9] and compositional engineering [10] approaches modifying the band structure of the perovskite layers lead to highly efficient and stable solar cells. Apart from engineering of the perovskite layer, charge selective contacts play a critical role in extracting charge carriers from absorber layer and in turn energy harvesting. Engineering of the extraction layers is a key parameter for efficient charge collection and harnessing of the maximum photovoltage attainable from the cell as proved by former studies [11-13]. N-type electron transport layers in perovskite solar cells are mostly semiconducting metal oxides like TiO_2 and ZnO for n-i-p configurations while counter p-type hole transport layers are mostly polymeric materials like spiro-OMETAD, P3HT and MEH-PPV [14]. Although

organic conjugated polymers can provide high efficiency values, the dilemma is the long term instability and higher cost of these materials.

Inorganic metal oxide p- type layers offer long term stability and abundance when cooperated in optoelectronic devices including OLEDs[15] as well as organic solar cells [16]. Nickel oxide (NiO) as the most appropriate p–type candidate, has been employed as hole transport layer in perovskite solar cells in inverted devices as a replacement for PEDOT:PSS as well as scaffolding layer in mesostructured [17] and carbon counter electrode based cells [18]. NiO based hole conductors are preferable to PEDOT:PSS due to hygroscopic nature of PEDOT:PSS and improved electron blocking ability is also expected for NiO having higher conduction band edge. Long term stability have already been demonstrated and great progress is going on the research of NiO based perovskite solar cells. Deposition of NiO layers were conducted by sol-gel spin coating methods [19,20], magnetron sputtering [21], spray pyrolysis [22] and pulsed laser deposition [23] so far. However, all these devices were constructed in p-i-n configuration inverted type concept [24,25] and unavoidably require a counter n-type electron transport layer, mostly PCBM, which is also a polymeric substance. You et al. [26] sandwiched the perovskite layer between solution processed NiO and a spin casted ZnO nanoparticulate layer on top of perovskite layer in an inverted cell. However, such a concept has not been studied in depth for n-i-p configuration yet, in which expensive and low stability spiro OMETAD and PTAA are the most widely preferred choices.

Inorganic hole conductors like CuSCN [27], FeS [28], and CuI [29] have been employed as hole conducting layers in n-i-p configuration and n-i-p NiO was demonstrated in a flexible cell [30]. The main difficulty of using two metal oxide layers arises from the fact that any solvent (water, DMF, 2-methoxyethanol) used for dispersing the metal oxide particles also has high solubility for perovskite layer itself, which in turn washing it away during spin coating. In addition, any residual surfactants used to stabilize the dispersions, may inhibit charge transfer between

particles as there is no way to remove those impurities other than high temperature treatment which is not possible on a perovskite deposited substrate.

In this work, a NiO nanoparticulate dispersion has been prepared in isopropanol without using surfactant or additives and deposited on top of perovskite layer at room temperature as the hole transport layer in a mesoscopic n-i-p cell for polymeric component free perovskite solar cell applications. We investigated size distribution of NiO nanoparticles produced by a precipitation technique and subsequent ball milling on the dispersibility in isopropanol and thickness of the deposited NiO layer on the device performance.

5.2 Experimental Studies

5.2.1 NiO nanoparticle dispersion preparation

NiO nanoparticles were synthesized by precipitation of 0.1M nickel acetate tetrahydrate (99%, Aldrich) aqueous solution with 10M NaOH aqueous solution. After adding the NaOH solution dropwise until no precipitation was observed, the precipitate was washed three times with DI water by centrifugation. Clean precipitates were dried at 100°C overnight and fired at 250°C, 300°C and 400°C for 5 min. Ball milling was conducted in a glass vial containing 2 mm zirconia balls and isopropanol. The ball to isopropanol to powder ratio was set as 25:1:1 by weight. Effect of milling time on particle size and distribution was studied. For spin coating, NiO particles were suspended in isopropanol (2% by weight) applying ultrasonic treatment for 1 h and stirring overnight.

5.2.2 Cell construction

All chemicals were used as purchased without purification. FTO glass substrates (10 ohm/sq Pilkington) were etched with zinc powder and 2M hydrochloric acid. Etched substrates were thoroughly cleaned in detergent, deionized water, acetone and

isopropanol. TiO₂ blocking layer was deposited on UV-Ozone treated substrates by spin coating (2000 rpm, 30 s) a solution of 0.15M titanium diisopropoxide bis(acetylacetonate) (75 wt% in isopropanol, Aldrich) dissolved in n-butanol. After drying at 125°C, a solution of titania paste (Dyesol NRT-18) dissolved in ethanol (1:3 weight) was spin coated at 2000 rpm for 10 s. After drying at 125°C and firing at 500°C, films were treated with 0.02M TiCl₄ aqueous solution at 90°C for 10 min and fired at 500°C again. For deposition of perovskite layer, adduct method was followed [31]. PbI₂ (99%, Aldrich), CH₃NH₃I (Dyesol) and dimethyl sulfoxide (99.5%, Aldrich) were dissolved in N,N-dimethylformamide (99.8% anhydrous, Aldrich) with a molar ratio of 1:1:1. Prepared solution was filtered through a 0.2 micron PTFE syringe filter and spin coated on the substrates at 4000 rpm for 25 s. During the fifth second of spinning, 0.5 ml diethyl ether (99.5%, Aldrich) was poured at once on the substrates. Transparent films were further crystallized at 100°C for 5 min which resulted in shiny black perovskite films. Prepared NiO/isopropanol dispersion was spin coated on the perovskite films at different spinning rates. The dispersion was dispensed on the film during spinning in order to minimize exposure duration of isopropanol to the perovskite layer. All depositions were conducted under laboratory conditions in a relative humidity between 30-40%.

5.2.3 Characterizations

X-ray diffraction patterns were recorded by Rigaku D/MAX 2200/PC using Cu K α radiation. Morphology of powders and devices were characterized using scanning electron microscopy (FEI Quanta 400 FEG equipped with EDX analyzer). Chemical and electronic analysis of the powders were conducted using X-ray photoelectron spectroscopy and ultraviolet photoelectron spectroscopy (UPS) (PHI 5000 VersaProbe). Surface area and particle sizes were analyzed by Brunauer–Emmett–Teller (BET) method using a Quantachrome Autosorb-6 and laser diffraction technique using helium neon laser red light (Malvern Mastersizer 2000). Photoluminescence (PL) data was recorded by a fluorescence spectrophotometer (Cary Eclipse) at an excitation wavelength of 420 nm. J-V curves of the cells were

recorded by a Yokogawa GS610 source measure unit under simulated AM 1.5 conditions using Newport solar simulator 67005. Active area of the cells were set at 0.07 cm^2 with the same mask used for gold evaporation. Electrochemical impedance spectroscopy was conducted using Gamry reference 3000 under illumination with white LED light (60 mW/cm^2) and fitting was conducted by Echem analyst software.

5.3 Results and discussion

In case of thin film solar devices, transport layers are kept in a thickness range varying from 50 nm to 200 nm for minimizing charge transfer resistances. For a nanoparticulate hole transport layer, it is essential to synthesize particles lower than 200 nm and free of agglomeration. Homogeneous layers can only be deposited from fine particle non-agglomerated dispersions because stability of the dispersion can only be achieved by particles smaller than a critical particle size. For most nanoparticle systems, particle size and degree of agglomeration primarily depend on heat treatment temperature and duration. NiO particles synthesized by precipitation were heat treated at 250°C , 300°C and 400°C in order to determine the minimum NiO formation temperature. Duration of the heat treatment was set to only 5 min to minimize particle growth.

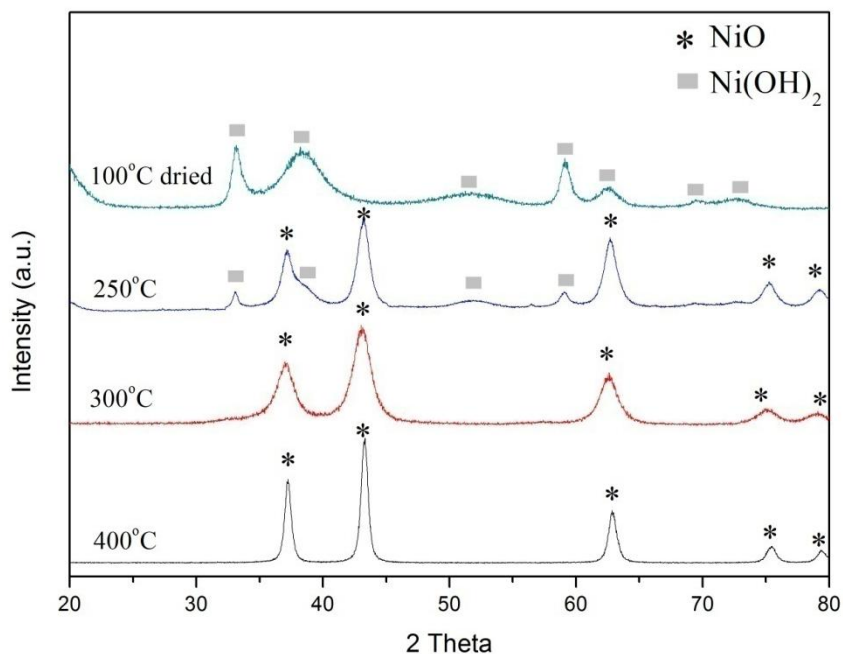


Figure 5.1 XRD spectra of NiO powders heat treated at different temperatures.

According to XRD spectra of powders given in Figure 5.1, as synthesized particles after drying are pure nickel hydroxide ($\text{Ni}(\text{OH})_2$) where peaks observed at 33.1° , 38.5° , 51.7° , 59.3° , 62.8° , 69.5° and 73.1° can be indexed to (100), (011), (012), (110), (111), (013) and (021) planes (JCPDS 14-0117), respectively. Upon increasing the temperature to 250°C , peaks associated with $\text{Ni}(\text{OH})_2$ vanishes dramatically and new peaks observed at 37° , 43.2° , 62.5° , 75.3° and 79.1° are assigned to (111), (200), (220), (311) and (222) planes of cubic rock salt structure NiO (JCPDS 78-0429). However, structure is a mixture of $\text{Ni}(\text{OH})_2$ and NiO. Fully conversion to NiO cubic structure completes at 300°C . Further increasing the temperature leads to narrowing of the peak width indicating particle size growth. The XPS spectra of the particles produced at 300°C is given in Figure 5.2 and 5.3. The deconvolution of electron binding energies to Gaussian fit for O 1s core levels for NiO and Ni_2O_3 were observed at 529.7 eV and 531.90 eV, for Ni $2p_{3/2}$ core levels binding energies for NiO and Ni_2O_3 are 854 eV and 855.8 eV, respectively [32].

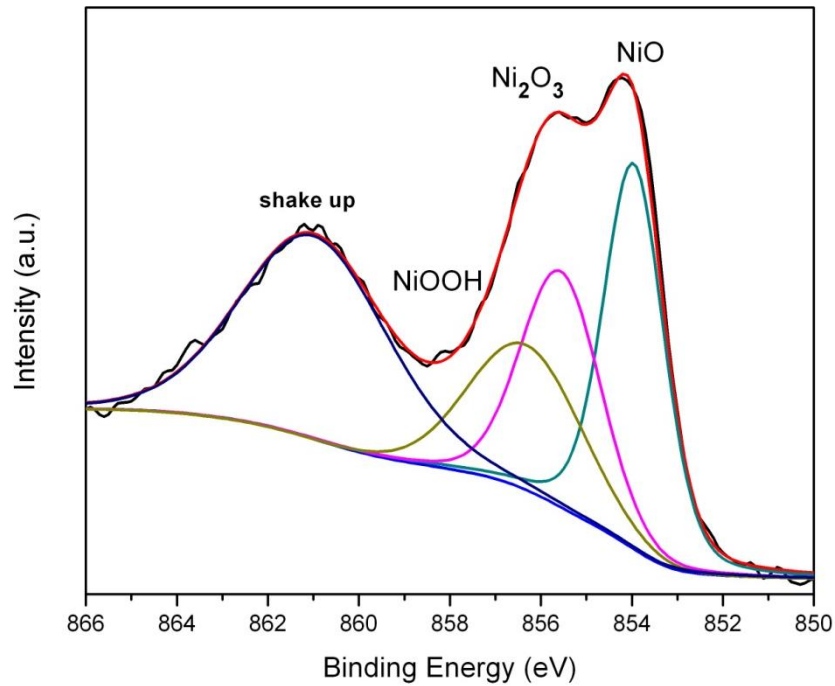


Figure 5.2 XPS spectra of powders heat treated at 300°C for 5 min showing Ni 2p core levels.

Presence of NiOOH can be related to surface adsorbed H₂O and formation of the hydroxides. Ni⁺³ ions in the structure show that there is excess oxygen or nickel deficiency which compels Ni⁺² to Ni⁺³ valence state. As long as there is no Ni₂O₃ as a secondary phase as seen from XRD results, we conclude that all Ni⁺³ ions are in the nickel oxide lattice and it is more appropriate to denote this compound as NiO_x. Actually, excess oxygen and Ni⁺³ ions in the lattice is the major reason governing p-type characteristics of NiO films which is quite beneficial by means of hole transport during device operation while pure stoichiometric NiO is a perfect insulator [33].

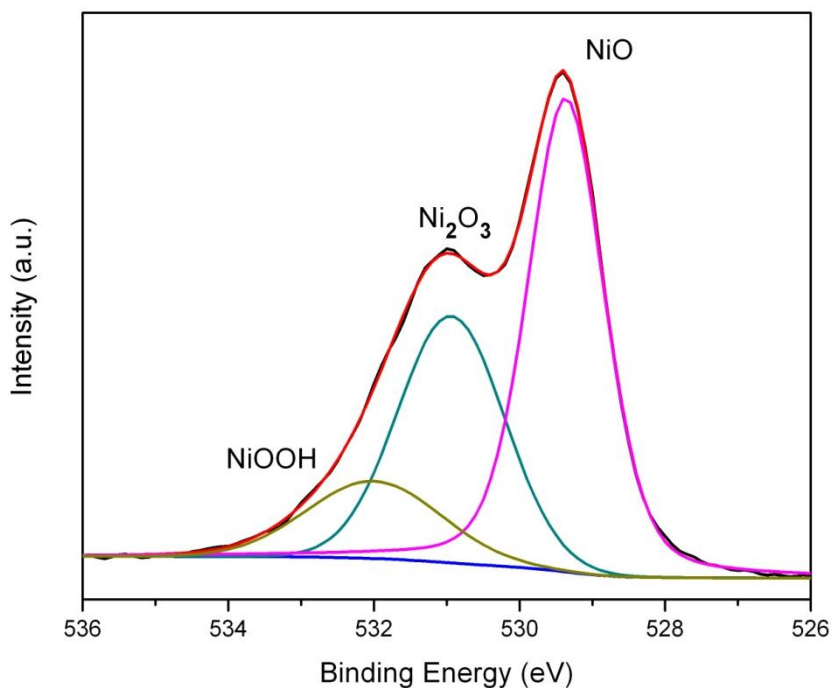


Figure 5.3 XPS spectra of powders heat treated at 300°C for 5 min showing O 1s core levels.

Determination of the actual particle size was carried out by BET surface area measurements and laser diffraction techniques. As synthesized particles possess high surface area reaching 236 m²/g and upon heat treatment at 250°C, surface area decreases to 186 m²/g. Powders exhibiting pure NiO structure at 300°C have a surface area value of 179 m²/g, slightly lower than 250°C. Table 5.1 summarizes BET surface area values and corresponding particle size values (D) extracted from BET measurements. Such high surface area values indicate very small particle sizes, however do not give any information about degree of agglomeration which can be detrimental to dispersion dynamics. Particle size distribution of nanoparticles heat treated at 300°C and subsequently ball milled for different durations is given in Figure 5.4. Without milling, particles possess wide size distribution from hundreds of nanometers up to 80 microns.

Table 5.1 BET surface area and corresponding particle size values of NiO nanopowders heat treated at different temperatures.

Heat treatment temperature (°C)	Specific surface area (m²/g)	Calculated particle size (nm)
100	236	3.8
250	186	4.8
300	179	5
400	110	8.1

According to BET measurements, expected particle size is about 5 nm, however, due to strong agglomeration, particles tend to come together forming large aggregates behaving like individual particles. Upon ball milling, these agglomerates are broken into smaller clusters and mean particle size is reduced to 2 micron range after 12 h of milling. Further extending the milling duration to 24 h ends up with particle size reduction down to 170 nm, which is small enough to suspend the particles in the dispersion. However, this value is still suspicious and must be distinguished from actual particle size or in this case crystallite size. Actual particle size is far less than this value as revealed by BET measurements, keeping in mind that resolving smaller individual particles is beyond the detection limit of laser diffraction technique. After a critical milling duration, it is no more possible to deagglomerate the particles into finer particles using milling method. Extending the milling duration has negative effect on the particle size where particle size starts to increase again due to some mechanical alloying effect. The tail in the distribution curve I with a particle size of 800 nm remaining from unbroken particles tend to precipitate at the bottom of the suspension and were removed from suspensions by collecting the supernatant solution. These suspensions were stable up to 3 days and have a 2% by weight NiO nanoparticles, calculated by collecting and weighing the precipitated particles. Non milled powders yield no stable dispersion and precipitate

in minutes. Effect of size reduction in stability of the dispersions is clearly visible from the inlet image given in Figure 5.4.

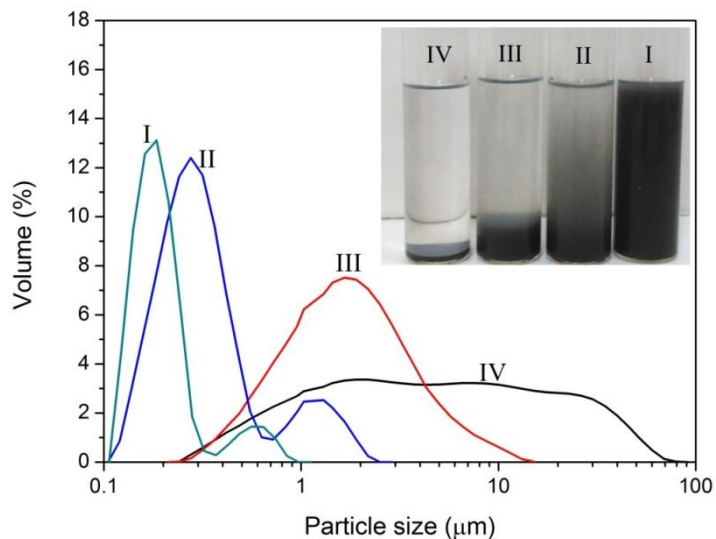


Figure 5.4 Particle size distribution of particles ball milled at 24 h (I), 48 h (II), 12 h (III) and non milled (IV), measured by laser diffraction. The inset image shows dispersions of the powders in isopropanol after storage of 3 days.

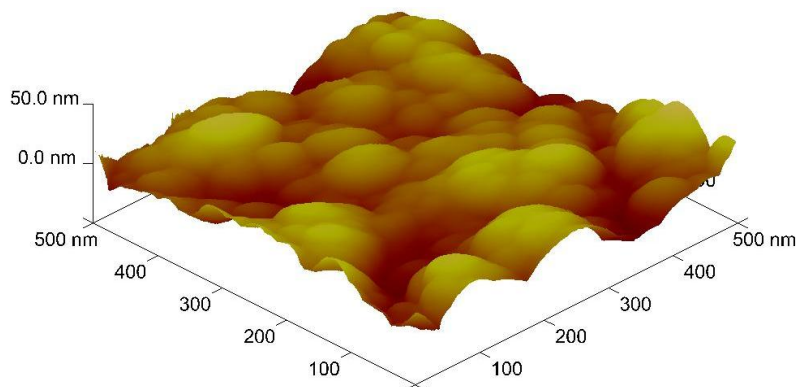


Figure 5.5 3D-AFM image of the powders deposited on glass substrates from stable dispersions.

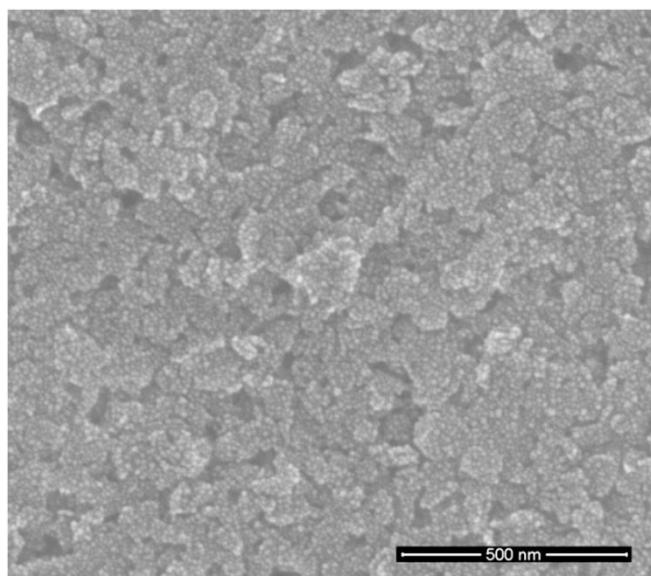


Figure 5.6 High resolution SEM image of the powders after milling for 24 h.

Agglomerates of 50-150 nm can also be seen from 3D-AFM image and high resolution SEM image given in Figure 5.5 and 5.6. Small crystallites of 5-7 nm forming the larger aggregates which were revealed by BET measurements, can be clearly distinguished in TEM image given in Figure 5.7.

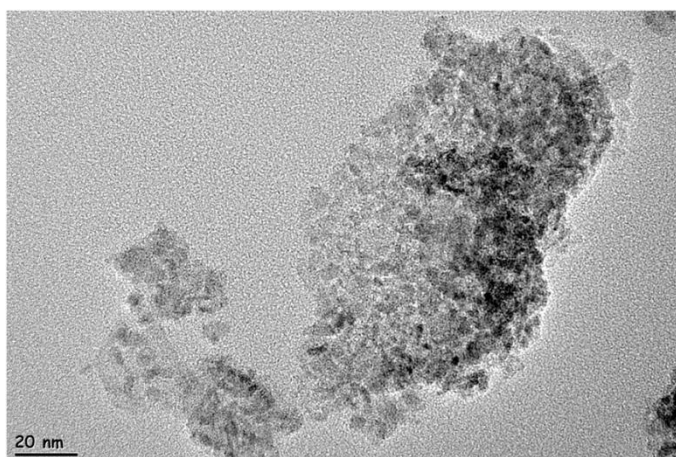


Figure 5.7 TEM image of the agglomerates, revealing the fine crystallite size about 5-7 nm.

Electronic structure of the NiO particles produced at 300°C and ball milled for 24 h were studied by ultraviolet photoelectron spectroscopy (UPS) using HeI emission (21.21 eV). Work function of NiO was extracted from cut-off energy which positions the fermi level to 4.27 eV with respect to vacuum level [34]. Difference between the fermi level and valence band maximum (VBM) was calculated to be 1.11 eV (Figure 5.8) from the onset energy and VBM is placed to 5.38 eV.

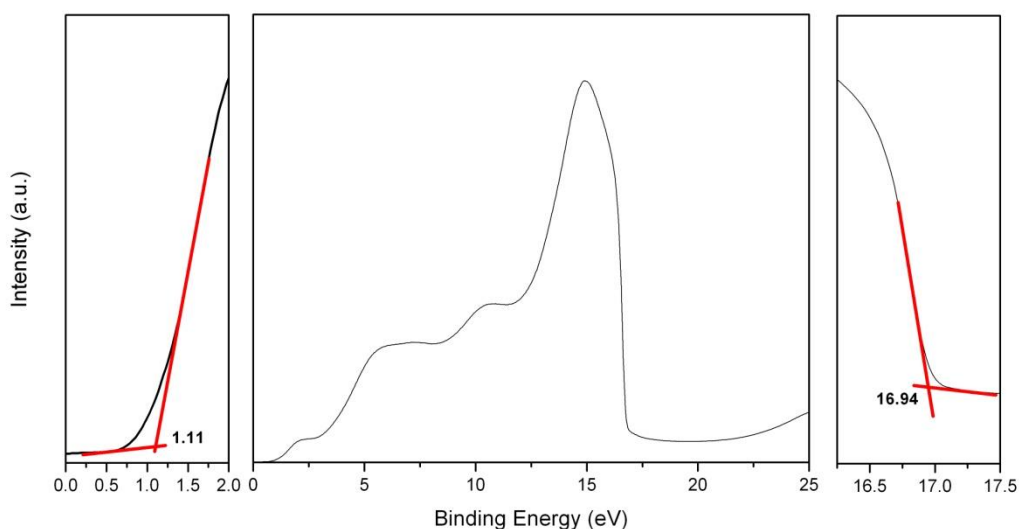


Figure 5.8 UPS spectra of the NiO powders employed in the perovskite cells at the cut-off and onset energies.

Position of the conduction band maximum is found to be 1.70 eV by adding the optical band gap value of 3.68 eV calculated from the Tauc plot given in Figure 5.9 with the light transmission spectrum of the NiO particle coating deposited on glass substrates from stable dispersions by spin coating. The position of fermi level lying 1.11 eV above the VBM which is below the middle of the band gap, justifies the p-type character of the powders as expected from the Ni vacancy formation proved by XPS study.

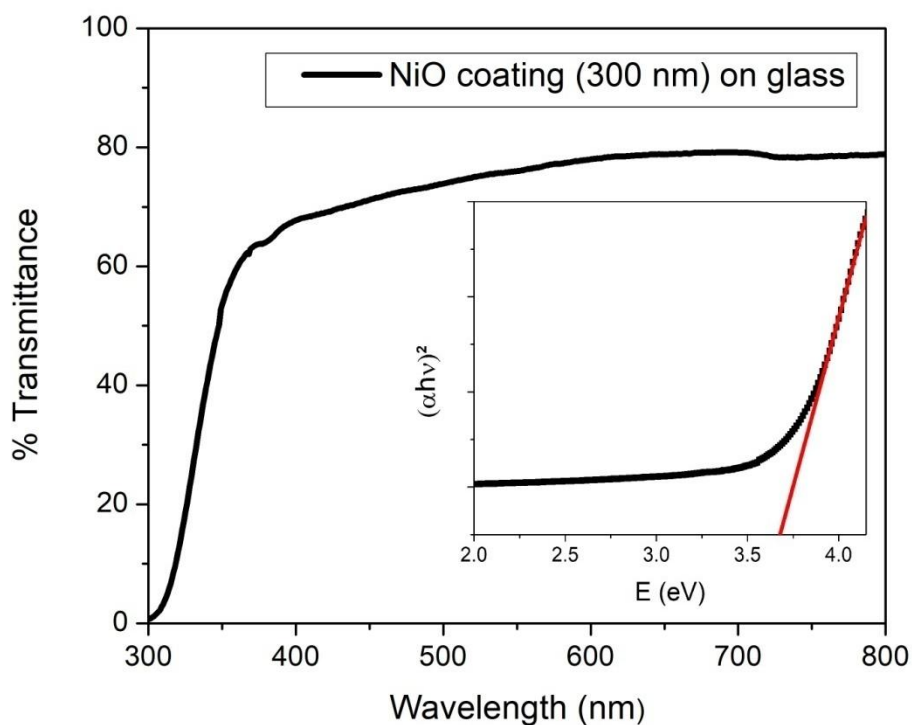


Figure 5.9 UV-Visible light transmission of the powders deposited from isopropanol dispersion on glass substrates and Tauc plot given in the inset image.

The band diagram of the NiO layer calculated in this work is depicted in Figure 5.10 with respect to perovskite layer. It is seen that VBM of the NiO layer and perovskite layer are close to each other with a difference of 0.05 eV. Such a small difference is quite favorable for a photovoltaic device, from point of view of both hole injection from perovskite to NiO and expected open circuit voltage (V_{oc}) loss which, in this case, is negligible.

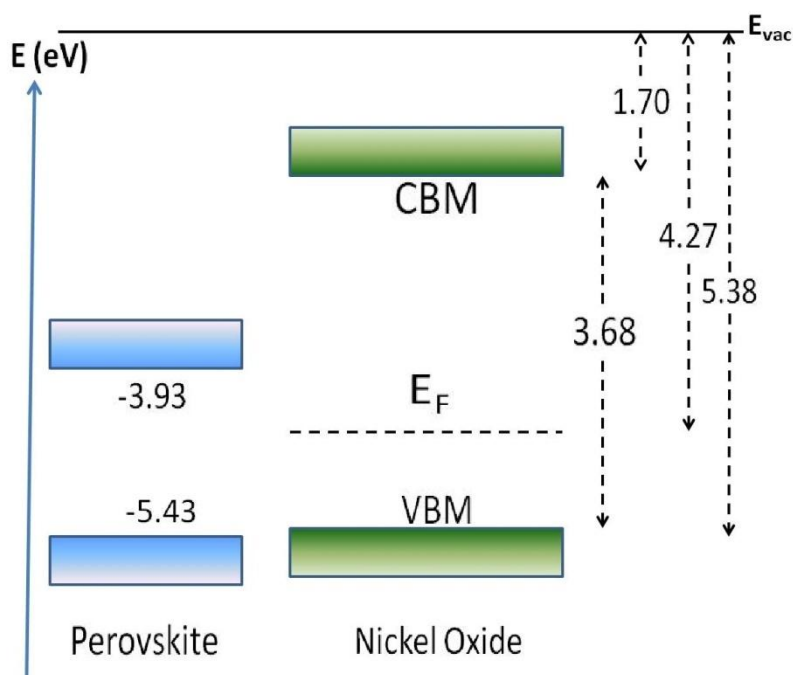


Figure 5.10 Band diagram of nickel oxide particulate films showing the fermi level (E_f), conduction band minimum (CBM) and valence band maximum (VBM) derived from UPS measurements with respect to that of perovskite.

Efficiency of charge transfer from produced NiO particles has been proven by photoluminescence (PL) quenching measurements given in Figure 5.11. The PL intensity of the perovskite layer deposited on glass substrate upon excitation with a laser beam of 420 nm wavelength is strongly reduced with the addition of a NiO layer underneath, indicating efficient hole transfer between NiO and perovskite layers. The large difference between CBMs of NiO and perovskite ensures prevention of electron transfer from perovskite to NiO and manifests NiO as an efficient electron blocker in the cells.

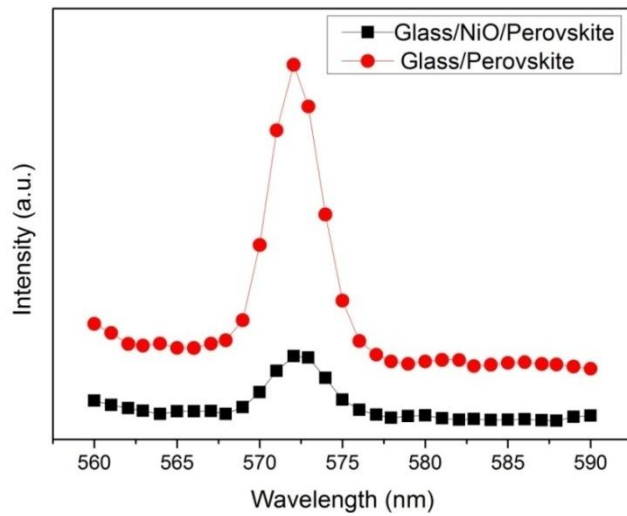


Figure 5.11 Photoluminescence quenching measurements of the perovskite films deposited on bare glass substrates and on the NiO layer.

Stable dispersions were used to deposit NiO nanoparticulate layers on top of a perovskite layer to be employed as a hole conductor layer. Structure consists of a blocking layer and a mesoporous TiO_2 layer, a perovskite layer embedded inside the mesoporous layer and as a separate capping layer. NiO nanoparticles were deposited on top of perovskite layer forming a mesoscopic n-i-p configuration solar device as given in Figure 5.12.

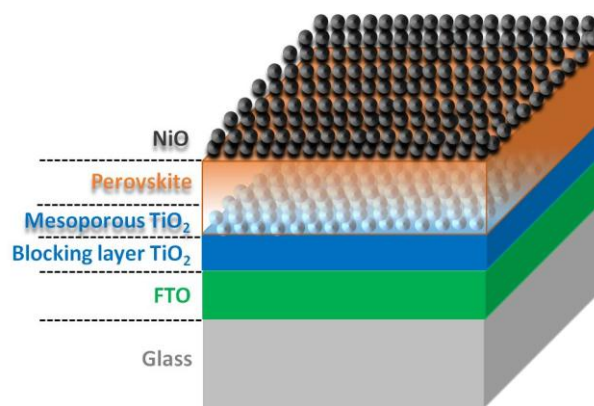


Figure 5.12 Schematic illustration of mesoscopic n-i-p configuration of perovskite solar cell constructed in this work.

For the case of n-i-p configuration, prepared nanoparticle dispersion should be dispensed directly on the perovskite layer, so a restriction for dispersion medium arises because polar solvents used to prepare nanoparticle dispersion also solve the perovskite crystals and damages the perovskite layer. Therefore, common solvents like ethanol, water, methanol, DMF, 2-methoxyethanol cannot be employed for dispersions. In addition, any additive like surfactants, which require high temperature treatment for removal, cannot also be used because perovskite layer restricts again high temperature heat treatment as it undergoes degradation at temperatures above 150°C and residual surfactant molecules inhibit charge transfer between particles. Isopropanol, with a polarity index of 3.9, has intermediate polar character between polar and apolar solvents and is the choice of dispersant medium. From SEM image of the cross section given in Figure 5.13, individual layers can be seen and there is no evidence of physical damage related to perovskite degradation due to isopropanol dispensing.

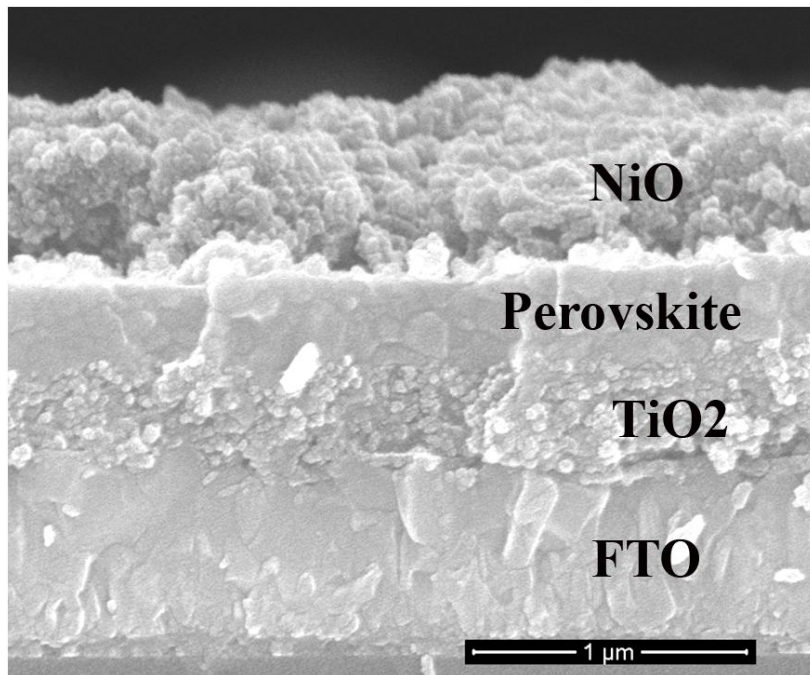


Figure 5.13 Cross sectional SEM image of the cells prepared in this work.

Completed cells after Au evaporation were characterized under AM1.5 conditions and parameters of the cells are shown in Figure 5.14 and tabulated in Table 5.2. Cells without a hole conductor yields an efficiency value of 6.48% due to p-type nature of perovskite layer itself which can hold a depletion layer together with an n-type mesoporous scaffold layer and possess hole conducting ability as evidenced by former studies [35,36].

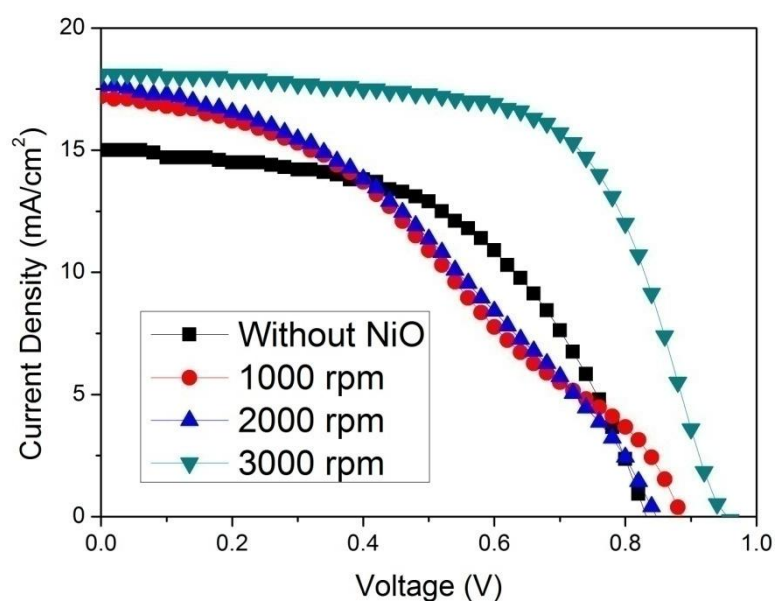


Figure 5.14 J-V curves of the hole conductor free and NiO based cells with different spin speeds under simulated AM 1.5 conditions.

Addition of NiO layer enhances both open circuit voltage and short circuit current simultaneously, however fill factors highly depend on spin speed of the NiO coating. Low spin rates deposit thicker NiO layers and cause resistance for hole conduction revealing itself as an S-shaped J-V characteristics which is mostly related to a problem of interfacial charge transport or excessive resistance [37]. Deposition at a spin rate of 3000 rpm gave the best results obtained in this work with an open circuit voltage of 0.97 which outperforms hole conductor free cell. Fill factor was also risen up to 0.62 yielding an overall efficiency of 10.89% for best cell measured at 500 mV/s under reverse scan (from V_{oc} to J_{sc}) conditions. Further

increasing the spin rate for this dispersion concentration causes inhomogeneous distribution of the NiO particles and it is not possible to deposit continuous films.

Table 5.2 Cell parameters of the devices prepared by different spin speeds of NiO dispersion.

	V_{oc} (V)	J_{sc} (mA/cm ²)	Fill factor	Eff.(%)
1000 rpm (Reverse)	0.89	17.22	0.36	5.51
2000 rpm (Reverse)	0.85	17.41	0.43	6.36
3000 rpm (Reverse)	0.97	18.12	0.62	10.89
3000 rpm (Forward)	0.94	17.43	0.60	9.73
Without NiO (Reverse)	0.83	15.03	0.52	6.48
Without NiO (Forward)	0.74	14.72	0.45	4.94

The strong dependence of fill factor on spin speed and efficiency of the cells can be explained by partially agglomerated character of the particles which allows film thicknesses no smaller than the agglomerate size, which is about 150 nm in this case. The efficiency distribution of 20 NiO based cells produced by a spin rate of 3000 rpm is given in Figure 5.15.

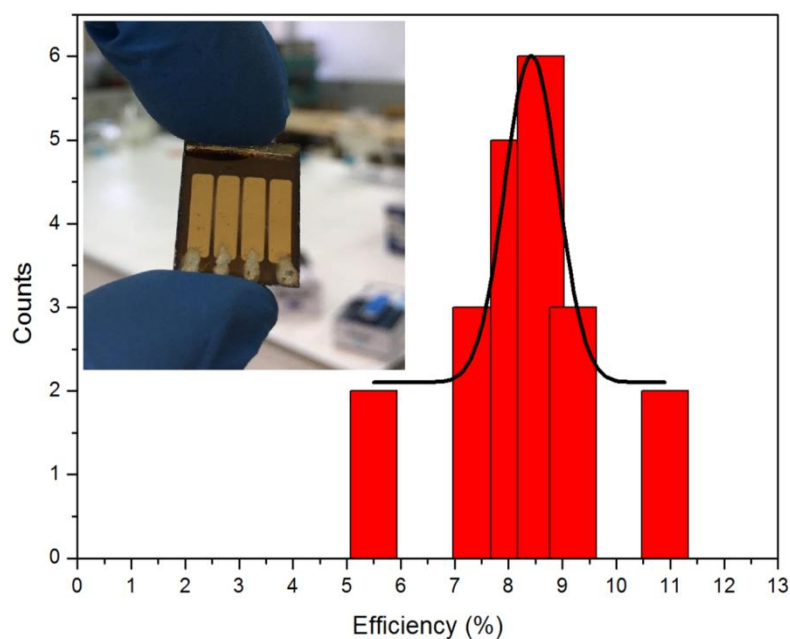


Figure 5.15 Efficiency distribution of NiO based perovskite solar cells deposited by 3000 rpm speed, using the NiO dispersion, calculated from 20 individual cells.

NiO layer not only increases the overall efficiency but also improves hysteresis behaviour observed in perovskite based cells. J-V curves recorded under forward and reverse scan conditions are given in Figure 5.16 and 5.17 for cells with NiO layer and hole conductor free configuration, respectively. NiO based cells exhibit slightly higher V_{oc} value and fill factor when measured in reverse direction compared to forward scan, however this effect is more obvious and clearly affects the overall efficiency for hole conductor free cells.

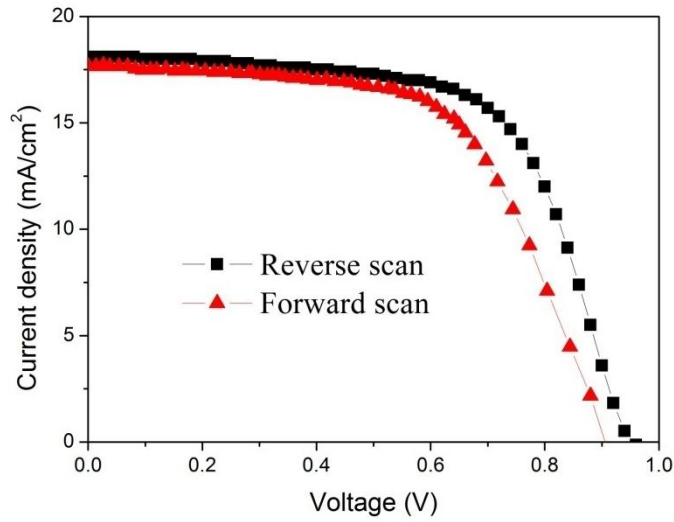


Figure 5.16 Dependence of J-V characteristics of the NiO based cell on scan direction.

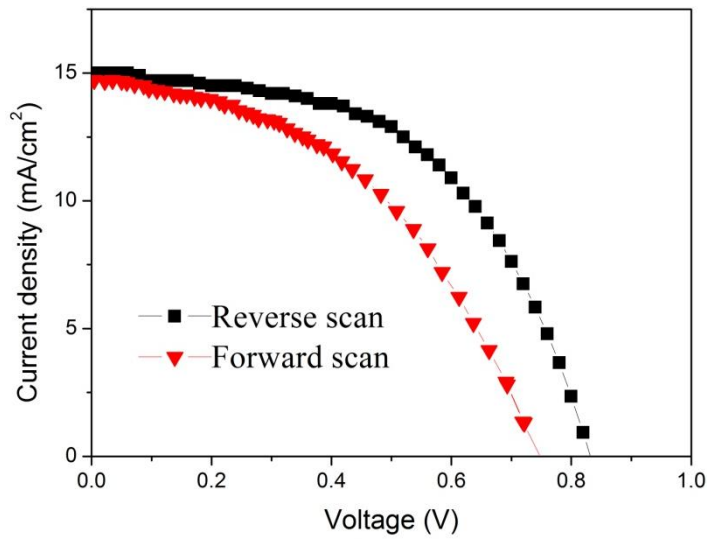


Figure 5.17 Dependence of J-V characteristics of hole conductor free cell on scan direction.

The photocurrent stability of the measurements given in Figure 5.18 also confirms the better performance of NiO based cell by means of stable current output where decline in the photocurrent for hole conductor free cell is severe and deposition of

the NiO layer greatly enhances the output stability of the cells. Origin of hysteresis have been investigated in depth and mostly related to internal defect density of the perovskite layer [38] and charge accumulation between individual layers [39]. NiO layer can effectively extract holes from perovskite layer and enhances the charge collection efficiency which inhibits accumulation of charges inside the perovskite layer and perovskite/Au interface. The remnant hysteresis in NiO based cells can be associated with defects and trap sites in the perovskite layer or small voids present in the nanoparticulate NiO layer. These voids are responsible from the direct contact of Au layer with the perovskite and may lead to shortage inside the cell, however, this situation is not detrimental to cell functioning. On the other hand, prevention of small voids and deposition of a fully compact void free structure would clearly enhance the performance and increase the maximum attainable voltage from cells.

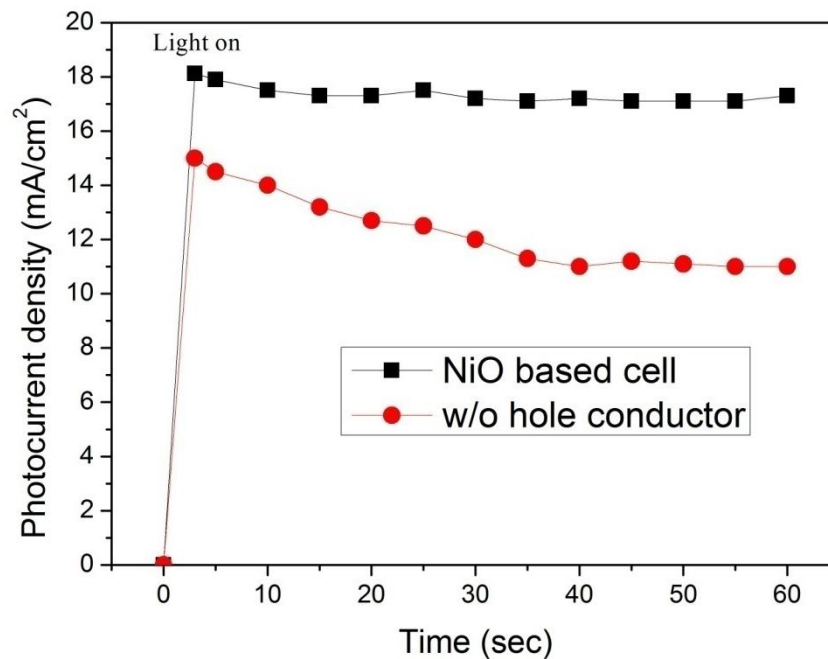


Figure 5.18 Stability of photocurrent density of hole conductor free and NiO based cells under constant illumination of 100 mW/cm² for 1 min.

In order to elucidate the role of NiO layer on device operation in depth, NiO containing and hole conductor free cells were characterized using impedance spectroscopy (IS). IS is a powerful tool to study recombination dynamics and transport phenomena in solar cells and have been employed in characterization of perovskite solar cells. Impedances of the cells were recorded under constant illumination of 60 mW/cm^2 white LED light for different applied bias voltages. In Nyquist plots of the cells at 0V and 0.5V applied bias given in Figure 5.19 and 5.20, two distinct arcs are observed for both types of cells. There are no transmission line or Gerischer feature seen in mesoporous solar cells, due to limited thickness of TiO_2 mesoporous layer deposited in the devices in this work which is no more than 200 nm [40].

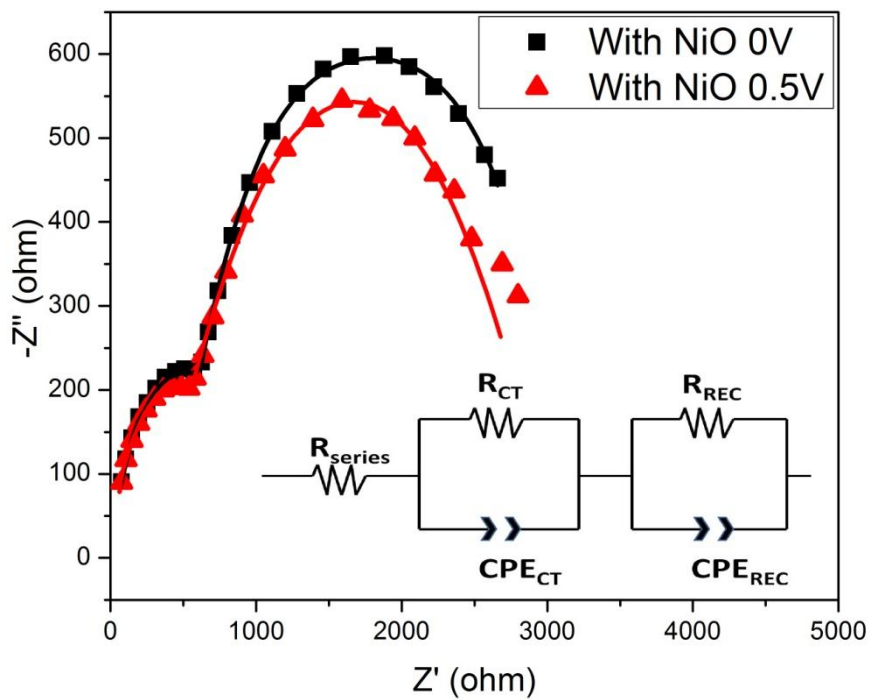


Figure 5.19 Nyquist plots of the perovskite solar cells with NiO layer at 0V and 0.5V. Inset image shows the equivalent circuit model used to fit impedance data.

The impedance spectrum were fitted by a simple equivalent circuit shown in the inset of Figure 5.19. The first arc appearing in high frequency region is related to

charge transfer resistances (R_{CT}) and associated capacitances in the selective contacts (NiO layer and TiO_2 blocking and mesoporous layers) [41,42]. For a better fitting, capacitances are represented with a constant phase element (CPE_{CT}) because both selective contacts may not fully cover the cell and contain pin holes. The low frequency arc is related to recombination resistance (R_{REC}) and capacitance (CPE_{REC}).

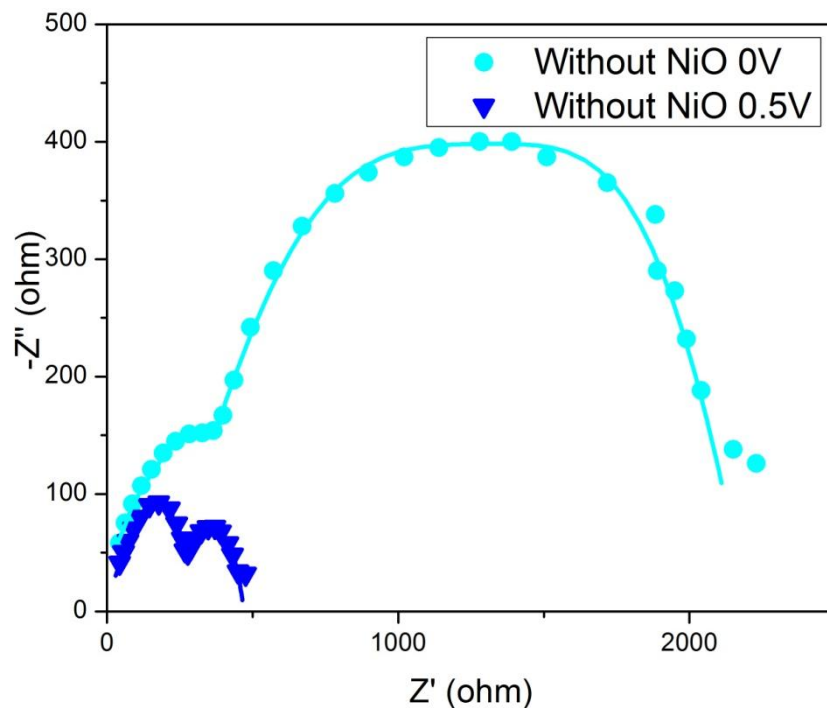


Figure 5.20 Nyquist plots of hole conductor free devices at 0V and 0.5V.

Figure 5.21 shows charge transfer resistances of the cells at applied bias voltages. As long as blocking and mesoporous TiO_2 layers are identical for both cells, charge transfer resistances are determined by hole transfer medium. Addition of NiO hole transport layer introduces a net increase to the charge transfer resistance of the cells at all applied voltages, nearly two fold higher than hole conductor free cell. Nanoparticulate nature of the NiO coating is the main factor for electrical resistance where hopping mechanism is the dominant carrier transport pathway in contrast to dense polymeric hole conductors used in perovskite solar cells. However, actual

contribution of the NiO layer manifests itself as an enhanced recombination resistance given in Figure 5.22.

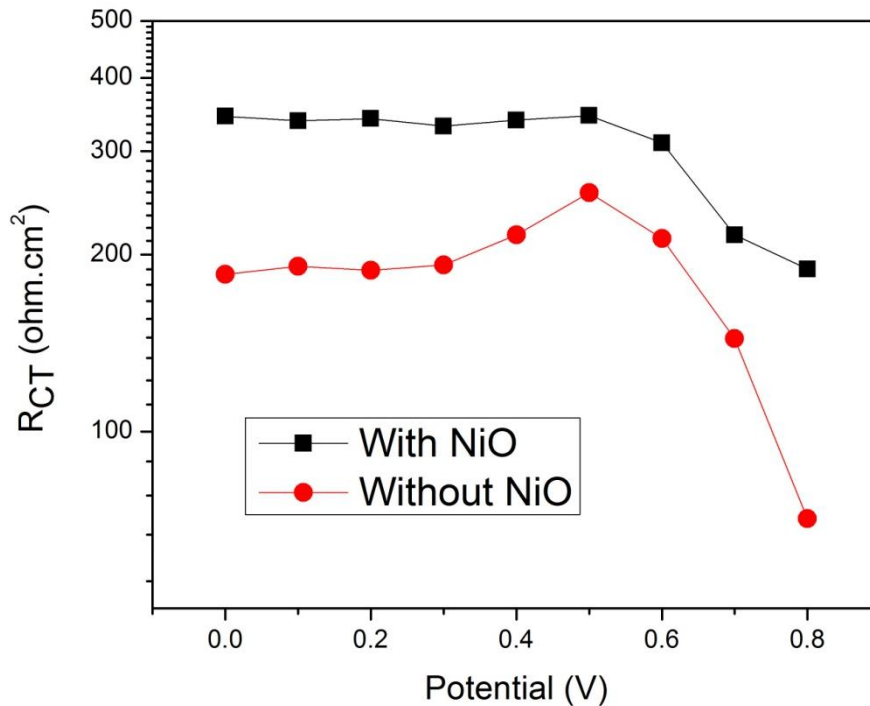


Figure 5.21 Charge transport resistances of two cells with increasing applied voltage.

At all applied voltages, recombination resistance of the cells with NiO layer is higher than the hole conductor free devices. Actually at 0V, hole conductor free cell has a considerable recombination resistance competing with NiO based cell, however as voltage increases, a sharp drop in the recombination resistance occurs. Meanwhile, cells with NiO layer can resist recombination up to 0.7V. This ability of resistance to recombination mostly arises from low electron affinity of NiO which makes it a perfect electron blocking material for perovskite solar cells. Reduced recombination in NiO based cells is the major advantage and leads to the enhancement in V_{OC} and fill factor compared to hole conductor free devices.

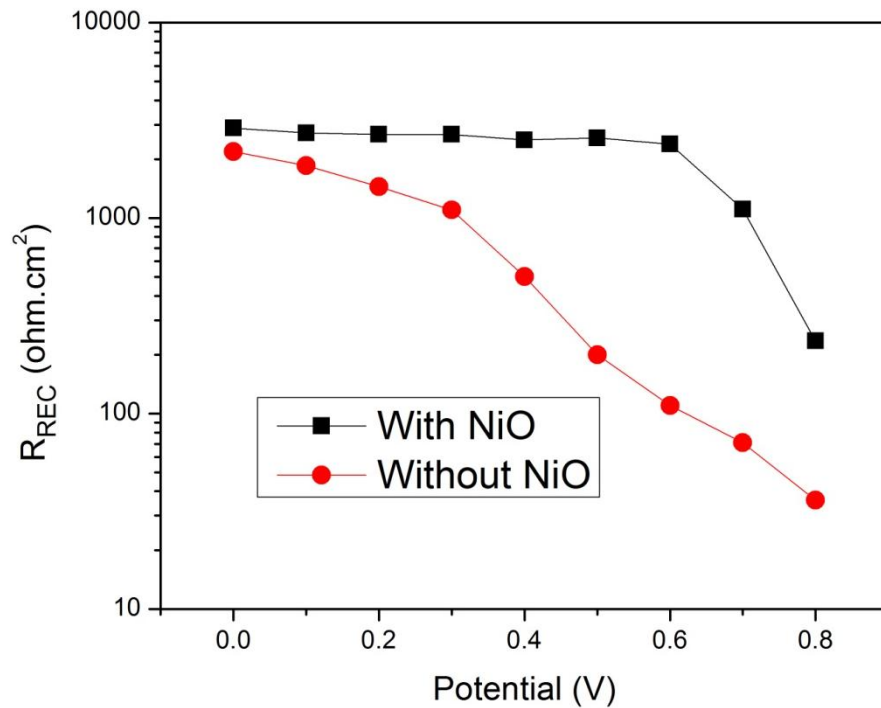


Figure 5.22 Recombination resistances of the cells with increasing applied voltage.

5.4 Conclusions

Overall efficiency of perovskite solar cells was enhanced by addition of a nanoparticulate NiO layer deposited on perovskite layer in mesoscopic n-i-p configuration. Particles produced by precipitation and subsequent ball milling were used to achieve stable dispersions in isopropanol which were used to deposit NiO nanoparticulate layers without damaging the underneath perovskite layer. Addition of the NiO layer strongly enhances the cell characteristics of the devices compared to hole conductor free configuration achieving 10.89% efficiency for the best cell and improves hysteresis characteristics and output stability of the devices. This strategy is believed to be applicable to other metal oxides for charge collection layers in solar cell devices avoiding polymeric charge carrier layers for prolonged stability.

REFERENCES

1. W. Nie, H. Tsai, R. Asadpour, J.-C. Blancon, A.J. Neukirch, G. Gupta, et al., High-efficiency solution-processed perovskite solar cells with millimeter-scale grains, *Science*, 347 (2015) 522–525.
2. O. Ergen, S.M. Gilbert, T. Pham, S.J. Turner, M.T.Z. Tan, M.A. Worsley, et al., Graded bandgap perovskite solar cells, *Nat. Mater.*, 16 (2016) 522–525.
3. N.J. Jeon, J.H. Noh, Y.C. Kim, W.S. Yang, S. Ryu, S.I. Seok, Solvent engineering for high-performance inorganic–organic hybrid perovskite solar cells, *Nat. Mater.*, 13 (2014) 897–903.
4. M. Xiao, F. Huang, W. Huang, Y. Dkhissi, Y. Zhu, J. Etheridge, et al., A Fast Deposition-Crystallization Procedure for Highly Efficient Lead Iodide Perovskite Thin-Film Solar Cells, *Angew. Chem. Int. Ed.*, 53 (2014) 9898–9903.
5. C. Zuo, L. Ding, An 80.11% FF record achieved for perovskite solar cells by using the NH₄Cl additive, *Nanoscale*, 6 (2014) 9935.
6. P.-W. Liang, C.-Y. Liao, C.-C. Chueh, F. Zuo, S.T. Williams, X.-K. Xin, et al., Additive Enhanced Crystallization of Solution-Processed Perovskite for Highly Efficient Planar-Heterojunction Solar Cells, *Adv. Mater.*, 26 (2014) 3748–3754.
7. J.H. Im, I.H. Jang, N. Pellet, M. Grätzel, N.-G. Park, Growth of CH₃NH₃PbI₃ cuboids with controlled size for high-efficiency perovskite solar cells, *Nat. Nanotechnol.*, 9 (2014) 927–932.
8. W.S. Yang, J.H. Noh, N.J. Jeon, Y.C. Kim, S. Ryu, J. Seo, et al., High-performance photovoltaic perovskite layers fabricated through intramolecular exchange, *Science*, 348 (2015) 1234–1237.
9. W. Zhang, S. Pathak, N. Sakai, T. Stergiopoulos, P.K. Nayak, N.K. Noel, et al., Enhanced optoelectronic quality of perovskite thin films with

- hypophosphorous acid for planar heterojunction solar cells, *Nat. Commun.*, 6 (2015) 10030.
10. X. Li, J. Yang, Q. Jiang, W. Chu, D. Zhang, Z. Zhou, et al., Enhanced photovoltaic performance and stability in mixed-cation perovskite solar cells via compositional modulation, *Electrochim. Acta*, 247 (2017) 460–467.
 11. Q. Hu, J. Wu, C. Jiang, T. Liu, X. Que, R. Zhu, et al., Engineering of Electron-Selective Contact for Perovskite Solar Cells with Efficiency Exceeding 15%, *ACS Nano*, 8 (2014) 10161–10167.
 12. B. Wang, Z.-G. Zhang, S. Ye, L. Gao, T. Yan, Z. Bian, et al., Solution-Processable Cathode Buffer Layer for High-Performance ITO/CuSCN-based Planar Heterojunction Perovskite Solar Cell, *Electrochim. Acta*, 218 (2016) 263–270.
 13. A.S. Subbiah, A. Halder, S. Ghosh, N. Mahuli, G. Hodes, S.K. Sarkar, Inorganic Hole Conducting Layers for Perovskite-Based Solar Cells, *J. Phys. Chem. Lett.*, 5 (2014) 1748–1753.
 14. J.H. Heo, S.H. Im, J.H. Noh, T.N. Mandal, C.-S. Lim, J.A. Chang, et al., Efficient inorganic–organic hybrid heterojunction solar cells containing perovskite compound and polymeric hole conductors, *Nat. Photonics*, 7 (2013) 486–491.
 15. S. Liu, R. Liu, Y. Chen, S. Ho, J.H. Kim, F. So, Nickel Oxide Hole Injection/Transport Layers for Efficient Solution-Processed Organic Light-Emitting Diodes, *Chem. Mater.*, 26 (2014) 4528–4534.
 16. M.S. Ryu, J. Jang, Enhanced efficiency of organic photovoltaic cells using solution-processed metal oxide as an anode buffer layer, *Sol. Energy Mater. Sol. Cells*, 95 (2011) 3015–3020.
 17. K.-C. Wang, P.-S. Shen, M.-H. Li, S. Chen, M.-W. Lin, P. Chen, et al., Low-Temperature Sputtered Nickel Oxide Compact Thin Film as Effective Electron Blocking Layer for Mesoscopic NiO/CH₃NH₃PbI₃Perovskite Heterojunction Solar Cells, *ACS Appl. Mater. Interfaces.*, 6 (2014) 11851–11858.

18. Z. Liu, M. Zhang, X. Xu, L. Bu, W. Zhang, W. Li, et al., p-Type mesoscopic NiO as an active interfacial layer for carbon counter electrode based perovskite solar cells, *Dalton Trans.*, 44 (2015) 3967–3973.
19. J.H. Kim, P.-W. Liang, S.T. Williams, N. Cho, C.-C. Chueh, M.S. Glaz, et al., High-Performance and Environmentally Stable Planar Heterojunction Perovskite Solar Cells Based on a Solution-Processed Copper-Doped Nickel Oxide Hole-Transporting Layer, *Adv. Mater.*, 27 (2014) 695–701.
20. J.-Y. Jeng, K.-C. Chen, T.-Y. Chiang, P.-Y. Lin, T.-D. Tsai, Y.-C. Chang, et al., Nickel Oxide Electrode Interlayer in CH₃NH₃PbI₃Perovskite/PCBM Planar-Heterojunction Hybrid Solar Cells, *Adv. Mater.*, 26 (2014) 4107–4113.
21. J. Cui, F. Meng, H. Zhang, K. Cao, H. Yuan, Y. Cheng, et al., CH₃NH₃PbI₃-Based Planar Solar Cells with Magnetron-Sputtered Nickel Oxide, *ACS Appl. Mater. Interfaces*, 6 (2014) 22862–22870.
22. W. Chen, Y. Wu, Y. Yue, J. Liu, W. Zhang, X. Yang, et al., Efficient and stable large-area perovskite solar cells with inorganic charge extraction layers, *Science*, 350 (2015) 944–948.
23. J.H. Park, J. Seo, S. Park, S.S. Shin, Y.C. Kim, N.J. Jeon, et al., Efficient CH₃NH₃PbI₃Perovskite Solar Cells Employing Nanostructured p-Type NiO Electrode Formed by a Pulsed Laser Deposition, *Adv. Mater.*, 27 (2015) 4013–4019.
24. X. Yin, P. Chen, M. Que, Y. Xing, W. Que, C. Niu, et al., Highly Efficient Flexible Perovskite Solar Cells Using Solution-Derived NiO_x Hole Contacts, *ACS Nano*, 10 (2016) 3630–3636.
25. J. Ciro, D. Ramírez, M.A.M. Escobar, J.F. Montoya, S. Mesa, R. Betancur, et al., Self-Functionalization Behind a Solution-Processed NiO_xFilm Used As Hole Transporting Layer for Efficient Perovskite Solar Cells, *ACS Appl. Mater. Interfaces*, 9 (2017) 12348–12354.
26. J. You, L. Meng, T.-B. Song, T.-F. Guo, Y.(M. Yang, W.-H. Chang, et al., Improved air stability of perovskite solar cells via solution-processed metal oxide transport layers, *Nat. Nanotechnol.*, 11 (2015) 75–81.

27. P. Qin, S. Tanaka, S. Ito, N. Tetreault, K. Manabe, H. Nishino, et al., Inorganic hole conductor-based lead halide perovskite solar cells with 12.4% conversion efficiency, *Nat. Commun.*, 5 (2014).
28. A.J. Huckaba, P. Sanghyun, G. Grancini, E. Bastola, C.K. Taek, L. Younghui, et al., Exceedingly Cheap Perovskite Solar Cells Using Iron Pyrite Hole Transport Materials, *ChemistrySelect.*, 1 (2016) 5316–5319.
29. G.A. Sepalage, S. Meyer, A. Pascoe, A.D. Scully, F. Huang, U. Bach, et al., Copper(I) Iodide as Hole-Conductor in Planar Perovskite Solar Cells: Probing the Origin of J-V Hysteresis, *Adv. Funct. Mater.*, 25 (2015) 5650–5661.
30. Z. Liu, A. Zhu, F. Cai, L. Tao, Y. Zhou, Z. Zhao, et al., Nickel oxide nanoparticles for efficient hole transport in p-i-n and n-i-p perovskite solar cells, *J. Mater. Chem. A*, 5 (2017) 6597–6605.
31. J.W. Lee, H.-S. Kim, N.-G. Park, Lewis Acid–Base Adduct Approach for High Efficiency Perovskite Solar Cells, *Acc. Chem. Res.*, 49 (2016) 311–319.
32. S. Oswald, W. Brückner, XPS depth profile analysis of non-stoichiometric NiO films, *Surf. and Interface Analysis*, 36 (2004) 17–22.
33. D. Adler, J. Feinleib, Electrical and Optical Properties of Narrow-Band Materials, *Physical Rev. B*, 2 (1970) 3112–3134.
34. D. Cahen, A. Kahn, Electron Energetics at Surfaces and Interfaces: Concepts and Experiments, *Adv. Mater.*, 15 (2003) 271–277.
35. W.A. Laban, L. Etgar, Depleted hole conductor-free lead halide iodide heterojunction solar cells, *Energy Environ. Sci.*, 6 (2013) 3249.
36. J. Shi, J. Dong, S. Lv, Y. Xu, L. Zhu, J. Xiao, et al., Hole-conductor-free perovskite organic lead iodide heterojunction thin-film solar cells: High efficiency and junction property, *Appl. Phys. Lett.*, 104 (2014) 063901.
37. W. Tress, A. Petrich, M. Hummert, M. Hein, K. Leo, M. Riede, Imbalanced mobilities causing S-shaped IV curves in planar heterojunction organic solar cells, *Appl. Phys. Lett.*, 98 (2011) 063301.

38. Y. Shao, Z. Xiao, C. Bi, Y. Yuan, J. Huang, Origin and elimination of photocurrent hysteresis by fullerene passivation in $\text{CH}_3\text{NH}_3\text{PbI}_3$ planar heterojunction solar cells, *Nat. Commun.*, 5 (2014) 5784.
39. B. Wu, K. Fu, N. Yantara, G. Xing, S. Sun, T.C. Sum, et al., Charge Accumulation and Hysteresis in Perovskite-Based Solar Cells: An Electro-Optical Analysis, *Adv. Energy Mater.*, 5 (2015) 1500829.
40. H.-S. Kim, I. Mora-Sero, V. Gonzalez-Pedro, F. Fabregat-Santiago, E.J. Juarez-Perez, N.-G. Park, et al., Mechanism of carrier accumulation in perovskite thin-absorber solar cells, *Nat. Commun.*, 4 (2013).
41. J.A. Christians, R.C.M. Fung, P.V. Kamat, An Inorganic Hole Conductor for Organo-Lead Halide Perovskite Solar Cells. Improved Hole Conductivity with Copper Iodide, *J. Am. Chem. Soc.*, 136 (2014) 758–764.
42. D. Liu, J. Yang, T.L. Kelly, Compact Layer Free Perovskite Solar Cells with 13.5% Efficiency, *J. Am. Chem. Soc.*, 136 (2014) 17116–17122.

CHAPTER 6

PRODUCTION OF MESOPOROUS LAYERS IN CARBON BASED PEROVSKITE SOLAR CELLS BY FLAME SPRAY METHOD

6.1 Introduction

Solution processed perovskite based solar cells have been breakthrough photovoltaic devices in the past five years. Organo lead halide perovskite materials offer outstanding photovoltaic performances thanks to their unique absorption and transport properties. Efficiencies over 20% have already been reached and huge efforts are being devoted to mass scale fabrication and commercialization of perovskite solar cell technology [1,2]. Design concepts of the perovskite solar cells like p-i-n or n-i-p configuration and mesoporous scaffolding or planar heterojunction devices have been studied extensively. There are numerous production routes for deposition of defect free, homogeneous conformal perovskite layers [3,4] and conjugated charge selective layers, which are mostly organic materials like spiro-OMeTAD [5,6] or PCBM [7,8]. These polymeric materials not only possess low mobility, low crystallinity and high cost, they also suffer from low stability and severe cell degradation during prolonged operation [9]. Although efforts have focused on the development of deposition of fully metal oxide charge selective layers [10,11], majority of high performance cells still employ organic p-type or n-type charge carrier layers which is limiting the commercialization

Carbon based monolithic perovskite solar cells have been attractive structures since their introduction [12]. They combine high performance of perovskite solar absorbers and ease of production thanks to the screen printing technology. The major advantage of these devices is the lack of any organic component causing cell

degradation and prolonged stability of these devices have been demonstrated [13]. The basic structure of a carbon based perovskite cell is a stack of mesoporous layers, an n-type electron collecting layer like TiO_2 , an insulating separation layer, like ZrO_2 , Al_2O_3 and the carbon collector electrode. Perovskite crystals are embedded inside the mesoporous network and act like the absorption layer and hole conducting medium, simultaneously. By modifying the distribution and preferential orientation of the perovskite crystals inside the mesoporous matrix, efficiencies over 15% have been reported by humidity assisted thermal treatment [14] or slow crystallization techniques [15]. NiO , which is a common hole conducting medium employed in inverted perovskite solar cells, has been successfully incorporated into this structure as an hole extracting and transporting medium, deposited on top of the insulating layer and enhancing the overall efficiencies [16,17]. The major contribution of the NiO layer is reduction of the recombination rate inside cell by extracting holes from perovskite and enhancing charge transfer rates, especially when used in conjunction with a separator layer [18,19]. However, with the introduction of each additional thick mesoporous layer, overall series resistance inside cell starts to be a dominant factor affecting the performance of the devices, especially limiting the open circuit voltage of the cells. Enhancing the conductivity of perovskite crystals by LiCl doping has been demonstrated for decreased series resistance [20]. Although doped charge selective metal oxide layers were reported to improve charge collection and proven to be an effective way of enhancing efficiency [21,22], such a concept has not been realized for mesoporous charge selective layers in carbon based devices yet.

In this work, a carbon based perovskite solar cell has been developed employing doped metal oxide nanoparticles for achieving a highly conducting charge transfer medium and reduced overall cell resistance. In order to ensure an effective doping of the metal oxides employed, flame synthesis method is chosen instead of the wet chemistry methods which are insufficient for doping purposes. A novel flame spraying method is introduced by means of nebulizing methanol based precursor solutions and flame synthesizing doped metal oxide nanoparticles, which we choose

to refer as “methanol combustion synthesis”. Yttrium doped TiO₂, MgO and lithium doped NiO nanoparticles were produced by this method and deposited in a stack configuration. Morphological, structural and electrical characterizations of the synthesized powders were conducted and correlated to device performance by means of electronic transport and interfacial charge transfer dynamics. Effect of doping on the transport properties and perovskite solar cell efficiency was studied.

6.2 Experimental

6.2.1 Production of metal oxide nanoparticles by flame spray

In order to synthesize metal oxide nanoparticles for construction of perovskite based solar cells, a flame spray apparatus made of a stainless steel pipe was used. Methanolic precursor solutions were nebulized to fine mist by an ultrasonic nebulizer operated at 1.63 MHz. This mist was fed into the tubular nozzle by nitrogen as the carrier gas, where they were mixed with oxygen until a stable flame is achieved. The flame was fed into a ceramic tube which is connected to vacuum pump. The particles were collected at a filter paper in front of the vacuum pump connection. For synthesis of TiO₂ nanoparticles, a 0.1 M solution of titanium bisacetylacetonate diisopropoxide in methanol was used. For deposition of MgO layers, Mg(NO₃)₂.6H₂O was dissolved in methanol with a molarity of 0.1 M. For deposition of NiO layers, a methanolic solution of 0.1 M Ni(OCOCH₃)₂.4H₂O was used, similarly. In order to dope TiO₂, Y(NO₃)₃.4H₂O was added to the precursor solution with varying molar concentrations. For Li doping of NiO, LiNO₃ was added to the precursor solutions similarly. Collected particles were ground inside a mortar with ethanol and suspensions were prepared by grinding and ultrasonic treatment. The ethanolic suspensions were mixed with ethyl cellulose and terpineol. A typical paste consists 2:1:10 weight ratio of powder, ethyl cellulose and terpineol respectively. Excess ethanol was evaporated by a rotary evaporator at 50°C.

6.2.2 Construction of carbon based perovskite solar cells

Carbon based perovskite solar cells were prepared by a one step technique using the flame spray coated FTO glass substrates. Deposition of the nanoparticles were conducted in the order of TiO₂, MgO and NiO, forming an n-i-p configuration. Before deposition of the particles by screen printing, a 50 nm blocking TiO₂ layer was deposited on the precleaned and UV-Ozone treated FTO substrate. For this purpose, a 0.15 M titanium bisacetylacetonate diisopropoxide solution in butanol was prepared and coated on the FTO substrates by spin coating at 2000 rpm for 20 s. After firing this layer at 500°C for 15 min and cooling down, nanoparticle pastes were deposited on the substrates by screen printing method. The formulation employed in this work yields approximately 500 nm thick films by using a 90 mesh size for screen printing. Thick films of TiO₂, MgO and NiO particles were deposited subsequently on top each other after drying the deposited pastes at 125°C for 5 min. The stacking layers were then subjected to heat treatment at 500°C for 15 min. After cooling down, 10 µm thick carbon layer was deposited by doctor blading a carbon paste Elcocarb B/SP, Solaronix. After firing at 400°C for 30 min, fresh electrodes were filled with 10 microliters of perovskite precursor solution at room temperature and waited for full impregnation for several minutes. Crystallization of the perovskite layer was conducted at 50°C for 90 min. The perovskite precursor solution was composed of 0.159 g of methylammonium iodide (Dyesol), 0.461 g of lead iodide (Sigma 99%) and 0.013 g of 5 ammonium valeric acid iodide (5-AVAI) dissolved in 1 ml of N,N-dimethylformamide. Synthesis of 5-AVAI was achieved by reacting equimolar amount of hydriodic acid and ammonium valeric acid at 0°C for 2 h, evaporating the solvent and recrystallizing with diethyl ether for 3 times. After completion, cells were kept under ambient conditions without any encapsulation in dark.

6.2.3 Characterizations

X-ray diffraction patterns for determination of phase analysis were recorded by Rigaku D/MAX 2200/PC using Cu K α radiation. Morphology of nanoparticles and devices were investigated by scanning electron microscopy (SEM) (FEI Quanta 400 FEG equipped with energy dispersive X-ray (EDX) analyzer). Chemical properties and electronic band structure determination of doped nanoparticles was conducted using X-ray photoelectron spectroscopy (XPS) and ultraviolet photoelectron spectroscopy (UPS) (PHI 5000 VersaProbe). J-V scans of the cells were conducted using Yokogawa GS610 source measure unit under simulated AM 1.5 illumination from a Newport solar simulator 67005. Electrochemical impedance spectroscopy (EIS) analyses of the produced cells was conducted using Gamry reference 3000 under illumination with white LED light (60 mW/cm²) and Echem analyst software was used for fitting.

6.3 Results

In order to determine crystallographic structure of the metal oxide powders produced by flame spraying method, X-Ray diffraction patterns of the produced nanoparticles coated on glass substrates and heat treated at 500°C were recorded and given in Figure 6.1. In Figure 6.1a, it is seen that undoped TiO₂ particles exhibit pure anatase structure where peaks observed at 25.51°, 37.91°, 48.19°, 54.23°, 55.26° and 62.86° were assigned to (101), (004), (200), (105), (211) and (204) planes of anatase structure of TiO₂, respectively. However, upon doping with yttrium even after 1%, rutile peaks starts to appear at 27.56°, 36.11° and 41.05°, assigning to (110), (101) and (111) planes, respectively. Intensity of the peaks tends to increase with increasing yttrium doping amount and structure starts to convert to rutile. There are no peaks associated with the Y₂O₃, the most intense peaks of which are expected to appear at 29.2° and 33.7°, are completely missing. This situation shows that all yttrium atoms are incorporated into TiO₂ lattice and promotes conversion of anatase to rutile. Tendency of the phase transition between anatase

and rutile upon yttrium doping was observed in previous studies similar to this work and related to decreased activation energy of rutile formation in the presence of a dopant [23,24]. XRD spectra of produced Li doped NiO nanoparticles are given in Figure 6.1b. Peaks appearing at 37.87° , 42.1° , 62.8° , 74.3° and 78.7° are assigned to (111), (200), (220), (311) and (222) planes of cubic rock salt structure NiO. There are no peaks associated with a secondary phase like Li_2O_3 , indicating the successful incorporation of Li atoms into NiO lattice, up to a doping amount of 20%. In Figure 6.1c, XRD spectra of MgO is given and peaks observed at 36.99° , 42.98° , 62.54° and 78.82° are assigned to (111), (200), (220) and (222) planes, respectively, showing successful formation of MgO powders.

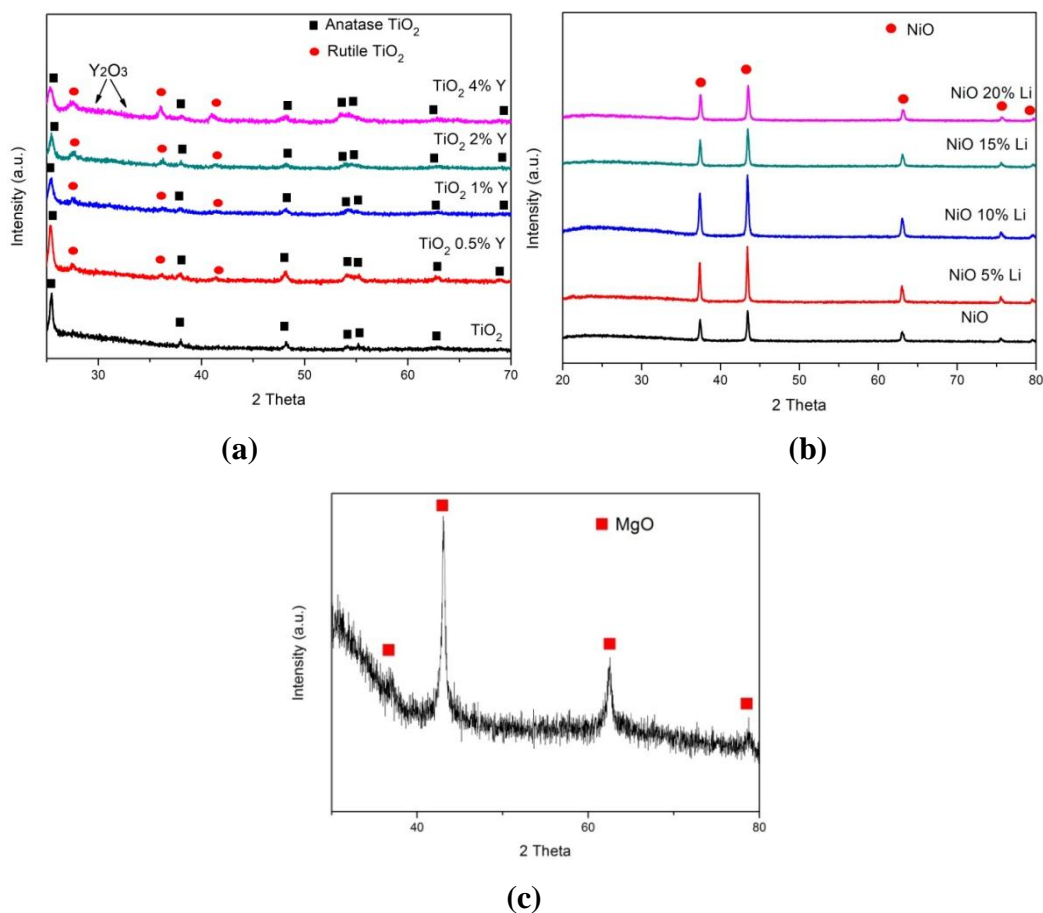


Figure 6.1 XRD spectrum of nanoparticles produced by flame spray method, TiO_2 (a), NiO (b) and MgO (c).

In order to determine the microstructural and morphological properties of the produced particles, scanning electron microscopy (SEM) studies were conducted on the particles deposited on FTO substrates and SEM images are given in Figure 6.2. From Figure 6.2 it is seen that, all particles exhibit nanoparticulate structures with a nanoparticle size ranging between 20 to 50 nm, showing the success of flame spray method to produce nanoparticles and mesoporous layers which is a prerequisite for perovskite solar cell applications. Morphology and the size of the powders are quite similar to each other.

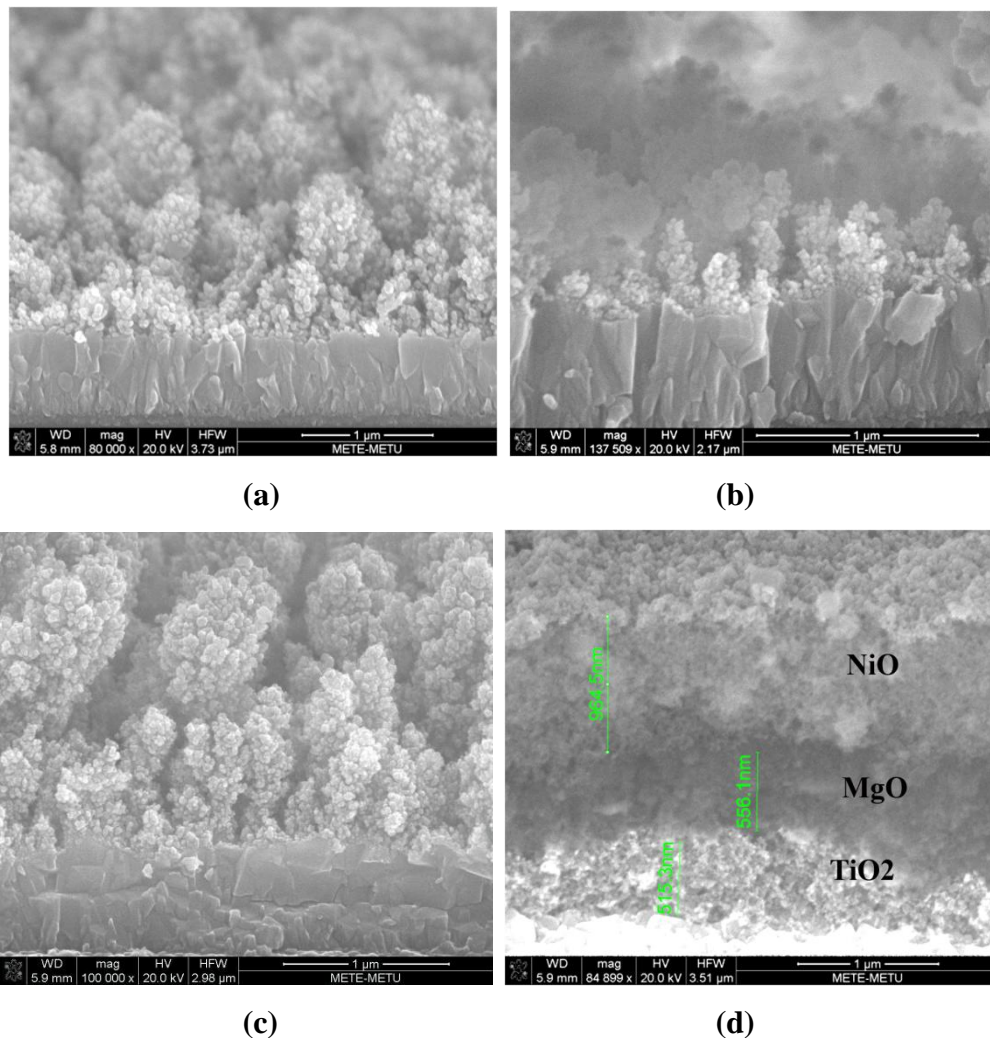


Figure 6.2 SEM images of nanoparticles produced by flame spray on FTO substrates, TiO₂ (a), MgO (b), NiO (c) and TiO₂, MgO, NiO stacking layers (d).

Table 6.1 BET specific surface area of the synthesized powders before and after heat treatment at 500°C.

Surface Area	TiO ₂	MgO	NiO
Before Heat Treatment (m ² /g)	66	70	63
After Heat Treatment (m ² /g)	49	54	51

In order to clarify the particle size similarity seen in the SEM images, BET surface area measurements were conducted on the as synthesized particles and after heat treatment at 500°C for 15 min and given in Table 6.1. Before heat treatment, particles possess high surface area value ranging between 65-70 m²/g. However, particles used for the construction of the mesoporous cells require a heat treatment for thick film deposition so actual surface area of the powders are the values after sintering at 500°C. Upon heat treatment, surface area of the powders reduce to values ranging between 50-55 m²/g, which is the optimum surface area for nanoparticles employed in construction of mesoporous photovoltaic devices like the dye sensitized solar cells or mesoscopic perovskite solar cells. It is interesting to note that, from both SEM analysis and BET surface area measurements, particle sizes and surface area value of the powders are quite identical for TiO₂, MgO and NiO nanoparticles produced by the methanol combustion method employed in this work. This method yields similar particle sizes and morphologies regardless of the materials or precursors used for production.

Yttrium doped TiO₂ and lithium doped NiO nanoparticles were produced with the same method for different doping concentrations in order to obtain enhanced electrical conductivity. TiO₂ particles were doped between 0.5-4% atomic ratio where lithium doping of NiO was conducted up to 20% atomic ratio due to high solubility of the lithium in the NiO lattice. The effect of the heavy doping on the resistivity of the produced particles are given in Figure 6.3.

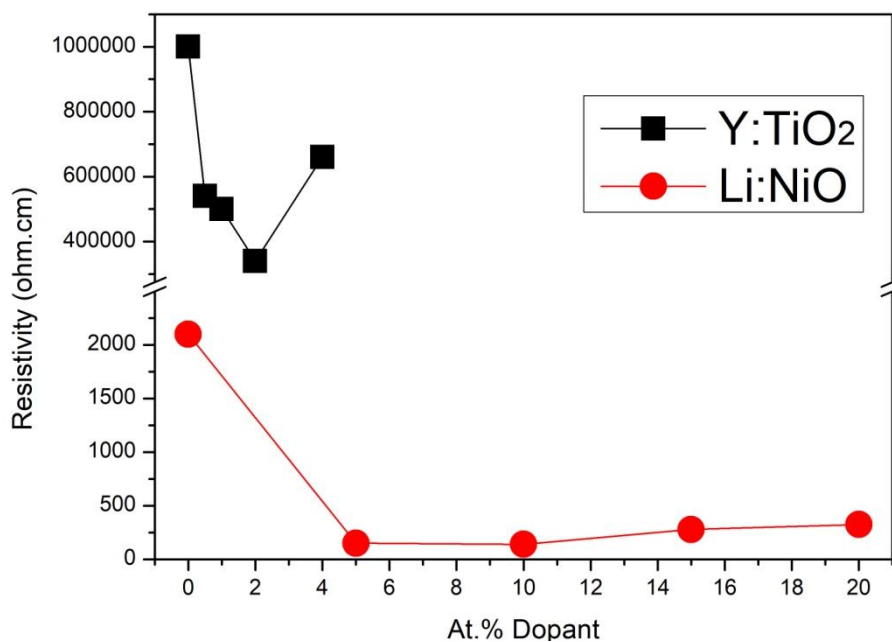


Figure 6.3 Two point resistivity values of Y:TiO₂ and Li:NiO nanoparticles depending on the dopant amount in the precursor solution.

The introduction of the yttrium dopant atoms into TiO₂ lattice results in a net decrease in the resistivity of the powders up to 2% doping amount from megaohm.cm values down to 340 kilohm.cm value. Further increasing the yttrium amount has negative effect on the electrical conductivity beyond 2% doping value. For the NiO based particles, lithium doping results in strong reduction in the resistivity and can be reduced down to 150 ohm.cm value at 5% doping amount. The conductivity quickly saturates upon lithium doping and stays around this value up to 20% doping amount, where lowest resistivity is achieved at 10% doping having 140 ohm.cm value obtained in this work. The doping concentrations given in Figure 6.3 represent the amount of dopant atoms in the precursor solution and actual value of the doping in the lattice is investigated on the produced powders by chemical analysis. For detection yttrium atoms in the TiO₂ powders were analyzed with EDX, where for detection of lithium atoms ICP-MS method was employed and results are given in Table 6.2.

Table 6.2 Actual doping concentration of powders compared to the precursor solutions of Y:TiO₂ and Li:NiO nanoparticles.

	Y:TiO ₂				Li:NiO			
% At. dopant in precursor	0.5	1	2	4	5	10	15	20
% At. dopant in powder	0.47 (EDX)	0.77 (EDX)	1.71 (EDX)	3.2 (EDX)	4.8 (ICP-MS)	7.7 (ICP-MS)	13.1 (ICP-MS)	15.7 (ICP-MS)

The amount of dopant atoms in the powders are slightly deviated from the concentration in the precursor solutions as derived from the chemical analysis. For both Y:TiO₂ and Li:NiO powders, this deviation increases with the doping concentration as it gets harder to introduce more atoms into the host lattice with increasing concentration. For Y:TiO₂ powders with 4% doping amount in the precursor solution, actual amount is found to be 3.2% and we believe this is the maximum solubility limit of yttrium in the TiO₂ lattice using the flame combustion method. However, the doping efficiency is still high for the powders produced and this proves the doping ability of the flame combustion method employed in this work. The advantage of the flame method is the rapid formation of the particles in the flame where there is not sufficient time for the dopant atoms to precipitate as a secondary phase compared to widely used precipitation methods for doping purposes. Oxidation of the host and dopant precursors occur simultaneously upon introduction of the precursors to the flame and dopant atoms can be trapped in the host lattice more efficiently. Former studies employing hydrothermal and sol-gel methods for production of yttrium doped TiO₂ nanoparticles fail to successfully introduce the dopant into the lattice where starting concentration of the dopant atoms are far less than the final particles [23, 25]. Chemical structure and effect doping on the produced metal oxide layers were further investigated using XPS analysis. XPS spectra of the undoped TiO₂ nanoparticles and Y:TiO₂ nanoparticles

with the 2% yttrium doping amount and deconvolution of Ti 2p core levels with the fitted spectrum on Shirley type background are given in Figure 6.4 and Figure 6.5 , respectively.

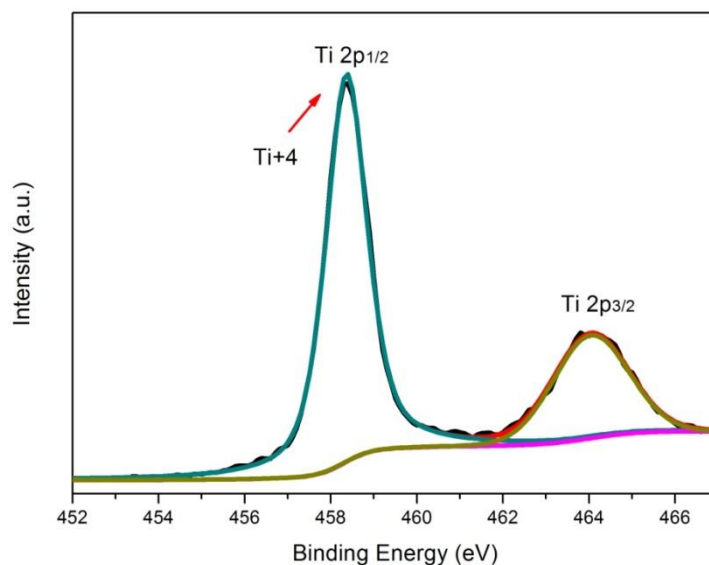


Figure 6.4 XPS spectra of Ti 2p core levels for undoped TiO₂ nanoparticles.

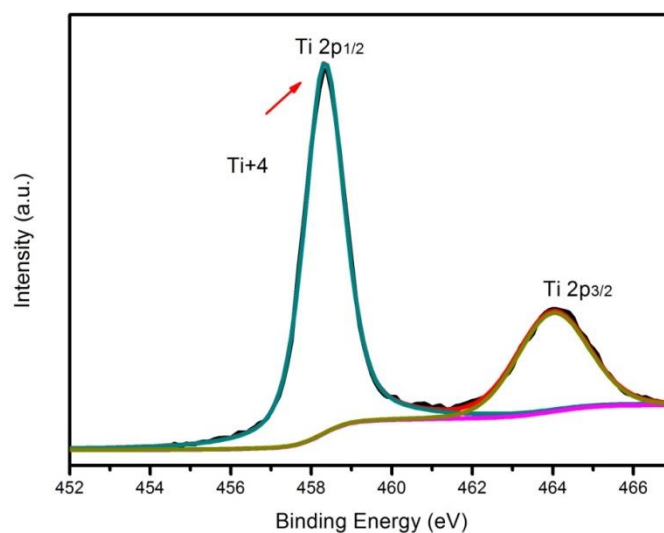


Figure 6.5 XPS spectra of Ti 2p core levels for 2% yttrium doped TiO₂ nanoparticles.

Deconvolution of O1s core levels and the fitted spectrum for undoped TiO₂ and 2% yttria doped TiO₂ nanoparticles and 3d core levels for yttrium are given in Figure 6.6, Figure 6.7 and Figure 6.8, respectively.

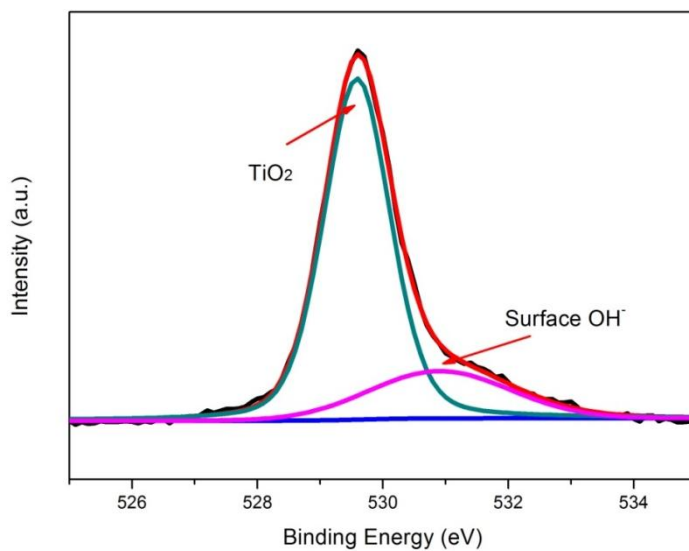


Figure 6.6 XPS spectra of O1s core levels for undoped TiO₂ nanoparticles.

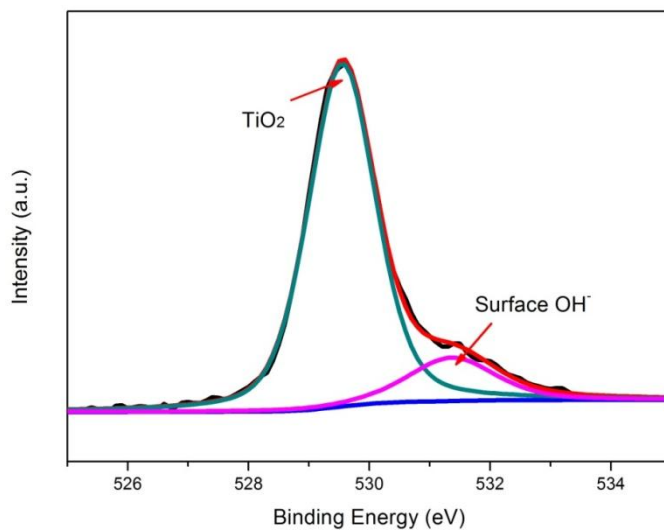


Figure 6.7 XPS spectra of O 1s core levels for 2% yttrium doped TiO₂ nanoparticles.

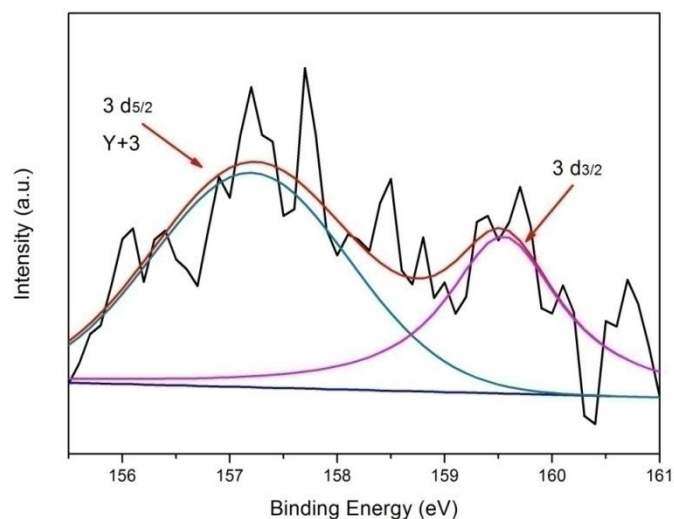


Figure 6.8 XPS spectra of Y 3d core levels for 2% yttrium doped TiO₂ nanoparticles.

The peaks observed at 458.4 eV and 464.1 eV are assigned to Ti 2p_{3/2} and Ti 2p_{1/2}, respectively, indicating the Ti⁺⁴ oxidation state which are consistent with literature reports. It is seen that both samples are quite identical and there is no chemical shift or shoulder assigned to another Ti state. Ti⁺³ state seen in oxygen deficient samples which appear at around 455 eV is totally absent which shows that structure is pure TiO₂. The same situation is valid for the O 1s spectra of the both samples which are again quite identical. Peak appearing at 529.6 eV is assigned to the TiO₂ while shoulder peak at 531.1 eV is related to the surface adsorbed hydroxyl groups. XPS spectra of yttrium 3d core levels given in Figure 6.8 show the peaks after deconvolution, which appear at 157.2 eV and 159.5 eV for 3 d_{5/2} and 3 d_{3/2} levels, consistent with the earlier reports. According to XPS analysis, structure is fully TiO₂ and we relate this situation to two factors. Addition of a trivalent cation of Y⁺³ prevents reduction of the Ti atoms to lower oxidation states for conservation of the charge neutrality, indicating that all Y atoms are incorporated into the TiO₂ lattice successfully. In addition, the flame spraying synthesis is conducted with excess oxygen and oxygen deficiency is not likely under the synthesis conditions. XPS spectra of the undoped NiO nanoparticles and Li:NiO nanoparticles with the 10%

lithium doping amount and deconvolution of Ni 2p core levels with the fitted spectrum on Shirley type background are given in Figure 6.9 and Figure 6.10, respectively.

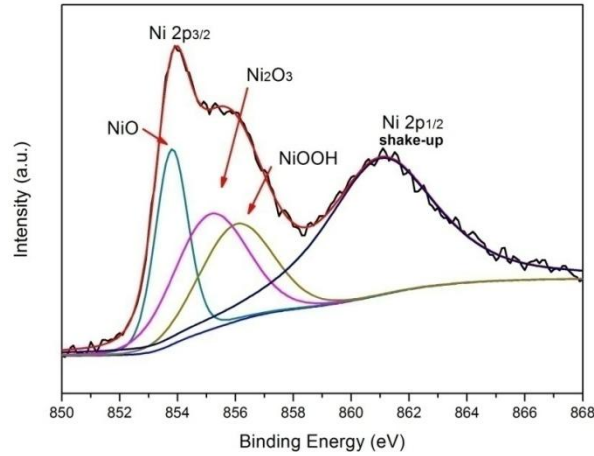


Figure 6.9 XPS spectra of Ni 2p core levels for undoped NiO nanoparticles.

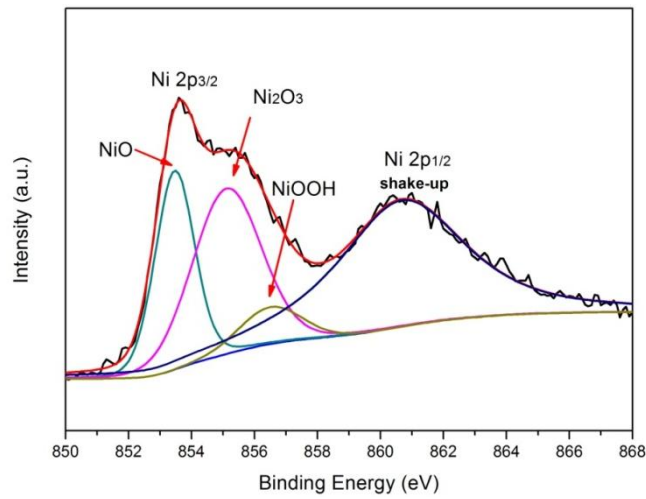


Figure 6.10 XPS spectra of Ni 2p core levels for 10% lithium doped NiO nanoparticles.

Deconvolution of O1s core levels and the fitted spectrum for undoped NiO and 10% lithium doped NiO nanoparticles are given in Figure 6.11 and Figure 6.12, respectively.

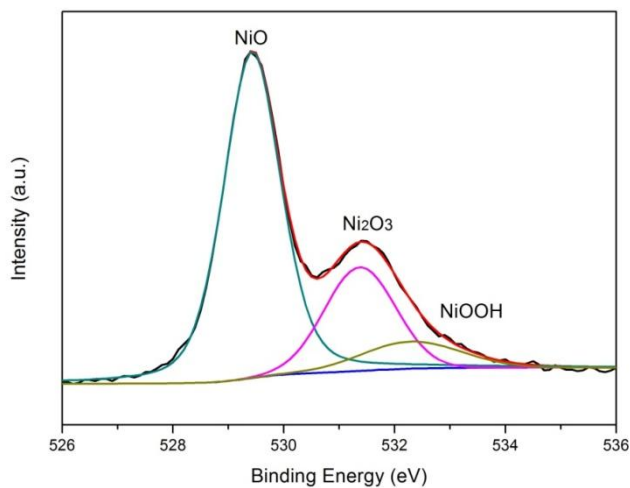


Figure 6.11 XPS spectra of O1s core levels for undoped NiO nanoparticles.

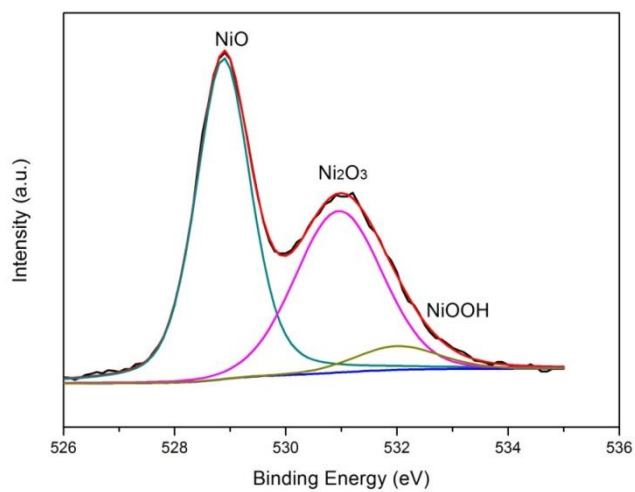


Figure 6.12 XPS spectra of O1s core levels for 10% lithium doped NiO nanoparticles.

For Ni 2p core levels of undoped NiO given in Figure, peaks observed at 853.7 eV, 855.3 eV and 856.1 eV are assigned to NiO, Ni₂O₃ and surface adsorbed hydroxyl groups forming NiOOH, respectively. Presence of intrinsic Ni⁺³ in the NiO is due to excess oxygen in the NiO lattice and is consistent with the previous studies., It is seen from deconvolution of Ni 2p states and the oxygen 1s states, upon doping with lithium, amount of Ni⁺³ increases with respect to Ni⁺² in NiO lattice. As long as there is no secondary phases like Ni₂O₃ from the XRD spectra, we conclude that introduction monovalent ion Li⁺¹ results in the increase in the Ni⁺³ concentration in the NiO structure due to conservation of charge balance. Actually, these ions are responsible from the enhancement of the hole concentration in the valence band and electrical conduction observed in the particles. Unlike doped TiO₂, the doping of the NiO with Li, a chemical shift in the XPS spectra of the NiO powders can be observed from O 1s levels. Peak appearing at 529.4 eV of O 1s levels of NiO for undoped samples, shifts to 528.8 eV binding energy, corresponding to a chemical shift of 0.6 eV. The high concentration of Li atoms and heavily doped nature of the particles produced in this work is believed to lead to the observed shift in the NiO particles, which could not be detected for TiO₂ samples.

In order to elucidate the performance of the produced nanoparticles in perovskite solar cells, these particle were deposited on FTO substrates by screen printing method and cells were constructed using the pastes produced in this work. For this purpose, firstly, standart carbon based cells employing screen printed TiO₂ and MgO cells were constructed and characterized for determining the optimized perovskite precursor solution conditions. J-V curves of the cells prepared from precursor solutions with and without 5-AVAI are given in Figure 6.13.

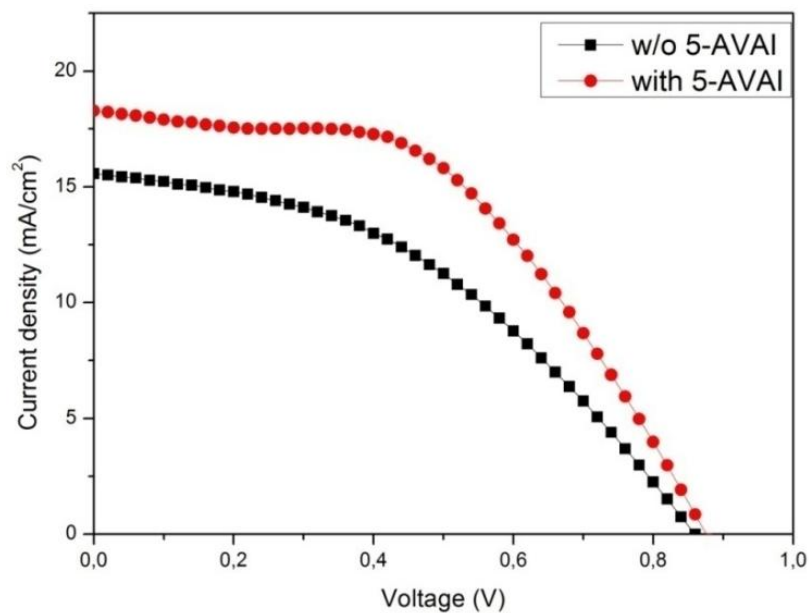


Figure 6.13 J-V curves of the carbon based cells with and without 5-AVAI addition to the perovskite precursor solution.

As seen from Figure 6.13, cells without 5-AVAI shows poor performance with a open circuit potential of 0.85 V, short circuit current density of 15.57 mA/cm² and fill factor of 0.42 , yielding an efficiency of 5.62%. However upon addition of 5-AVAI, cell parameters dramatically increase, especially short circuit current density and fill factor which are risen up to 18.28 mA/cm² and 0.55, yielding an efficiency of 7.95%. 5-AVAI is known to grow perovskite crystals inside the mesoporous network in a more regular fashion and larger crystals can be formed thanks to the wettability property of the ammonium valeric acid and this fact is considered to be the major factor of the improvement in the cells. Using the same precursor solution containing 5-AVAI, carbon based perovskite solar cells were constructed from flame spray synthesized nanoparticles and J-V curves were given in Figure 6.15 and Figure 6.16 and cell parameters were tabulated in Table 6.3.

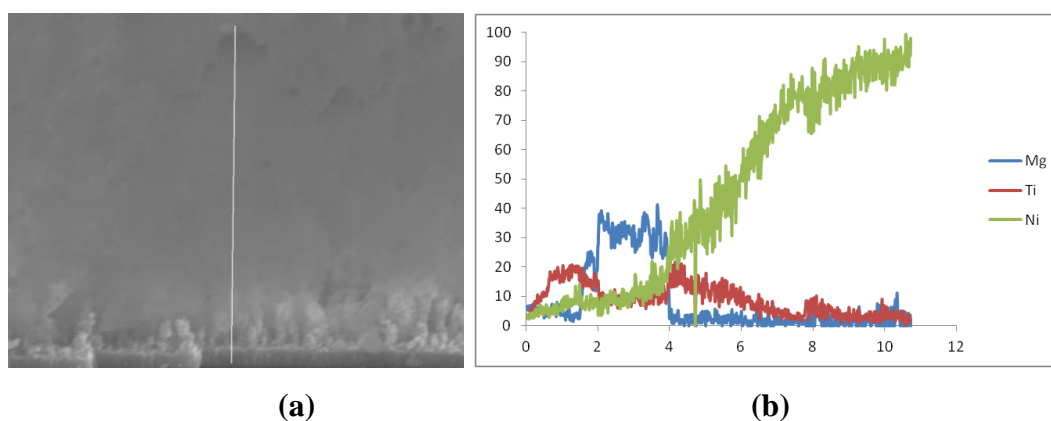


Figure 6.14 SEM image of a stacking layer of $\text{TiO}_2/\text{MgO}/\text{NiO}$ (a) and the corresponding line EDX analysis (b).

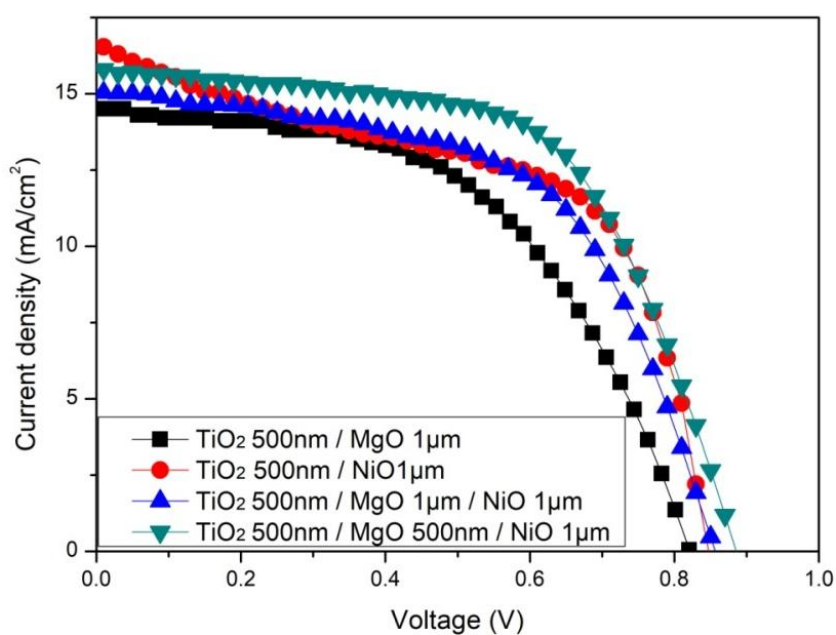


Figure 6.15 J-V curves of the carbon based perovskite solar cells constructed using undoped particles.

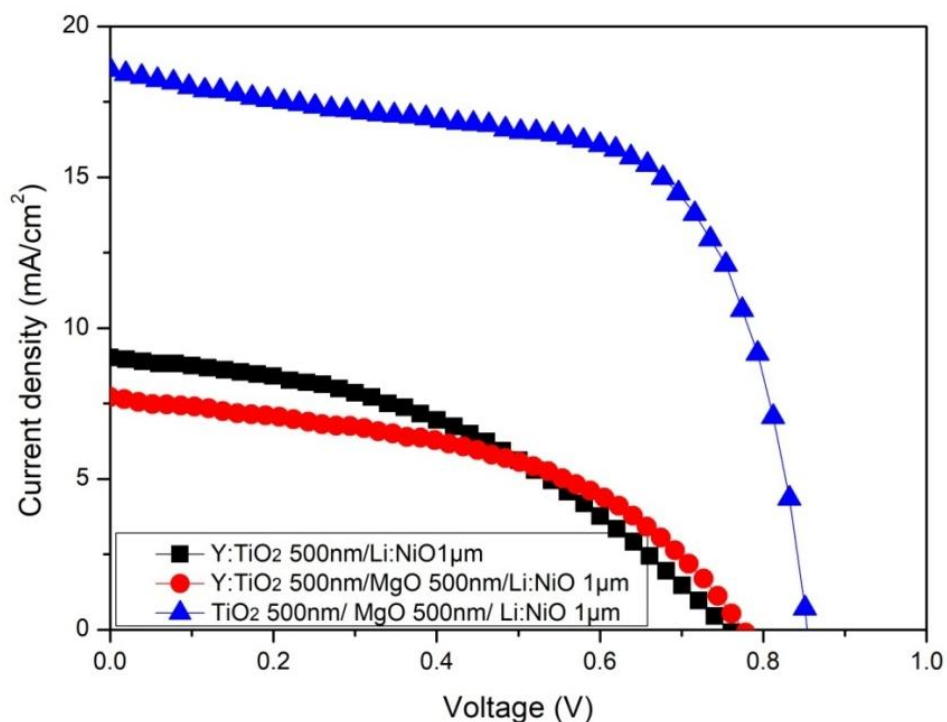


Figure 6.16 J-V curves of the carbon based perovskite solar cells constructed using doped particles.

Table 6.3 Cell parameters of the carbon based solar cells constructed using flame spray deposited nanoparticles.

Cell	Voc (V)	Jsc (mA/cm ²)	FF	Eff. (%)
TiO ₂ 500nm / MgO 1µm	0.82	14.3	0.51	5.93
TiO ₂ 500nm / NiO 1µm	0.85	16.4	0.55	7.66
TiO ₂ 500nm / MgO 1µm / NiO 1µm	0.87	15.1	0.57	7.48
TiO ₂ 500nm / MgO 500nm / NiO 1µm	0.87	15.8	0.61	8.38
Y:TiO ₂ 500 nm / Li:NiO 1µm	0.76	9.1	0.39	2.69
Y: TiO ₂ 500nm / MgO 500nm / Li:NiO 1µm	0.77	7.7	0.47	2.78
TiO ₂ 500nm / MgO 500nm / Li:NiO 1µm	0.88	17.2	0.64	9.63

Cells constructed from undoped nanoparticles were preliminarily optimized for layer thicknesses and it was found that for TiO₂ layer, 500 nm and for NiO layer, 1 μm are the optimum values. Cells with different stacking layers and configurations were constructed and characterized. It is seen from Table 6.3 that addition of the NiO layer instead of the MgO layer results in an enhancement in the efficiency of the cells increasing the fill factor and current density values. The p-type mesoporous layer has the ability to conduct holes efficiently leading to improved charge collection and as a result a net increase in the current density is observed. However, the TiO₂-NiO interface is a direct recombination center for holes in the NiO valence band and the electrons in the TiO₂ conduction band. Addition of a thin MgO layer insulates the two charge collection layers and due to the suppressed recombination, open circuit potential and the fill factor values are improved and overall efficiency is enhanced for an n-i-p configuration cell for a 500 nm thick MgO interlayer. Cells were constructed from the synthesized heavily doped particles and performances were investigated in the same configuration. For production of doped particle based cells, particles with highest conductivity were employed, which are 2% yttrium doping for TiO₂ and 10% lithium doping for NiO. It is seen that addition of the Y:TiO₂ layers greatly reduces the overall efficiency of the devices compared to undoped TiO₂ particles. Apart from the reduction in open circuit potential and fill factors, there is a strong decline in the photocurrent, indicating that charge transfer between the perovskite layer and the TiO₂ electron collector layer is severely inhibited. On the other hand, Li:NiO particles contribute to overall cell efficiency greatly by means of improvement in the photocurrent density and the fill factor, indicating that enhanced electrical conductivity of the powders lead to improved charge collection efficiency and reduced internal resistance. An efficiency of 9.63% for the best performing cell was achieved by employing highly conductive Li:NiO nanoparticles in this work.

Origin of the reduction in efficiency values and detrimental effect of yttrium doping on TiO₂ particles is a vital issue to be addressed for understanding the fundamental parameters for construction of high efficiency solar cells. For this purpose UPS

measurements were conducted on the produced particles and effect of doping on the electronic band structure was examined. Fermi levels (E_f) and energy difference of the top of the valence band and the Fermi level ($E_f - E_{vbm}$) were extracted from the cutoff energy and onset energy of the UPS spectra, respectively, for undoped and doped metal oxides as given in Figure 6.17.

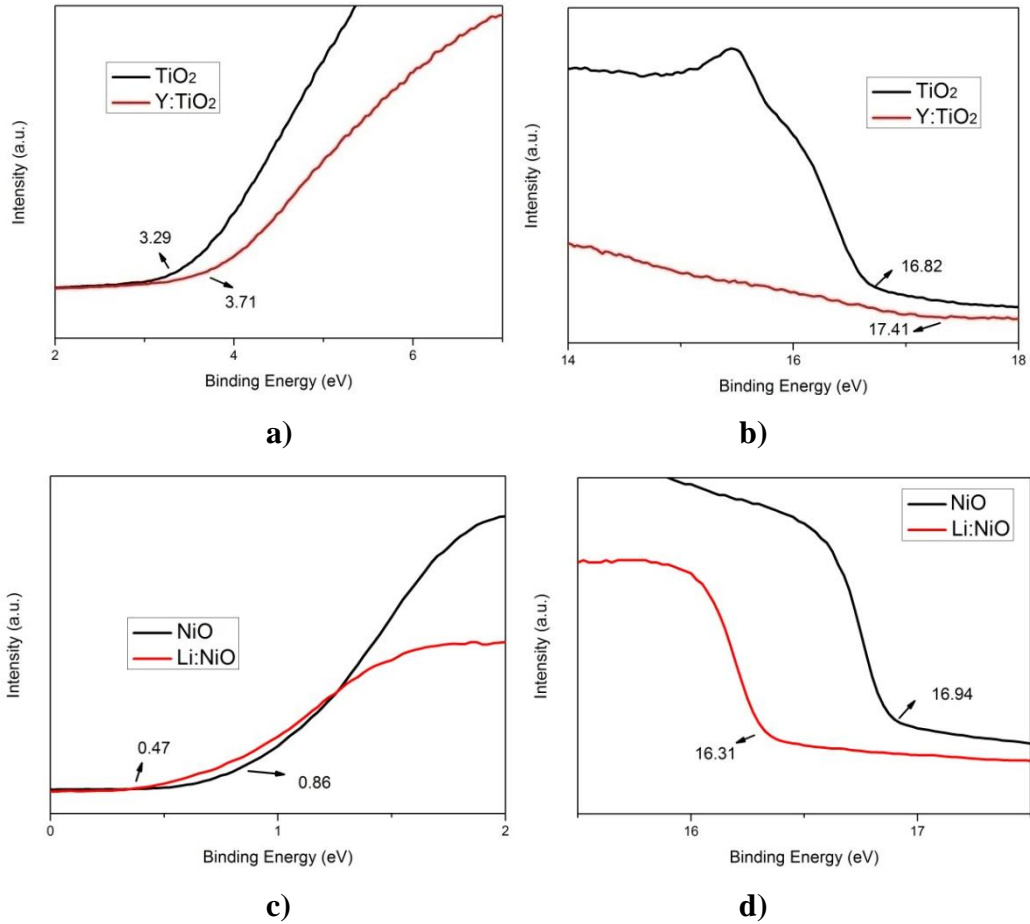


Figure 6.17 Onset (a) and cut-off (b) energies of TiO₂ nanoparticles and onset (c) and cut-off (d) energies of NiO nanoparticles extracted from UPS measurements.

It is seen from Figure 6.17 that upon doping both Fermi energies, which determines the work function of materials, and the difference with the valence band maximum of both particles are modified. For Li:NiO particles, energy difference between the Fermi level and the valence band maximum is increased by two folds upon doping

as an expected situation taking into account the strong increase in the conductivity of the Li:NiO particles. It is also interesting to note that undoped NiO nanoparticles produced by the flame synthesis method shows considerable amount of conductivity as well as the difference of the valence band maxima and Fermi level is smaller compared to the particles produced by the precipitation method investigated in the previous chapter. We relate this to the oxygen rich synthesis conditions of the flame method which results in increased amount of Ni⁺³ ions and shows a doping effect similar to the Li⁺¹ ions. By adding the optical band gap values of TiO₂ and NiO to the valence band positions obtained by UPS, position of conduction band minima values are determined and the resulting band structures are depicted in Figure 6.18 together with the perovskite and the MgO layer.

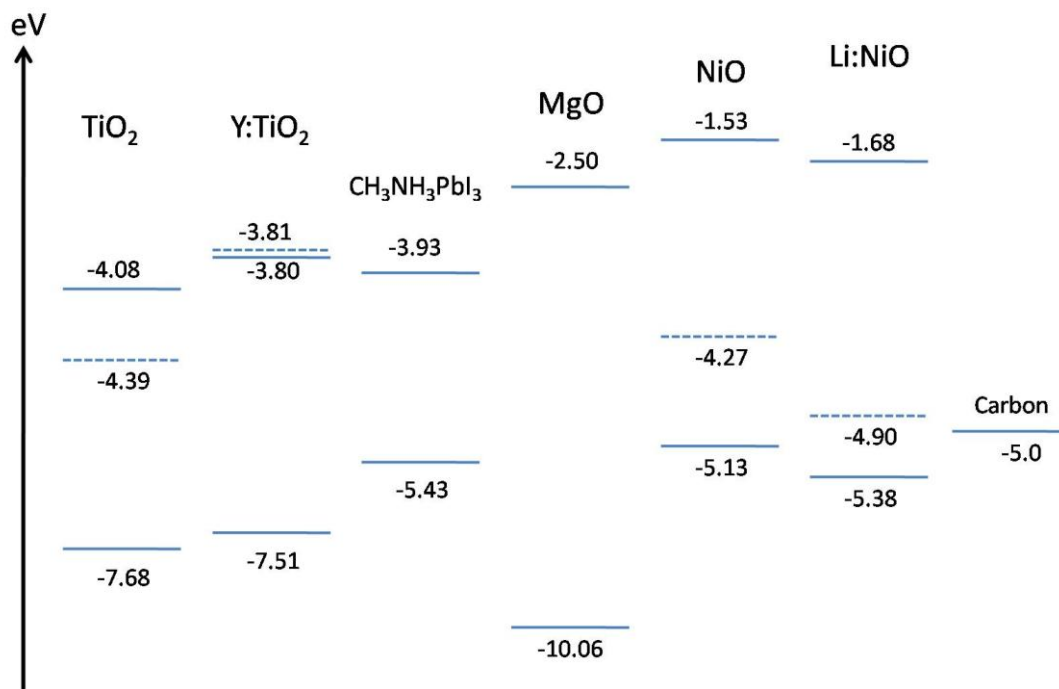


Figure 6.18 Schematic representation of band structures of the particles produced in this work extracted from UPS measurements, together with that of perovskite and MgO layer.

The deep lying valence band position and high conduction band minimum of MgO layer ensures the blocking of holes and electrons to confine into the corresponding layer. Valence band maximum of NiO layer is altered to more negative values. Li doping also results in decreased work function which is close to the work function of carbon and lower lying valence band position favor the hole transfer between each layer which explains the enhanced charge transfer and increased photocurrent extracted from the Li doped cells. For both doped and undoped NiO layers, hole extraction from the perovskite layer is favorable and high conduction band maxima efficiently blocks electron injection from the perovskite layer. However, for yttrium doped TiO₂ particles a high degeneracy is observed and Fermi level lies above the conduction band of the TiO₂ due to heavy doping. Calculated conduction band minima of Y:TiO₂ particles at 3.80 eV is above the conduction band maxima of the perovskite layer and this situation leads to unfavorable electron transfer from perovskite crystals to the TiO₂ nanoparticles, which in turn suppresses charge injection and causes high charge transfer resistance.

For further investigating the possible origin of reduced photocurrent in Y:TiO₂ based cells and prove the above statements, electrochemical impedance analyses of the cells were conducted for better insight to the charge transfer processes inside the cells. For this purpose, best performing TiO₂/MgO/Li:NiO configuration cell was compared with the undoped cell with TiO₂/MgO/NiO configuration and the Y:TiO₂ based cell with Y:TiO₂/MgO/Li:NiO configuration. In Figure 6.19, Nyquist plots of a Li:NiO based cell measured under dark and illumination conditions and under different bias voltages. In contrast to planar or mesoporous based cells, carbon based devices yield three semi circles or arcs where the low frequency arc is related to the ionic motion inside the cell because of the thickness of the carbon based cells reaching above 2 micron values. The impedance responses of carbon based cells are similar to solid state dye sensitized cells and possess four different features. A series resistance including the overall resistance of the setup, a charge transfer resistance and the capacitance at carbon electrode and the hole conductor appearing at high frequency region, a recombination resistance and related capacitance between

perovskite layer and TiO_2 layer appearing at intermediate frequency region and ionic motion resistance and capacitance at low frequencies [26].

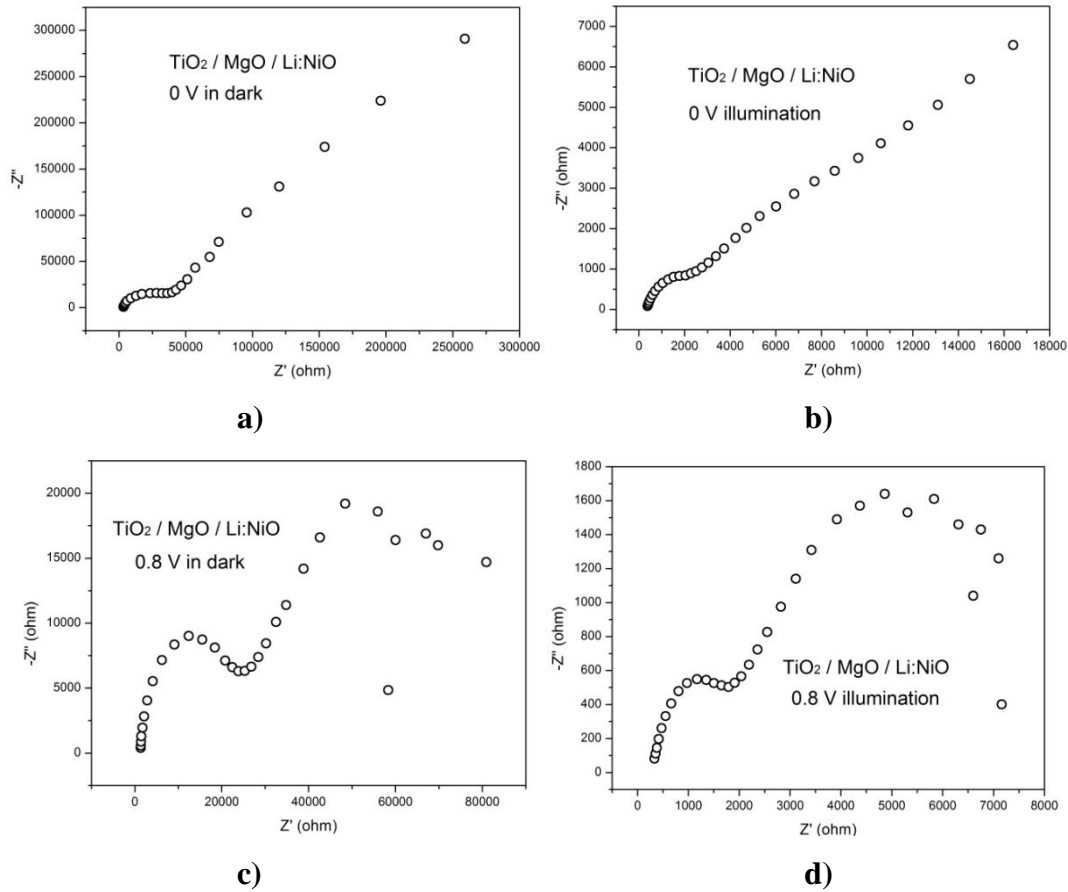


Figure 6.19 Nyquist plots of the best performing cell in a $\text{TiO}_2/\text{MgO}/\text{Li:NiO}$ configuration recorded under dark and illumination for 0V and 0.8 V applied bias.

It is seen from Figure 6.19a and b that upon illumination, semi circles are simply reduced and are shifted to higher frequencies indicating that charge accumulation occurs inside the cells. Under applied bias also, semi circles are reduced to lower resistances and individual arcs become more apparent, while the arc related to ionic motion at low frequencies is highly reduced because of the easier motion of the ions under applied potential. For investigating the effect of Li doping on NiO particles, Li:NiO and undoped NiO based cells were characterized under illumination.

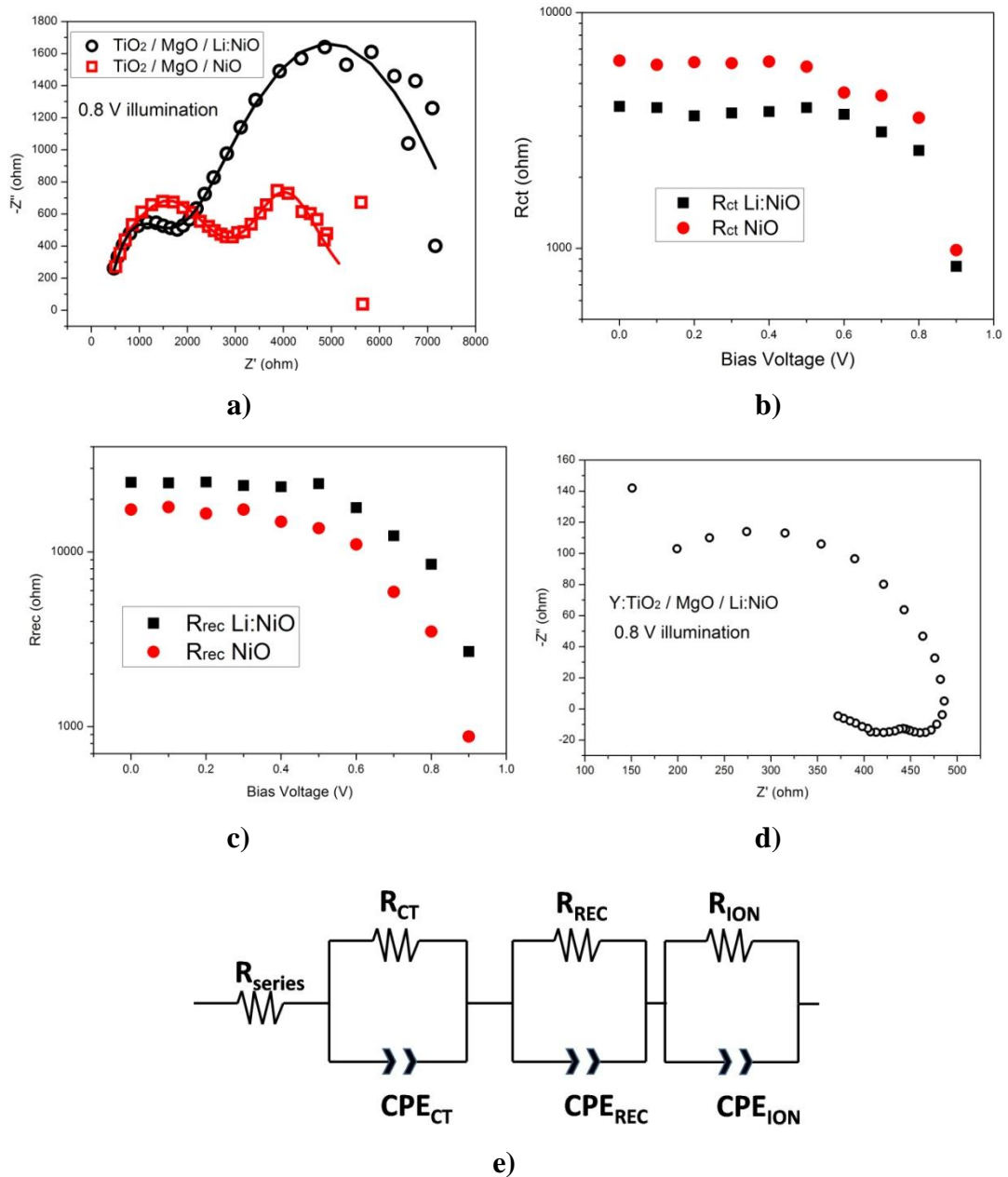


Figure 6.20 Nyquist plots of doped and undoped NiO cells (a), variation of charge transfer resistance at the carbon electrode (b) and recombination resistance at TiO_2 /perovskite interface (c), Nyquist plot of yttrium doped TiO_2 based cell (d) and the equivalent circuit used to fit the data.

Figure 6.20 shows the Nyquist plot of doped and undoped NiO based cells at 0.8 V bias and illumination conditions, together with the calculated charge transfer resistance (R_{ct}) at the carbon electrode and the recombination resistances at the TiO₂/perovskite interface (R_{rec}) of the cells for applied bias potentials up to open circuit voltage of the cells. In Table 6.4, calculated values of the charge transfer resistance and recombination resistances were tabulated with the error values in parentheses.

Table 6.4 Charge transfer resistance (R_{ct}) and recombination resistance (R_{rec}) values of the NiO and Li:NiO based cells calculated from the impedance data.

Applied Bias	NiO based cell		Li:NiO based cell	
	R_{ct}	R_{rec}	R_{ct}	R_{rec}
0 V	6250 (4.1%)	17456 (1.5%)	4012 (3.1%)	25043 (6.6%)
0.1 V	6024 (3.7%)	18012 (1.4%)	3952 (8.9%)	24830 (6.2%)
0.2 V	6157 (0.8%)	16589 (2.4%)	3647 (4.4%)	25101 (0.7%)
0.3 V	6106 (4.3%)	17456 (9.5%)	3754 (0.3%)	24034 (0.4%)
0.4 V	6198 (1.1%)	14879 (4.7%)	3814 (0.6%)	23580 (5.1%)
0.5 V	5891 (12.2%)	13658 (4.0%)	3950 (7.1%)	24598 (1.1%)
0.6 V	4578 (2.1%)	11032 (4.6%)	3709 (3.1%)	17891 (3.7%)
0.7 V	4444 (0.3%)	5899 (11.1%)	3114 (3.3%)	12357 (6.1%)
0.8 V	3578 (1.5%)	3511 (1.5%)	2617 (1.3%)	8501 (12.3%)
0.9 V	983 (3.2%)	879 (2.2%)	839 (2.7%)	2689 (11.1%)

For all bias voltages, charge transfer resistance of the cells at carbon electrode are lower for Li:NiO based cells. This resistance also includes the transport of holes in the hole conducting medium and taking into account the fact that carbon layers are identical for each cell, it is clear that lithium doping can efficiently enhance hole transport and leads to better charge collection at the p-type layer which directly influences the photocurrent and the fill factors. This improvement is a result of both increased conductivity of the powders and more favorable charge transfer between

the carbon layer and the NiO layer upon lithium doping as indicated by the UPS results. Enhanced charge collection at the p-type layer and efficient transport also have a positive impact on the recombination dynamics at the TiO₂ electrode as evidenced by the Figure 6.20c, where at all applied bias voltages, recombination resistance of the Li:NiO based cells are higher than the NiO based cells. Faster hole transport in turn prevents charge accumulation inside the cells and reduces the chance of capturing a hole in the perovskite crystals by the TiO₂ layer. In order to determine the factors underlying the poor performance of the cells, impedance response of the Y:TiO₂ based cells were also recorded and as it can be seen from the Figure 6.20d, a large inductive loop element is observed for such cells. Inductive elements in perovskite solar cells are common and origin of the loop behavior and negative capacitance is considered to be the charge accumulation inside the layer due to poor interfacial charge transfer because of the lack of perovskite layer quality or a strong contact between individual layers [27]. The negative capacitance arises from sudden charge injection from the cell to the system that have accumulated at the interfaces. Due to unfavorable and inhibited electron injection from the perovskite layer to the Y:TiO₂ layer as shown by the UPS analysis, generated electron hole pairs tend accumulate at the perovskite crystals and the NiO layer which then undergo recombination processes. The resulting poor fill factors and strong decline in the photocurrent is related to recombination arising from charge accumulation and insufficient interfacial charge transfer inside the cells as evidenced by both UPS and impedance spectroscopy analyses.

6.4 Conclusions

In this work, flame synthesis method was successfully employed to synthesize yttria doped TiO₂ and lithium doped NiO nanoparticles for carbon based perovskite solar cell applications. XRD and SEM studies showed that pure TiO₂ and NiO nanoparticles can be obtained using the novel methanol combustion method. Lithium doping up to 20% has no observable effect on NiO powders; however yttria doping in small amounts results in formation of rutile phase in the TiO₂ powders. It

was shown that electrical properties of the powders can be enhanced via doping. Chemical analyses of the powders showed that dopant atoms can be effectively incorporated into the host lattice and they are responsible from the observed enhancement in the conductivity of the powders. Electronic band structure study showed that Fermi level and band alignment of the powders can be tuned via doping and yttria doped TiO_2 particles possess degenerate structure. Upon J-V measurements of the cells constructed using the synthesized powders, it was seen that, yttria doping greatly affects the performance of the TiO_2 layers, declining the photocurrent values due to the high conduction band edge of the Y: TiO_2 powders. In contrast, Li:NiO particles increases the charge collection and transport properties and by reducing the overall resistance of the cell, efficiency values were enhanced compared to undoped NiO based cells. Best efficiency value of 9.63% in this work was obtained in FTO/ TiO_2 /MgO/L:NiO/Carbon configuration, proving that doping is an effective way to improve charge collection efficiency in carbon based cells, however amount of doping should be carefully adjusted without inhibiting the electronic band alignment and charge transfer properties for attaining the highest performance from these type of layers.

REFERENCES

1. W. Nie, H. Tsai, A. D. Mohite et al., High-efficiency solution-processed perovskite solar cells with millimeter-scale grains, *Science* 347 (2015) 522-25.
2. O. Ergen, S. M. Gilbert, T. Pham, S. J. Turner, M. T. Z. Tan, M. A. Worsley, A. Zettl, Graded bandgap perovskite solar cells, *Nat. Mater.*, 16 (2016) 522-25.
3. M. Xiao, F. Huang, W. Huang, Y. Dkhissi, Y. Zhu, J. Etheridge, A. G. Weale, U. Bach, Y. Cheng, L. Spiccia, A fast deposition-crystallization procedure for highly efficient lead iodide perovskite thin-film solar cells, *Angew. Chemie*, 126 (2014) 10056-0061.
4. C. Zuo, L. Ding, An 80.11% FF record achieved for perovskite solar cells by using the NH_4Cl additive, *Nanoscale*, 6 (2014) 9935.
5. J. H. Im, I. Jang, N. Pellet, M. Grätzel, N. Park, Growth of $\text{CH}_3\text{NH}_3\text{PbI}_3$ cuboids with controlled size for high-efficiency perovskite solar cells, *Nat. Nanotechnol.*, 9 (2014) 927-32.
6. J. H. Heo, A. Sarkar, Md. K. Nazeeruddin, M. Grätzel, S. I. Seok et al., Efficient inorganic-organic hybrid heterojunction solar cells containing perovskite compound and polymeric hole conductors, *Nat. Photonics*, 7(2013) 486-91.
7. J. Y. Jeng, K. C. Chen, T. Chiang, P. Lin, T. Tsai, Y. Chang, T. Guo, P. Chen, T. Wen, Y. Hsu, Nickel oxide electrode interlayer in $\text{CH}_3\text{NH}_3\text{PbI}_3$ perovskite/PCBM planar-heterojunction hybrid solar cells, *Adv. Mater.*, 26 24 (2014): 4107-113.
8. J. H. Park, J. Seo, S. Park, S. S. Shin, Y. C. Kim, N. Jeon, H. Shin, T. K. Ahn, J. Noh, S. C. Yoon, C.S. Hwang, S. I. Seok, Efficient $\text{CH}_3\text{NH}_3\text{PbI}_3$ perovskite solar cells employing nanostructured p-type NiO electrode formed by a pulsed laser deposition, *Adv. Mater.*, 27(2015) 4013-019.

9. J. H. Heo, S. H. Im, Md. K. Nazeeruddin, M. Grätzel, S. I. Seok et al., Efficient inorganic–organic hybrid heterojunction solar cells containing perovskite compound and polymeric hole conductors, *Nat. Photonics*, 7 (2013) 486-91.
10. S. Ito, Inorganic hole-transporting materials for perovskite solar cell, *Organic-Inorganic Halide Perovskite Photovoltaics*, (2016) 343-66.
11. A. S. Subbiah, A. Halder, S. Ghosh, N. Mahuli, G. Hodes, S. K. Sarkar, Inorganic hole conducting layers for perovskite-based solar cells, *J. Phys. Chem. Lett.*, 5 (2014) 1748-753.
12. Z. Ku, Y. Rong, M. Xu, T. Liu, H. Han, Full printable processed mesoscopic $\text{CH}_3\text{NH}_3\text{PbI}_3/\text{TiO}_2$ heterojunction solar cells with carbon counter electrode, *Sci. Rep.*, 3 (2013) 3132.
13. A. Mei, X. Li, J. Chen, Y. Yang, M. Grätzel, H. Han et al., A hole-conductor–free, fully printable mesoscopic perovskite solar cell with high stability, *Science*, 345 (2014) 295-298.
14. S. Hashmi, S. M. Zakeeruddin, Michael Gratzel et al., High performance carbon-based printed perovskite solar cells with humidity assisted thermal treatment, *J. Mater. Chem. A*, 5 (2017) 12060.
15. C. Tsai, C. Wang, Eric W. Diau. et al., Control of preferred orientation with slow crystallization for carbon-based mesoscopic perovskite solar cells attaining efficiency 15%, *J. Mater. Chem. A*, 5 (2017)739.
16. Z. Liu, M. Zhang, X. Xu, L. Bu, W. Zhang, W. Li, Z. Zhao, M. Wang, Y. Cheng, H. He, p-Type mesoscopic NiO as an active interfacial layer for carbon counter electrode based perovskite solar cells, *Dalton Trans.*, 44 (2015) 3967.
17. Z. Liu, M. Zhang, X. Xu, H. He et al., NiO nanosheets as efficient top hole transporters for carbon counter electrode based perovskite solar cells, *J. Mater. Chem. A*, 3 (2015) 24121.
18. X. Xu, Z. Liu, Z. Zuo, M. Wang et al., Hole selective NiO contact for efficient perovskite solar cells with carbon electrode, *Nano Lett.*, 15 (2015) 2402–2408.

19. K. Cao, Z. Zuo, M. Grätzel, M. Wang et al., Efficient screen printed perovskite solar cells based on mesoscopic TiO₂/Al₂O₃/NiO/ carbon architecture, *Nano Energy*, 17 (2015) 171–179.
20. Y. Sheng, Y. Hu, A. Mei, H. Han et al., Enhanced electronic properties in CH₃NH₃PbI₃ via LiCl mixing for hole-conductor-free printable perovskite solar cells, *J. Mater. Chem. A*, 42 (2016) 16731.
21. W. Chen, Y. Wu, M. Grätzel, L. Han et al., Efficient and stable large-area perovskite solar cells with inorganic charge extraction layers, *Science*, 350 (2015) 944.
22. H. Zhou, Q. Chen, G. Li, S. Luo et al., Interface engineering of highly efficient perovskite solar cells, *Science*, 345 (2014) 542.
23. A. K. Chandiran, F. Sauvage, L. Etgar, M. Graetzel, Ga³⁺ and Y³⁺ cationic substitution in mesoporous TiO₂ photoanodes for photovoltaic applications, *J. Phys. Chem. C*, 115 (2011) 9232–9240.
24. A. Ahmad, S. Buzby, C. Ni, S. I. Shah, Effect of Nb and Sc doping on the phase transformation of sol-gel processed TiO₂ nanoparticles, *J. Nanosci. Nanotechnol.*, 8 (2008) 2410.
25. H. Wang, Q. Chen, H. Chen, Y. Yang, et al., Improving the TiO₂ electron transport layer in perovskite solar cells using acetylacetonate-based additives, *J. Mater. Chem. A*, 3 (2015) 9108-9115.
26. A. Dualeh, T. Moehl, M. K. Nazeeruddin, M. Grätzel, Temperature dependence of transport properties of spiro-MeOTAD as a hole transport material in solid-state dye-sensitized solar cells, *ACS Nano*, 7 (2013) 2292–2301.
27. F. Galatopoulos, A. Savva, I. T. Papadas, S. A. Choulis, The effect of hole transporting layer in charge accumulation properties of p-i-n perovskite solar cells, *APL Materials*, 5 (2017) 076102

CHAPTER 7

CONCLUSIONS AND SUGGESTIONS

Nickel(II) oxide, NiO, is a popular stable wide band gap material, which attracts extensive attention from the solar cell industry and investigations on applications in perovskite based solar cells is still ongoing with promising results. It is the most promising material for robust, highly stable and low-cost third generation solar devices in the solar research society and huge progress have been achieved. It has already been demonstrated that thin-film NiO can be used as a transparent p-type (semi) conducting layer in the perovskite solar cells effectively. In this study, intrinsic and doped NiO nanoparticles and thin films were developed and applied as the hole transport medium in perovskite solar cells. For production of NiO, many routes and methods were studied and summarized in the following.

- In the experimental studies, in order to synthesize intrinsic and lithium doped nickel oxide (Li:NiO) nanoparticles, firstly solvothermal method was chosen. As a novel approach, a direct precipitation method was developed, where decomposition of nickel precursor was conducted in absence of a precipitating agent, only using solvothermal treatment. For deposition of Li:NiO thin films, ultrasonic spray pyrolysis (USP) method was used. In this part of the study, high surface area nickel oxide in nanosheet form were synthesized and doped with lithium successfully. Upon lithium doping, it was observed that electrical conductivity of the powders can be extensively enhanced compared to intrinsic nickel oxide. Resistivity value of the undoped NiO is enhanced from several ohm.cm down to a minimum of 10 ohm.cm value for a Li/Ni atomic ratio of 0.2 in the starting solution. The

hole mobility and carrier concentration values of this sample measured by Hall effect studies are $5.1 \text{ cm}^2 \cdot \text{V}^{-1} \cdot \text{s}^{-1}$ and $9.7 \times 10^{17} \text{ cm}^{-3}$. For the case of sprayed films, lowest resistivity value was observed for the sample having Li/Ni ratio of 0.6 in the starting solution with a resistivity value of 355 ohm.cm. Hole mobility and carrier concentration values are $12.4 \text{ cm}^2 \cdot \text{V}^{-1} \cdot \text{s}^{-1}$ and $1.6 \times 10^{16} \text{ cm}^{-3}$.

- Both lithium doped nickel oxide particles and thin films were produced by ultrasonic technique. These films were grown on FTO substrates in order to form a heterojunction and characterized. Particles were produced using a tubular oven design and characterized by means of electrical and morphological properties. Mixed halide ($\text{CH}_3\text{NH}_3\text{PbI}_{3-x}\text{Cl}_x$) based perovskite solar devices were constructed in spiro-ometad containing and hole conductor free carbon based monolithic configurations and characterized. It was seen for high molarities particles tend to form large and irregular shaped hollow spheres. By decreasing molarity of the solution, regular spheres can be obtained and size of the particles can be reduced down to 100 nm. I-V characteristic of the formed heterojunction for $\text{Li}_{0.1}\text{Ni}_{0.9}\text{O}$ films deposited on the FTO substrate clearly indicate the diode behaviour of the heterojunction which shows the succesful formation of an internal depletion layer and an electrical field for a device of 600 nm FTO layer and 200 nm Li:NiO film. The hole conductor based device yields an efficiency of 2.0%. Monolithic structure yields efficiency of 1.5%. Although monolithic structure gives higher open circuit potential and current density values than hole conductor based device, such cells suffer from low fill factor value which may be attributed to high sheet resistance value of the carbon based collector layer.

- Lithium doped nickel oxide thin films were produced by spin coating technique. These films were grown on FTO substrates and bare glass substrates. Mixed halide ($\text{CH}_3\text{NH}_3\text{PbI}_{3-x}\text{Cl}_x$) based perovskite solar devices were constructed in spiro-OMETAD containing and hole conductor free configurations and characterized. It was seen that spiro-OMETAD based cells show poor efficiency while hole conductor free approach yielded up to 4.35% efficiency. Blocking layer thickness dependent and mesoporous layer thickness dependent studies showed that blocking layer thickness of 70 nm and mesoporous layer thickness 400 nm gave the best efficiencies. For this optimized conditions, two step perovskite deposition and adduct methods were also tried and gave efficiencies up to 4.5%. Most obvious difference between the cells was observed to be open circuit voltages where island like non-continuous nature of lead chloride based method decreases the open circuit voltage. This situation can be explained by the short circuit formation between electron transporting TiO_2 layer and gold back contact which was not observed in two step and adduct methods.
- Inverted type perovskite solar cells and conventional solar cells employing nickel oxide nanoparticles were constructed and characterized. Inverted type solar cells exhibited poor efficiency due to shorting problems and internal charge injection problems. Cells made from NiO nanoparticles and CuSCN in classical configuration were constructed. For this purpose NiO nanoparticles were produced by fuel assisted polymerization technique yielding nickel hydroxide nanoparticles which were converted to nickel oxide after heat treatment. These particles were dispersed in isopropanol and coated on mesostructured TiO_2 based perovskite layers by doctor blading. From photoluminescence studies, it was seen that both CuSCN and NiO can effectively extract charges from perovskite. From I-V measurements, it was seen that CuSCN devices perform better than NiO devices because CuSCN layers can be deposited more homogeneously than NiO layers. In both cases,

CuSCN and NiO can effectively improve device characteristics of the hole conductor free devices by acting like a hole collecting layer.

- Alcohol based NiO nanoparticle dispersion was prepared and used to deposit hole conductor medium for a polymeric substance free perovskite solar cell in mesoscopic n-i-p configuration. In contrast to conventional p-i-n configuration or inverted type perovskite solar cells, nickel oxide layer was spin coated directly on perovskite layer and the perovskite layer was sandwiched between two metal oxides, TiO₂ and NiO, resulting in n-i-p configuration. High surface area nickel oxide nanoparticles were synthesized by precipitation and successfully dispersed in isopropanol with the aid of ball milling, which was confirmed to breakdown the aggregates and stabilize the dispersion without the assistance of a stabilizing agent. This strategy leads to deposition of nickel oxide nanoparticles on perovskite layer without damaging the underneath layer and inhibiting the charge transfer between individual nanoparticles, confirmed by scanning electron microscopy, photoluminescence quenching and J-V measurements. Ultraviolet photoelectron spectroscopy analysis showed excellent matching of the band alignment of nickel oxide layers with that of perovskite. An efficiency of 10.89% was achieved after optimizing the nickel oxide layer thickness and comparative analysis of the cells with a hole conductor free device using J-V measurements and electrochemical impedance spectroscopy revealed that nickel oxide layer possess excellent electron blocking ability and reduces the recombination rate, which also in turn stabilizes the power output and hysteresis of the cells. This strategy is believed to be applicable for other metal oxides employed in charge selective layers of perovskite and organic solar cells.

- Mesoporous carbon based perovskite solar cells have been attracting alternative to thin film perovskite devices by means of low cost and ease of production, reaching efficiencies up to 15%. High internal resistances due to thick mesoporous layers employed is a major problem limiting the performance of this technology. In this work, for the first time charge selective mesoporous layers of TiO₂ and NiO were heavily doped for enhanced electrical conductivity by a novel methanol combustion flame synthesis method. Yttrium doped TiO₂, lithium doped NiO and intrinsic MgO nanoparticles were successfully produced by this method possessing high surface area around 50 m²/g after heat treatment. XRD analyses showed that addition of yttrium atoms into TiO₂ lattice promotes rutile formation without any yttrium oxide phase where lithium addition up to 20% atomic ratio has no structural effect on NiO particles. Addition of dopant atoms results in dramatic increase in the conductivity of powders which were used to construct a conductive mesoporous network in TiO₂/MgO/NiO/C configuration. Although heavily doped Y:TiO₂ layers inhibits charge transfer between perovskite layer, conductive Li:NiO layers lead to enhanced efficiencies compared to undoped particles reaching 9.63% efficiency values for optimized devices which is related to decreased internal resistance and improved charge transport inside the mesoporous network proven by the impedance analysis.

In this work, it has been shown that NiO nanoparticles can be effectively employed as the hole transport medium in conventional n-i-p configuration perovskite cells instead of the low stability polymeric counter parts. It was observed that efficiency of the cells strongly depend on the thickness of the NiO layer, so careful control of the deposition parameters is crucial for attaining the highest efficiency from the cells. In addition, as seen from the impedance spectroscopy results, remnant holes and nanoparticulate structure leads to small hysteresis inside the cells and it is important to develop smaller particles sizes

than 20 nm and deposit these particles homogeneously and hole free on the perovskite layer without damaging the underlying layer, which will lead to higher performance cells.

Effect of heavy doping of the metal oxide charge collecting layers in carbon based solar cells was investigated and it was demonstrated that by increasing the electrical conductivity of the powders, it is possible to enhance the charge collection and efficiency of the devices is possible. However, as seen in the yttrium doped TiO_2 nanoparticles, increased conductivity is not the only parameter, but position of the conduction band and charge transfer effectiveness between individual layers must be taken into account for successful cell operation. For future applications, amount of doping must be optimized for not attaining the highest electrical conductivity, it must be tuned to have proper band alignment with the perovskite layer. In addition, doping the TiO_2 lattice with a trivalent cation like Nb^{+3} instead of the pentavalent Y^{+5} can be a more effective way for increasing the overall conductivity of the TiO_2 particles which can lead to enhanced efficiency of the cells similar to the lithium doped NiO nanoparticles as proven by this work.

CURRICULUM VITAE

PERSONAL INFORMATION

Surname, Name: İçli, Kerem Çağatay

Nationality: Turkish (T.C.)

Date and Place of Birth: 3 August 1984, Ankara

Marital Status: Single

Phone: +90 312 210 59 17

Email: cagatayicli@yahoo.com

Education

2011 - 2018

Middle East Technical University

Micro and Nanotechnology Program, Ph.D

Thesis: K.C. İcli, “Production of Inorganic Charge Selective Layers For Mesoscopic Perovskite Solar Cells”, Ph D. Thesis, Middle East Technical University, May 2018

Supervisor: Prof. Dr. Ahmet Macit ÖZENBAŞ

2007 - 2010

Middle East Technical University

Micro and Nanotechnology Program, M.S.

Thesis: K. C. İcli, “Core Shell Type Nanocrystalline FTO Photoanodes For Dye Sensitized Solar Cells”, M.S. Thesis, Middle East Technical University, August 2010

Supervisor: Prof. Dr. Ahmet Macit ÖZENBAŞ

2002 - 2007

Istanbul Technical University

Metallurgical and Materials Engineering, B.S.

Thesis: K. C. Icli, E. Seckin, A. A. Kunt, F. Satır, S. Aras, “Boyar Maddeli Güneş Pilleri için Geniş Yüzey Alanlı Anot Yapımı”, B.S. Thesis, Istanbul Technical University, May 2007

Supervisor: Prof. Dr. Mustafa ÜRGEN

Research Interests

- Dye sensitized solar cells
- Perovskite solar cells
- Thin films (Transparent conducting oxides)
- Spray pyrolysis deposition
- Sol-gel chemistry of nanoparticle production

Job Experience

- 2006** EREĞLİ Demir ve ÇelikFabrikaları T.A.Ş.- Internship
- 2004** SARKUYSAN Elektrolitik Bakır Sanayi ve Ticaret A.Ş. – Internship
- 2012-2014** “Püskürtme piroliz teknolojisi ile iletken cam geliştirilmesi ve düşük maliyetli boya duyarlı güneş modüllerinde kullanımının araştırılması” Project Assistant, SANTEZ Project

Publications

- **K. C. Icli**, B. C. Kocaoglu, M. Ozenbas, “Comparative study on deposition of fluorine-doped tin dioxide thin films by conventional and ultrasonic spray pyrolysis methods for dye-sensitized solar modules”, Journal of Photonics for Energy, 8(1) (2018) 015501.
- **K.C. Icli**, M. Ozenbas, “Fully metal oxide charge selective layers for n-i-p perovskite solar cells employing nickel oxide nanoparticles”, Electrochimica Acta, 263 (2018) 338-345.
- M. Cosar, **K. C. Icli**, M. Ozenbas, “Plasma assisted low temperature electron beam deposited NiO thin films for electro-optic applications”, Journal of Vacuum Science and Technology A, 36 (3) (2018) 031501.

- **K. C. İcli**, M. Ozenbas, “Dye Sensitized Solar Modules with Embedded Silver Lines”, *MRS Advances*, 1(14) (2016) 991-996.
- B. C. Kocaoglu, **K. C. İcli**, M. Ozenbas, “Optimization of Selective Electrophoretic Deposition and Isostatic Compression of Titania Nanoparticles for Flexible Dye-Sensitized Solar Cells”, *Electrochimica Acta*, 196 (2016) 535–546.
- A. Ghobadi, H. I. Yavuz, T. G. Ulusoy, **K. C. İcli**, M. Ozenbas, A. K. Okyay, “Enhanced Performance of Nanowire-Based All-TiO₂ Solar Cells using Subnanometer-Thick Atomic Layer Deposited ZnO Embedded Layer”, *Electrochimica Acta*, 157 (2015) 23–30.
- **K. C. İcli**, H.I. Yavuz, M. Ozenbas, “Production of core–shell type conducting FTO/TiO₂ photoanode for dye sensitized solar cells”, *Journal of Solid State Chemistry*, 210 (2014) 22–29.
- A. Hoesseini, **K. C. İcli**, M. Özenbaş, Ç. Erçelebi “Fabrication and characterization of spin-coated TiO₂ films”, *Energy Procedia*, 60 (2014) 191 – 198.
- B. Cosar, **K. C. İcli**, H.I. Yavuz, M. Ozenbas, “Photovoltaic performance of bifacial dye sensitized solar cell using chemically healed binary ionic liquid electrolyte solidified with SiO₂ nanoparticles”, *Electrochimica Acta*, 87 (2013) 425– 431.
- A. Hosseini, **K. C. İcli**, H. H. Güllü, “Preparation and characterization of porous TiO₂ thin films by sol-gel method for Extremely Thin Absorber-ETA solar cell applications”, *Turkish Journal of Science & Technology*, 8(2) (2013) 69-79.

Conferences

- **K. C. İcli**, E. Seckin, A. A. Kunt, F. Satır, S. Aras, M. Ürgen, “TiO₂ Nanotube Arrays Produced on ITO Glass for Dye-Sensitized Solar Cell Applications”, *Nano-Tr 3 Nanoscience and Nanotechnology Conference*, Ankara, 11-14 June, 2007.
- **K. C. İcli**, A. M. Özenbaş, “Core-Shell Type Nanoporous SnO₂ Photoanodes for Dye Sensitized Solar Cells” *Solar Tr-1 First Turkish Solar Energy Conference and Exhibition*, Ankara / Türkiye, April 29-30, 2010.
- **K. C. İcli**, A. M. Özenbaş, “Production of Core-Shell Type FTO/TiO₂ Photoanodes for Dye Sensitized Solar Cells” *15. International Metallurgy and Materials Congress*, İstanbul/Türkiye, December 11-13, 2010.
- **K. C. İcli**, H. İ. Yavuz, A. M. Özenbaş, ”Production of Core-Shell Type FTO/TiO₂ Nanoparticles for Dye Sensitized Solar Cells”, *26th European*

Photovoltaic Solar Energy Conference and Exhibition, Hamburg, Germany, 5-9 September, 2011.

- **K. C. İçli**, A. M. Özenbaş, “Surface Modification of FTO Nanoparticles for Enhanced Efficiency of DSSCs”, Solartr-2: Solar Electricity Conference and Exhibition, Antalya, November 7-9, 2012.
- **K. C. İçli**, H. İ. Yavuz, A. M. Özenbaş, “Production and surface modification of FTO nanoparticles for enhanced efficiency of DSSCs”, The 2013 MRS Fall Meeting & Exhibit, Boston, December 1-6, 2013.
- **K. C. İçli**, A. M. Özenbaş, “Production and Characterization of High Performance FTO and ITO Thin Films Using Ultrasonic Spray Deposition For Dye Sensitized Solar Cell”, 2nd International Surface Treatment Symposium, İstanbul, 25-27 June, 2014.
- **K. C. İçli**, A. M. Özenbaş, “An Innovative Silver Line Embedded Substrate Design for Dye Sensitized Solar Modules” 17. International Metallurgy and Materials Congress, İstanbul/Türkiye, September 11-13, 2014.